UNIVERSITY OF LEEDS

High Resolution Imaging of Massive Young Stellar Objects and a Sample of Molecular Outflow Sources

Luke Thomas Maud

Department of Physics and Astronomy

University of Leeds

Submitted in accordance with
the requirements for the degree of

Doctor of Philosophy

September 2013

This thesis is dedicated to my best friend Kyle Luke Stock (1987-2012) and his beautiful daughter Amber Mae Stock. I will always try to be the smartest guy you know.

Acknowledgements

I would like to thank my main supervisors Melvin Hoare and Stuart Lumsden for their guidance throughout my PhD, and Toby Moore for his helpful insight. Furthermore I would like to thank René Oudmaijer for his valuable comments and open door policy, but mainly for being who I consider as my 'physics dad'. I am eternally grateful to Cormac Purcell for withstanding my 'Plague of the day' questioning and support through the first year of my PhD. I also wish to extend a thank you to all Astrophysics department members for their friendly and approachable nature while at Leeds.

I must extend a big thanks to all fellow students who have helped me to keep a reasonable level of sanity and have endured some of my work related rants. Thank you John and Jonny for the admiration you have openly displayed for me through comical motivational posters and extensive lists of my random and sometimes stupid sayings. Thanks to all my friends from home, they know who they are and we've all been through a lot together. I'd like to thank my Grandfather, Otto, for indulging me throughout the bombardment of 'what and why' questions in my early life and continuing that to the stage of intellectual discussion as I have grown.

Last but not least I must thank my Parents Chris and Heidi, and my sister Laura. Without such a loving and supportive family I would not be who and where I am today. They have been my rock and always managed to help me see the positives. I love you all, thank you.

Preface

Chapters of this thesis contain work presented in the following jointly authored publication:

High angular resolution millimetre continuum observations and modelling of S140-IRS1, **L. T. Maud**, M. G. Hoare, A. G. Gibb, D. Sheperd, R. Indebetouw, 2013, MNRAS, 428, 609.

Chapter 2 contains the observational material from the paper. The main author (L. T. Maud) was responsible for the reduction of the data (except that from OVRO) that was obtained via successful proposals by the main author (CARMA A) and by the co-authors (CARMA B and OVRO). The SMA data was recovered from the data archives. The imaging, analysis and interpretation of the data was undertaken by the main author. The primary author wrote the paper for publication and incorporated comments from the co-authors in the final submitted version.

Chapter 3 contains the modelling aspect of presented in the paper. Modelling the environment of the massive young stellar object S140 IRS1 was undertaken by the primary author (L. T. Maud) using existing models developed by Barbara A. Whitney et al. (MC code) and Rémy Indebetouw (Ray tracing code). The resulting ideal images

and output data were compared with those from the observations and from the literature. The comparisons were undertaken with the help of custom programs developed by the main author and those commonly available in the reduction software. As above, the primary author wrote the paper for publication and incorporated comments from the co-authors in the final submitted version.

Abstract

This thesis contains a study of millimetre wavelength observations of massive young stellar objects (MYSOs) both via interferometric and single dish observations. First, the high angular resolution observations (up to $\sim$0.1") from a variety of interferometers of the MYSO, S140 IRS1, are presented. This source is one of only two prototypes that have ionised equatorial emission from a radiatively driven disc wind. The observations confirm that IRS1 has a dusty disc at a position angle compatible with that of the disc wind emission, and confirms the disc wind nature for the first time.

Secondly, the observations of S140 IRS1 are modelled using a 2D axi-symmetric radiative transfer code. Extensive models producing synthetic data at millimetre wavelengths were developed. These models show that on the largest scales, typically accessible with single dish observations or compact interferometric configurations, the spectral energy distribution is relatively unchanged by the addition of a compact dust disc. However, a disc is required to match the interferometric visibilities at the smaller scales. The position angle of the disc is well constrained via a newly developed 2D visibility fitting method. The models however, are degenerate and there are a range of realistic best fitting discs.

The third section presents the single dish observations of the core material traced by $C^{18}O$ around 99 MYSOs and compact HII regions from the RMS survey. A method to calculate the core masses and velocity extent is reported. The method is accurate and robust, and can be applied to any molecular line emission. An updated distance limited sample contains 87 sources and is complete to 10^3 $L_\odot$. It is a representative sample of MYSOs and HII regions. All of the cores harbour at least one massive protostar.

Finally, methodologies to establish outflow parameters via ^{12}CO (3-2) and ^{13}CO (3-2) data are investigated. Multiple techniques are trialed for a well studied test source, IRAS 20126+4104, and a repeatable outflow analysis pathway is described. In more complex regions using the ^{12}CO emission to identify outflows and determine the mass is more difficult and an alternative method is suggested. Moreover, the dynamical timescale of the outflows and the dynamical parameters are estimated in a spatial sense rather than using a simple average. Such analysis will aid in categorising different outflows from the full sample.

Abbreviations

ACSIS	Auto Correlation Spectral Imaging System
AGN	Active Galactic Nuclei
ALMA	Atacama Large Millimetre Array
arcsec/arcsecond	Seconds of Arc
ATCA	Australia Telescope Compact Array
au	Astronomical Unit
CARMA	Combined Array for Research in Millimeter-wave Astronomy
CMB	Cosmic Microwave Background
CMF	Core Mass Function
CO	Carbon Monoxide
CV	Cataclysmic Variable
FWHM	Full Width Half Maximum
GMC	Giant Molecular Cloud
HARP	Heterodyne Array Receiver Program
IMF	Initial Mass Function
IR	Infrared
IRAS	Infrared Astronomical Satellite
IRDC	Infrared Dark Cloud
ISM	Interstellar Medium
JCMT	James Clerk Maxwell Telescope
LSB	Lower Side Band
LSR	Local Standard of Rest
LTE	Local Thermodynamic Equilibrium

MERLIN   Multi-Element Radio-Linked Interferometer Network
MHD   Magneto Hydro-Dynamic
MIDI   MID-infrared Interferometric instrument
MIRIAD   Multichannel Image Reconstruction Image Analysis Display
MSX   Mid-course Space Experiment
MYSO   Massive Young Stellar Object
OMC   Orion Molecular Cloud
OVRO   Owens Valley Radio Observatory
PA   Position Angle
PACS   Paired Antenna Calibration System
RMS   Red MSX source
R-J   Rayleigh Jeans
RT   Radiative Transfer
SCUBA   Sub-millimetre Common-User Bolometer Array
SED   Spectral Energy Distribution
SMA   Sub-Millimetre Array
SNR   Signal to Noise Ratio
SOFIA   Stratospheric Observatory For Infrared Astronomy
UCHII   Ultra Compact HII
USB   Upper Side Band
UV   Ultra Violet
YSO   Young Stellar Object
ZAMS   Zero Age Main-Sequence

Contents

List of Figures

List of Tables

Chapter 1

Introduction

1.1 High Mass Star Formation

Over the last few decades observations have unearthed the sites of star formation, namely dusty, dense molecular clouds in the interstellar medium (Shu *et al.*, 1987). The giant molecular clouds (GMCs) rival globular clusters as the largest and most massive objects in the galaxy with spatial scales of the order 100 pc, masses sometimes exceeding 10^5 M$_\odot$ and mean H$_2$ densities around 100 - 300 molecules cm^{-3} (Lada & Shu, 1990). The intrinsically cold (10 - 20 K), dusty, dense clouds are opaque to visual and shorter wavelengths of light and can only be probed at infrared, sub-millimetre/millimetre and radio wavelengths. Early investigations of these regions discovered that stars are likely to form in condensed cores within the much larger scale clouds (Myers *et al.*, 1983). The dust in these star forming clouds can effectively absorb visual and UV radiation emitted by obscured young stellar objects (YSOs) in their infancy. The radiation subsequently heats the cloud which then re-radiates over infrared and longer wavelengths. Thanks to technological

advancements the regions of star formation can now be probed in some detail at these wavelengths. Figure 1.1 shows the complex distribution of material in the Cygnus X star formation region as traced by an isotope of carbon monoxide, ^{13}CO (1-0). Cygnus X is one of the richest and most massive regions of star formation nearby, at a distance of less than 3 kpc, and is known to contain many OB stars, HII regions and high mass star formation sites.

Essentially YSOs form from the gravitational collapse of a dense core in a molecular cloud. This formation scenario is generally accepted for low mass stars (0.3 - 8 $M_\odot$) (Shu *et al.*, 1987). A core within an isothermal spherical cloud loses magnetic and thermal support and ultimately undergoes gravitational collapse. The collapsing core produces a protostar and disc. An accretion disc is the natural result of angular momentum conservation for the rotating collapsing cloud. While the protostar is accreting material from the disc, jets and outflows are driven in the direction parallel to the axis of rotation. When the infall/accretion terminates, the surrounding disc begins to disperse and provide conditions in which a planetary system may form. The final remnants of material from the formation process are driven away as the star ignites and begins life on the main sequence burning hydrogen.

Massive stars ($M_\star \geq 8$ $M_\odot$) are very important in the grand scheme of star and galaxy formation. They disrupt the interstellar medium (ISM) during formation and evolution, be it from large expanding HII regions or in cataclysmic supernova explosions. Massive stars inject ionising UV photons and enriched elements into the environment throughout the majority of their lives. They have been thought to halt local formation of stars due to energetic winds, outflows and explosions (Herbig, 1962), but can also stimulate and trigger successive formation deeper in
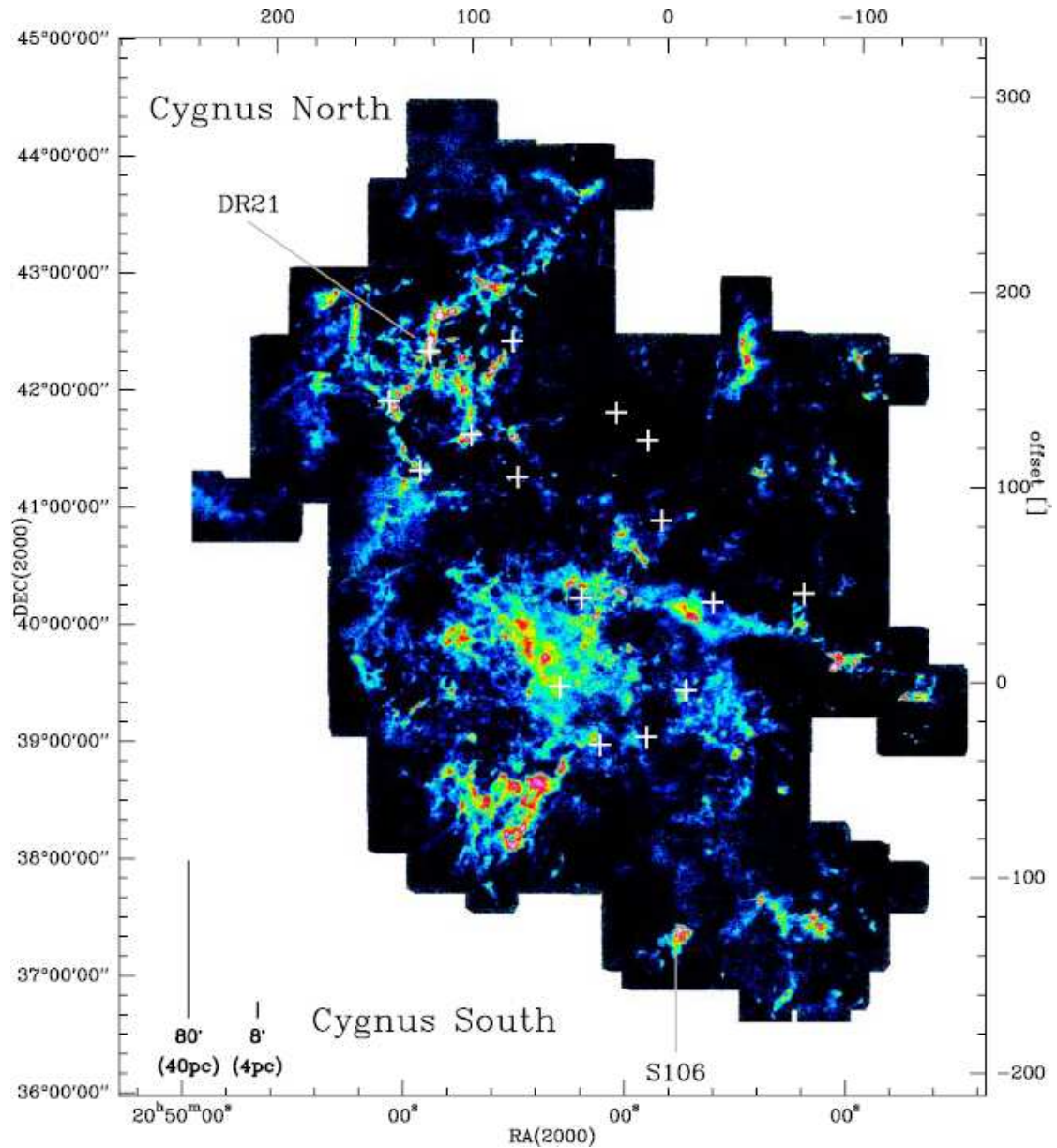
Figure 1.1: Intensity map of ^{13}CO in the Cygnus X region. White crosses mark the position of thermal HII regions and the massive star formation sites DR21 and S106 are labelled. Taken from Schneider *et al.* (2011)

the cloud (Elmegreen & Lada, 1977). Despite new technologies and intensive research, their formation mechanisms are poorly understood (see the detailed review by Zinnecker & Yorke, 2007)

1.1.1 The Problem in Context

Unlike low mass stars, high mass stars are rare objects. Due to the intrinsic rarity and requirement of a large mass reservoir, massive young stellar objects are at much greater distances than their low mass siblings. Massive stars are born in cluters, where any single formation region could contain multiple stars at varying stages of evolution. Most observations therefore cannot probe the formation sites with sufficient resolution to disentangle the evolutionary stages and the energetic processes that are ongoing.

Moreover, high mass protostellar phases do not lend themselves to observations at short wavelengths, where current telescopes have high spatial resolution abilities. Massive YSOs are still deeply embedded in the natal cloud when hydrogen burning begins as their evolution is much more rapid. This is best exemplified with a simple comparison of the dynamical, free fall time of the dense cloud core and the Kelvin-Helmholtz timescale for contraction. The timescale for the gravitational collapse of a dense core is given by,

$$\tau_{ff} = (\frac{3\pi}{32G\rho_c})^{1/2} \qquad (1.1)$$

where G is the gravitational constant and ρ_c is the cloud density. For a typical number density of a GMC ~ 300 cm^{-3} the upper limit for the conversion of molecular material into stars would be around 2×10^6 years. Molecular clouds

are known to be hierarchically clumpy on all scales which effectively decreases the free fall time for denser gas on smaller lengthscales. Furthermore, the collapse of clouds can also be affected by stellar feedback from HII regions, winds, outflows and supernova. However, such details are not required for a simple comparison of timescales presented here.

During gravitational collapse, the molecular clouds heat up to the point where a protostar core is massive and luminous enough to begin hydrogen burning on the main sequence. The Kelvin-Helmholtz timescale for this contraction is given by,

$$\tau_{KH} = \frac{GM_\star^2}{R_\star L_\star} \tag{1.2}$$

where $M_\star$, $R_\star$ and $L_\star$ represent the protostellar mass, radius and luminosity respectively. Using parameters for a solar mass star the time scale is quite long, of the order 3×10^7 years in comparison to that of a 20 M$_\odot$ star where $\tau_{KH} \sim 2 \times 10^4$ years. High mass stars ($M_\star \geq 8$ M$_\odot$) have $\tau_{KH} < \tau_{ff}$, and hence are still deeply embedded while being highly luminous and actively accreting in a collapsing cloud. MYSOs therefore do not have well defined, observable, pre-main sequence formation stages, unlike low mass sources (see Adams *et al.*, 1987; Lada & Shu, 1990).

1.1.2   A Theoretical Picture

One major question arises for massive star formation as MYSOs achieve a high luminosity, according to the luminosity mass relationship (L$_\odot \propto$ M$_\odot^{3.3}$), in a very short time, given by the Kelvin-Helmholtz timescale. The question is, 'how can ac-

cretion continue and produce massive stars in the face of such an intense outwards radiation pressure from the protostar on the surrounding dust envelope?' An initial numerical analysis of the radiation problem by Kahn (1974) established that a star of approximately 20 $M_\odot$ could be formed by invoking an idealised spherical infall. However, this mass is much lower than the most massive stars observed. Using interstellar dust opacities, Wolfire & Cassinelli (1987) find that infall cannot occur and produce massive stars. Only when the dust is modified to be of a lower opacity or the accretion rate is increased to $\sim 10^{-3}$ $M_\odot$ yr^{-1} (orders of magnitude larger than expected at the time) can massive star formation take place. Early evidence for massive star formation via a disc-like structure was seen by Yorke & Sonnhalter (2002). Here the collapse of a slowly rotating, spherical, massive cloud was followed. For all cloud masses investigated a deviation away from spherical symmetry is observed as the protostar evolves. Radiation forces on the dust act to remove material in the polar directions while accretion continues in the equatorial plane via a dense, flattened, disc-like structure. For the most massive molecular cloud (~ 120 $M_\odot$) a star of 40 $M_\odot$ was formed.

Subsequently, some theories find that high stellar densities ($> 10^8$ star pc^{-3}) can form high mass stars via coalescence of low mass cores within typical formation times (Bonnell & Bate, 2002). The stellar densities required are 10^5 times greater than in the Orion Nebula Cloud. Bonnell & Bate (2002) found that for a cluster of 1000 low mass stars, 19 mergers occur while material is continually accreted from the surrounding gas. The mergers of lower mass stars in the denser, clustered regions produce the most massive stars in the simulations. These massive stars are generally formed in binary systems or small sub-groups. Interestingly a circumbinary disc structure is observed around the most massive binary in the

system and could be linked with an outflow, although discs are not found around the other massive sources.

In competitive accretion models, stars accrete material in a highly non-uniform manner dependent upon their location with a cluster (Bonnell *et al.*, 1997). In this scenario the most massive stars are formed in the deepest gravitational potential well at the centre of the cluster. Stars that spend less time near the deep potential well on the outskirts of the cluster are much less massive than those located centrally. The final stellar masses in the cluster are dependent mainly on the accretion process and independent of the seed stars' initial masses. However, different initial masses have a noticeable effect on the masses of stars in binaries. These stars are sufficiently close such that they will accrete from the same region of the cluster and any initial mass difference will be amplified by competitive accretion of the gas. Otherwise initially equal mass stars will accrete at a similar rate.

Within models by McKee & Tan (2003) the cores are not supported by thermal pressure as in low mass isothermal cores, but by the turbulence in the region. Observed turbulent velocities are seen to increase with increasing core radius (Larson, 1981). The turbulent support leads to denser cores which have short free fall times when they begin to collapse. Consequently, the accretion rates for massive stars produced from the collapse of a small and very dense core are high. The turbulent core model overcomes the accretion rate problem by incorporating turbulence and high pressures in the region (McKee & Tan, 2003). The time to form massive stars is many times the free fall time of the very dense core but is roughly the free fall time of the of the region or clump the core is embedded in. As these regions are denser than for an isothermal solution the characteristic formation time is $\sim 10^5$ years. The corresponding accretion rate is therefore naturally high at 10^{-3} $M_\odot$

yr^{-1}.

More recently, high resolution modelling in 2D and 3D indicate that accretion onto the central protostar is moderated by a disc and can overcome the extreme radiation pressures opposing collapse (Krumholz *et al.*, 2009; Kuiper *et al.*, 2010, 2011). In all models flattened disc structures similar to those seen by Yorke & Sonnhalter (2002) emerge but are much longer lived. The discs are responsible for the highly anisotropic density distribution and the thermal radiation pressure escapes much easier in the less dense polar directions. Once an outflow (and cavity) forms it can evolve as the star continues to accrete material. Currently these models are the most promising for an up scaled version of low mass star formation applied to massive stars that can also reproduce some observables.

To some extent each scenario may play a role in massive star formation, however there is no present consensus as to the most important or dominant pathway and how the models may combine.

1.2 An Evolutionary Sequence

Due to the hierarchical structure of molecular clouds it is a difficult task to separate sub-structures and investigate the changing environment of massive star formation in detail. Such issues are compounded by ongoing formation occurring in complex regions on differing timescales. The current consensus is that stars form within dark cloud complexes and GMCs. The formation stages for massive stars within GMCs have been described by many authors (e.g. Beuther & Shepherd, 2005; Beuther *et al.*, 2007; Evans *et al.*, 2002; Hoare & Franco, 2007). Notably, there is no consensus to the nomenclature of these smaller scale stages. Table 1.1 lists

the names and parameters of the stages adopted here. The following subsections review each formation stage in chronological order.

Table 1.1: Physical properties for star forming structures. Adapted from Beuther *et al.* (2007); Klessen (2011); Kurtz *et al.* (2000).

	Size (pc)	Mean Density (cm^{-3})	Mass ($M_\odot$)	Temperature (K)
GMC complex	~ 50	100 - 300	$\sim 10^6$	10-15
Local cloud region/clumps	5-20	10^2 - 10^4	10^2 - 10^4	10 - 30
Cold Core	< 0.5	10^4 - 10^6	10^3 - 10^4	10 - 50
Hot Core	~ 0.1	10^5 - 10^7	10^2 - 10^3	100 - 300
UCHII region	< 0.1	$> 10^4$	-	$\sim 10^4$

1.2.1 Clumps, Cold Cores, IR-dark Clouds

The precursor to all star formation are cold, dense condensations of material within large irregular complexes. These dense cores are the regions that collapse and eventually heat up to create stars. GMCs, as mentioned, are huge clouds complexes ($\sim$ 100 pc) with a large mass reservoir and above average number densities compared to the ISM. They are highly clumpy in nature and harbour denser cores and condensates. The locally dense ($> 10^4$ cm^{-3}) regions or cores are cold $\sim$ 10-30 K and many molecules can be frozen out in the form of ices on dust grains making observations to probe their parameters difficult (see Klessen, 2011). In some regions the densities may reach up to 10^6 cm^{-3} and are regarded as cold, pre-stellar cores. Note, some authors name such regions high-mass starless cores, if the mass reservoir is large enough such that massive stars can potentially form (Beuther *et al.*, 2007). These very early regions of star formation are prior to the formation

of any heating source and are strong cold dust and gas emitters (N_2H^+, CO, NH_3, HCN, HCO^+) at millimetre and sub-millimetre wavelengths (e.g. Mauersberger *et al.* (1992); Schneider *et al.* (2011); Simpson *et al.* (2011) and Evans (1999) for review). Consequently there are no characteristics of active star formation, such as complex chemistry or bipolar outflows. For a historical review on the evolution molecular clouds see Larson (1994), or, Klessen (2011) for a more recent account.

Infrared-dark clouds (IRDCs) (e.g. Egan *et al.*, 1998) are a classification of objects that has recently emerged. These objects are seen as large dark filamentary complexes (extinction features) against the bright infrared background of the galaxy and are a substructure within GMCs. Confusingly, some IRDCs have ongoing star formation and have hierarchical regions or clumps within them that can harbour dense, cold cores and hot cores (see next sub-section), and protostars (e.g. Rathborne *et al.*, 2011). IRDCs themselves cannot be classified as an actual evolutionary stage, however they are important targets in which to investigate star formation. IRDCs are much more massive analogues of 'Bok globules' (Bok & Reilly, 1947) which are known sites of relatively isolated low mass star formation (e.g. Launhardt *et al.*, 2010). 'Bok globules' also have a hierarchical structure with small dense, cold cores within larger, less dense clumps. They have similar parameters to IRDCs, however they are simply much less massive and will only form one or two low mass star in comparison to multiple massive stars and clusters of low mass stars in IRDCs. IRDCs without active star formation are therefore excellent candidate sites for studying cold cores and the very earliest stages of massive star formation.

Observations of these initial stages of star formation are important for understanding the processes by which stars form. Star formation theories must correctly

represent the initial mass function (IMF). This is the distribution of stellar masses at 'birth'. The IMF itself maybe set at an early stage and intrinsically related to the mass distribution of the cold pre-stellar cores, the core mass function (CMF). The IMF originally investigated by Salpeter (1955) indicates that the mass distribution follows a power law, $dN/dm \propto m^{-\alpha}$ where $\alpha \sim 2.3$, for masses m, above about 1 $M_{\odot}$. Now it can be considered a 2 part power law for masses > 0.08 $M_{\odot}$ (Figure 1.2). $\alpha \sim 1.3$ for masses between 0.08 and 0.5 $M_{\odot}$ and α follows the Salpeter power law for masses > 0.5 $M_{\odot}$ up to a maximum mass of ~ 150 $M_{\odot}$(see Kroupa, 2002). Works by many authors (e.g. Ikeda & Kitamura, 2011; Lada *et al.*, 2008; Simpson *et al.*, 2008, and references therein) present CMFs that are very similar in shape to the IMF (also see Figure 1.2). Although scaling efficiency factors are required for a complete overlap in different regions, it appears that the mass of the cold cores alone could set the birth mass of the stars, and that subsequent evolution may follow very specific pathways. It may not be necessary to have a one to one ratio of core to star mass, simply that the CMF shape is maintained throughout various star formation models and feedback processes such that the IMF closely matches what is currently observed (e.g. Chabrier & Hennebelle, 2010; Smith *et al.*, 2009; Swift & Williams, 2008). Such results are still the subject of great debate.

1.2.2   Hot Cores

Hot cores are defined as such due to their temperature ($T > 100$ K). Initially investigated in detail by Cesaroni *et al.* (1992, 1994) they are dense, hot and compact regions within the larger molecular cloud complex. With high angular resolution observations (1") probing the optically thick, high brightness temperature molec-
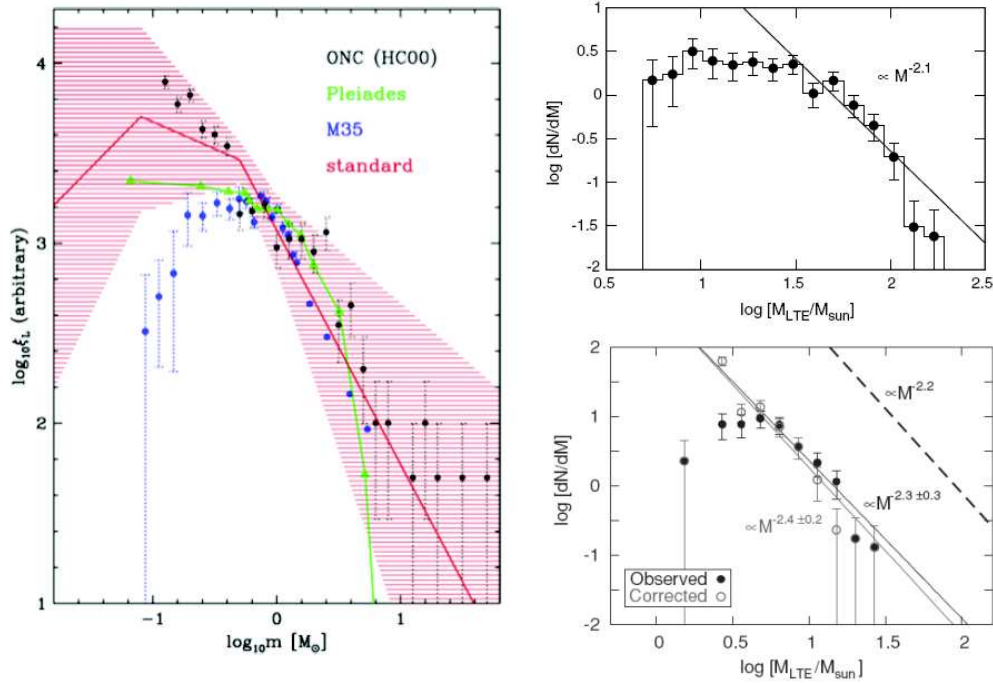
Figure 1.2: Left: Initial mass function (IMF) of nearby star clusters, taken from Kroupa (2002). Right: (Top) Core mass function (CMF) of the Lynds 1204 molecular cloud as traced with $C^{18}O$ (1-0), taken from Ikeda & Kitamura (2011). (Bottom) CMF of Orion molecular cloud 1 region traced with $C^{18}O$ (1-0), taken from Ikeda & Kitamura (2009). Note the striking similarity between the slopes.

ular lines, they are seen to have densities $> 10^7$ cm^{-3} and physical diameters $<$ 0.1 pc (Kurtz *et al.*, 2000). Hot cores are the immediate site for massive star formation, and may contain a single source or a cluster of protostars at a range of evolutionary stages. Due to the central heating by high mass protostars they are chemically rich in organic molecules and are observable in high excitation molecular lines (e.g. Cesaroni *et al.*, 1994; Plume *et al.*, 1992). However, some hot cores may not be internally heated, but are in the close proximity to an external HII region acting as the heating agent (e.g. Mookerjea *et al.*, 2007).

The hot core, G31.41+0.31, mapped by Cesaroni *et al.* (1998) has a temperature increase towards the central region, providing evidence for a central heating candidate. The strong centimetre continuum emission on sub-arcsecond scales suggests the presence of deeply embedded MYSOs that are likely powering radio jets (Cesaroni *et al.*, 2010). Even at the high resolution of these observations it is difficult to disentangle the velocity structure of the distant (~ 8 kpc) hot core. The velocity gradient seen in the CH_3CN molecular tracer can be attributed to both a large scale, rotating, infalling toroid structure (Beltrán *et al.*, 2004, 2005) or a bipolar outflow (Araya *et al.*, 2008). There could be a complex interplay between rotation and outflow, and the infalling material that would be expected if material is being channelled to a central massive protostar. Subsequent observations of outflow and rotation tracers, CO and CH_3CN still cannot distinguish the source of the velocity gradient (Cesaroni *et al.*, 2011).

Recent high angular resolution observations by Jiménez-Serra *et al.* (2012) of the hot core AFGL2591-VLA3 reveal a temperature gradient, and a clear chemical segregation. The chemical species are distributed in three concentric shells about the hot core on scales < 3000 au. H_2S is peaked at the source location, whereas HC_3N shows a double peaked structure about the continuum peak location and CH_3OH forms a larger ring like structure surrounding the continuum emission. Such segregation likely relates to the physical structure of the hot core. The more centrally located tracers have higher gas temperatures compared with the lower temperatures of tracers in the more distant shells. The temperature gradient on these scales are indicative of internal heating of the hot core by a high mass protostar. Interestingly the global kinematics of the molecular envelope are fitted well with a Keplerian like rotation, suggesting a single physically bound entity.

Clearly there is evidence of outflow activity and large scale Keplerian rotations, suggestive of infall and accretion. It is however unclear if these are caused by a single source or multiple sources given the typical distance to the hot cores (d $\geq$ 2 kpc). Is the internal heating source at an early evolutionary stage, such that it is simply a gravitationally collapsed core, hot enough to release the molecules from ices, or is there a more developed luminous source heating the surrounding clump and causing the complex chemistry (e.g. G10.47+0.03 Cesaroni *et al.*, 2010)? Is the large scale rotation an extension of a much smaller accretion disc on the scale of $\sim$ 100 au? Similarly, are the large scale outflows only driven by a single massive protostar within the hot core or a cluster of low or high mass sources?

1.2.3 MYSOs

Here one single internal heating source of a hot core is regarded as a massive young stellar object (MYSO). MYSOs are also known as a high mass protostellar object (HMPO) (e.g. Beuther *et al.*, 2007). These are luminous ($\geq 10^4$ L$_\odot$) mid-infrared bright point sources that have not yet ionised their surroundings (e.g. Davies *et al.*, 2011). Their thermal emission peaks at $\sim$ 100 μm. They are known to drive large scale outflows, analogous to low mass YSOs (Beuther *et al.*, 2002c; Ridge & Moore, 2001; Zhang *et al.*, 2001, 2005) (see Section 1.5 for details) and have compact, weak, ionised stellar winds (e.g. Tofani *et al.*, 1995) and/or radio jets (Marti *et al.*, 1993). MYSOs are distinguishable from Ultra Compact HII regions (UCHIIs) where the ionised material originates from the surrounding medium rather than material from the star/disc itself in the ionised wind phase (Hoare & Franco, 2007). However, there are only a few examples of circumstellar discs around these objects (e.g. Cesaroni *et al.*, 1999; Patel *et al.*, 2005; Shepherd & Kurtz, 1999) (see Section 1.3

for more details).

Figure 1.3 presents a collection of literature figures depicting the emission from the exemplary source IRAS 20126+4104. IRAS 20126+4104 is a close source (d < 2 kpc) and has been observed at a wide range of wavelengths including the infrared, X-ray, millimetre and radio. It is one of the best known disc/jet-outflow systems. Rotation signatures are seen in transitions of the CH_3CN molecule and large, high velocity outflows have been traced using the CO molecule (Cesaroni *et al.*, 1997, 1999; Shepherd *et al.*, 2000). Interestingly the MYSO is embedded in a core of around 230 $M_{\odot}$ and diameter of roughly 0.4 pc, slightly larger than the usual hot core description (Estalella *et al.*, 1993). The large scale bipolar CO outflow appears to have a north-south geometry, whereas the H_2, HCO^+ and SiO tracing the outflow closer to the source have a more southeast-northwest orientation. The difference of direction could be caused by the precession of the outflow axis. Cesaroni *et al.* (2013) use sub-arcesecond near-IR observations to detect scattered light from the innermost region of the disc/jet and trace the jet itself (see Section 1.5). The H_2 emission delineates the jet, however it appears very asymmetric and brighter at the location of the red-shifted outflow lobe. This is the opposite to what is expected given the orientation of the outflow as the lobe pointing toward the observer should be brightest. Although this source is an MYSO, there are still contributions to the tracers observed from other sources within the system which could complicate the interpretation. Overall, a general picture is emerging of a few MYSOs forming in a similar scenario to their low mass siblings, however, it is not clear whether these MYSOs are representative of the general population.

MYSOs are rare due to the IMF slope and their short formation timescales, as previously mentioned, hence obtaining evidence for disc/jet-outflow systems is dif-
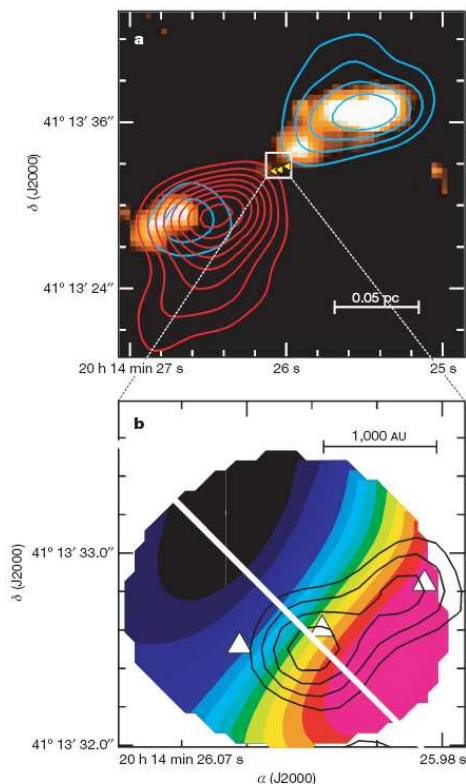
Figure 1.3: Illustration of the disc and bipolar outflow source IRAS 20126+4104. Top: Colour scale indicating the H_2 (2.2 μm) emission line tracing the jet path overlaid by the bipolar molecular outflow traced by HCO^+ (1-0) line. The blue and red contour colours indicating blue and red shifted outflow lobes. The triangles are H_2O maser spots. Bottom: The 3.6 cm continuum map in contours overlaid on a velocity map measured by the $C^{34}S$(5-4) line, where blue and red now indicate blue and red shifted rotation. Note the rotation axis is almost perfectly perpendicular to the outflow axis, as expected in a disc/jet-outflow system.

ficult. Initial surveys using the IRAS point source catalogue (Molinari *et al.*, 1996; Sridharan *et al.*, 2002) are biased to objects away from the bright galactic plane and suffered source confusion due to the poor angular resolution (2-5 arcmin) at 100 μm (where the source emission peaks). The Red MSX [1] Source (RMS) survey (Lumsden *et al.*, 2002, 2013) is an unbiased survey of MYSOs drawn from the

---

[1]http://www.ast.leeds.ac.uk/RMS/

much higher angular resolution (18 arcseconds) MSX mid-infrared survey of the Galactic plane (Egan *et al.*, 2003). Extensive multi-wavelength follow-up observations with resolutions of 1-2 arcseconds have been conducted to identify source properties, contaminant sources and to attempt to resolve the distance ambiguity (see Cooper *et al.*, 2013; Mottram *et al.*, 2010; Urquhart *et al.*, 2007, 2008, 2009, 2012). The result is a sample of around 500 candidate MYSOs. Interestingly, there appears to be a genuine lack of MYSOs above 10^5 $L_\odot$ as shown in Mottram *et al.* (2011a). The authors suggest that the progenitors to the most massive UCHII regions could be mid-IR faint or dark. Furthermore, the lack of very luminous sources is consistent with the fact that the MYSO lifetime is comparable or less than the Kelvin-Helmholtz timescale where the star would become luminous enough to ionise its surrounding. Hence very luminous sources would not have an MYSO phase as they would already be ionising the region.

1.2.4 UCHII regions

UCHII regions are produced when massive stars are hot and luminous enough to generate copious amounts of Lyman continuum radiation and ionise their environment. As these sources are ionising the surrounding medium they represent more evolved sources at the later stages of star formation. However, due to the compact nature of the UCHII region, the powering source must be relatively young in terms of a massive star's lifetime, i.e. a newly born massive star. These regions characteristically have diameters < 0.1 pc and electron densities upwards of 10^4 cm^{-3} (Wood & Churchwell, 1989a).

The characteristic size of a spherical UCHII region formed in a uniform, neutral medium is given by the Stromgren radius (Strömgren, 1939). The volume of

the ionised material is such that the rate which the star produces ionising photons equals the rate at which hydrogen recombines. Typically the UCHII front will progress in an irregular fashion as the density of the surrounding medium varies. Surveys (e.g. Wood & Churchwell, 1989b) find a variety of different morphologies, deviating from the idea spherical case, such as cometary, core-halo, shell and irregular. Inside UCHII regions the temperatures are of the order 10^4 K and destroy the complex chemistry (e.g. Cyganowski *et al.*, 2012). However, UCHII regions clearly provide a heating source for the surrounding material, liberating molecules and developing a rich organic chemistry as depicted by studies of some hot cores outside the ionisation front. The pressure gradient between the hot ionised gas and surrounding medium causes the UCHII region to further expand, and develop into a larger HII region.

Amongst other problems surrounding UCHII regions, one puzzle is why MYSOs do not ionise their surroundings (and become UCHII regions) when they are luminous enough. Hoare & Franco (2007) argue that the suggested quenching of ionised regions (Walmsley, 1995), causing them to be small and dense, is unrealistic as this would require perfectly spherical infall. Observationally, the density environment surrounding MYSOs is not uniform and is likely effected by bipolar outflows from the source itself in earlier evolutionary phases. One solution is the removal of the ionising radiation in the MYSO phase. Recent modelling, with accretion rates up to 10^{-3} M$_\odot$ yr^{-1}, indicate that the radius of a protostar with a mass of $\sim$ 6 M$_\odot$ will swell up and exceed 100 R$_\odot$. The swelling causes a decrease in the effective temperature of the MYSO and reduces the amount of Lyman continuum photons that would ionise the medium. It is the redistribution of entropy that causes the outer layers to puff up as the inner regions become less opaque and

heat is transported to the outer layers (Hosokawa & Omukai, 2009). Deuterium burning occurs in these models but is not a major contributor to the swelling as was previously thought (Palla & Stahler, 1992). With such high accretion rates, the effective temperatures will not be great enough to produce ionising photons until the contraction phase. In the models contraction begins when the energy flux reaches the surface of the protostar and escapes without being absorbed, causing the star to lose heat and contract. During the contraction phase the temperature increases until hydrogen burning begins. For high accretion rates (10^{-3} M$_\odot$ yr^{-1}) the protostar must grow to ~ 20 M$_\odot$ before it joins the main sequence and becomes hot and luminous enough to power a UCHII region. At these accretion rates the stellar temperature is lower for a given mass and main sequence burning is postponed (Hosokawa & Omukai, 2009). At lower accretion rates contraction begins at a lower stellar mass. Realistically, the contraction phase may be occur earlier as the accretion rate decreases in time as the mass reservoir runs out.

1.2.5 Overview

The evolutionary stages presented for massive stars are complex and overlapping. Although different stages are evident, it is not fully understood how they combine and how the observables change. Due to the hierarchical structure in the star forming environment, one cloud may harbour a wide variety of formation stages making the isolation and observation of each difficult given the distances and angular resolutions involved. Furthermore, the stages do physically overlap as star formation is a continual process. Each stage cannot be compartmentalised start to finish. Finally, there is also an issue with the loose use of nomenclature, to describe, what is to all intents and purposes the same source/region/complex/cloud/clump.

The schematic shown in Figure 1.4 is presented in an attempt to summarise the structures discussed.
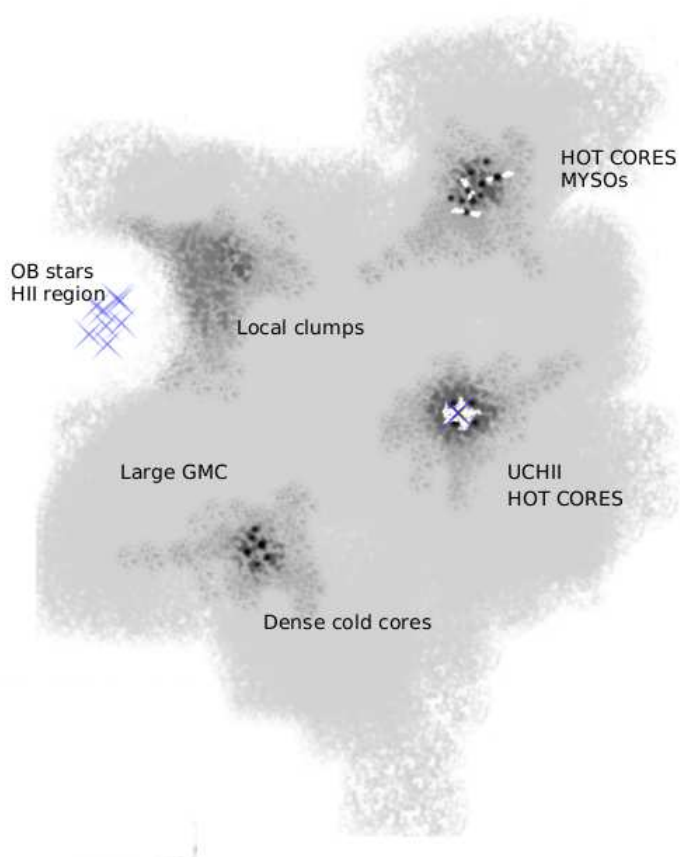
Figure 1.4: Schematic summarising the various star formation evolutionary stages observed within a GMC. Hot cores can be associated with MYSO or UCHII heating sources, as text. Outflows can be driven from MYSO regions. Dense cold cores are located within the local clump over densities in comparison with the larger scale GMC. A cluster of main sequence OB stars driving an expanding HII regions is the end result of star formation process.

1.3 Discs

Discs surround stars throughout their formation stages and in some cases well into their main sequence lives. Accretion discs are the natural consequence of a collapsing, rotating structure where angular momentum is conserved. They are viscous and allow the accretion of matter on to the YSO as angular momentum can be removed from the system. Discs may also provide the launching platform for jets and outflows. Discs around low mass YSOs can be observed directly over a range of wavelengths. While protostars are still embedded in a dusty environment their discs can be detected at sub-millimetre and millimetre wavelengths (e.g. Eisner *et al.*, 2008; Jørgensen, 2011). However, once the surrounding envelope has dispersed and the protostar is no longer deeply embedded, shorter wavelength observations can be undertaken to image discs (e.g. Burrows *et al.*, 1996). Furthermore, these low mass sources are plentiful and nearby (50-200 pc) such that scales of ~ 10 au are easily accessible. In the context of massive star formation, accretion discs are a promising scenario for building up high mass stars (as previously mentioned, Krumholz *et al.*, 2009; Kuiper *et al.*, 2010, 2011), however, observational evidence is currently lacking.

Despite the fact that MYSOs are still deeply embedded in their natal envelopes and are much more distant, observations using similar techniques to those used in low mass YSO studies have been employed. Utilising interferometry at sub-millimetre and millimetre wavelengths the dust and molecular emission from discs on scales of ~ 500-1000 au can be probed for typical source distances of ~ 2 kpc, and on slightly smaller scales for the few closer MYSOs. One such example of a nearby source is that of IRAS 20126+4104 where molecular observations detect a

rotating structure perpendicular to a bipolar outflow (see section 1.2.3). Another disc source is Cep A HW2. Observations of molecular lines and dust continuum indicate a rotating disc (Patel *et al.*, 2005; Torrelles *et al.*, 2007) which is in a perpendicular orientation to 600 km s^{-1} proper motion jets observed at radio (centimetre) wavelengths (Curiel *et al.*, 2006). The left panel of Figure 1.5 shows the disc emission perpendicular to the jet emission while the right hand panels shows how the radio jet 'knots' evolve overtime.

One major problem with dust continuum observations at millimetre wavelengths is that of disentangling the envelope dust emission with that emanating from a compact dust disc. As massive protostars are still deeply embedded in their natal clumps it is hard to decouple the disc and surrounding envelope, even at subarcsecond resolutions. The most reliable method of disc detection is via molecular line observations where velocity gradients can be attributed to rotation (Cesaroni *et al.*, 2007). With the full commissioning of the Atacama Large Millimetre/submillimetre Array (ALMA), unprecedented resolutions will be achieved and allow much smaller structures to be probed around MYSOs, focusing on dust and molecular emission from compact accretion discs. Furthermore, the image quality will be revolutionary given the significant increase, by a factor of ~ 20, in the number of baselines compared to current millimetre facilities. The ability to probe both small and large scales simultaneously could find a distinction between clump, core, envelope and disc scales.

Currently there is more evidence for large scale, disc-like, Keplerian rotating structures known as toroids (as briefly mentioned in section 1.2.2) than for small scale ~ 100 au rotating discs. Toroids are associated with hot cores as they are chemically complex. It is the velocity gradients of the complex molecular
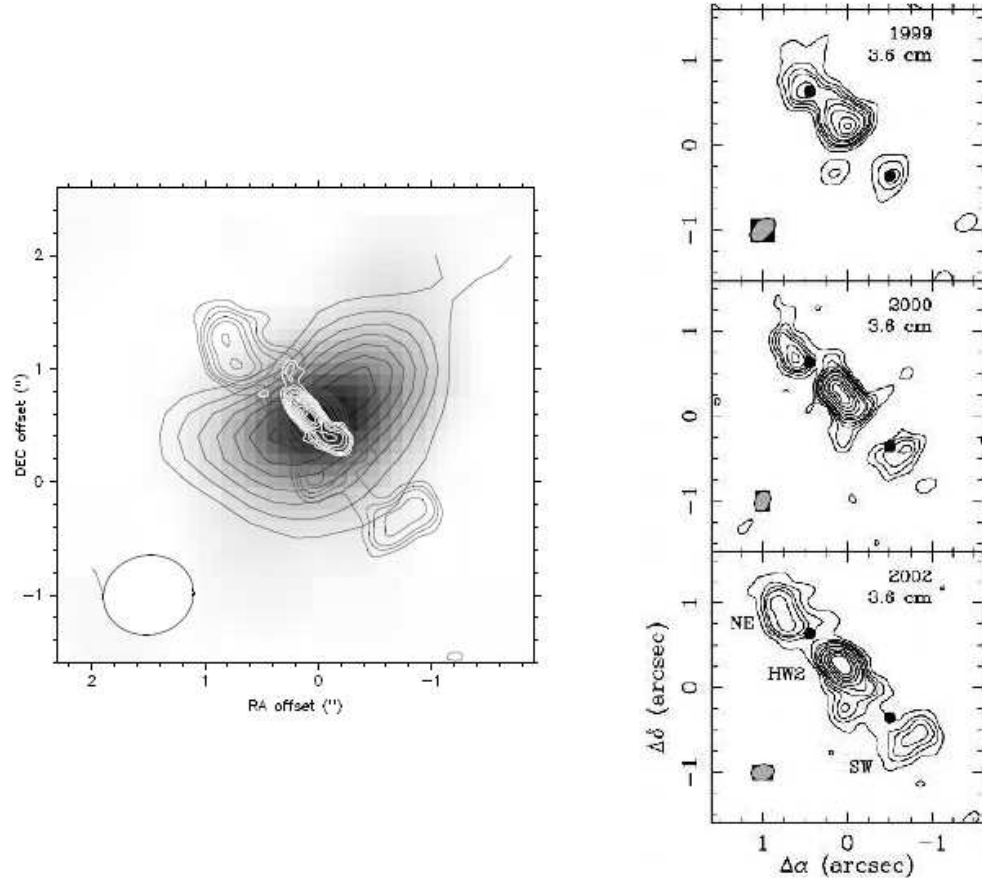
Figure 1.5: Left: The dust continuum image of Cep A HW2 overlaid with the integrated CH$_3$CN in dark contours and 3.6 and 1.3 cm radio jet emission in the light grey and white contours respectively. The CH$_3$CN emission is consistent with a rotating disc and is perpendicular to the radio (jet) emission. Right: The evolution of the 3.6 cm radio jet emission is depicted. The jets have ~ 600 km s^{-1} proper motions after correction for the system inclination. Taken from Hoare & Franco (2007).

tracers which imply rotation. Beltrán *et al.* (2011a) detail CH$_3$CN and ^{13}CO observations of 3 hot cores. One has an embedded UCHII region while the others are in close proximity to UCHII regions and likely contain MYSOs. All of the hot cores show evidence of rotation in the CH$_3$CN tracer, however, the emission is not

fully perpendicular to the outflows as traced by the ^{13}CO emission. On the physical length scales probed, outflow, and possibly infall could contaminate the observed CH_3CN line emission assumed to be tracing pure rotation. However, the resolution at present is currently insufficient to understand the degree of contamination. The model by Wang *et al.* (2012) including both Keplerian rotation (perpendicular to the outflow) and radial expansion suitably matches the observations of HDO and $H_2^{18}O$ for the previously discussed hot core AFGL2591-VLA 3. Interestingly, these tracers are not reported to be significantly influenced by the outflow and it is the outwards radial motion that causes the peculiar velocity maps where the orientation between the rotational and outflow tracers are not perpendicular.

There appears to be a divide between disc and toroid sources. The latter are usually associated with more distance sources that cannot be probed on small physical scales but appear to have large scale rotation. This is exemplified in a table of sources presented in Beltrán *et al.* (2011a), where the most distance sources are more massive and have much larger rotational radii. Cesaroni *et al.* (2007) note that toroids typically have masses comparable or greater than that of the embedded massive star compared to 'true' discs which have masses less than the protostellar mass. The detection of rotation in toroids could suggest some form of underlying disc. However, without high resolution observations of a particular embedded source or sources within the hot core it remains unclear whether the large scale rotation is related to a much smaller protostellar disc.

Observations are not constrained solely to the sub-millimetre/millimetre regimes. Recently Ilee *et al.* (2013) presented high spectral resolution observations of the CO 2.3 μm band-head emission from 20 MYSOs selected from the RMS survey. This is the largest study to date for MYSOs and is analogous to early observations

of low mass YSOs (e.g. Carr, 1989). The band-head can be fitted assuming emission from a disc and can offer insights into the structure and orientation of the inner disc region a few au from the MYSO itself. Infrared interferometric observations can now probe scales of tens of au around MYSOs and directly resolve the emission from hot disc material. 2.4 mas (milli arcsecond) resolution observations at near infrared wavelengths by Kraus *et al.* (2010) resolve a $\sim 13 \times 18$ au disc around the source IRAS 13481-6124, while their complementary observations at other wavelengths indicate the presence of an outflow perpendicular to the disc via local CO emission and distant faint bow shocks. However, IRAS 13481-6124 is a particular case where observations of the source in the near infrared are possible, likely due to its slightly more evolved nature (Kraus *et al.*, 2010). Due to the surrounding large molecular envelope and unfavourable viewing angles, typically, most MYSOs cannot be observed directly in the near infrared and only scattered light can be used to investigate the source (e.g. GGD27, Aspin, 1994).

Davies *et al.* (2010) find that IR emission from the southern nebula around the MYSO, W33A, is from scattered light as a ratio between CO and Brγ emission is constant with position, i.e. both trace the same structure. This would not be expected were the regions emitting directly. Comparison of the emission directly from the source and that scattered from the southern nebula allows the investigation of line profiles with source inclination. The CO band-head emission is interpreted as arising from a disc as emission from the source has a broader velocity profile than the scattered emission from the southern nebula where the path of light to the disc is at lower inclinations. Less rotational broadening of the scattered emission is consistent with the disc being orientated perpendicular to the outflow.

A noteworthy disc detection technique using IR and optical wavelength emission is that of spectro-astrometry (Oudmaijer *et al.*, 2011; Wheelwright *et al.*, 2012). Here, the photo-centre position of emission can be found as a function of velocity. Position-velocity plots of the emission are well fitted by that of a Keplerian rotating disc. This technique can be applied to emission from Be type stars. Due to the larger optical depths it might not be possible to detect the same spectral lines towards massive protostars and the technique may not be applicable. Davies *et al.* (2010) however, use this technique to investigate the Brγ emission from the MYSO, W33A, and attribute it to a fast outflow (see Section 1.5).

1.4   Ionised Winds

Interferometric observations at centimetre wavelengths are typically employed to study the emission from UCHII regions or the strong ionised stellar winds and jets from MYSOs. Evidence for winds can also come from infrared observations of the HI emission lines (e.g. Bunn *et al.*, 1995). The width of the Brα, Brγ and Pfγ indicate sources with outflowing material at velocities of 100-200 km s^{-1}. The ionised wind phase can take the form of a jet that is aligned with the bipolar outflow such as the MYSO, Cep A HW2. These ionised jets could be driven by magnetohydrodynamical forces as for low mass YSOs (see Section 1.5). On the contrary there are a couple of sources that exhibit the opposite morphology. S106 IR (Hoare *et al.*, 1994) and S140 IRS1 (Hoare & Muxlow, 1996) have radio emission elongated perpendicular to the outflow axis, i.e. aligned with the inferred axis of a disc. These observations suggest the emission is from an ionised disc wind. Multi-epoch observations of S140 IRS1 by Hoare (2006) are consistent with the emission

arising from a disc wind, as proper motions do not support a jet interpretation. Figure 1.6 shows no evidence of jet like motion for S140 IRS1, compared to the clear jet evolution for the MYSO, Cep A HW2 (Curiel *et al.*, 2006). Hoare (2002) suggest that disc winds could be part of the evolutionary sequence as other more deeply embedded MYSOs such as Cep A HW2 (de Wit *et al.*, 2009) and GGD27 have well resolved radio jets. Furthermore, in the very earliest stages MYSO discs could be magnetically active and form well collimated jets, whereas more evolved sources become radiatively dominated and equatorial disc winds develop. More observational evidence is required.

A promising model for disc wind emission in MYSOs has been developed by Drew *et al.* (1998). They suggest that radiation from the disc and protostar in a near main sequence configuration can act upon matter in the surface of an accretion disc. The radiation pressure acting on the spectral lines produces a slow, dense, equatorial wind and can have a faster, low density, bipolar component. This model could explain the equatorial disc wind from S140 IRS1 as well as the velocities of the infrared HI lines.

Disc wind emission is also though to be present in other disc systems. A radiation driven disc wind from an accretion disc around Active Galactic Nuclei (AGN) consists of a slow, dense, vertical flow of material lifted from the disc, that is then blown radially from the strong UV radiation of the central source (Proga, 2004; Proga *et al.*, 2000). However, these disc winds differ due to the addition of ionising X-rays that effect the line driving force. Disc outflows are also seen in cataclysmic variables (CVs) via P Cygni profiles of strong UV lines. The updated radiation driven wind models indicate the agreement of the bulk wind properties and a qualitative consistency of the line profiles with observations

for CVs, i.e. the disc wind scenario is responsible for the disc outflows observed (see Proga, 2003; Proga *et al.*, 1998, and references therein). Furthermore, Proga *et al.* (1998) suggest that one of their models can be crudely applied to an MYSO with an accretion disc. In this case, the mass loss would be in a steady state and equatorial. Notably, these cases all consider purely radiatively driven disc winds and do not include magnetic fields. Magnetically driven winds do not require radiation pressure and can be important in low luminosity systems, like low mass YSOs and in highly over-ionised systems, in AGN (Proga, 2004, 2007). In the context of star formation the magnetic fields are thought to be responsible for collimating the outflowing material into a jet (see Section 1.5).
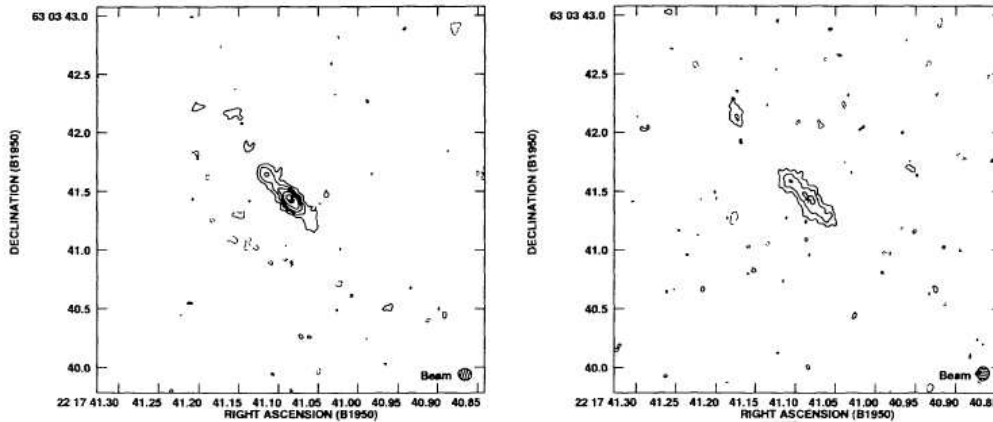
Figure 1.6: 5 GHz MERLIN observations of the disc wind source S140 IRS1 taken 5 years apart. The 0.11" resolution clearly resolves the disc shape of the emission. Taken from Hoare (2002).

1.5   Jets and Outflows

Much like discs, jets and outflows are also a ubiquitous phenomena. Jets and outflows are present on a multitude of scales, black holes at the centre of AGN power relativistic jets (see Lister *et al.*, 2009), young stars, both low and high mass have jets and outflows (e.g. Arce *et al.*, 2007; Bally *et al.*, 2007; Richer *et al.*, 2000) and even brown dwarfs, failed stars, can have weak outflows (Whelan *et al.*, 2005). It is not surprising then, that these jet/outflow sources are ones with discs, as discs and jets are intrinsically related. Outflowing material can provide a means to remove angular momentum from the system and even aid accretion by punching holes in the surrounding envelope and allowing radiation pressure to escape (e.g. Pudritz *et al.*, 2009). The study of molecular outflows from protostars therefore gives some insight into the formation of these objects at more easily accessible resolutions compared to discs, i.e. at millimetre wavelengths outflows can be investigated in large samples with single dish telescopes, whereas discs require much more time intensive interferometric observations. For more distant sources interferometric observations are still required, but the resolution constraints are generally within the limitations of current observatories. Jets and outflows from protostars can be probed by a variety of different wavelengths, from X-rays to radio, and emit both continuum radiation and spectral lines and are associated with masers. Thus a wide range of observations can be undertaken.

1.5.1   Low Mass Protostars

Jets from low mass star forming sites can sometimes extend to parsec scales in length and shock excite Hα and forbidden lines such as [SII], [OI], [OII] and [FeII]

(e.g. Agra-Amboage *et al.*, 2011; Reipurth *et al.*, 1997). Optical and near-infrared observations are possible for some more evolved lower mass sources that are not as deeply embedded as their higher mass counterparts. Observations of molecular tracers such as CO and SiO at sub-millimetre and millimetre wavelengths can probe younger, more deeply embedded low mass YSOs, (and deeply embedded MYSOs) (see reviews by Arce *et al.*, 2007; Richer *et al.*, 2000). Figure 1.7 shows the striking CO outflow of HH211 observed by Gueth & Guilloteau (1999). Here the fast CO outflow is more highly collimated and lies within a cavity of slower moving material. The low mass source itself is thought to be young due as it is not detected in the optical/infrared and has a low dynamical timescale for the outflow. Infrared H_2 emission is detected and traces the shocked material coincident with the head of the CO outflow well away from the source. This suggests a jet driven origin for the molecular flow. Furthermore, millimetre continuum emission at the base of the outflow is well resolved into an elongated structure and is likely emission from the compact accretion disc. Such results depict the ideal formation scenario of low mass YSOs with an accretion disc and a large scale bipolar jet/outflow.

For low mass YSOs there appears to be an evolutionary development of CO outflows. Richer *et al.* (2000) and Arce *et al.* (2007) indicate that younger, more embedded sources (e.g. HH211) have jet driven, collimated molecular outflows not seen in the optical, whereas less embedded sources (e.g. B5 IRS1 Velusamy & Langer, 1998) have wide angle, hollow cavities reminiscent of reflection nebula in similar systems. Here the CO must be flowing down the cavity walls driven by a much wider angle wind. The two most successful outflow driving models describe fast jets that produce highly collimated outflows and winds that generate poorly collimated, wide opening angle outflows (see Cabrit *et al.*, 1997). In both of these
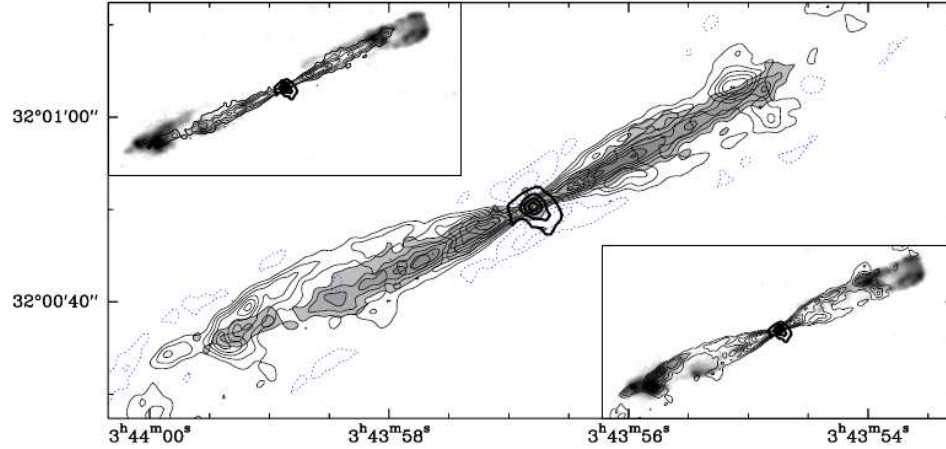
Figure 1.7: Image of the HH211 outflow. In the main panel the greyscale filled contours depicts the fast CO outflow while the low velocity CO outflow is overlaid as unfilled contours. The black contours show the 1.3 mm dust emission, likely arising from a disc. The top left and bottom right panels show the H$_2$ shocked emission overlaid with contours of the fast and slow molecular outflow components respectively. Image taken from Richer *et al.* (2000).

models the molecular material is swept up from the local, ambient environment. Neither the jet driven or wind driven models can explain the full range of morphologies and a superposition of both driving forces, weighted according to the evolutionary stage of the source, maybe required (Arce *et al.*, 2007).

The models discussed in the review by Cabrit *et al.* (1997) detail the observables after injecting the jet or wind individually into the surrounding medium, they do not however, detail how such driving forces are actually created. Therefore, the bigger question is how is the driving force itself generated, and how does it evolve? Two prominent models are those of magnetically collimated disc winds (Pudritz *et al.*, 2009) and magnetically generated X-winds (Shu *et al.*, 1988, 2000).

In the X-wind model, at the x point the effective gravity is reversed allowing a centrifugally blown wind to be pushed away from the central protostar. In a simplified sense the x point is the region where the disc and star meet. In circumstances without a magnetic field the infalling material would not be rotating fast enough to orbit at the larger radii and would be redirected onto the star. Shu *et al.* (1988) discuss that if the magnetic field is sufficiently strong the material will co-rotate with the star (and disc) and be accelerated parallel with the magnetic field lines and away from the protostar. The focusing of the X-wind would be enough to create bipolar outflows, but they would not be collimated enough to produce the pencil beam like collimated flows. However, Shu *et al.* (2000) report that as the X-wind expands into a less dense ambient medium, the local low collimation will produce highly collimated jets on parsec scales, as are observed.

The collimated disc wind model, in contrast to the X-wind model, drives and collimates material from the magnetised disc itself at radii around 0.5 au (Pudritz *et al.*, 2009). dependent upon the amount of mass in the disc wind the degree of collimation can change and reproduce the wide range of collimated flows observed. In both cases the magnetic field lines would become wound and material should flow up parallel to them. Recent observations by Klaassen *et al.* (2013) suggests such a geometry. Her ALMA science verification observations of the CO outflow indicate a corkscrew morphology, similar to the winding of magnetic field lines. Such observations are very promising for the study of disc and outflow systems around YSOs.

1.5.2   High Mass Protostars

Massive molecular outflows and radio jets are observed in regions of high mass star formation. The previously mentioned MYSOs, Cep A HW2 and IRAS 20126+4104, have proper motion radio jets and, a H_2 jet and molecular outflow, respectively. IR observations of W33A by Davies *et al.* (2010) find evidence that Brγ emission is from the outflow using spectro-astrometry. The position angle of the very high velocity small scale emission is coincident with that of the much larger scale CO molecular outflow.

Observations at millimetre wavelengths are similar to those of young low mass star forming regions (e.g. Beuther *et al.*, 2002c; Ridge & Moore, 2001; Shepherd & Churchwell, 1996; Zhang *et al.*, 2001). Molecular outflows are ubiquitous to MYSOs. However, the detection of the outflow phenomena itself is not enough to simply link low mass and high mass star formation scenarios, i.e. to confirm discs as the accretion source in MYSOs and the driver of outflows (see below). A similar formation picture maybe plausible if there were a unified outflow generation mechanism related to accretion discs. If outflow parameters of MYSOs are similar (scaled up) to low mass sources they could imply a similar outflow driving mechanism and a similar formation scenario. The key evidence of a scaled up formation scenario is provided by Cabrit & Bertout (1992) and Shepherd & Churchwell (1996) who report a correlation spanning five orders of magnitude, between the outflow force, power and the mass flow rate with the bolometric luminosity (L_{bol}) of the source.

One problem is that MYSOs sources are typically drawn from heterogeneous samples that may be subject to Malmquist type biases, i.e. brighter sources are

preferentially detected. Beuther *et al.* (2002c) study 26 MYSOs and young HII regions, from a sample subject to a rather strong luminosity-distance bias, and find some evidence of outflow parameter correlations with luminosity, similar to lower mass sources. The small sample size and possible biases could be a major factor driving the trends seen. A counter example is the study of Ridge & Moore (2001) who investigate 11 outflows from MYSOs at the same distance of 2 kpc in an attempt to minimise biasing. The correlation in outflow dynamics and source luminosity is weak, but again, the sample is small. Wu *et al.* (2004) compiled an up to date sample of 391 high velocity outflows at the time of publishing. Although this sample is heterogeneous and observations were taken with a range of different telescopes it is believed that the statistical results from a large number of sources will prevail. However, the surveys used to select higher mass sources will still be biased towards more luminous targets. Overall there appears to be a correlation of outflow mass, luminosity and force with the bolometric luminosity of the source. The relationship suggests a general trend between low and high mass star formation and is shown in Figure 1.8. Although they discuss uncertainties it is unclear whether all outflow parameters are calculated consistently between the compiled samples. To date no such investigation has been performed. The results are promising, but a study of a well selected sample of sources using a consistent analysis methodology is still required.

A particularly hard parameter to establish for MYSO outflows is the collimation. Single dish surveys typically lack the spatial resolution to resolve the outflows and disentangle them from other confusing flows from other sources (this can also be the case for some low mass outflows (e.g. HH288 Gueth *et al.*, 2001)). Beuther & Shepherd (2005) detail 15 interferometric observations of outflows from MYSOs
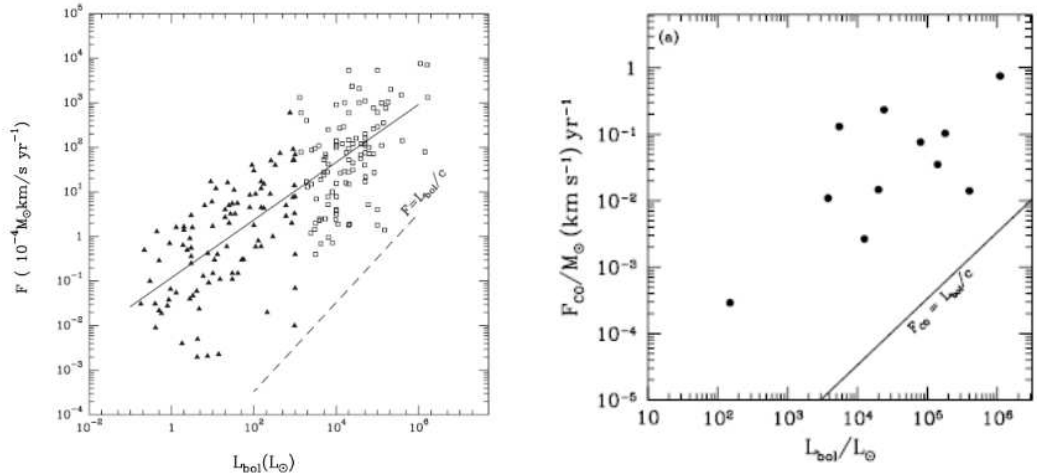
Figure 1.8: Outflow force vs. the bolometric luminosity of the source for the up to date sample from Wu *et al.* (2004) (left) and from the distance limited sample from Ridge & Moore (2001) (right). Both have similar trends scaling with source luminosity, however either the samples could have selection biases or are simply too small to draw firm conclusions.

and suggest a possible evolutionary trend analogous to that of low mass YSO outflows (see Figure 1.9). In a simplistic fashion, younger objects have well collimated outflows, supporting a similar outflow driving mechanism, and hence similar formation scenario as low mass objects. When older sources ionise their surroundings and UCHII regions develop they drive less collimated winds and therefore produce less collimated outflows. There are caveats with such a picture. It is not clear whether the dynamical timescale is representative of a source's evolutionary status (e.g. Curtis *et al.*, 2010) or whether outflow collimation is a function of source mass or luminosity. The collimated flows from early B type stars could be similar to those of low mass objects, whereas the wide angle outflow from O type stars (e.g. Sollins *et al.*, 2004) could be intrinsically different and not related to evolution. Beuther & Shepherd (2005) report that the lack of collimated flows in O

stars could actually be due to the rapid source evolution. It would be extremely rare to detect O stars very early in their MYSO phase and they may already have developed strong ionising winds and wide angle CO outflows when they are detected. A much more intensive investigation at high spatial resolutions is required. Such a study will be possible with ALMA.
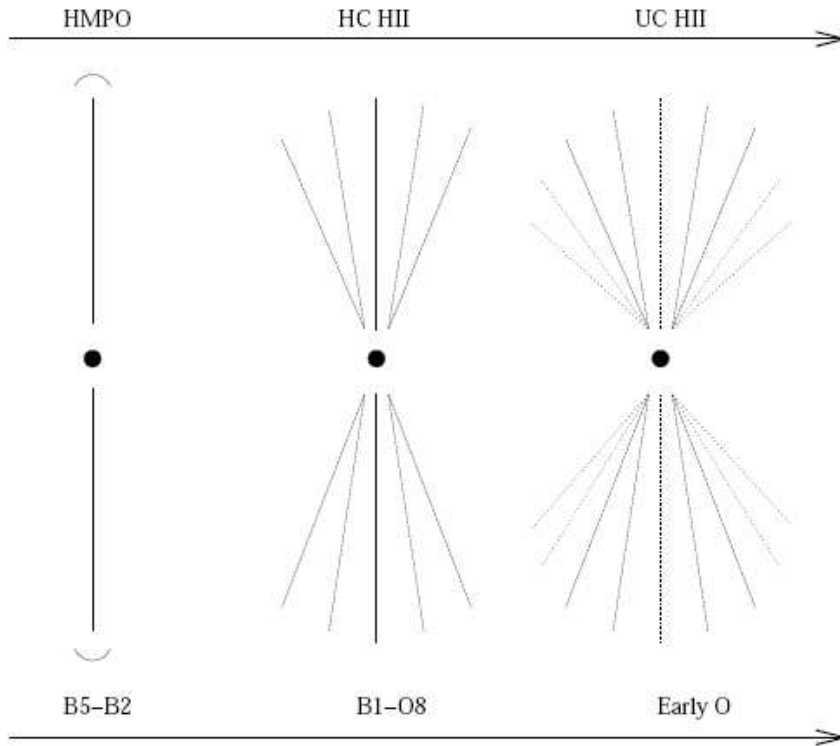
Figure 1.9: The evolutionary picture presented by Beuther & Shepherd (2005) indicate a change of collimation with source evolution from MYSOs (HMPOs) to compact HII region. Furthermore, the suggestion is also made that stellar type may have a role.

One model presented that supports the outflow evolution scenario is that of Vaidya *et al.* (2011). Here outflows are launched from the massive protostars in

the same manner as low mass sources via magnetocentrifugal acceleration. Observations support this argument as magnetic fields are estimated from the emission in the HH80-81 jet, assuming the emission is non-thermal and due to synchrotron electrons (GGD27, Carrasco-González *et al.*, 2010). The model investigates a variety of parameter space to give a comprehensive view of outflow evolution with respect to stellar mass, magnetic flux and radiation driving strength. In a simplistic sense the addition of the radiation force acts to decollimate the flow when it is turned on. This has a more profound effect when the magnetic field strengths are weak. As the MYSOs evolve to larger masses the radiation force increases according to the stellar evolution models of Hosokawa & Omukai (2009). The relatively stronger radiation pressure acts to increase the decollimation with increasing mass. One caveat as noted by Vaidya *et al.* (2011) is the lack of true knowledge regarding the exact jet launching radius. The launch radius could influence how the radiation forces effect the geometry of the outflow. Nevertheless, the model provides the first detailed investigations on the effect of the radiation pressure from MYSOs on magnetically collimated outflows. Extremely high resolution observations to probe the jet launching scales are ideally required. Unfortunately such observations are even beyond the capabilities of ALMA.

1.6 Aims and motivation of this thesis

There are two approaches to understanding massive star formation that are presented in this thesis. They are the very high spatial resolution studies of one particular source and a large observational sample of many objects at lower spatial resolutions.

The high resolution work is focused on the prototype equatorial ionised disc wind source S140 IRS1, introduced in Section 1.3. The aim here is to detect a dusty disc around the source to either confirm or oppose the suggested radiatively driven equatorial disc wind nature of the radio emission. A follow on to the observational work is the modelling of the source environment using the well established models of Whitney *et al.* (2003a,b) as applied to low mass sources. The aim here is to establish whether a scaled up disc and outflow environment can reproduce the observations at high resolution and the multi-wavelength information presented in the literature.

The lower spatial resolution work focuses on a sample of 99 MYSO and UCHII sources extracted from the RMS sample. These objects are observed in the CO (3-2) molecular line transition. In addition to the usual ^{12}CO molecular outflow tracer, both isotopologues ^{13}CO and C^{18}O are observed. One aim is to establish whether the observed core properties of the regions vary significantly with typical source properties or evolutionary status. The second is to establish a systematic method to calculate outflow parameters in a consistent and reproducible manner with the view to compare and contrast outflow properties for the large number of sources.

The high resolution observations will help understand where S140 IRS1 fits in the massive star formation scenario, while the low resolution sample will investigate possible trends in source parameters.

Chapter 2

High resolution millimetre continuum observations of S140 IRS1

High spatial resolution observations of only a few sources can aid in piecing together a comprehensive massive star formation scenario. The detailed observations can probe much smaller structures than are accessible with much larger surveys, especially at millimetre wavelengths. At these wavelengths single dish telescopes can at best reach single figure arcsecond resolutions, whereas using combinations of dishes, or antennae in an interferometric array can achieve sub-arcsecond resolutions. At these scales and wavelengths the colder emission from dust discs around YSOs can be investigated.

This Chapter presents, analyses and discusses the high spatial resolution interferometric observations at millimetre wavelengths of the S140 region. Each set of observations are taken with different interferometric arrays in a range of configurations, each sensitive to different spatial scales. These observations, in conjunction

with literature data at other wavelengths, are used to provide new insights into the S140 region and the MYSO, S140 IRS1.

2.1   Introduction

The Sharpless 140 (S140) star forming region (Sharpless, 1959) associated with the Lynds 1204 dark dust cloud (L1204 Lynds, 1962) is at a distance of 764 ± 27 pc (Hirota *et al.*, 2008). An embedded source, S140 IR, was originally discovered by Blair & Vanden Bout (1974) as the brightest new infrared source associated with a CO peak in their observations. Later observations of S140 by Beichman *et al.* (1979) resolve the infrared emission into three distinct sources, IRS1, 2 and 3. S140 IRS1 (here after IRS1, formerly S140 IR) is the brightest with an estimated luminosity of $\sim 8.5 \times 10^3$ $L_\odot$ (see Chapter 3). Plot a) in Figure 2.1 shows the embedded infrared source in the dense molecular cloud core within the extended Lynds 1204 dark cloud while the sub plots are those taken from subsequent observations presented in this section that probe the S140 region in more detail at higher resolutions and over a range of wavelengths.

At millimetre wavelengths a large bipolar CO molecular outflow was discovered by Blair *et al.* (1978) and investigated further by Hayashi *et al.* (1987) and Minchin *et al.* (1993). They find the outflow to be extended along a southeast-northwest axis. The blue and red shifted flows are at position angles of $\sim 160°$ and $\sim 340°$ respectively and IRS1 appears to be the driving source. Further studies in the 80's and 90's began to uncover the complexity of the region around IRS1. Minchin *et al.* (1995a) detected three dust emission peaks at 450 and 850 μm. The peak corresponding to the source SMM1 is roughly coincident with the NH_3
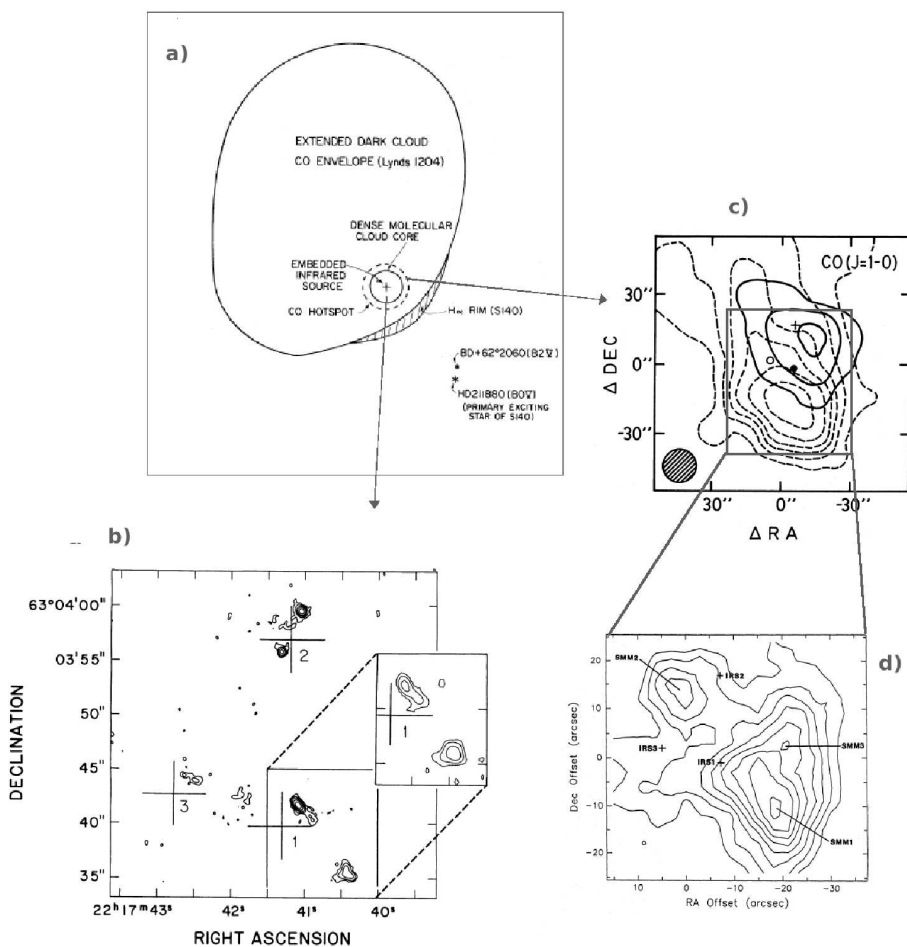
Figure 2.1: a) Schematic of the Lynds 1204 / S140 dark molecular cloud and the nearby exciting stars as would be viewed from the Earth. The dense core is where IRS1 is located. Taken from Blair *et al.* (1978). b) High resolution radio observations by Schwartz (1989) at wavelengths of 6 cm and 20 cm (inset). The crosses indicate the IR emission sources IRS1, IRS2 and IRS3. The elongated emission around IRS1 is is perpendicular to the large scale outflow in plot c). c) CO(1-0) image of the outflow from IRS1 (black dot). The integrated blue and red shifted emission are shown by the dashed and solid lines respectively. Adapted from Hayashi *et al.* (1987). d) 450 μm image of the region from Minchin *et al.* (1995a). The IR sources (crosses) and sub-millimetre dust peaks are labelled. Note that the offsets in some of the figures are not referenced from the same central location.

peak observed by Zhou *et al.* (1993) to the south west of IRS1. None of the sub-millimetre dust peaks are coincident with the IR sources and are probably younger cores. Forrest & Shure (1986) detect IRS1 and IRS3 in their 2 μm infrared image. The IR source locations are consistent with two of the nebulous objects previously seen at near infrared wavelengths (0.9 μm) by Dinerstein *et al.* (1979). They also see a faint arc like structure to the south of IRS1 and a separate structure to the north. These are possibly due to scattered light from IRS1 or shocks created by jets or outflows.

Early radio observations at 6 cm by Beichman *et al.* (1979) detect two components coincident with IRS1, one resolved and one unresolved. They also detect an extended source around IRS2. IRS3 is not detected but a source to the north west of IRS3 is detected. This NW source aligns directly with a nebulous region seen at 0.9 μm. Subsequent 1.3 cm observations by Simon *et al.* (1983) detect IRS1, IRS2, NW and an additional source to the southwest of IRS1, named VLA4. Radio and infrared observations by Evans *et al.* (1989) detect all three infrared sources and the NW and VLA4 sources at 2 and 6 cm radio wavelengths and all sources except IRS2 are detected at 1.6 and 2 μm. The authors come to the conclusion that IRS1, 2 and 3 are embedded B type stars in their formation stages and that the sources NW and VLA4 are caused by scattered light escaping from IRS1. To facilitate such emission there must be an evacuated cavity which could have been created by a stellar wind. The coincidence of the radio emission at NW and VLA4 could be due to shocks of the wind impacting the denser cloud regions. Why cavities would be cleared perpendicular to the molecular outflow and the proposed collimated stellar wind is unclear in their picture. Higher angular resolution radio observations made by Schwartz (1989) at 1.5, 4.9 and 15 GHz (20, 6, 2 cm with

corresponding resolutions of 1, 0.3 and 0.1 arcseconds) indicate an elongation of the radio emission associated with IRS1 in the southwest-northeast direction, at a position angle of $\sim 44°$. The orientation of the radio emission from IRS1 is almost perpendicular to that of the large scale CO outflow. The usual jet interpretation of such an elongated radio source was therefore highly problematic as it would be perpendicular rather than parallel to the bipolar molecular outflow.

The region around S140 IRS1 is very complex, however, much more recent, multi-wavelength, higher resolution observations have been able to shed more light on the environment. Figure 2.2 shows a collection of these more recent observations. Near-infrared speckle imaging detect a bright mono-polar reflection nebula at a $PA \sim 154°$ (Alvarez *et al.*, 2004a; Hoare *et al.*, 1996; Schertl *et al.*, 2000) centred upon the location of IRS1. The centro-symmetric pattern of high polarisation in the nebula is consistent with light from the central source being reflected from the clumpy inner surface of an evacuated cavity (Schertl *et al.*, 2000). Their very high resolution observations, at 76 milli-arcsecond, confirm IRS1 at the centre of the bipolar molecular outflow and delineate the cavity excavated by it. de Wit *et al.* (2009) detect the IR sources and NW and VLA4 at 24.5 μm. For NW and VLA4 this is the first time the radio sources have been detected at these wavelengths. The authors note the complexity of the emission at these resolutions and separate faint structures are consistent with shocked regions.

VLA radio observations by Tofani *et al.* (1995) report the elongated structure of IRS1 in 8 GHz maps, while MERLIN radio observations by Hoare (2006); Hoare & Muxlow (1996) show the very elongated structure of IRS1 with a 7:1 axis ratio at 5 GHz. The latter observations presented by Hoare (2006) are taken at multiple epochs. As detailed in Chapter 1, the elongated nature of the radio emission
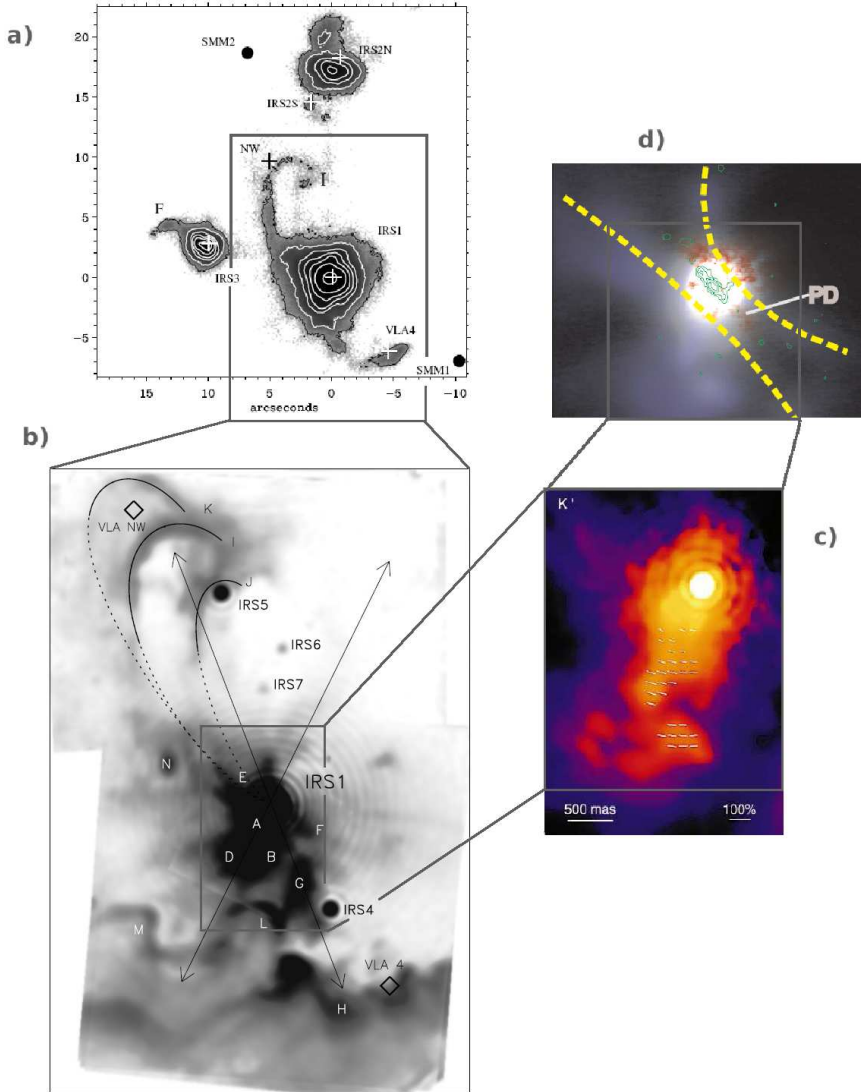
Figure 2.2: a) The 24.5 μm map taken from de Wit *et al.* (2009) showing detections of all IR sources and the arc like structures NW and VLA4. b) 76 mas resolution near-IR speckle images of the K-band emission focusing in on IRS1. VLA4 appears more complex than in plot a). The proposed secondary outflow trajectory that intersects with the bow shocks near the NW source is over plotted. Image from Weigelt *et al.* (2002). c) The same k-band image shown in plot b) but overlaid with polarisation vectors. The centro-symmetric pattern of high polarisation is consistent with scattered light from the central source (Schertl *et al.*, 2000). d) Pseudo-colour image of pure brightness (red) and polarisation brightness (blue) as presented by Jiang *et al.* (2008) overlaid with the 5 GHz emission from Hoare (2006). The polarisation and ionised disc wind emission are aligned and both perpendicular to the reflected light from the outflow cavity. Note that the polarisation brightness correlates with the structures seen in plot c). The grey boxes roughly link the regions observed.

is consistent with the emission arising from a disc wind, as proper motions do not support a jet interpretation. S140 IRS1 is one of only two sources known to have disc wind emission, the other being S106 IR (Hoare *et al.*, 1994). However, S106IR is unusual in already powering a bipolar HII region whereas IRS1 is a genuine MYSO with disc wind emission but no surrounding UCHII region. Gibb & Hoare (2007) also indicate the elongated disc wind nature of IRS1 in their high frequency observations, where IRS1 is clearly resolved on scales down to ~ 40 au at 43 GHz revealing a point symmetry previously noted in the 5 GHz MERLIN images. Further support of the disc wind scenario is presented by (Jiang *et al.*, 2008) who observe a polarisation disc (an elongated low-polarisation structure) aligned with the radio emission at a position angle of $\sim 45°$.

Contrary to the disc wind picture there have also been suggestions of IRS1 actually driving outflows in different directions. Weigelt *et al.* (2002) and Preibisch & Smith (2002) analyse more near-IR speckle images of the K-band and H_2 line emission and conclude that IRS1 is driving bow shocks at a distance of ~ 10 arcsec away at a PA of $\sim 20°$ and is responsible for more distant knot features. The secondary outflow is misaligned with the elongated radio emission from IRS1, however they still suggest a jet interpretation of the radio emission. Such an arrangement with mis-aligned bipolar molecular outflow and radio jet may be possible if IRS1 is part of a close, non-coplanar binary system with a precessing circumstellar disc, as suggested for the similar object, IRAS 20126+4104 (eg, Lebrón *et al.*, 2006; Shepherd *et al.*, 2000). In the case of IRS1, a binary is not detected in the 76 milli-arcsec resolution observations by Weigelt *et al.* (2002). The authors note a slight extension in the FWHM diameter of IRS1 could indicate a possible companion at ~ 20 au, but these are beyond the resolutions attainable with current

observations. Weigelt *et al.* (2002) also detect two infrared point sources associated with the NW and VLA4 regions which could have previously confused the lower resolution studies and conclusions (e.g. Evans *et al.*, 1989; Harker *et al.*, 1997). The VLA4 region is very complex and not simply an arc structure driven by a jet from IRS1 (as they appear at 24.5 μm, (de Wit *et al.*, 2009)). Conversely, there are sets of well defined bow shocks in the NW region. These lead the authors to believe IRS1 is powering a jet/outflow in this direction. Given that the perfectly centro-symmetric polarisation vectors and the polarisation disc/outflow configuration of the system is explained by a single powering source, IRS1, Jiang *et al.* (2008) suggest another source, such as IRS4, could be responsible for the bow shocks.

To draw firm conclusions regarding the disc wind nature of the radio emission and the multiple outflow nature of IRS1 millimetre continuum observations are presented. These are centred upon IRS1 and have an angular resolution up to $\sim$ 0.12 arcsec. Additional observations of the CO molecular line tracer are also presented. The aim of the observations is to disentangle the complex regions at scales down to $\sim$ 100 au and to detect a dust disc at the location of IRS1 to confirm the disc wind scenario. The observations and reductions are discussed in the following sections. Subsequently, the results, discussion and a conclusion are given.

2.2   Observations

The observations as listed here are presented in chronological order and coincidentally with increasing angular resolution. The reduction of all data and imaging

was conducted utilising the MIRIAD reduction package (Sault et $al.$, 1995), except where noted.

Owens Valley Radio Observatory (OVRO) $\sim$ 3 mm wavelength observations were made using all 6 $\times$ 10.4 m antennas in the compact array configuration. The observations took place on 1998 May 26 and May 30 with on source times of 7.25 hours and 8.17 hours respectively. The former observations were at central frequencies of 86.4 GHz for the LSB and 89.8 in the USB while the latter were at 112.4 GHz for the LSB and 115.3 GHz in the USB, corresponding to wavelengths of approximately 3.5 and 2.7 mm and maximal resolutions of $\sim$ 6 and 4.5 arcsec respectively. The correlator setup provided a single 1 GHz wide bandwidth for all continuum observations. During the first epoch, the correlator was configured to observe SiO(2-1) in the LSB and H^{13}CO$^+$ in the USB. The bandwidths for the lines were 32 MHz and 8 MHz, resulting in velocity resolutions of 1.3 km s^{-1} and 0.33 km s^{-1} respectively. The chosen correlator frequencies for the second epoch observations encompass the ^{12}CO (1-0) line in the USB and the C^{17}O line in the LSB. The bandwidths were also 32 MHz and 8 MHz, resulting in a velocity resolution of 1.3 km s^{-1} for ^{12}CO(1-0) and 0.33 km s^{-1} for the C^{17}O line. The phase calibrator BL Lac was observed throughout both tracks while the amplitude correction was performed via comparison with observations of Neptune. 3C345 was targeted at the start of the runs as the bandpass calibrator. The data were calibrated and reduced by D. Shepherd and A. G. Gibb, however images and maps presented here were solely produced by L. T. Maud.

1.3 mm wavelength observations taken with the Sub-Millimetre Array (SMA) (Ho et $al.$, 2004) were retrieved from the data archive. The array was arranged in the compact configuration and observations were taken over a 14 hour track on

2007 July 23 (PI Franco-Hernández). The aim of the proposal was to investigate the outflow nature of S140 IRS1. The baseline range of the 8 array telescopes (6 m each) was ~ 6.5 to ~ 115 m, resulting in a potential resolution of ~ 3.0 arcsec. The continuum frequencies were centred upon 220.52 GHz and 230.52 GHz for the LSB and USB, both with a bandwidth of 2.0 GHz, therefore encapsulating many possible emission lines including ^{12}CO(2-1) and ^{13}CO(2-1) to trace the outflow material. The effective velocity resolution was 1.05 km s^{-1}, sufficient to detect any outflow velocity structure. Observations were frequently made of the bright phase calibrator BL Lac over a total of 13 hours. Amplitude correction was accomplished via scaling of the visibilities to a model for Callisto while 3C273 was targeted for bandpass corrections. Due to the nature of the SMA, data were corrected for system temperature variation, small frequency corrections and baseline based calibrations. These calibration steps are very simple multi-line commands issued in the reduction software package. The subsequent reduction followed the standard procedure.

The first sub-arcsecond resolution observations of S140-IRS1 were made using two 3 hour tracks with the Combined Array for Research in Millimetre-wave Astronomy (CARMA) (Bock *et al.*, 2006) in the B configuration. The array is composed of 15 telescopes (6 $\times$ 10.4 m and 9 $\times$ 6.1 m) and observations were undertaken on 2008 January 19 and February 9 after the recent commissioning of the instrument. The central continuum frequencies were 220.86 GHz and 226.96 GHz for the LSB and USB respectively, each with a bandwidth of 500 MHz. The correlator was also configured to observe 3 emission lines, ^{13}CO(2-1), CH$_3$CN(12-11) and HC$_3$N(25-24), with a resolution about 0.67 km s^{-1}. The baseline range of the B-array configuration from ~ 50 m to ~ 1000 m offers a maximal potential

resolution of ~ 0.3 arcsec. Observations were made of the closest phase calibrator 2038+513 (J2000), 18° away, with additional observations of a brighter phase calibrator BL Lac, 22° away, as a back up calibrator. Amplitude calibrations were performed via comparison with MWC349 assumed as an absolute calibrator with flux density of 1.91 Jy and the planet Neptune. The data were reduced in the standard manner with bandpass, phase and amplitude calibration. The CARMA raw data additionally required a small correction of baseline distances due to physical pad shifts that occurred during the previous winter period. The final data were calibrated with BL Lac as the phase calibrator as the nearer phase calibrator 2038+513 required significant flagging due to poor phase tracking of the weaker source. Antenna 2 data were also flagged due to increased system temperatures throughout the observations.

The highest resolution observation currently accessible at 1.3 mm (to date) were made using CARMA in the A configuration throughout 2011 November and December. The maximal baseline of ~ 2000 m results in a nominal resolution of ~ 0.12 arcsec (dependent on the imaging weighting scheme). The observations were purely continuum based and the receivers were tuned to a local oscillator frequency (LO) of 220.0 GHz. The total calculated bandwidth for the continuum was slightly less than 7.8 GHz after accounting for slight overlaps in each correlator sub-band. The requested observation time was 8 hours to achieve high sensitivity and obtain good visibility coverage. However, due to weather constraints a single 8 hour track was unfeasible and multiple observing runs from 2011 November 29, December 8,9,10 and 11, were combined to meet the time quota. Observations were made of the source 3C454.3 to correct the frequency dependent bandbass, while frequent observations of BL Lac were used to correct for the time dependent

atmospheric phase gains and instrumental effects. During observations the Paired Antenna Calibration System (PACS) was employed. Here smaller 3.5 m diameter antennas observe a nearby quasar at 1 cm wavelengths in order to correct for atmospheric fluctuations of the millimetre data on timescales shorter than the cycle time. Neptune, Uranus and MWC349 were targeted for absolute flux calibration. As the planets are resolved in the A array the flux scaling was only calculated using visibilities with projected baselines $\leq$ 500 m. Consistency checks were made with the scaled data and observatory flux calibration services to corroborate the flux values.

2.3   Data reduction

This section is not intended as a comprehensive review on interferometry and data reduction, but rather a basic understanding of the theory and processes involved in producing high resolution synthesis images with direct reference to the actual data presented in this thesis. Detailed information on the vast topic of interferometry is available in Taylor *et al.* (1999) and Thompson *et al.* (2001) for example. The underlying basis of interferometry is the ability to combine data signals from an array of telescopes and produce synthesis images with a resolution according to $\theta \sim \lambda/B$. In this case 'B' corresponds to the maximal baseline (separation) of a pair of antennas in the array rather than the conventional use of the antenna diameter in single dish observations. Clearly, the larger the baseline, the higher the resolution attained.

2.3.1   Synthesis Imaging

Interferometers do not directly measure the brightness distribution of a source on the sky, i.e. they do not directly map the source. Instead interferometers measure the the spatial coherence function (Taylor *et al.*, 1999), also known as the interferometric 'complex' visibilities, between antennae. It is useful to write the spatial coherence function in terms of sky coordinates (x, y) and antenna baseline coordinates (u, v),

$$V_\nu(u, v) = \int \int I_\nu(x, y) e^{-2\pi i(ux+vy)} \, dxdy \qquad (2.1)$$

which can be inverted via a Fourier transform,

$$I_\nu(x, y) = \int \int V_\nu(u, v) e^{2\pi i(ux+vy)} \, dudv \qquad (2.2)$$

to obtain the intensity distribution and map the source.

There are two parts to the complex visibilities, the amplitude and the phase. In a crude sense the amplitude is simply the magnitude of the emission, while the phase is related to the position or focusing of that emission. The $(ux + vy)$ in the exponent of the above equations is the geometric phase difference. This is the phase difference between path lengths of emission from the source into each antenna of the baseline pair referenced to a known phase tracking source. Conceptually if a source is directly overhead on a parallel plane to the telescope baseline(s) then the phase delay is zero. The path length to each antenna is the same. As the Earth rotates the source does not remain overhead and the phase delay is non-zero and must be corrected for such that the positions of the amplitudes are mapped correctly and the intensity distribution $I_\nu(x, y)$ can be estimated. These phase

delays are calculated and applied while observing takes place, however the true complex visibilities are not the final result. The observed visibilities are effected by complex gains which must also be corrected for. These gains can be from drifts in the equipment and instrumentation, e.g. unstable electronics, or due to atmospheric fluctuations. The atmosphere causes the emission from a source to be refracted and errors in transmission strength or phase delay to the antennas can occur. Section 2.3.3 onwards details the calibration with respect to the millimetre wavelength observations presented here.

2.3.2   Deconvolution

Once the complex gains have been deduced they can be applied to the source data and the imaging process can begin. In the ideal case, where visibility space (u, v) is fully sampled the intensity distribution, i.e. image or map, would be represented directly by Equation 2.2. However, the intensity distribution recovered is actually the corrected visibilities at discrete samples of (u, v) visibility space. These discrete samples are described by the sampling function $S(u, v)$. The sampling function is related to the antenna positions and the coverage of visibility space over the time of the observations. Figure 2.3 shows the (u, v) coverage of the CARMA observations of S140 IRS1. It is clear that visibility space (u, v) is sparsely sampled. The data recorded by the interferometer are actually the complex visibilities multiplied by the sampling function. The Fourier transform of these, after gain corrections actually produces what is known as a dirty image or dirty map:

$$I_\nu^D(x, y) = \int \int V_\nu(u, v) S(u, v) e^{2\pi i (ux + vy)} \, du dv \qquad (2.3)$$
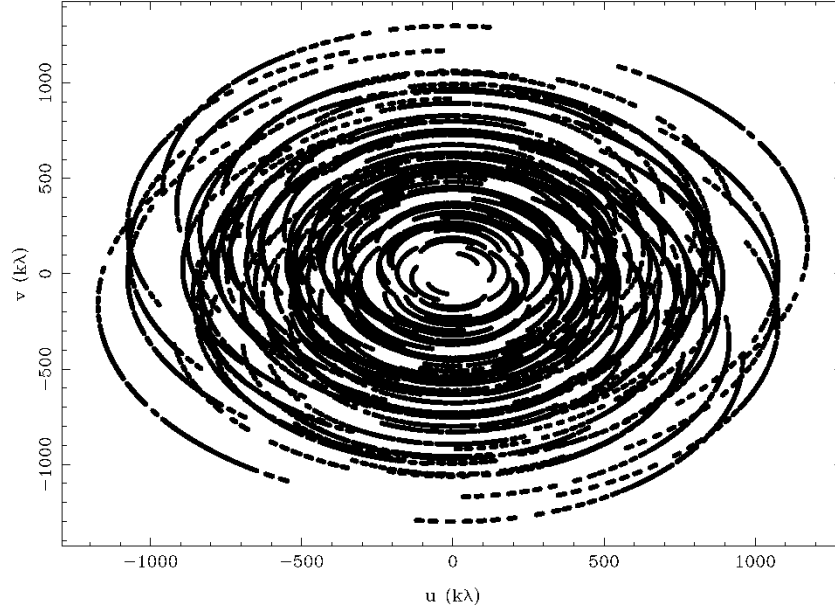
Figure 2.3: The visibility (u, v) coverage of the target source IRS1 observed with CARMA A on multiple nights. The images shows concentric curves where different regions of (u, v) space are sampled, i.e. where data are recorded on the target source.

The sampling function itself can independently be Fourier transformed to give the dirty beam:

$$B(x, y) = \int \int S(u, v)e^{2\pi i(ux+vy)} \, dudv \qquad (2.4)$$

Deconvolution of the dirty image with the dirty beam is undertaken to generate the ideal intensity distribution as:

$$I_\nu^D = I_\nu * B \qquad (2.5)$$

This process is undertaken by the CLEAN command within the reduction software and is detailed Taylor *et al.* (1999) or Thompson *et al.* (2001). The ideal intensity

distribution is then re-convolved with a clean beam which is the representation of the beam of the interferometric array assuming it was a single extremely large antennae rather an a sparse array. The result is the final cleaned image ready for analysis.

The (u, v) coverage or sampling of visibilities space is very important in interferometry as this determines the quality and accuracy of the final image. An easy way to visualise this is by considering a single antenna dish, which recovers all the emission within its beam, as an array of smaller dishes all next to each other. The single antenna diameter is now the baseline of the array and as the 'smaller antennas' are touching the visibility space is fully sampled out to the maximal baseline. For a real interferometric array with a few antennas at different physical locations the visibilities are not fully sampled and the final image must be reconstructed from incomplete data. One problem here is that the total source flux can be underestimated as the very shortest spatial frequencies or small baselines corresponding to large scale structures are missing. The flux from all material on a larger scale than that sampled by the smallest baseline is simply not detected. Another problem is that the Fourier transforming process producing the final image from poorly sampled/missing (u, v) space can contain artifacts such as large negative bowls or 'holes' around peaks of emission. These artifacts can make accurate conclusions of source structure very difficult.

Missing (u, v) spacings, particularly at shorter spacial frequencies, can be filled using single dish or more compact interferometric array observations. Spacings from zero to the smallest array baselines can be recovered by converting single dish data into visibilities and merging them with interferometer data. Ideally, the more antennas in the array, together with the addition of single dish short

spacings, the more accurate the image reconstruction will be. Realistically, this can be accomplished by merging data from interferometric arrays in different antenna configurations.

During the deconvolution/imaging process the sampled visibilities are weighted. The weightings can be changed to account for under/over sampled regions of (u, v) space to improve either the resolution or sensitivity. The two extremes are natural weighting, where all sampled points are treated equally, and uniform weighting, where data are weighted according to the inverse of the number of samples within a symmetric region of the (u, v) plane. Natural weighting improves the sensitivity at the expense of resolution, whereas uniform weighting emphasises the longer, less sampled baselines to increase the resolution at the expense of sensitivity. Between these extremes, the Brigg's robust parameter (a number between -2 and +2 corresponding to uniform and natural weighting respectively) can be used as a middle ground weighting scheme to optimise resolution and sensitivity of the data.

2.3.3 Gain Calibration

Prior to imaging, the observed visibility data must be corrected for the aforementioned instrumental and atmospheric effects. The complex gains encompass both these effects and they cannot be intrinsically separated. To calibrate source visibilities a reference target must be observed at regular intervals. The gain source, or phase reference source, is a bright source in the vicinity of the sky local to the target source. Moreover, the reference source must be a point source at the resolution of the observations and not variable over the time extent of the observations. The rational behind these reference observations is that the visibilities of a point source are very easily modelled as the amplitudes at all baselines are constant and

the phase delays (after sky position corrections) are zero. Hence, a solution can be calculated for the reference source and applied to the target source to correct its visibilities. Note, one caveat is that some objects can be self-calibrated directly if they are bright and the visibilities are known or have been previously modelled. Self-calibration negates observations of a calibrator source and maximises on target time. It can also be employed to improve calibration after an initial solution with a calibrator source has been established.

Typically over the duration of the observations the general instrumental drifts are smooth and therefore it is more important to consider the atmospheric effects in order to establish an observing strategy prior to observations.

2.3.4 Atmospheric Fluctuations

For millimetre wavelength observations the troposphere has adverse effects on the observed amplitudes and phases. The troposphere is the lowest layer of the atmosphere and extends to an elevation around 10 km. Variations in the water vapour column density can dramatically effect the path length, i.e. phase delay, of the emission from a source to each antenna in a baseline pair. This can cause a loss of amplitude (de-coherence) over the integration time, pointing errors and loss of resolution. The incorrect path lengths are seen as phase noise by the interferometer. Figure 2.4 depicts the nature of the atmosphere according to the 'Taylor hypothesis'. The hypothesis details the variation of water vapour in a turbulent layer of the troposphere. The turbulent layer has a thickness less than its height above the array (few km maximum). Sometimes called the frozen screen approximation, the hypothesis states that if turbulence is of low intensity and is roughly stationary and homogeneous, then the turbulent region is largely unchanged over
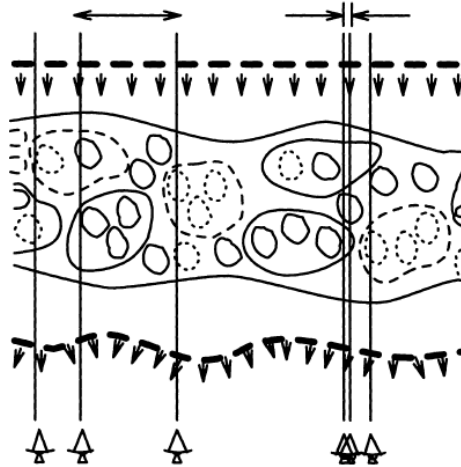
Figure 2.4: A schematic of the structure of the Troposphere above an interferometric array taken from Lecture 28 of Taylor *et al.* (1999) (Carilli *et al.*, 1999). The circles represent different size scales of excess (solid) and deficit (dotted) water vapour that cause phase fluctuations.

the timescales of interest and only advected by the mean wind (see Taylor *et al.*, 1999). Thus temporal and spatial fluctuation scales can be related to baseline length, weather conditions, wind speed and time.

Essentially large phase fluctuations can occur over long time periods and are partially correlated between antennas, whereas small fluctuations occur over short time scales and can be uncorrelated between antennas, depending on the baseline length. The turbulence of the layer follows Kolmogorov theory which predicts a power law distribution of the spatial fluctuations from small (mm) to large scales (km), linking baseline length to phase error. Fluctuations on scales smaller than the antenna dish are averaged together and do not contribute to phase error, while structures on scales larger than the array baselines are common to the antennas in the array and cancel out (Pérez *et al.*, 2010). The phase error, or phase noise actually scales with baseline length. This makes accurate long baseline, high res-

olution observations more difficult to conduct than shorter baseline observations where more of the turbulent variations are common to the antennas. Furthermore, the atmospheric variations also change with varying weather conditions. Observations at high and dry sites at night would provide optimal conditions, whereas observations during a storm, at sea level during the day would represent the opposite and observations would be futile.

2.3.5 Observing Strategy

In consideration of the spatial and temporal fluctuations different observing strategies can be employed for different array configurations dependent upon weather conditions. Conceptually, in order to correct for the variations in the atmosphere, data must be sampled on a timescale smaller than the fluctuation timescales. If the turbulent layer conforming to the Taylor hypothesis is moving across the sky at a given speed then sampling at a fast rate would minimise the layer's physical motion during the observations. Fast switching is one solution and is the switching between the target source and the calibrator source on timescales of minutes or tens of seconds. Due to baseline dependent phase fluctuations, given the same weather conditions, fluctuations will be smaller for compact array configurations compared with extended configurations over the same cycle times. In these cases cycle times can be relaxed, i.e. increased, for compact array configurations and attain more on source time while phase errors are kept to an acceptable level. The top sub plot of Figure 2.5 shows the phase tracking of the calibrator BL Lac over $\sim$ 11 hours of the SMA observations. On the short baseline between the antennas the phase does not fluctuate largely on small timescales and varies quite smoothly on long timescales. It would appear that more time could be spent on source rather

than the calibrator when viewing the smooth phase tracking on short baselines.

Unfortunately optimal weather conditions are not always available and cycle times must be adjusted to account for an increased level of atmospheric fluctuation, while the fluctuations still scale with baseline length. The cycle time can be decreased such that the more rapid fluctuations are traced and can be corrected for. The lower sub plot of Figure 2.5 shows the phase tracking of BL Lac for the SMA observation on one of the longest baselines. Here the fast switching, of the order 4 minute cycle times, is required to track how the atmosphere varies on short timescales and to allow corrections in the calibration process. At early and late times (before 10h and 14h on the plots) the phase fluctuations are noticeably larger where the atmospheric conditions are worse. These large fluctuations cannot be seen as significantly in the upper sub plot on much shorter baselines. Weather constraints are even more stringent for baselines over 1 km for millimetre observations as phase variations are intrinsically larger given the same cycle time as the above, for example. One caveat to fast cycle times is that the calibrator source itself must be sufficiently bright such that the phase error incurred by the signal to noise ratio (SNR) is less than that incurred from atmospheric fluctuations. This is not usually a problem as there are numerous extragalactic sources that are both bright and point sources for the current interferometric arrays.

Ideally due to fast switching the variations in phase are now on timescales larger than the switching, i.e. shorter than the crossing time of the turbulent tropospheric layer, such that solutions can be established to correct the phase at the times when the calibrator source is observed. The phase solutions can be reliably interpolated and applied to the target source as the atmosphere should not be varying significantly on the timescales between observations of the calibrator
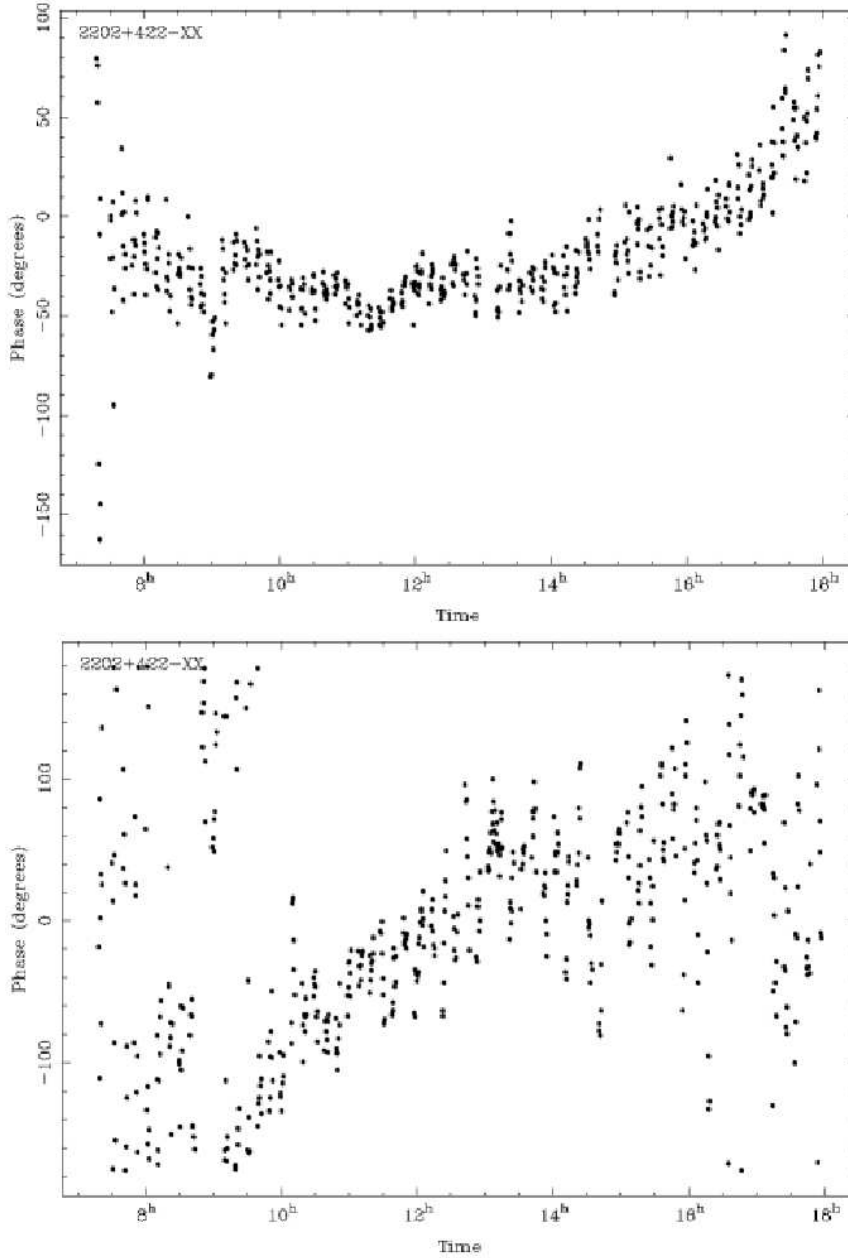
Figure 2.5: Top: The plot shows the phase tracking of BL Lac on one of the shorter baselines of the SMA. There is no significant phase variation on short timescales and the large timescale phase variation is smooth. Bottom: The phase tracking of BL Lac on one of the longest baselines in the array. The short timescale phase variations are intrinsically larger than on shorter baselines when the weather conditions are good, between 10 and 14 h. Where weather conditions are worse (before 10 h and after 14h) there is considerably more phase scatter on short timescales in comparison to the short baseline in the top plot. On large timescales the (average) phase variation is relatively smooth.

source. At certain times adverse weather conditions may arise and data can be flagged such that it is no longer included in the final data set as it may degrade the result due to the uncertainty of the solutions. Fast cycle times of around 4 minutes were employed for the SMA observations to counteract atmospheric variations in average weather conditions although data still required flagging in regions where the weather degraded and phase fluctuations were significantly elevated, as previously indicated in Figure 2.5. Interpolation of the phase solutions from the flagged regions to the target source are not reliable due to the uncertainty of the phase when the target source is being observed assuming it is similar to the very scattered phases while the calibrator was being observed.

The weather conditions for the CARMA B array observations were good for the most part with only the poorer conditions affecting the last 30-40 minutes of the observations. Figure 2.6 indicates the phase tracking on typical short and long baselines on the upper and lower sub plots respectively. The effect of poor weather is clearly evident by the significant increase in phase scatter on the long baseline at shorter timescales. There is some scatter within the phase over the scan time on the calibrator source which is intrinsic to the cycle time, weather conditions and baseline length. Clearly variations on the timescales of the cycle times are solved but variations shorter than this are not probed. Similar to the SMA observations the long timescale variations in the phase are relatively smooth and the shorter baseline phase variations are noticeably less than those of the longer baselines. The weather for these kilometre baseline observations must be better than average due to the larger fluctuations at longer baselines.
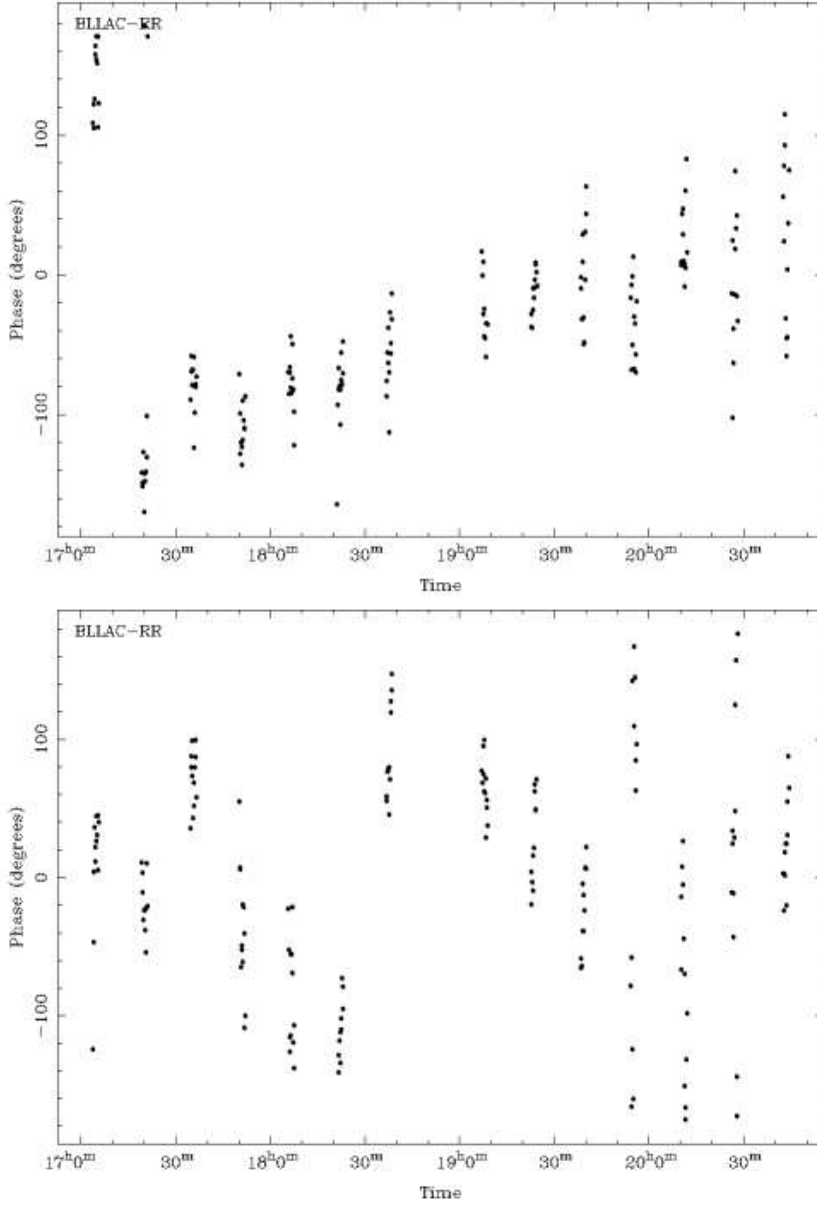
Figure 2.6: Top: The phase tracking of BL Lac on a short baseline ($\sim$ 75 m) of the CARMA B array over $\sim$ 4 hours of observations. The phase variation is not traced on timescales shorter than the cycle time but the variations on longer timescales are traced. In the last 30 minutes when the weather conditions worsen the phase variation increases slightly. Bottom: As top but for one of the longest baselines ($\sim$ 800 m) in the array. Again the the phases are tracked on timescales longer than the cycle time but there is still variation on shorter times. Note that on the longer baselines the phase tracking is poor for last 30 minutes of observations in worse weather conditions. This data was subsequently flagged and no solutions were attempted.

2.3.6 Kilometre Baselines with CARMA

The most recent CARMA A array observations were undertaken in excellent weather conditions. Weather condition constraints are a prerequisite to observations at these long baselines, where the largest baseline is ~ 2 km, to maximise atmospheric stability. Cycle times were set to 4 minutes to track atmospheric fluctuations. Ideal cycle times would have been reduced for faster switching, however the chosen cycle time was a compromise between on source time and feasibility given the calibrator source at ~ 20 degrees sky separation. Furthermore, observations on long baselines with CARMA employ an additional calibration technique using a paired antenna calibration system (PACS). Here 3.5 m antennas observing at centimetre wavelengths are paired with the longer baselines antennas observing at millimetre wavelengths. Essentially the small antennas monitor a calibrator source throughout the entire observations. Long and short timescales solutions can then be created which attempt to solve for the instrumental slow offsets and drifts and the small timescale atmospheric fluctuations independently. Assuming the atmosphere fluctuates in a common way at both the centimetre and millimetre wavelengths the short timescale PACS solutions can be applied to the millimetre observations with a simple scaling applied. More details of the technique specific to CARMA observations are presented by Pérez *et al.* (2010).

Figure 2.7 shows the phases for a baseline employing PACS. The millimetre phase is tracked well for the calibrator source BL Lac on very short timescales, although it is clear to see variation thought the scan cycle time. The paired antennas observing at ~ 35 GHz track the calibrator source 2230+697 (~ 0.7 Jy) and the phases are clearly tracked and fluctuate much less due to the longer
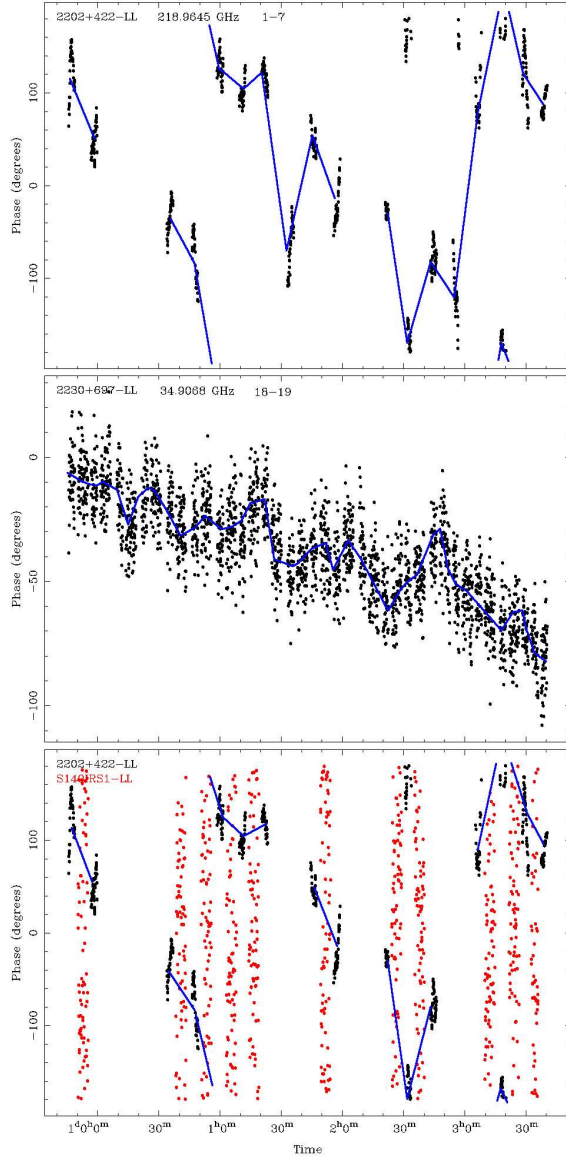
Figure 2.7: Top: Phase tracking of BL Lac with the CARMA A array on one of the paired baselines (1-7 antenna baseline, ~ 1100 m length) before flagging. At 3h the phase scatter is larger than at other times. Middle: Phase tracking of the source 2230+697 at 1 cm wavelengths with the paired antenna system baseline 18-19. At the longer wavelengths the phase variation is much smaller. The tracking of the phase of the two sources at millimetre (top) and centimetre are similar. At 1h 30m and 3h there are very large phase jumps on small timescales. Bottom: As top but after flagging and including phases for the source S140 IRS1 (Red). The source has been flagged in regions where there is no suitable interpolation solution. The blue line represents a crude linear interpolation of the phases between the calibrator observations.

wavelength of these observations. Due to the scaling value between the centimetre and millimetre observations and a weak centimetre calibrator the application of the PACS solution actually increases the phase noise for the CARMA A data. In the case of the final reduction of the CARMA A data PACS was not employed. Notably, as is clear in Figure 2.7, the phases at both the millimetre and centimetre follow a similar pattern (Top and Middle). The phase variations on long baselines of the paired antennas were investigated to check the variability at the times when the millimetre array was observing the target source. Such checking allowed a confident application of the interpolated solutions obtained from BL Lac to the target source as the phase variations were not significant at the times off calibrator, and were varying smoothly. Similar to the previously mentioned reduction, data were flagged where the phases were noticeably varying for the millimetre calibrator prior to and after a scan cycle on the target source in the standard millimetre data. Additionally, data were also flagged where the phases were noticeably variable for the centimetre calibrator at the corresponding times when the millimetre target was being observed in the main array. Flagged data are not included where the phases are very unstable and thus solutions are not created or applied to the target source where the interpolation of these solutions are uncertain. The missing data in the bottom plot of Figure 2.7 is a result of flagging.

2.3.7   Other Calibrations

Two other important calibration stages that have not been discussed so far are bandpass and flux corrections. Very simply, flux calibration is a straight forward scaling of visibility amplitudes to those of a known target which is routinely observed. Usually, flux calibrators are planets, meaning they are often resolved with

high resolution interferometers. Planetary visibilities can be modelled and compared with actual observations in order to scale the observed visibilities correctly. Typically due to uncertainties in the calibration or models the accuracy of the flux scaling is reported to be of the order 10-20 percent.

Bandpass calibration corrects for the response of the antenna electronics with frequency. Observations of a bright, unresolved source with a featureless spectrum must be conducted for this step. Over the frequency range, or bandwidth covered by the electronics most millimetre calibrators have a flat spectrum, i.e. the flux of the calibrator is constant over frequency. The response of the electronics at a given frequency can thereby be corrected such that it is now constant with frequency via a solution derived from the bandpass calibrator. Figure 2.8 shows the bandpass of the CARMA A observations of the calibrator source 3C454.3 on a single baseline over the entire bandwidth before and after calibration. It is evident that the response of the antennas have been scaled such that the flux of the calibrator source is now constant over the entire bandpass.

Once all calibration steps have been undertaken and cleaned images have been made the analysis can begin.
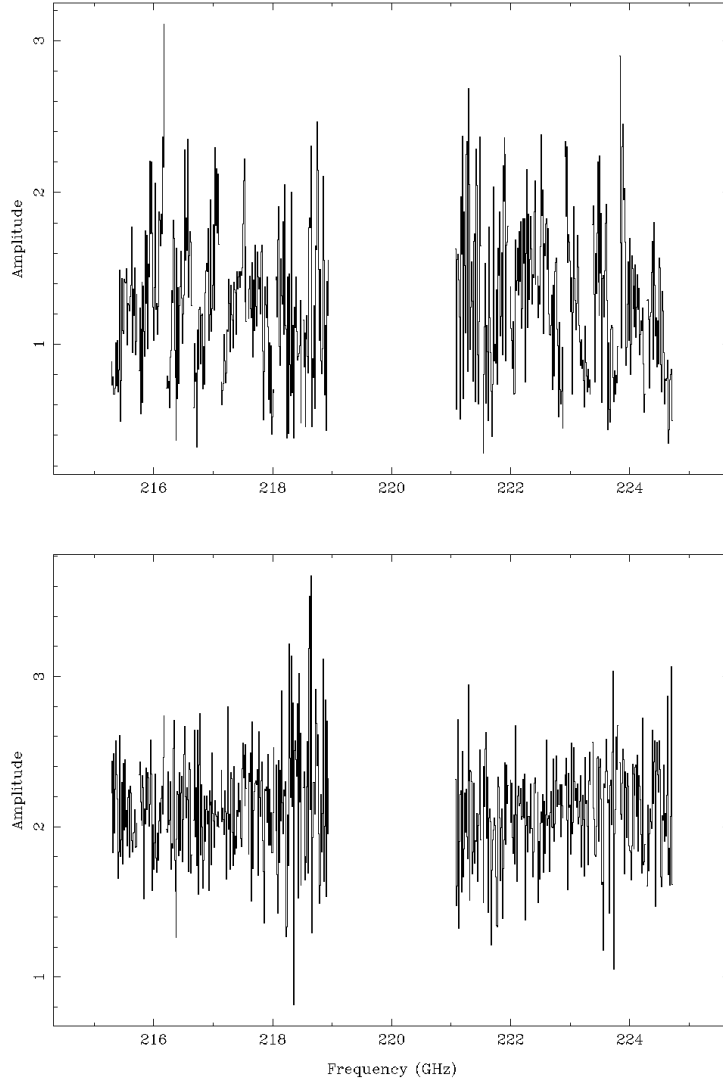
Figure 2.8: Top: The bandpass of 3C454.3 between ∼ 215 and ∼ 219 GHz for the LSB and ∼ 221 and ∼ 225 GHz for the USB as observed on the 1-7 baseline and averaged over the on source time. 3C454.3 is a point source and should have a constant amplitude with frequency but clearly the response of the antenna electronics is not uniform for every frequency channel (∼ 12.5 MHz wide). Each sideband is split into 8 windows and the response for each is clearly different. Bottom: As top but after bandpass correction has been applied. The flux for 3C454.3 is now constant at ∼ 2.2 Jy.

2.4 Results and Discussion

In all data sets the corrections from the phase and amplitude calibrators were applied to the target source where the solution could be interpolated with confidence. The continuum emission was extracted and mapped separately for all sets of observations. Continuum maps were made be combining all line-free channels onto a single plane except for OVRO which used only one wideband channel for the continuum during observations. The CARMA B and A array data used only 15 and 39 channels to cover each 500 MHz wide continuum window respectively and were combined after calibration during the imaging process.

All images were produced using a Briggs Robust parameter of 0.5 which yielded the optimum sensitivity and resolution trade off, except the CARMA A array images which used a Robust parameter of 0. The slight decrease in Robust parameter weights the image slightly towards longer baselines compared with a robust of 0.5. This weighting showed a slight improvement in resolution without a significant decrease in sensitivity (see Section 2.3.2). Due to the combination of observations on multiple nights and a very large total continuum bandwidth (~ 8 GHz) the sensitivity is higher than all previous observations. Table 2.1 lists the observations, dates and frequencies along with the final beam parameters of the continuum images in reverse chronological order. All maps are primary beam corrected excluding the CARMA maps. As CARMA is a heterogeneous array combined of mixed antenna sizes (6 and 10 metres) the primary beam correction is difficult. The fluxes of sources near the pointing centre will not be affected where the correction factor for the primary beam is unity. The 1σ RMS noise levels reported in Table 2.1 are an average of emission free regions in each of the maps respectively.

Table 2.1: Continuum observation parameters for the various antenna arrays.

Observation	Freq. (GHz)	Date	Beam Size (")	Beam PA (°)	Noise(1σ) (mJy/beam)
CARMA A	220	2011 Nov-Dec	0.13×0.11	52.4	0.5
CARMA B	225	2008 Jan 19	0.37×0.30	-78.2	2.2
SMA	225	2007 July 23	3.05×2.00	72.5	4.8
OVRO 112	112	1998 May 30	4.41×3.56	-61.2	1.6
OVRO 86	86	1998 May 26	6.13×4.66	-33.0	2.3

The resulting continuum images were sufficiently strong to perform self calibration of the phase for the CARMA data based upon the maps produced via the normal calibration process. Importantly during self calibration the solution timescale is that of the scan time. Shorter solution timescales such as the integration timescale, of the order a few seconds, cannot be used as the phase fluctuations for the source are not accurately tracked and solutions may artificially over correct the data. In both data sets the effect of the self calibration process was to increase the source flux as the phase solutions improved. On short baselines where IRS1 would appear as a point source, the phases on IRS1 itself were correlated enough to show a general phase tracking after the solution from BL Lac was applied. However, before self calibration at a few time scans the phase average was slightly offset from the general trend. Due to the (u, v) coverage of the CARMA array, snapshot type images of IRS1 were generated over a single scan time to investigate any variations in the maps. At times where the phase solution averages were offset the images showed a slightly different source position than the full integrated map and the other snapshot images at time scans following the general phase trend. Hence the application of the BL Lac phase solution did not fully correct for the at-

mospheric phase variations. After phase self calibration based upon the integrated image as a model, the phase solutions for IRS1, where phase tracking could be seen, were now aligned and followed the general trend. Inspection of the snapshot type images also indicated the source centre was shifted to the correct location. With all snapshot type images aligned and correlated the flux of IRS1 in the final integrated image over the entire observation time was slightly increased. There was no change in the morphology of the source.

To image the line emission, the continuum was subtracted from the data. No lines were detected towards IRS1 in the higher resolution CARMA B data and none were targeted in the pure continuum observations with CARMA A. No hot core tracers were found in any observations even though the SMA and CARMA B observations covered the CH_3CN transition. The continuum flux uncertainty is estimated to be of the order 10-20 percent after comparison with the observatory data archives for the respective calibrators.

The results are present below in the chronological order of the observations as were described in Section 2.2.

2.4.1   Low Resolution Continuum Maps

The OVRO observations produce the lowest resolution images. Figure 2.9 shows the 2.7 mm (112 GHz) continuum emission overlaid with contours of both the 2.7 and 3.5 mm (86 GHz) observations. The longest wavelength 3.5 mm observations strongly detect two sources, IRS1 and SMM1. In the shorter wavelength 2.7 mm observations peaks of emission are also detected at both locations of IRS1 and SMM1. Furthermore, emission above the 3σ level is detected at positions northeast of SMM1 and in the vicinity of SMM2 as well as a peak at the location of
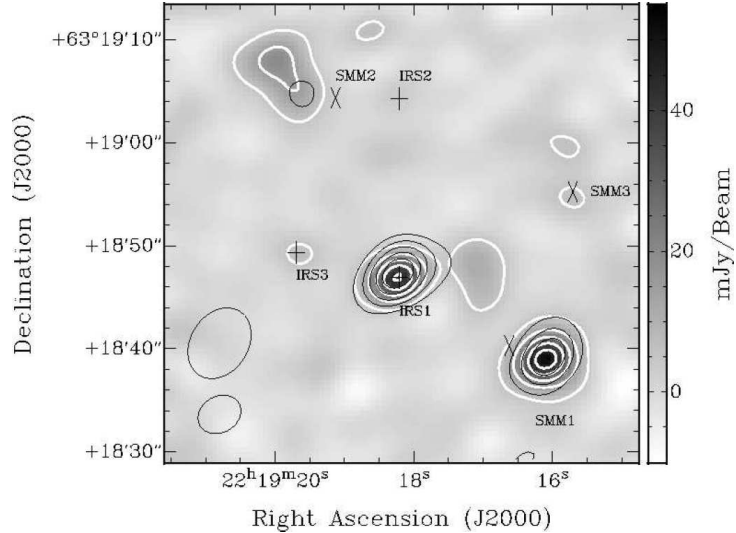
Figure 2.9: Cleaned 2.7 mm OVRO continuum map of S140. The plus symbols mark the positions of IRS1, 2 and 3 (Evans *et al.*, 1989), with the sub-millimetre peaks SMM1, 2 and 3 from Minchin *et al.* (1995a) indicated by the crosses. White contours show the 2.7 mm emission from 3σ noise to peak value in steps of 10 mJy. The overlaid black contours are of the lower resolution OVRO 3.5 mm continuum image from 3σ noise to peak value in steps of 5 mJy. IRS3 is only detected at 2.7 mm. The synthesised beams for both the 2.7 and 3.5 mm observations are indicated in the bottom left corner, the larger beam is that of the lower resolution 3.5 mm observations. The primary beam FWHM for the 2.7 and 3.5 mm OVRO observations are $\sim$ 67 and 87" respectively and lie outside the imaged region.

IRS3.

Table 2.2 indicates the fluxes from the Gaussian fits to the sources. The integrated and peak fluxes for IRS1 are comparable at both observed OVRO wavelengths. Additionally, the source sizes are that of the synthesised beams (within errors) and obviously at these wavelengths the emission from IRS1 is unresolved down to the sensitivity limit. Note the OVRO 86 and OVRO 112 images were generated from the combination of the LSB and USB data at 86 and 89 GHz and 112 and 115 GHz respectively.

Figure 2.10 presents the SMA 1.3 mm continuum map comprised of the merger

of both the LSB and USB visibilities after the removal of line emission. The cores of IRS1 and SMM1 are clearly detected. The fainter infra red source IRS3 is also detected with a $\sim 5\sigma$ level peak. Diffuse emission northeast and west of IRS1 is evident. This diffuse emission splits into distinct structures, the main central one joining with IRS1 and SMM1 at the 3σ level and the other approximately 15-20" to the NE of IRS1 encompassing the region of IRS2 and SMM2. The dust forms a linear ridge appearing to point from SMM1 in the direction of SMM2 (Minchin *et al.*, 1995a). A clear emission peak is not detected directly at the locations of the infra-red source IRS2 or the sub-millimetre sources SMM2 and SMM3; however there is residual 3σ level emission surrounding SMM3. SMM1 is actually the dominant source in this map with a peak flux roughly double that of IRS1. It is likely that SMM1 is a much younger source that is more deeply embedded than IRS1, which is already heating its natal envelope as indicated by the bright infra red emission it emits. Interestingly the emission at 1.3 mm is reminiscent of the 450 and 850 μm emission presented by Minchin *et al.* (1995a) except that the distinctive structures are now resolved with the interferometric observations. Furthermore, there is a clear deficit in dust emission in the direction of the CO molecular outflow originating from IRS1 to the NW and SE. Such a deficit is also evident in the maps of Minchin *et al.* (1995a).

The 1.3 mm wavelength SMA data shows a higher integrated flux than peak flux per beam for both IRS1 and SMM1 suggesting there is a contribution to the flux on scales larger than the beam (e.g. for a modelled point source of 1 Jy integrated flux, the peak flux is 1 Jy beam^{-1}). The envelope emission around IRS1 and SMM1 is resolved. The diffuse emission from IRS1 appears relatively isolated and likely associated with the source envelope only. However, even at the higher
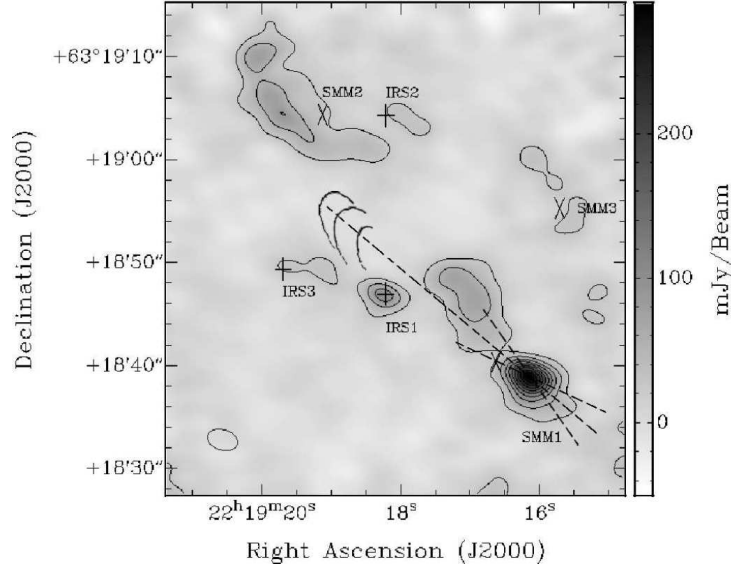
Figure 2.10: Cleaned 1.3 mm SMA continuum map of S140. The plus symbols mark the positions of IRS1, 2 and 3 (Evans *et al.*, 1989), with the sub-millimetre peaks SMM1, 2 and 3 from Minchin *et al.* (1995a) indicated by the crosses. All sources are labelled. The bow shock curves are adapted from Weigelt *et al.* (2002) while the heavy dashed line depicts the possible jet originating from SMM1 as traced by proper motion masers (Asanok *et al.*, 2010). The faint dashed lines indicate a $\pm$ 15° (3σ) range of the jet trajectory. See Section 2.4.6. Contours are from 5σ noise to peak value in steps of 30 mJy. The SMA beam is indicated in the lower left of the image. Note the faint emission as described in the text to the north east of SMM1 and to the north and east of IRS1. The primary beam FWHM is $\sim$ 55", and hence lies outside the field imaged.

resolution of the SMA observations compared to those of the OVRO observations, it is clear to see the difficulties in disentangling the substructure of this complex star forming region as the diffuse emission to the west of IRS1 joins both IRS1 and SMM1 at the 3σ level.

The gas masses for all observations can be derived, under the assumption that the millimetre emission is optically thin and the gas to dust ratio is constant throughout the region, using the equation:

Table 2.2: Fitted images parameters for IRS1, SMM1 and IRS3 observed at each frequency with various array configurations.

Array	Source	Freq. (GHz)	Peak Flux (mJy/beam)	Int. Flux (mJy)	Mass [a] M$_\odot$	T_{mb} [b] (K)	Size (Major × Minor) (")	Pos. Angle [c] (°)
CARMA A	IRS1	220	60±0.5	74±1	0.37	119	0.15±0.001 × 0.12±0.001	41±1
CARMA B	IRS1	225	83±2	95±4	0.42	17.2	0.38±0.01 × 0.32±0.01	90±6
SMA	IRS1	225	95±12	145±29	0.68	0.4	3.71±0.49 × 2.52 ±0.33	75±13
OVRO	IRS1	112	47±3	46±5	2.4	0.3	4.54±0.28 × 3.37±0.21	112±8
OVRO	IRS1	86	32±2	31±4	4.0	0.2	6.26±0.46 × 4.34±0.32	122±8
CARMA A[d]	SMM1	220	25±0.5	72±1	0.36	59	0.22±0.004 × 0.18±0.003	28±4
CARMA B[d]	SMM1	225	38±2	42±6	0.2	7.9	0.51±0.03 × 0.48±0.02	176±10
SMA	SMM1	225	261±12	531±35	2.5	1.0	4.12±0.19 × 3.00±0.14	63±6
OVRO	SMM1	112	50±3	66±6	3.5	0.3	4.85±0.27 × 4.20±0.34	115±16
OVRO	SMM1	86	21±2	21±4	2.8	0.1	6.01±0.68 × 4.74±0.54	144±19
CARMA A[d]	IRS3(E)	220	5.4±0.5	5.1±1	0.03	10.4	0.15±0.01 × 0.09±0.01	50±7
CARMA A[d]	IRS3(W)	220	6.3±0.5	7.2±2	0.04	12.4	0.15±0.01 × 0.11±0.01	58±13
SMA	IRS3	225	30±12	61±34	0.29	0.1	4.99±2.00 × 2.46±0.98	83±21
OVRO	IRS3	112	6.6±2.9	5.2±4.3	0.27	< 0.1	4.16±1.83 × 2.94±1.29	80±50

[a]Masses calculated directly from integrated fluxes as observed (see Section 2.4.1).

[b]Temperatures calculated assuming the Rayleigh-Jeans approximation.

[c]Sizes and position angles are as measured directly from images and are not deconvolved.

[d]CARMA SMM1 and IRS3 parameters to be used with caution as primary beam correction has not been undertaken. CARMA is a heterogeneous array combined of 6 and 10 metre antennas and thus absolute primary beam corrections are difficult.

$$M = \frac{g \, S_\nu \, d^2}{\kappa_\nu \, B_\nu(T_d)} \tag{2.6}$$

where S_ν is the source flux, g is the gas-to-dust ratio $= 100$, $B_\nu(T_d)$ is the Planck function for a black-body at dust temperature T_d, d is the distance to the source and κ_ν is the dust opacity coefficient (Beltrán *et al.*, 2006). The dust opacity coefficient is dependent upon both the frequency of the observation and the dust opacity index β. Section 2.4.2 will discuss the observed spectral indices towards IRS1 specifically. A β value of 1.5 is adopted for the mass estimates of all sources presented here. The corresponding dust opacity coefficients ($\kappa_\nu = \kappa_0 \, (\nu/\nu_0)^\beta$) are therefore 0.20, 0.29, 0.82 and 0.85 cm^2 g^{-1} at 86, 112, 220 and 225 GHz respectively after adopting $\kappa_0 = 1.0$ cm^2 g^{-1} at 250 GHz (Ossenkopf & Henning, 1994). The dust temperature $T_d = 50$ K is taken from the far-IR observations of Lester *et al.* (1986) and used for IRS1, SMM1 and IRS3. Table 2.2 lists all masses calculated directly from Gaussian fits of the observed integrated source fluxes. The masses for IRS1 are likely too high as they include a contribution from free-free emission (Gibb & Hoare, 2007). The choice of temperature and dust opacity coefficient at the wavelengths and resolutions probed can also cause significant variations in calculated masses of the other sources. Interpretation of these mass values is difficult as they could be severely affected by the amount of diffuse emission resolved out by the interferometer and the incorrect association of the emission from the diffuse surroundings with a source and its envelope.

The SMA and OVRO (2.7 mm) data both detect the third reported strong infra red source IRS3 east of IRS1. IRS3 has a luminosity of $\sim 1.4 \times 10^3$ L$_\odot$ and is part of a multiple system as seen in high resolution images (Preibisch *et al.*,

2001). IRS3 is detected as a single weak point source in both maps, slightly above the 3σ at 2.7 mm but at $\sim 8\sigma$ in the SMA map.

2.4.2 Spectral Energy Distribution

Using the SMA 1.3 mm continuum emission, the OVRO 2.7 and 3.5 mm emission and the centimetre fluxes of Gibb & Hoare (2007), a spectral energy distribution (in the mm and cm regime) for IRS1 can be produced to investigate the dust continuum emission. Notably, comparing fluxes from interferometric arrays, where the synthesised beams are up to a factor of 5 different in area, is not valid for extended emission regions. At lower resolutions more extended emission is recovered compared to the higher resolution observations, as shorter baselines, sensitive to larger scale emission, are sampled. Furthermore, the lower resolution images may not be able to separate different structures that may or may not be associated with the source in question. In order to compare the fluxes in a consistent manner, and more specifically to establish sub-mm/mm wavelength spectral indices, the images must have the same (u, v) coverage and hence same resolution probing the same physical scales (for example, see Galván-Madrid *et al.* (2010) section 3.1.2). As a first order correction the resolution of the SMA data can be limited to that of the OVRO data. Here the arrays themselves sample the (u, v) plane differently and so the fraction of un-recovered flux will still differ, although this should not be as significant as the initial resolution difference. Using a limited (u, v) range with baseline lengths of 5 to 35 kλ concordant coverage images from OVRO 86, OVRO 112 and SMA observations are produced.

After re-imaging the S140 region with the restricted (u, v) range all images are re-fitted. Table 2.3 presents all observations for which the (u, v) range could

Table 2.3: IRS1 restricted (u, v) range fluxes and free-free subtracted integrated fluxes.

Array	Freq. (GHz)	$S_{5-35k\lambda}$ (mJy)	S_{ff} (mJy)	$S_{5-35k\lambda}-S_{ff}$ (mJy)
SMA	225	183 ± 57	29 ± 3	154 ± 57
OVRO 112	112	47 ± 3	19 ± 2	28 ± 4
OVRO 86	86	26 ± 2	16 ± 2	10 ± 3

be limited and hence does not include CARMA data as the smallest baseline is below the upper (u, v) limit. Note the increase in flux of the (u, v) range limited lower resolution SMA observations in Table 2.3 compared to the full resolution SMA data in Table 2.2. The flux increase is due to emission from the surrounding envelope now being associated with the source. The flux change re-emphasises the difficulty with lower resolution images in separating the emission attributed to compact core emission filling the beam, the source envelope and any diffuse emission either associated with the source envelope or not.

Column 4 of Table 2.3 shows the extrapolated free-free fluxes to millimetre wavelengths. The cm wave observations would appear as point sources in the comparatively large synthesised beams of the SMA and OVRO observations. The major axis sizes extrapolated from the 43 GHz size observed by Gibb & Hoare (2007) using $\theta \propto \nu^{-0.6}$ for stellar winds (Wright & Barlow, 1975) are 0.053, 0.046 and 0.030" at 86, 112 and 225 GHz respectively, i.e. unresolved by OVRO and SMA. The spectral index of ionised emission from IRS1 is well constrained (α=0.62 $\pm$ 0.03, Gibb & Hoare, 2007) and can be directly extrapolated to 86, 112 and 225 GHz in order to establish the free-free flux contribution at the millimetre wavelengths. The ionised emission component at 1.3 mm is 17 percent, however
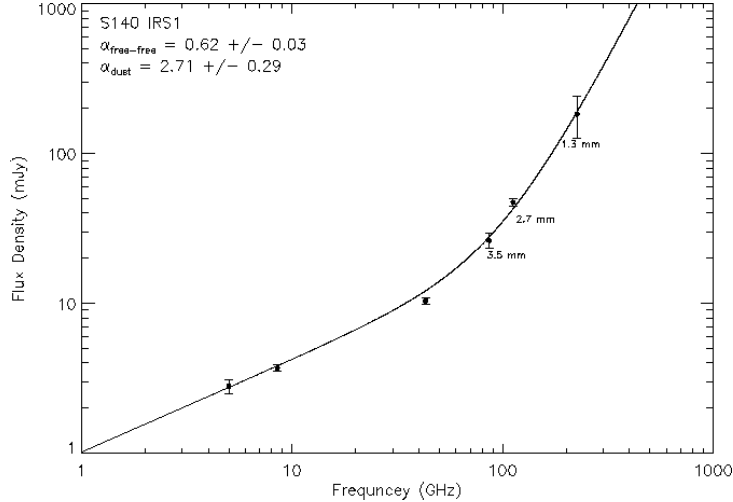
Figure 2.11: Integrated flux density SED for the source IRS1. This combines (u, v) range limited data from the 1.3 mm SMA data with 2.7 and 3.5 mm OVRO observations and those from Gibb & Hoare (2007). The line indicates the summation of the independently established least squares power law fits to free-free radio data and dust only (free-free subtracted) data. The slopes of these best fitting lines are indicated in the upper left corner of the figure.

at 3.5 mm the ionised wind emission makes up a significant fraction of the flux, $\sim$ 60 percent. Gibb *et al.* (2004) noted in their investigation of MYSOs that 3 mm wavelengths are heavily contaminated by the free-free ionised emission. Figure 2.11 shows the observed mm/cm wavelength SED for IRS1. The best fitting line indicated is the summation of the independently established free-free emission best fit (α=0.62 $\pm$ 0.03, Gibb & Hoare, 2007) and the dust only best fit lines (α=2.7 $\pm$ 0.3, this work). The dust only best fitting line was calculated after the removal of the free-free flux contribution at those wavelengths, i.e. from the fluxes presented in Table 2.3.

In the Rayleigh-Jeans (R-J) approximation the spectral index is $\alpha = 2 + \beta$, where β, the dust opacity index is intrinsic to the dust around the emission source. If the dust surrounding MYSOs was both optically thin and similar to interstellar

dust the expected spectral index would be have an α value of $\sim 3.8 \pm 0.2$ using the average measured value of ISM dust with a β value of 1.8 ± 0.2 (Draine, 2006). For massive star forming regions and hot cores the typical values are $\beta \sim$ 1-2 (e.g. Cesaroni *et al.*, 1999; Galván-Madrid *et al.*, 2010; Zhang *et al.*, 2007). The SED for the dust only emission from IRS1 after removal of the free-free emission yields a spectral index of α=2.7 $\pm$ 0.3, resulting in a value of $\beta \sim 0.7$. Draine (2006) discussed studies of discs and material around low mass pre-main-sequence stars where typical values of $\beta \sim$ 0.5-0.7 are found both direct from observations and model fitting. At the distance of IRS1 the interferometric observations are probing scales down to $\sim$ 6000 au where emission is much more likely dominated by the central core or possibly a compact disc.

Such low spectral indices could be explained if the material probed does not follow the optically thin regime. Low β values are replicated in models with $\tau >$ 1 where the input dust opacity index is ≥ 1.5 (Hoare *et al.*, 1991). In the case of IRS1, if the dust emission at 1 mm was optically thick (i.e. not all the emission is detected by the observer) but that at 3 mm was optically thin the spectral index would be artificially lower than in the regime where all dust emission is optically thin. The T_{mb} values in Table 2.2 for both SMA and OVRO observations appear to follow the optically thin assumption, with values much lower than the likely dust temperature.

The alternative interpretation of opacity indices <1 is the concept of grain growth in the proto-stellar discs. Draine (2006) shows that following the standard dust particle power law distribution with an increased maximum particle size $a_{max} \geq 3$ mm, the dust opacity index will be $\beta(1 \text{ mm}) < 1$. This assumes proto-planetary discs are simply comprised of a similar material to interstellar grains

with physical particle sizes extending to ~ 3 mm due to grain growth (Calvet
et al., 2002; Natta *et al.*, 2004; Testi *et al.*, 2003). The low opacity index for IRS1
combined with the spatial scales probed would suggest the grain growth is occur-
ring and could be mediated by a compact disc. The typically larger dust opacity
indices found in more distant hot cores could be an effect of angular resolution.
The change of dust opacity with resolution is depicted by Beuther *et al.* (2004)
where they select interferometric baselines measuring large and small scales. The
smaller scales indicate $\beta \sim 0.5$ suggesting grain growth in a disc for the more
compact emission, compared to the larger scale value of $\beta \sim 1.2$ where dusty enve-
lope emission provides a large influence. On the very largest scales probed, when
incorporating emission from the surrounding envelope, the dust opacity index is
larger than when probing smaller scales with less influence from the surrounding
material.

2.4.3   Molecular Outflow from IRS1

For completeness, the molecular gas emission detected in the lower resolution im-
ages is presented. The OVRO and SMA data trace the ^{12}CO(1-0) and ^{12}CO(2-1)
molecular emission respectively. The channel maps for both observations are shown
in Figures 2.12 and 2.13. It is clear to see the blue shifted outflow lobe situated
to the south-east of IRS1 while the red shifted outflow lobe is in the north-west.
The high velocity blue and red shifted outflow wings integrated between -32 and
-18 km s^{-1} and 2 to 10 km s^{-1} respectively are shown more clearly in Figure
2.14. Due to the nature of interferometry and the visibility coverage some of the
extended emission is resolved out and there are 'holes' in the maps at certain ve-
locities. The missing large scale emission is clearly evident when comparing with

single dish observations where the outflow lobes cover 60 × 60 arcsec or larger regions (e.g. Hayashi *et al.*, 1987) compared to these interferometric observations. This is expected as the OVRO and SMA arrays are not sensitive to scales ≤ 5 kλ corresponding to emission regions larger than ~ 50". The problem is more evident in the SMA channel map where emission on scales larger than the synthesised beam is clumpy, making it difficult to identify precisely the centre of the high velocity components of the blue and red shifted lobes. A line connecting the outflow lobes yields a position angle of 150-160° in agreement with the single dish data of Hayashi *et al.* (1987) and Minchin *et al.* (1993). Both outflow lobes are spatially separated here which supports the interpretation of an intermediate outflow axis inclination. This is contrary to the much lower resolution single dish studies where the blue and red shifted outflows overlap, leading to a conclusion of a more pole-on outflow axis inclination.

Following Scoville *et al.* (1986) the outflow lobe masses associated with the CO line emission can be calculated. A conservative approach is chosen as a low value for the excitation temperature $T_{ex} \sim 15$ K is used along with a simple average for the ^{12}CO optical depth, $\tau \sim 4$ (Minchin *et al.*, 1993). Given that interferometers are insensitive to the largest scale emission the mass of the outflow lobes and subsequent parameters based on the masses are likely significant underestimates, although not strictly lower limits. Table 2.4 summarises the physical properties of the outflow lobes. Momentum and energy parameters follow the definitions outlined by Beuther *et al.* (2002c). The systemic velocity for IRS1 is taken as $V_{LSR} = -8$ km s^{-1} as noted by Minchin *et al.* (1993). Hence the ranges of the blue and red shifted outflow velocities with respect to the source velocity are -24 to -10 km s^{-1} and 10 to 18 km s^{-1} respectively.

82
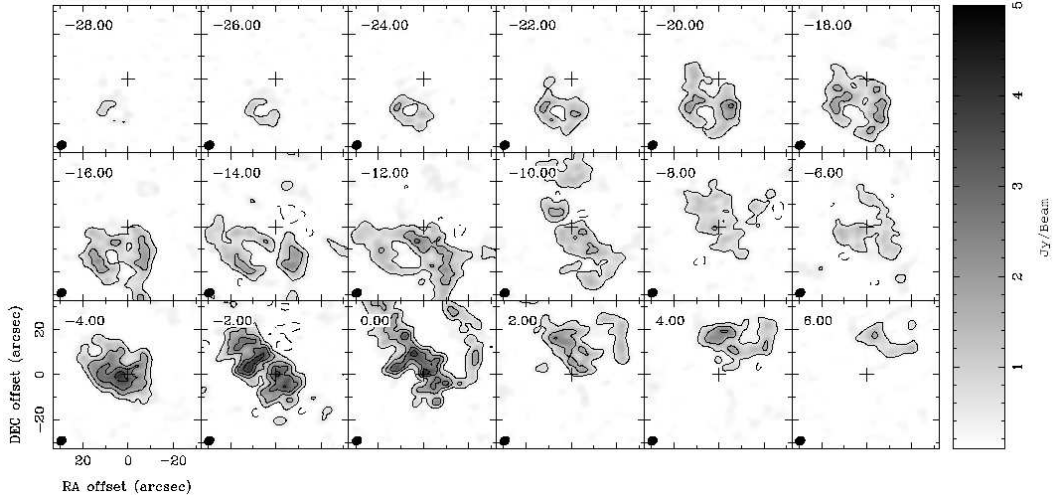
Figure 2.12: Channel map for OVRO CO(1-0) emission. The plus symbol marks the location of IRS1. The velocity is indicated in the top left of each sub-plot and is in km s^{-1}. The OVRO beam for the line observations is indicated in the lower left of each sub-plot and is 4.3×3.5 arcsec with a position angle of $-60.7°$. The grey scale images show all emission from 5σ, where 1σ is 97 mJy/beam as measured in line free channels. Contour levels are from 5σ to the peak in steps of 1 Jy. The distinct offset of the blue shifted outflow lobe in the south-east and the red shifted lobe in the north-west is evident.

The higher resolution SMA observations indicate a smaller physical size of the outflow lobes compared to the OVRO data, because more extended, large scale emission is resolved out. This results in a further reduced mass estimate for the outflow lobes. The reduction by a factor of three is carried to subsequent parameters calculated from SMA data when compared with those from OVRO data. Both the interferometric observations do however show similar masses for both the blue and red shifted lobes, contrary to previous single dish data where a clear asymmetry was noted (Minchin *et al.*, 1993). This is possibly due to the different velocity range selected to integrate over, but the different range of detected spatial scales could also play a role. The blue and red shifted outflow
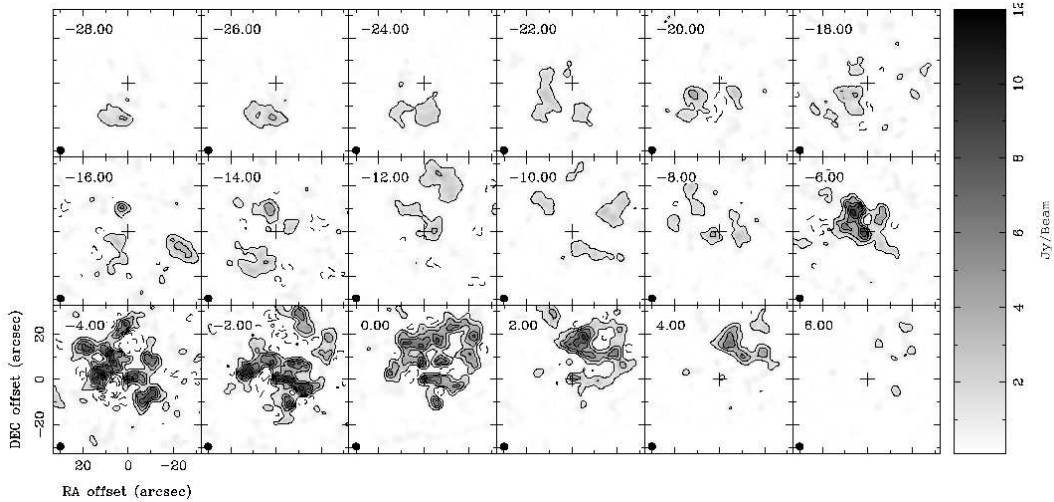
Figure 2.13: Channel map for SMA CO(2-1) emission. Velocities and IRS1 position as Figure 2.12. The beam size of 3.2×2.9 at PA of $72.4°$ is indicated in the lower left of each sub-plot. The grey scale images show emission from 10σ, where 1σ is 86 mJy/beam as measured from line free channels. Contours are from 10σ to the peak in steps of 2 Jy. As Figure 2.12 the shift from blue lobe in the SE to red lobe in the NW is evident. Note how the diffuse emission is broken up into many peaks due to the interferometer sampling and use of the clean algorithm.

Table 2.4: IRS1 outflow parameters calculated from OVRO and SMA observations

Parameter	Value (OVRO)	Value (SMA)
Outflow mass (assuming $\tau \sim 4$):		
Redshifted($M_\odot$)	0.16	0.06
Blueshifted($M_\odot$)	0.25	0.07
Total($M_\odot$)	0.41	0.13
Momentum ($M_\odot$ km s^{-1})	8.9	2.8
Kinetic energy (ergs)	1.9×10^{45}	0.6×10^{45}

lobes in previous work have been integrated between -30 to -11 and -4 to 10 km s^{-1} which includes more low velocity outflow/core material. The velocity ranges here are selected to be symmetric about the V_{LSR} and extend out to the maximal
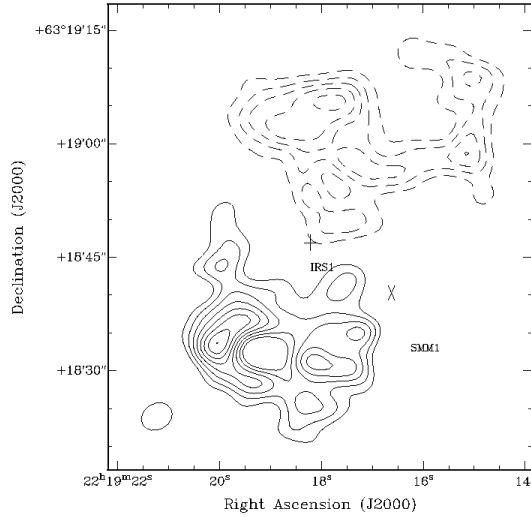
Figure 2.14: Integrated OVRO CO(1-0) outflow emission image. Solid contours correspond to the blue outflow wing between -32 km s^{-1} to -18 km s^{-1} with dashed contours representing the red wing from 2 km s^{-1} to 10 km s^{-1}, note the V_{LSR} is -8 km s^{-1}. The RMS noise levels are 0.87 and 0.51 Jy/beam km s^{-1} for the blue and red outflow lobe images respectively. Contour levels are from 5σ to peak emission in 2 Jy/beam km s^{-1} steps for both lobes. The synthesised beam is indicated in the lower left corner and is 4.3×3.5 arcsec. IRS1 is marked by a plus symbol and located at the centre of the massive outflow while the sub-millimetre source SMM1 indicated by the cross is positioned to the south-west.

velocities of each lobe. Figures 2.12 and 2.13 indicate morphologically distinct red and blue shifted material at velocities ~ 10 km s^{-1} from the V_{LSR} which sets the limits of the velocity ranges. The noticeable mass asymmetry is evident if the velocity ranges used by Minchin *et al.* (1993) are applied and more core material, or low velocity outflow emission is included. For the crude estimation using a fixed optical depth, which is clearly not realistic, less than 10 percent of the mass calculated by Hayashi *et al.* (1987) is recovered. Both the reduced velocity range and the missing large scale material are significant contributors.

2.4.4 CARMA Continuum Maps
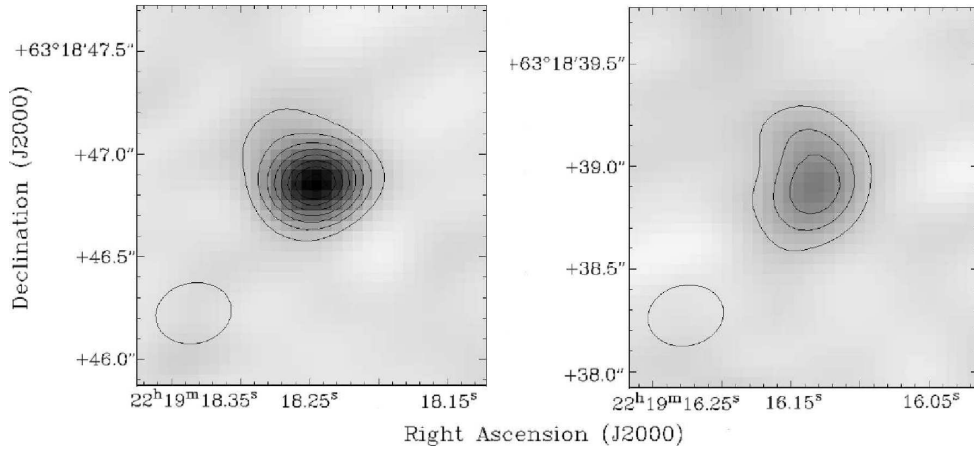
Figure 2.15: Image of IRS1 (Left) and SMM1 (Right) at 1.3 mm produced with Robust parameter 0.5. Contours levels are from 5σ noise to peak value in steps of 10 mJy. The beam is indicated in the lower left of each image for clarity. IRS1 appears to be marginally resolved and exhibits a slight elongation in the NE-SW direction.

The high resolution CARMA B continuum observations detect compact emission from both IRS1 and SMM1 (Figure 2.15). The diffuse emission previously detected by the SMA and OVRO observations is resolved out by the interferometer. The left panel of Figure 2.15 shows a modest elongation of the emission surrounding IRS1. Although the deconvolved size for IRS1 (see Table 2.5) has large errors and is consistent with being unresolved, the position angle is significantly different from the beam PA and is in the direction of the small extension to the NE. If the compact dust emission originates from a flattened envelope, or indeed the accretion disc itself, then it is amongst the smaller scale of millimetre discs observed (Fernández-López *et al.*, 2011a; Torrelles *et al.*, 2007).

Figure 2.16 shows the full CARMA A map of the S140 region within approximately 15" of IRS1. For reference the infrared sources and sub millimetre peaks

Table 2.5: Fitted source size and position angle parameters for IRS1 observed in CARMA A and B configurations after free-free flux subtraction. The image and deconvolved parameters are indicated. Sizes in au are calculated to nearest 10 au using the distance from Hirota *et al.* (2008) of 764 ± 27 pc. Note the slightly different position angles after free-free removal compared to Table 2.2.

Array Config. (Image/decon.)	Size (")	Size (au)	PA (°)
A Image	0.17×0.12	130×90	35 ± 1
B Image	0.41×0.35	310×270	72 ± 12
A Decon.	$0.116 \pm 0.003 \times 0.031 \pm 0.005$	90×20	30 ± 2
B Decon.	$0.16^{+0.03}_{-0.16} \times 0.06^{+0.11}_{-0.06}$	120×50	37 ± 15

detected are labelled. IRS1 is the strongest source at the highest resolution, owing to the emission from a small compact object, likely a disc. However, primary beam corrections have not been applied. Interestingly SMM1 is resolved and has a similar appearance to the previous CARMA B image. Given the high sensitivity nature of the observations, where a noise level of 0.48 mJy/beam was achieved, there are 10 unresolved sources detected above 5σ. These were not detected in the previous observations CARMA B configuration maps.

The binary source IRS3 (Preibisch *et al.*, 2001) is resolved with a separation of ~ 0.68", corresponding to ~ 520 au and a point source is detected east of the location of SMM2 and is consistent with the peak emission near SMM2 in the $\sim$ 3" resolution SMA map. The high resolution detection could mark the position of SMM2 as a core. Furthermore, another point source is coincident with the location of IRS2 as detected with the SMA and at other wavelengths. These four sources are all above the $\sim 15\sigma$ level. There are 6 other unresolved peaks of emission in the region which do not appear to have strong counterpart detections at other wavelengths. If the map noise follows a Gaussian distribution and these sources
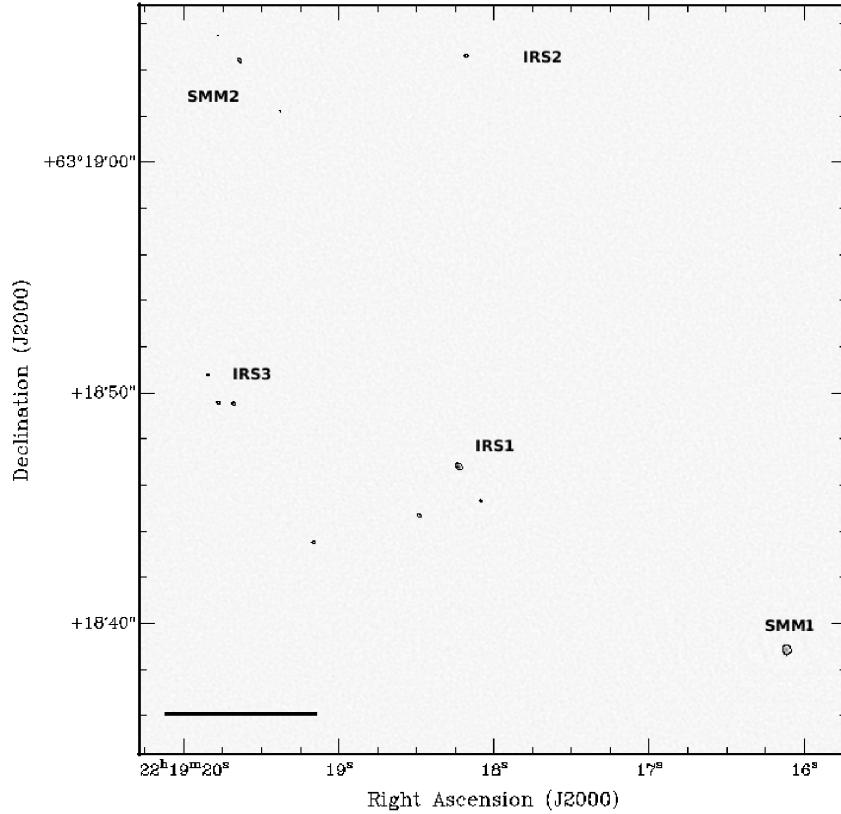
Figure 2.16: Map of the S140 region at 1.3 mm observed with CARMA A. As described in the text, IRS1 and IRS2 are detected as is the binary source IRS3. SMM1 is also detected as is a peak of emission near SMM2. The single black contour corresponds to the 5σ level, while the solid line in the bottom left corner corresponds to a ~ 5000 au scale.

are at the 5σ flux limit then they correspond noise fluctuations. One of these detections could be real as it is detected at the 10σ level, although there is no indication of a source in the IR map by Weigelt *et al.* (2002).

Figure 2.17 shows the zoomed in map of IRS1 (left) after the free-free flux contribution has been subtracted and SMM1 (right) taken directly from the main image (Figure 2.16). As noted in Section 2.4.2 the physical size of the free-free emission is 0.03 arcsec at 225 GHz after extrapolation from the resolved 40 GHz

observations, and hence a point source is removed from the CARMA A data of IRS1. The elongated morphology of IRS1 is not affected by the free-free correction. IRS1 appears resolved with an image position angle of $35.4 \pm 1.5°$ and major and minor axes of 0.17 and 0.12" respectively, from Gaussian fitting in the image plane. The deconvolved source parameters reported are $\sim 0.12 \times 0.03$" for the major and minor axes with a position angle of $\sim 30°$. Table 2.5 indicates the image and deconvolved sizes and position angles. The synthesised beam itself has a position angle of $51.5°$ and is not significantly elongated, with major and minor axes of 0.13 and 0.11" respectively, and hence supports the conclusion that the dust emission around IRS1 is resolved along the major axis. Analysis of the visibilities with the uvfit task also reports a deconvolved source size of $\sim 0.13 \times 0.05$" with a position angle of $\sim 31°$, assuming a Gaussian source.

Accordingly the deconvolved PA is interpreted as indicating that a dust disc structure is orientated approximately perpendicular to both the larger scale CO bipolar outflow and sub-arcsec speckle image of the reflection nebula attributed to the blue shifted outflow lobe at $PA \sim 154°$ (Schertl *et al.*, 2000; Weigelt *et al.*, 2002). The deconvolved position angles of the 1.3 mm CARMA A and CARMA B continuum maps of IRS1 are coincident with that of the very elongated 5 GHz ionised emission at $45°$ (Hoare, 2006). The agreement with the dust disc parameters further supports the disc wind interpretation of the radio emission. Moreover, the alternative jet interpretation of the 5GHz ionised emission (Preibisch & Smith, 2002) would imply a dust disc at a $PA \sim 135°$ if the disc were perpendicular to the jet. Due to the continuum nature of the observations it cannot be established whether the structure is rotating as is observed in other disc sources (e.g. Cesaroni *et al.*, 1999; Galván-Madrid *et al.*, 2010; Qiu *et al.*, 2012). However, given the high
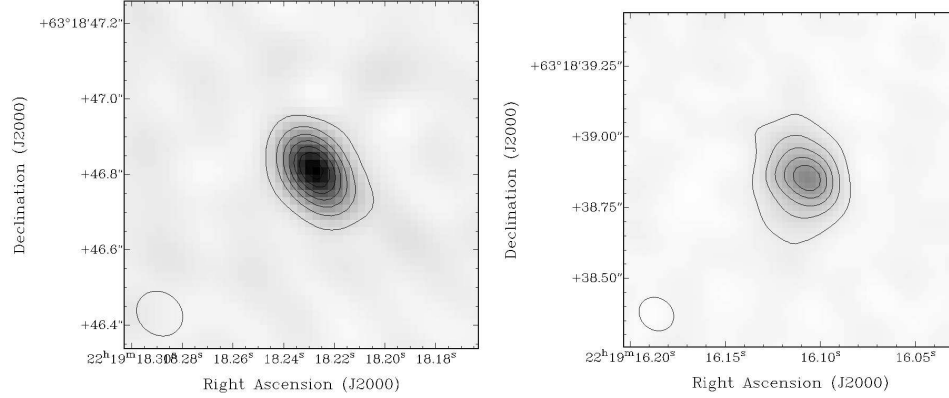
Figure 2.17: Left: Image of IRS1 after the subtraction of the free-free flux contribution. IRS1 is clearly resolved and the dust continuum emission traces a disc with an image PA of $\sim 35°$, almost perpendicular to the large scale bipolar outflow the source drives. The contour levels are from 5σ to peak in 5 mJy steps while the dashed lines indicate the outflow direction. The beam is indicated in the left hand bottom corner. Right: Image of SMM1 taken from Figure 2.16. SMM1 is resolved and has a similar structure to that seen on the slightly larger scales in CARMA B maps. The contours are also from 5σ to peak in 5 mJy steps and the beam is indicated in the bottom left corner.

resolution and high sensitivity the very compact emission on these scales must come from a compact object such as a disc.

The integrated flux of IRS1 has decreased slightly in comparison to the estimate from the CARMA B observations, see Table 2.6. The scale of the decrease is well within the expected 10-20 percent uncertainties in the calibration processes. In addition, the A array configuration is less sensitive to larger structures in comparison with the B configuration as more antennas are at longer baselines. For both sets of CARMA observations the estimated T_{mb} are much greater than the low resolution observations. Crudely, the CARMA B observations are less than the assumed source temperature from IR fitting by Lester *et al.* (1986) of ~ 50 K and the emission is likely optically thin. However, the CARMA A data has a T_{mb} of ~ 119 K. If the observations are optically thick the calculated temperature will

Table 2.6: Fluxes for IRS1 observations in CARMA A and B configurations after free-free flux subtraction.

Array Config.	Peak Flux (mJy/beam)	Integrated Flux (mJy)
CARMA A	35.2±0.5	49.5±1.0
CARMA B	52.1±2.2	68.3±4.6

tend to the source temperature (see Section 3.2.1). Galván-Madrid *et al.* (2010) find that temperature of the material surrounding MYSOs can reach to ~ 300 K which would suggest that the CARMA A observations are tending towards $\tau \sim 1$. The temperature is also consistent with the modelling of W33A by de Wit *et al.* (2010) who indicate the temperature of the dust is > 300 K at a radius of ~ 250 au (see Chapter 3). Note, as shown in Table 2.6 the integrated flux decreases noticeably after the removal of the free-free emission and hence the T_{mb} estimate will also decrease. The optically depth is becoming important as the CARMA A observations are probing regions much closer to the MYSO

Data merging of the CARMA A and B array observations was undertaken and proved to be challenging due to slightly different referencing coordinates for the calibrators and therefore the source itself. Once the correct positions were established the images were merged. However, during the imaging process to produce a single continuum map there is less weighting applied to the most noisy observations, hence the superior sensitivity CARMA A data were much more favourably weighted and the final image did not change noticeably. Ideally, each observational setup would have the same (or a more similar) bandwidth and on source time to produce fully compatible data sets. Here this is not possible as CARMA had been significantly upgraded between the early 2008 and late 2011 observations.

2.4.5 Nature of the Disc Wind

A compact dust disc around the prototype disc wind source confirms its disc wind nature. This has the implication that radiation pressure is important during the formation of massive stars, where the unique source IRS1 is one piece of the complex puzzle. In the models of Drew *et al.* (1998) radiation pressure, from the star and disc, on the surface of the disc can drive an equatorial disc wind from the source, given typical main sequence source parameters. However, massive stars are thought to be very swollen and cooler in the very early stages when they are accreting (Hosokawa & Omukai, 2009; Hosokawa *et al.*, 2010). Furthermore, the modelling by Hosokawa & Omukai (2009) and Hosokawa *et al.* (2010) show that the outer layers of the protostar are convective during the swelling stages which could be important in generating magnetic fields which help drive collimated MHD jets and outflows (e.g. Vaidya *et al.*, 2011). Radiative pressure is only likely to become important when the protostar begins to contract and heat up after accretion has slowed or stopped. When the source has become sufficiently hot, it will generate copious amounts of Lyman continuum radiation and ionise the surrounding medium to form a HII region. In the case of IRS1 the ionised emission is consistent with a disc wind, i.e. the ionised material is from the source itself and not the surrounding medium. In order to produce a disc wind, IRS1 must have contracted or be undergoing contraction to provide the radiation pressure required, but not be so hot that it begins to ionise the surrounding environment. The contraction would mean IRS1 would have near main sequence parameters, such as mass, luminosity and radius, much like the source modelled by Drew *et al.* (1998).

The picture of IRS1 as a contracted/contracting MYSO with near main sequence parameters fits with the models available and suggests that an ionised disc wind could be part of the evolutionary process in massive star formation after the major accretion and swelling episode. The disc wind scenario is supported by the radio and millimetre interferometric observations. Complex molecules are not detected around IRS1, possibly due to high temperatures close to the source and the dust disc. The disc mass is no more than ~ 0.4 M$_\odot$ (as Table 2.2) using typical hot core parameters and is likely much less assuming a hotter disc temperature and correcting for the observed dust opacity index. The prototype disc wind source IRS1 is thereby suggested to be a pre-UCHII region essentially in a late stage of evolution where accretion is slowing or has stopped, the disc is beginning to disperse and decrease in mass and before the source is so hot that it forms a large HII region. IRS1 is only one of two distinct disc wind sources (S106 IR the other) and more investigation is required at both millimetre and centimetre wavelengths to provide a statistical study of MYSO disc wind or radio jet sources.

2.4.6 SMM1 and associated outflow phenomena

An alternative driving source of the bow shock structures seen at $\sim 20°$ north east of IRS1 is the source SMM1. H$_2$O masers detected by Asanok et $al.$ (2010) are directly positioned over the new, precise location of SMM1 from the CARMA observations (in comparison with the low resolution observations of Minchin et $al.$ (1995a)). The direction of the maser proper motions are directly opposed about the centre of SMM1 and are likely tracing a jet emanating from the source. The position angle of the proposed jet projects adjacent to the previously discussed diffuse emission in the SMA image. A linear regression of all the maser locations

in the region of SMM1 (see Asanok *et al.*, 2010, Table 4) results in a position angle of $50 \pm 5°$ for the jet trajectory. The bow shock region is directly in the path of the SMM1 jet, hence suggesting that the collision of the jet with the ambient medium results in the H_2 bow shock emission (Preibisch & Smith, 2002; Trinidad *et al.*, 2007; Weigelt *et al.*, 2002). Furthermore, the weighted position angle of the two identified proper motion maser pairs (see Asanok *et al.*, 2010, Table 4, maser groups 'e and f') agrees within 1σ of the more basic linear regression value. Interestingly, the PA of SMM1 ($\sim 28°$) from the CARMA A observations is not perpendicular to the proposed jet. The fitting appears to follow the more northern extension seen in the right hand plot of Figure 2.17. However, the image clearly shows that SMM1 is extended in south-east direction at the 5σ level. This extension is roughly perpendicular to the proposed jet. It is unclear whether the resolved morphology is also effected by the location of SMM1 at the edge of the primary beam for the 10 m antennas in the CARMA array. Further observations targeting SMM1 are required.

As discussed by Hoare (2006), the weaker bow shocks, in comparison to the main northwest-southeast outflow tracers for IRS1, are probably produced by a jet from a different source impacting the surroundings. It appears that SMM1 is in fact a protostar in the early stages of jet production and accretion. It is still deeply embedded and not detected in the IR (e.g. Evans *et al.*, 1989) and has no evidence of ionised emission at centimetre wavelengths (Gibb & Hoare, 2007). The luminosity estimate for SMM1 of $\sim 10^3$ $L_\odot$ by Minchin *et al.* (1995a) and the estimated mass of the central object ~ 10 $M_\odot$ by Zhou *et al.* (1993) is suggestive of an MYSO in the process of formation. In conclusion it is proposed that the maser traced jet from SMM1 is the likely source of the H_2 bow shock emission NE

of IRS1 and that IRS1 is not responsible itself for multiple outflows. Figure 2.18 shows a schematic of the region in light of these new observations.
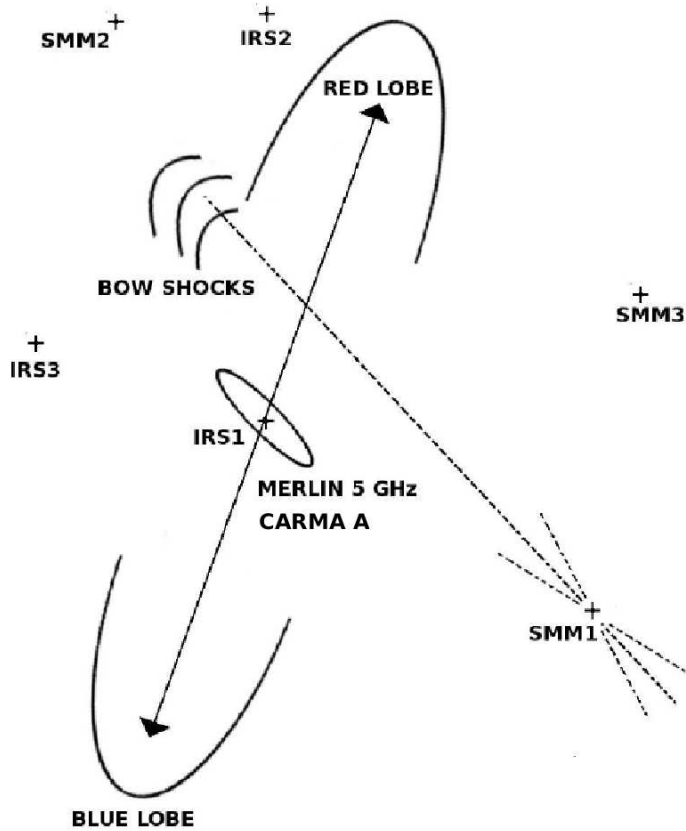
Figure 2.18: Schematic of the S140 region as it is currently viewed. The oval shape around IRS1 indicated the CARMA A dusty disc and the MERLIN 5 GHz disc wind emission. The outflow lobes as traced by the CO bipolar outflow from IRS1 are labelled. The other IRS and SMM sources are also indicated in correct positions relative to IRS1. The dashed line represents the maser traced jet originating from SMM1 (Asanok *et al.*, 2010) with a position angle of 50° (see § 2.4.6) that intercepts the bow shocks seen by (Weigelt *et al.*, 2002) north of IRS1. The shorter dashed lines indicate a 3σ spread in the jet trajectory ($\pm$ 15°).

2.5 Conclusions

Images have been presented from high resolution interferometric observations of the S140 region taken with the CARMA A and B arrays and with OVRO and SMA in the compact configurations. The lower resolution images indicate a dense ridge stretching across the S140 regions extending from the source SMM1, past IRS1 and up to SMM2. The ridge could provide a reservoir for other YSOs to form in the region. There is also a notable deficit of dust emission in the regions of the CO molecular outflow lobes. Fitting of the millimetre spectral energy distribution of the IRS1 by combining the OVRO and SMA data at comparable resolutions results in a dust opacity index of 0.7 and may point to dust grain growth in a disc. The detection and updated position of the more embedded young source, SMM1, identifies it as an alternative source for the H_2 bow shock emission to the NE of IRS1 as indicated by the trajectory of the proposed jet traced by the proper motions of H_2O masers.

The very highest resolution observations with the CARMA A array detect all IRS sources and SMM1 along with multiple possible low mass sources. The high resolution map of IRS1 after the removal of free-free flux contamination indicates the detection of a compact dust disc structure associated with the MYSO. The orientation of the dust structure is consistent with the elongated radio emission from an ionised disc wind. The dust emission is perpendicular to both the CO emission and near-IR speckle image tracing the outflow. The data disagree with previous interpretations of IRS1 as being the driving source of a radio jet. More-over, the detection of the compact disc around S140 IRS1 is the first confirmation of a small scale disc, of the order ~ 100 au, in a disc wind system. Confirming

the disc wind nature of the source has the implication that radiation pressure on the disc surface is an important feedback process in the latter stages of massive star formation. IRS1 is suggested as a pre-UCHII region source that is possibly contracting towards having main sequence parameters and heating up such that radiative pressure is important. Further studies of other candidate MYSOs are required to build a more comprehensive picture of these processes.

Chapter 3

Radiative Transfer modelling of S140 IRS1 at millimetre wavelengths

Interpretations of the structures, morphologies and geometries of astrophysical sources, such as MYSOs, are often based directly on the observed radiation received at the Earth. In some cases, after observations, the origin of the source emission cannot be deduced with firm conclusion and more information is required. Modelling of the source structure and environment is useful in providing a means to confirm or disprove conclusions drawn from observations and could provide alternative interpretations for the emission. Understanding the models can help with understanding observations and in the context of massive star formation, can help piece together an evolutionary sequence.

Radiative transfer is used as it describes the propagation of light, electromagnetic radiation, through a medium. Radiation is affected by absorption, emission and scattering processes as it travels through a medium before reaching the Earth.

Radiative transfer modelling is required in order to understand the observed emission from embedded MYSOs.

This chapter details the models generated to reproduce the observed millimetre emission from the MYSO, S140 IRS1, using the publicly available radiative transfer code by Barbara A. Whitney (Whitney & Hartmann, 1992; Whitney *et al.*, 2003b) and unpublished ray tracing code by Rémy Indebetouw. The results from model testing, investigation and comparison with observations are presented and discussed.

3.1 Introduction

In the context of star formation, observations alone do not always provide a clear cut conclusion regarding the source of emission. Generally, multiple observations at a range of wavelengths are required in order to piece together a picture of the environments around embedded stars in the early stages of formation (as is the case for the MYSO, S140 IRS1, as detailed in Chapter 2). Observations of multiple sources can then be used to piece an evolutionary picture together. Radiative transfer (RT) modelling can be undertaken as a standalone process, separate from observations, to investigate theoretical environments of star formation and output data that could be similar to observations. Moreover, the effects of different physical structures, such as discs, dense envelopes and non-spherical or clumpy structures can be investigated along with how they might evolve with time (e.g Dullemond *et al.*, 2001; Whitney *et al.*, 2003a, 2005). Typically the output of such models are spectral energy distributions describing how the strength of emission at a range of wavelengths varies with different parameters, different geometries

and viewing angles, and evolution. Notably, some models output images of the regions at particular wavelengths that are accessible with current telescopes for direct comparison with observations.

The combination of RT models and observations can provided a powerful tool in describing the source environment and understanding single or multiple sources and how they compare. The most comprehensive study of massive star forming regions was undertaken by van der Tak *et al.* (1999, 2000). Here both continuum and spectral line emission taken with single dish telescopes and interferometric arrays of 14 sources are compared with one dimensional spherical RT models in order to understand the density and temperature structure of the source environments. Comparisons of their observed and modelled SEDs (continuum emission) with different dust grain models (only in van der Tak *et al.*, 1999) indicate a match at wavelengths longwards of ~ 50 μm (Figure 3.1). The models however, underestimate the flux at the near-IR wavelengths, even for different density distributions, and the interferometric visibilities van der Tak *et al.* (in both 1999, 2000) are not matched. The incompatible near-IR fluxes are likely due to a deviation from non-spherical geometry where less opaque cavities would allow the transmission of more flux at these shorter wavelengths. Overall van der Tak *et al.* (2000) find that the density distribution is flatter than those of low mass sources, suggesting MYSOs and their envelopes are supported by a different means to low mass sources where the density distribution exponent is ~ 2.

To better understand the formation sequence of lower mass sources (< 8 M$_\odot$) and motivated by the unsatisfactory fitting of previous models to the infrared emission (as found in the 1D models of van der Tak *et al.* (2000)) Whitney *et al.* (2003a,b, 2004) produce more realistic two dimensional axisymmetric model envi-
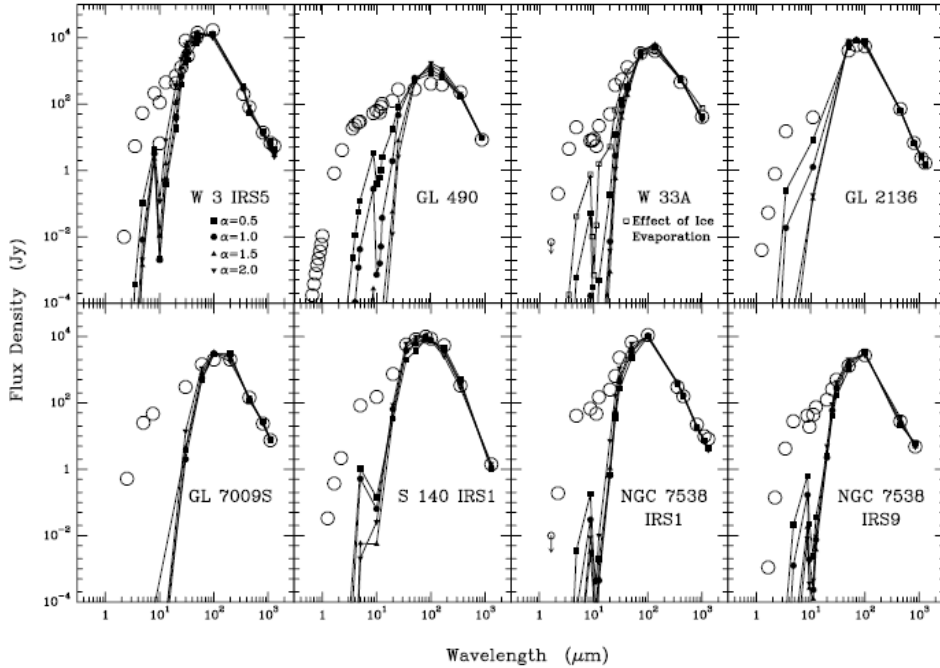
Figure 3.1: Observed spectral energy distributions of 8 sources compared with models of differing density distributions. Note the variation and bad fits of the models at IR wavelengths in comparison to the agreement at longer, sub-mm and mm wavelengths. Taken from van der Tak *et al.* (2000).

ronments. The envelope geometry follows a rotationally flattened infalling solution as prescribed by Ulrich (1976) and Terebey *et al.* (1984). A dense central disc and excavated bipolar cavities are also included, based upon observations of embedded sources with outflows and discs. In the series of papers different effects are investigated, i.e. different geometries, inclination effects, evolution of the envelope and variation of the stellar temperature.

Whitney *et al.* (2003b) show that the deviation from a simple envelope to the inclusion of a disc and cavities can have a profound effect on the output images and SED (Figure 3.2). Much more IR flux is present for models with cavities, but the range of fluxes varies much more with the inclination angle compared to 1D

models. In edge on geometries the addition of a disc causes a much broader and deeper silicate feature at 10 μm, as is often seen in observed SEDs. In colour-colour plots the sources with cavities appear bluer than those without. The implication here is that previous 1D models would require less envelope mass to provide the same colours and hence underestimate the envelope mass and incorrectly imply an older source based upon sources becoming bluer and brighter as the envelope disperses. The second paper of the series details the evolutionary scenario and presents SEDs and images of each stage as the low mass protostars evolve (Whitney *et al.*, 2003a). Here the envelopes and discs disperse overtime and outflow cavities increase in opening angle as material is thought to be blown away. A key result is that the SEDs and colour-colour plots show considerable overlap between different evolutionary stages depending on the source inclination. In their last instalment Whitney *et al.* (2004) explore the effects of stellar temperature and for the first time apply their model environment to more massive stars. One result is that although the thermal SEDs from all sources are very similar in shape, the hotter, more massive sources have more thermal emission overall and less contribution from the direct and scattered emission. Colour-magnitude diagrams clearly separate the different temperature sources and indicate a trend of sources becoming bluer as they evolve, something which can be used as a proxy for age in observations of MYSOs.

An application of 2D RT models to observations of an MYSO was undertaken by de Wit *et al.* (2010). They modelled the mid-IR visibilities probing scales of ~ 100 au as well as near-infrared images of the W33A using the above Whitney prescription applied to an O type star. With multiple interferometric baselines at different position angles the 2D models can be used to find deviations away
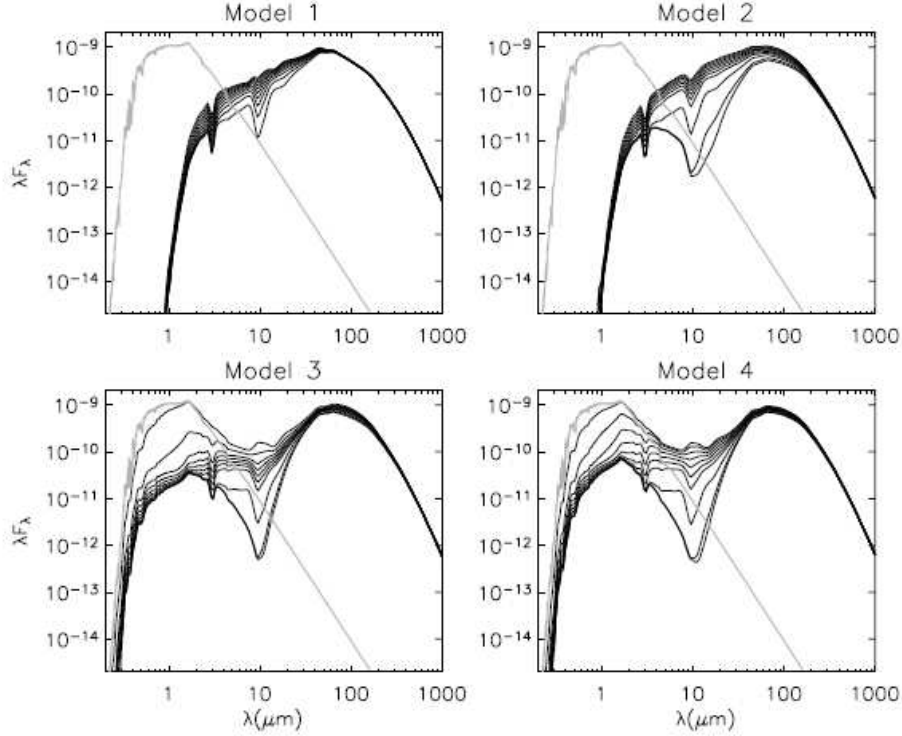
Figure 3.2: The SEDs for 4 geometries, 1) Flattened envelope, 2) as 1 with a disc, 3) as 2 with conical cavity, and 4) as 3 with polynomial shaped cavity. The various grey shade line show the SED at 10 different inclination angles. Both models without cavities have a distinct lack of optical/IR flux in comparison to the models with cavities. Note the more noticeable variation in the SEDs with inclination for models with cavities where the optical depth significantly changes when viewing pole on down a cavity or edge on through a disc. Taken from Whitney *et al.* (2003b).

from a spherical structure. Models with and without discs were compared with the observations, including the SED, the IR interferometric visibilities and a 350 μm image. Due to the many free parameters of the models, observations and literature values are used to constrain initial estimates along with less time intensive scattering models to establish the cavity opening angle. de Wit *et al.* (2010) find a trade off between increased mass infall and inclination angle in replicating the

silicate feature and IR visibilities. The dominant emission regions at the wavelengths sampled by the visibilities are the cavity walls. The cavity is hotter than the surrounding material but of such low density that it does not contribute a significant fraction of the emission. The 2D geometry is required over a simple 1D prescription (de Wit *et al.*, 2007) to correctly match the IR visibilities and the SED simultaneously.

Modelling of MYSOs with 2D geometries for comparison with millimetre interferometric observations have so far not been undertaken, although some progress has been made for closer, low mass sources (e.g. Hughes *et al.*, 2009). This Chapter presents unique work modelling the source S140 IRS1 following in a similar vein to de Wit *et al.* (2010), but for comparison to very high angular resolution observations in the millimetre regime (presented in Chapter 2). First, radiative transfer is discussed briefly and then the specific modelling of S140 IRS1 is detailed.

3.2   Radiative Transfer

The change in the intensity of the radiation from any source of emission as it passes through a medium is described by the radiative transfer (RT) equation:

$$\frac{dI_\nu}{ds} = -\kappa_\nu I_\nu + j_\nu \tag{3.1}$$

where I_ν is the specific intensity of the radiation at the frequency ν, κ_ν is the absorption coefficient and j_ν is the emissivity (emission coefficient). Both the absorption and emission coefficients are functions of distance through the medium, s. Assuming emission through a uniform slab, integrating and substituting $d\tau_\nu = -\kappa_\nu ds$ (where τ_ν is the optical depth, the amount of absorption suffered through

the path length, ds) results in the solution to the RT equation:

$$I_\nu = I_{\nu,0}e^{-\tau_\nu} + \frac{j_\nu}{\kappa_\nu}(1 - e^{-\tau_\nu}) \qquad (3.2)$$

The general solution for radiative transfer in a homogeneous medium presented in Equation 3.2 shows that the intensity of the detected radiation is the sum of that attenuated from the emission source (a star or background emission), $I_{\nu,0}$, and that emitted from the medium that the radiation is propagating through. With increasing optical depth more radiation from the source is attenuated and a larger contribution to the observed radiation is from the surrounding medium. At low optical depths the source radiation is dominant. The absorption and emission coefficients fully describe the properties of the dust grains in the medium as a function of frequency and describe how radiation is absorbed, reprocessed and re-emitted.

3.2.1 Brightness Temperature

In thermodynamic equilibrium the emission and absorption are not independent and are linked by Kirchoff's Law:

$$j_\nu = \kappa_\nu B_\nu(T) \qquad (3.3)$$

where $B_\nu(T)$ is the Planck function. Hence, $j_\nu/\kappa_\nu = B_\nu(T)$ and the medium re-emits as a blackbody governed only by the temperature, T. It is also useful to relate the intensity of a source to the brightness temperature, $T_{b,0}$, which is the temperature a source would have if emitting as a blackbody:

$$I_\nu = B_\nu(T_{b,0}) = \frac{2h\nu^3}{c^2} \frac{1}{e^{h\nu/kT_{b,0}} - 1}$$

$$\approx \frac{2v^2 kT_{b,0}}{c^2}, \text{ where } h\nu/kT_{b,0} \ll 1 \tag{3.4}$$

where h is Planck's constant, k is the Boltzmann constant and c is the speed of light. The Rayleigh Jeans Law $h\nu/kT_{b,0} \ll 1$, is suitable for long wavelength/small frequency emission (millimetre and centimetre regimes). From the above relationships the radiative transfer solution can be represented as:

$$T_b = T_{b,0}e^{-\tau_\nu} + T(1 - e^{-\tau_\nu}) \tag{3.5}$$

where T_b is the brightness temperature measured, $T_{b,0}$ is the source temperature and T is the temperature defining the medium. For the millimetre emission presented in Chapter 2 the case was made that the emission from the region was optically thin based upon the estimated brightness temperatures of the observed emission. This can be understood by using a special case of Equation 3.5. Although the embedded MYSO does not provide emission in millimetre regime the sky itself does due to the cosmic microwave background (CMB) with an effective temperature of ~ 2.73 K. Provided the emitting medium is warmer than this $T_{b,0} \sim 0$. Hence the millimetre emission comes from the surrounding medium, the envelope and disc around the MYSO. There are two cases for $T_b = T(1 - e^{-\tau_\nu})$:

$$T_b = T\tau, \text{ where } \tau \ll 1 \tag{3.6}$$

and

$$T_b = T, \text{ where } \tau \gg 1 \tag{3.7}$$

So for optically thin millimetre emission, as assumed in Chapter 2, the estimated brightness temperature would be low as τ is the only variable given the temperature of the medium is known. Conversely, the uncorrected CARMA A data is becoming optically thick as the temperature is approaching values found for discs around other MYSOs (Galván-Madrid *et al.*, 2010).

3.2.2 Basics of the Radiative Transfer Code

This subsection provides a brief description on radiative transfer code by Whitney *et al.* (2003a,b, 2004) that is used here to model the environment of the massive young stellar object, S140 IRS1.

Radiative transfer is solved in three dimensions, although the actual structure of the environment around protostars is modelled in a two dimensional axisymmetric sense. The density of the environment is described by the rotationally flattened infalling solution prescribed by Ulrich (1976) and Terebey *et al.* (1984) and parabolic cavities and a dusty disc are included (see Whitney *et al.* (2003b)). The density distribution is gridded on a spherical grid that has variable spacings. The radial spacing is logarithmically for the disc, to resolve the smaller inner regions and then follows a power law spacing for the envelope. The density within each grid element is constant. The parameters for the dust throughout the model are known and are tabulated. These dust parameters are the albedo, the ratio of scattered to extincted (scattered and absorbed) flux and the dust opacities, both as a function of frequency (note the polarisation can also be modelled but is not the

subject of the study of S140 IRS1). Simplistically, the code uses a Monte Carlo technique of propagating photons from the luminous central source based upon sampling of a probability functions for position, propagation direction and τ. The photons paths are followed and parameters of flux, wavelength and temperature of the environment are calculated along the way, hence building up information for the SED, images and temperature structure.

A photon is output from the central region with a value of τ (describing how far it can travel), sampled from an $e^{-\tau}$ probability distribution, and a direction of propagation (Whitney, 2011). Each grid cell corresponds to an optical depth at the photon frequency. The photon and grid cell optical depths are compared to see whether the photon propagates into the next cell or interacts in the current one. This process is ongoing until the specified number of initial photons are followed and leave the defined environment. Upon interaction the albedo function is sampled to define a scattering or absorption event. If scattered, the optical depth and direction functions are re-sampled and the photon continues with the new values but at the same frequency. Absorbed photons are more complex to calculate parameters for as they generate new photons based upon thermal emission.

The frequency of the photon emitted is different to that absorbed based upon the dust temperature of the region. At the start of the modelling process the temperature is unknown and is initially set at a low value (~ 3 K). The re-emitted photons are assigned a new frequency when they are emitted according to the temperature of the environment and the opacity function. However, due to the erroneous start temperature the environment is not in equilibrium as more energy is absorbed than re-emitted. The temperature of the cell is therefore increased and when the next photon interacts the input and output energies are re-checked.

This continues as many photons interact and the temperature converges as the heating (absorption) and cooling (re-emission) become balanced. In the Whitney code, the radiative equilibrium method of Bjorkman & Wood (2001) is modified to establish the temperatures (see Whitney *et al.*, 2003b, for details).

The user of the code specifies the number of starting photons to run. The more photons followed the less noisy the output but the longer computational time. Photons are not lost or destroyed anywhere and they are traced until they leave the environment. The Whitney code produces SEDs at ten different inclination angles as well as allowing the option to peel off photons at a particular angle and produce a unique SED and images covering the IR bands at this inclination for a more specific comparison. The more details known about the source to be modelled, then the more constraints that can be employed. The following sections describe the modelling processes, followed by the output results and the conclusions after modelling S140 IRS1 using the Whitney prescription.

3.3   Modelling S140 IRS1

In this section the modelling procedure for the dust continuum emission from the source S140 IRS1 (hereafter IRS1) is described. The modelling process follows the approach undertaken by de Wit *et al.* (2010). Scattering models are used initially followed by a comprehensive analysis using the thermal RT code by Whitney *et al.* (2003b). The scattering only model (Whitney & Hartmann, 1992, 1993) is used to establish the cavity shape, inclination and opening angles by matching near-IR observations. The much more computationally intensive full thermal radiative transfer code is then utilised to constrain the remaining parameters, i.e. the in-

fall rate, envelope size and disc parameters, for example. The scattering model is specifically used to reduce computation time and find a baseline set of geometric parameters rather than running an intensive grid of all possible scenarios with the thermal code. In the final steps the code outputs are processed and model images are produced at millimetre wavelengths along with simulated visibilities for direct comparison with the observations presented in Chapter 2. The aim, however, is not to produce an exhaustive list of models that match observations, but rather to use data presented here (from literature) and in Chapter 2 to constrain as many variables as possible. The modelling work undertaken will be presented in a chronological fashion as the most intensive modelling was done prior to obtaining the highest resolution interferometric data. The initial comparisons between thermal code models and observations will detail the CARMA B data. A separate section will then specifically detail modelling with reference to the more recent, highest resolution CARMA A observations.

3.3.1   Central Source Parameters

The luminosity estimates of IRS1 range from $\sim 4.2 \times 10^3$ L$_\odot$ at 25 μm (Beichman *et al.*, 1979) up to an IRAS luminosity of $\sim 2.4 \times 10^4$ L$_\odot$ (Mozurkewich *et al.*, 1986). Here the multi-wavelength SED fitting approach following Mottram *et al.* (2011b) is adopted. The Robitaille *et al.* (2007) SED fitter is used with fluxes from the literature (listed in table 3.1), while fixing the distance to IRS1 as 764 pc. From the top ten models for IRS1 the mean bolometric luminosity of $\sim (8.5 \pm 2.7) \times 10^3$ L$_\odot$ is calculated. The estimate is reasonable considering it is lower than the earlier IRAS luminosity that includes both IRS2 and IRS3 in the beam and is larger than the 25 μm only estimate which is not where the SED peaks.

There are no un-saturated Spitzer data available for IRS1 or the S140 region. The effective temperature of ~ 25000 K is adopted for IRS1 given the luminosity, using the main sequence properties for massive stars in Mottram *et al.* (2011a). Hence the model assumes IRS1 is a zero age main sequence (ZAMS) B1 type star. The self-consistent estimates of radius and mass then follow as 4.92 $R_\odot$ and 11.1 $M_\odot$. The mass, temperature and radius are properties of the central source and remain fixed. They have little effect on the emergent SED (see 3.3.4).

3.3.2   Initial Environment Parameters

The three main elements contributing to the environment are the protostellar envelope, the evacuated bipolar cavities and an optional dusty disc. The envelope density follows the Terebey, Shu and Cassen solution of a slowly rotating collapsing structure, the 'empty' cavities can either be described by a parabolic 'U shaped' or streamline 'V-shaped' geometry and the optional dusty disc follows a standard flared accretion disc density distribution where the scale height increases with increasing radius according to a power law. The accretion energy can also be included as an additional source of radiation, although it has minimal effects (Whitney *et al.*, 2004). MYSOs that generate wide-angle winds produce 'U' shaped cavities and can be easily represented by a polynomial (Parkin *et al.*, 2009). As noted by Whitney *et al.* (2003b), the parabolic, curved shape produced the most realistic IR images of cavities when compared with recent observations. This cavity shape is adopted throughout the modelling process for IRS1. The cavity material consisting of dust and gas has a number density typical of MYSO outflows between $\sim 5 \times 10^3$ and a few times 10^4 cm^{-3} (Beuther *et al.*, 2002c) and is fixed.

The envelope approaches an n $\propto$ r$^{-1.5}$ radial density power law for pure infall

Table 3.1: Photometric fluxes for IRS1 taken from literature.

Wavelength (μm)	Flux (Jy)	Reference
1.255	0.06	a
1.65	0.45	a
2.10	1.74	a
2.86	5.88	a
3.39	11.4	a
4.07	33.0	a
7.07	136.5	a
8.19	143.5	a
8.99	67.5	a
9.44	54.4	a
10.97	134.4	a
12.69	377.4	a
24.5	1170	b
31	1585	c
37	2624	c
50.0	3840	d
100.0	3320	d
450.0	< 20.0	e
800.0	< 5.50	e
1300.0	< 1.34	f

(a) Representative sample taken from the spectra of Willner *et al.* (1982), (b) de Wit *et al.* (2009), (c) Harvey *et al.* (2012), (d) Lester *et al.* (1986), (e) Upper limits from Minchin *et al.* (1995a), (f) Upper limit from Guertler *et al.* (1991). Flux uncertainties are 30, 10, 20 and 50 percent for each of the references (a), (b), (c) and (d) respectively.

outside the centrifugal radius, R_c. A transition occurs below this radius where the envelope follows a flatter n $\propto$ r$^{-0.5}$ radial density power law. For consistency with previous works the centrifugal radius is initially set at $R_c = 50$ au (Alvarez *et al.*, 2004b). The infall rate parametrises the density of the envelope, which is also related to the central source mass. It should be noted that it is simply a parameter of the density distribution and not a true measure of the infall rate as no measurements of velocity have been made. The outer radii of the envelope is initially estimated to be at a radial distance of ~ 30" based upon the extent of the bipolar molecular outflow as observed in single dish observations (Minchin *et al.*, 1995a). The interferometric outflow data presented in Chapter 2 are not used as these are insensitive to the large scale diffuse emission. The angular size corresponds to ~ 23000 au (0.11 pc) at the distance of IRS1. The ambient number density is set to a typical value of molecular clouds $\sim 10^4$ cm^{-3} as used in previous modelling (Whitney *et al.*, 2003a). Only where the envelope density as described by the radial power laws drops below the specified ambient density is it set to that value, i.e. where the density distribution no longer follows that prescribed by the infall rate. These initial parameter estimates are fixed throughout the scattering model (except for the infall rate) but are varied in the thermal modelling detailed in section 3.3.4.

3.3.3 Scattering Modelling

The near-IR nebula around IRS1 is modelled with the less computationally intensive scattering model of Whitney & Hartmann (1992, 1993). The scattering of a single frequency of photons is considered only, no temperature structure or thermal reprocessing of photons is undertaken. When comparing model images with

the observed IR image (Weigelt *et al.*, 2002) it is assumed to be free of significant thermal emission. The goal of this modelling step is to establish a suitable cavity opening angle, shape and range of inclination angles only. A disc is not included in these models. Although the details of the dust type are not important for this modelling process it is noted that the dust has a coating of water ice. Comparisons of dust types are detailed in Section 3.3.4 during the thermal modelling. Below, checks are undertaken to ensure that for this dust type the infall rate, and hence optical depth are consistent with observations.

The polynomial shape of the cavity is described by:

$$Z = Z_{max} \left(\frac{R}{R_{max}} \right)^{\gamma} \tag{3.8}$$

where γ is the cavity shape exponent, Z is the height of the cavity at a cavity radius R measured from the polar axis (cylindrical radius), Z_{max} is the point where the cavity intersects the spherical outer boundary of the envelope (i.e. $= R_{outer}$) and R_{max} is the radius of the cavity at that intersection. In cylindrical coordinates (R,ω,Z) the cavity is azimuthally symmetric. R_{max} is defined by the model inputs, Z_{max} and the specified cavity angle θ (which is the half cavity opening angle):

$$R_{max} = Z_{max} tan\theta \tag{3.9}$$

Note, where the outer envelope radius is varied (i.e. Z_{max}) for a given cavity angle, the physical shape of the cavity will differ due to the polynomial nature. For the same opening angle but with a variable outer radii, the measured opening angle will be the same (as specified) when measured from the outer radius to the central source but the polynomial shape will be different between two models. In order to

ensure the cavity shape Z/R^γ is constant, $Z_{max}^{1-\gamma}/(tan\theta)^\gamma$ must be fixed. The value $\gamma = 1.5$ is also fixed here as this best replicates the polynomial shape of the cavity. As the cavity shape is described by the cavity angle and outer radius, the outer envelope radius is fixed to ensure that the cavity angle can be parametrised in the scattering models.

Initially the cavity angle and infall rate are set at $10°$ and 7.5×10^{-4} M$_\odot$ yr^{-1} respectively, according to the model for the MYSO, W33A. It was assumed that these starting parameters are closer to those for IRS1 than those for low mass protostars provided with the Whitney code. A range of inclinations are investigated for all cavity angles and infall combinations. The initial infall rate was too large as no or little emission was present at any inclination and a reduction by almost an order of magnitude was required before variations were seen at different inclinations.

The model images indicate that for inclination angles $< 30°$ (where $0°$ is pole on), more envelope density is required (larger infall rate) to reduce the dominance of the central star as the line of sight passes through less envelope material. However, for more edge-on geometries less infall is required compared to low inclinations as this allows more flux from the central region and provides a more suitable match to the observed image. Simple comparisons were made of the flux contour levels to establish whether the central source is too dominant, if the red-shifted lobe is visible in model images, and if the cavity shape is compatible.

The observed IR speckle image used to compare with the models was not received with flux calibrated units. The initial comparisons with model images were done based upon the percentage flux contours referenced to the peak emission of the central source. In order to provide a more accurate comparison between the

models and the observed image attempts were made to match the K-band optical depth (τ_K). IRS1 has $\tau_{Si}(9.7\mu m) = 3.97$ (Willner *et al.*, 1982) and a total visual extinction $A_V \sim 72$ from modelling (Guertler *et al.*, 1991). These are consistent following Draine & Lee (1984). Using the reddening law of Rieke & Lebofsky (1985) a K-band attenuation A_K of ~ 8 mag is calculated. This results in the final K-band optical depth τ_K of ~ 7.4. The infall rate is varied accordingly to attain suitable values of τ_K at each inclination and then the corresponding flux contour levels can be checked. Due to the degenerate nature in fitting three model parameters (cavity angle, inclination and infall rate), mini grids of models were generated at various inclination angles with different infall rates and cavity angles.

At low inclination angles ($\sim 30°$) the contours are generally more circular/ellipsoidal in appearance and are not extended away from the source as is clearly evident in the observations. This sets the rough lower inclination limit. The upper inclination limit is constrained when the reverse lobe becomes significantly extended from the central source at the 0.01 percent level, typically evident at inclinations $> 70°$. The range of inclinations, although not well constrained, are compatible with the CO observations presented in Chapter 2. A value of $45°$ is adopted in subsequent modelling as the intermediate value (note the SED can be used in the subsequent thermal modelling as a consistency check). Both the infall rate and inclination are degenerate in setting the line of sight optical depth. An inclination of $45°$ and an infall rate of $\sim 0.4 \times 10^{-4}$ $M_\odot$ yr^{-1} results in $\tau_K \sim 7.4$.

The cavity shape does not vary for a fixed inclination and variable infall rate, only the contour levels are effected. The cavity shape if best replicated with a cavity angle of $7°$. However, with an infall rate of 0.4×10^{-4} $M_\odot$ yr^{-1} the contour levels are slightly too distant when compared with the observed image. As the

shape of the cavity remains unchanged with infall rate the best fitting scatter model with a 7° cavity angle has an infall rate of 0.3×10^{-4} $M_\odot$ yr^{-1}. Here $\tau_K \sim$ 6, lower than assumed. Alternatively the inclination angle can be slightly increased to provide a better match to τ_K for this infall rate (more edge on). However, the increase changes the contour levels again such that they are no longer an optimal match. The final adopted parameters are an infall rate of 0.3×10^{-4} $M_\odot$ yr^{-1} and cavity and inclination angles of 7° and 45°.

Figure 3.3 compares the K-band image of the S140-IRS1 nebula with the best scattering model run. The model image has been rotated by $\sim 160°$ in the plane of the sky such that the modelled emission aligns with the observation. The raw output image is sampled at three times the resolution of the K-band speckle image while the comparison image (as shown) is convolved with a Gaussian point spread function to achieve the same resolution. The contour levels at the adopted inclination and infall rate are reasonably matched. From a visual inspection of the 8000 au size observed image the cavity half angle appears to be $\sim 20°$ when estimated from the polar axis to a line drawn from the central source to the lowest contour level at the edge of the cavity wall. However, in terms of the cavity geometry adopted, the half angle is only 7° for an outer radius of 23000 au.

3.3.4 Envelope only Thermal Models

Using the constrained cavity geometry from the scattering models the more computationally intensive thermal model is utilised to establish the effects of the remaining parameters and to investigate the presence of a disc. Models without a disc are explored before a disc is included in order to investigate whether a flattened, large scale rotating envelope with 'empty' bipolar cavities can reproduce
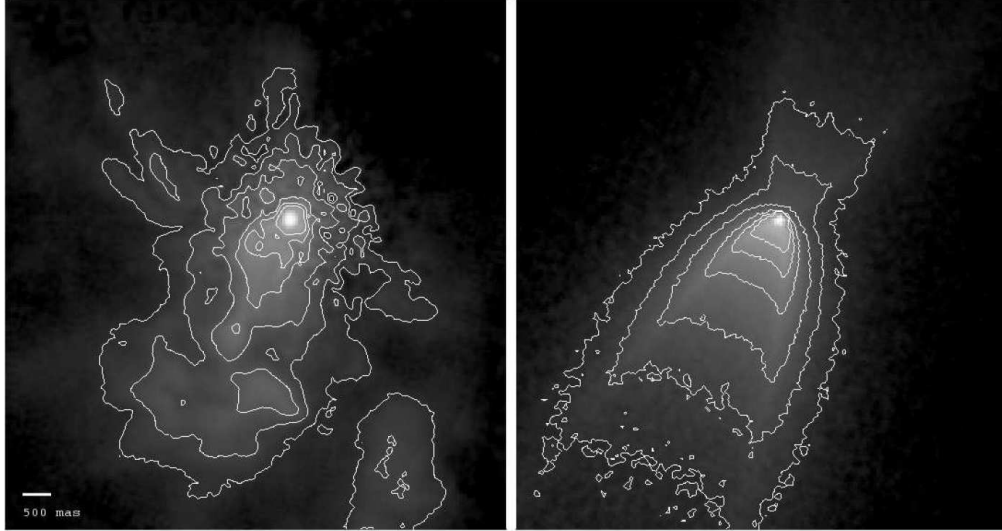
Figure 3.3: Left: K-band speckle image of IRS1 (centred) from (Weigelt *et al.*, 2002), the 500 milli-arcsecond scale is indicated in the lower left corner. Right: Best fitting scatter model image with $\tau_k \sim 6$, a cavity angle of $7°$ and an inclination angle of $45°$. The pixel scale for both images is ~ 27 milli-arcseconds. The contour levels are at percentages levels of the peak at 0.05, 0.1, 0.2, 0.5, 1.0, 2.0. A logarithmic intensity policy is used to highlight the faint emission as all emission above the 5 percent level is centralised on IRS1.

the observables. Although not observed in IRS1, large toroid structures are seen in some hot cores and MYSOs which could be represented by the flattening of the envelope around the source, rather than requiring a separate disc.

The dust type used throughout the envelope and cavities is a mix of interstellar 'warm silicates' and amorphous carbon which provides the best fit to the observable silicate absorption feature (de Wit *et al.*, 2010). A comparison with other dust types are undertaken in the following sections. At this stage only CARMA B array observations were available and the subsequent modelling detailed is with reference to these data only. At this stage the dust disc around IRS1 was not confirmed.

The output model SEDs are compared with the literature values as listed in

Table 3.1. The near and mid-IR fluxes are a representative sample taken from the spectrum of Willner *et al.* (1982) and cover the silicate feature while the 24.5 μm value is from SUBARU observations by de Wit *et al.* (2009) and the SOFIA mid-IR 31 and 37 μm fluxes are the deconvolved values listed by Harvey *et al.* (2012). The far-IR fluxes are taken from the super resolution estimates by Lester *et al.* (1986). The flux ratio between the three far-IR sources, from which the flux values are deduced, appears quite uncertain given the large beam size and small separation of the targets. A generous 50 percent error is included here as not to over weight the fitting to these fluxes. IRS1 is not detected in the sub-mm directly by Minchin *et al.* (1995a). From their Figure 1 the flux measured at the contour corresponding to the location of IRS1 within one beam is used to set an upper limit to the sub-mm flux value. This is a flux within a 9" beam and emission is likely to be more extended than this if it follows a similar structure as indicated by the interferometric data presented in Chapter 2. These values are very uncertain and are regarded as upper limits to account for the inclusion of extended, diffuse emission. The 1300 μm flux from Guertler *et al.* (1991) is also regarded as an upper limit as the 11" beam includes emission from SMM1 and the diffuse emission between SMM1 and IRS1 as seen with the interferometric data.

To determine the goodness of fit the reduced chi-squared value is calculated for each model following van der Tak *et al.* (2000),

$$\chi^2_{SED} = \frac{1}{N} \sum \left(\frac{F_{obs} - F_{mod}}{\sigma} \right)^2 \qquad (3.10)$$

where F_{obs} are the observed fluxes from literature and σ their associated errors, F_{mod} are the fluxes from the model SED and the sum is made over all N flux

values measured. The sub-mm and mm fluxes are not included in the goodness of fit calculation as they are upper limits. The model outputs are checked visually and numerically to ensure a reasonable match to the observations. Due to the importance of checking the sub-mm and mm fluxes, more photons are required in the models initially, such that a larger number are absorbed and re-emitted at these wavelengths. The number of photons required for a suitable SED was found to be $\sim 10^7$. The envelope only models take around 2.5-3.0 hours to run on one ~ 2 GHz processor of a desktop machine.

Fitting the SED is important and suggests that these 2D model environments are suitable for describing MYSOs, as hinted at in Whitney *et al.* (2004). However, the main aim here is to establish whether the interferometric data can be reproduced by such models and what implications that may have on the observations. One limitation of the thermal code is that it cannot trace a sufficient number of photons to produce images in the millimetre regime. Instead the grid of dust density and temperature parameters at each spatial point produced by the thermal code are used as inputs into a radiative transfer ray tracing code. By integrating the fluxes at the same wavelength as the interferometric observations model images of the source environment can be generated. To check consistency between the codes the entire image flux is calculated and compared to the flux in the SED generated from the thermal code. All model images yield the same integrated flux as that indicated in the thermal model SED.

Subsequently, processing the 1300 μm model images using the MIRIAD reduction software results in images and visibilities as would be observed with the CARMA B configuration (note the distinction that the model images are from the ray tracing code and the simulated images are after processing with MIRIAD and

are directly comparable with the observations). The simulated images and visibilities are compared with the free-free corrected observed image and visibilities. For each model, much like the goodness of fits tests for the SEDs a corresponding goodness of fit is undertaken for the visibilities. The visibilities are averaged in time and baseline and the reduced chi-squared (χ^2_{vis}) is calculated between each model and the observations following equation 3.10. Although not strictly correct, a simple one-dimensional analysis in the Fourier plane is sufficient at this stage, i.e. azimuthally averaged in u, v space. IRS1 is not sufficiently elongated in the CARMA B array data to warrant a two-dimensional analysis.

As the visibility amplitudes are, by definition, positive values the noise will be non-Gaussian for low signal to noise data. A Rice distribution (see Thompson *et al.*, 2001) should be used to calculate the most probable location of a model given the spread of data when the signal to noise ratio (SNR) < 1, as the reduced chi-squared is only valid when the noise is Gaussian. In such cases a fitted model will lie below the mean amplitude value of the data as the noise, according to the Rice distribution follows a Rayleigh distribution (e.g. Lay *et al.*, 1994). Where the SNR > 2 the noise distribution becomes Gaussian and a reduced chi-squared test is sufficient to establish the most probable model given the data (see Figure 6.8 Thompson *et al.*, 2001). The SNR is > 2 for all CARMA B visibilities and thus χ^2_{vis} is a reasonable estimator of good fitting models.

The first thermal model (baseline model) was run with the parameters copied directly from the scattering model to ensure the cavity geometry was correctly represented and to investigate whether the previous scattering only hypothesis for the near IR emission was correct. The SED (Figure 3.4) at the chosen inclination angle clearly overestimates the near and mid IR fluxes while underestimating the
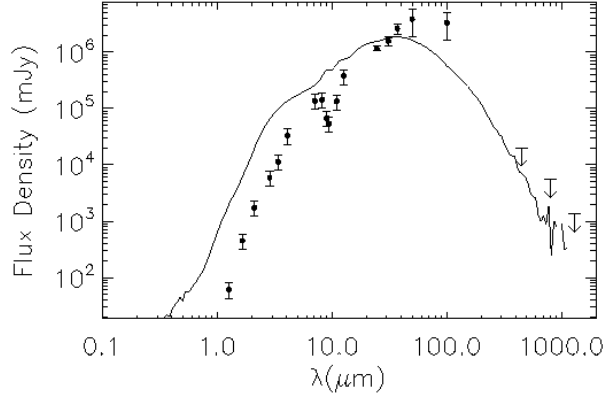
Figure 3.4: SED for first thermal model run with parameters copied directly from those found during scattering modelling as described in the text. The model (solid line) overestimates the observed (solid circles) near/mid IR fluxes and underestimates the sub-mm/mm fluxes (upper limit arrows). The envelope is not dense enough to absorb the required amount of IR photons and re-emit them at sub-mm/mm wavelengths to match the observations.

sub-mm and mm fluxes. χ^2_{SED} is ~ 11 when using the scattering model parameters. The thermal model K-band images showed that the flux is more centrally dominated and increased by a factor of ~ 2 in relationship to the faint emission. The cavity shape, as expected is unchanged. The increased emission is due to the addition of thermal emission from hot dust close to the star. Clearly a larger infall rate is required to attenuate the central source more. For IRS1 it does not appear that the entire K-band flux can be assumed to be due to scattered light only. Each subsequent model run builds from the base model starting from the scattering parameters. The infall rate, outer radius, centrifugal radius and the cavity and ambient dust densities are varied and are the only free parameters in the envelope only models.

Prior to the variation of the above parameters, the source temperature and radius were adjusted with a fixed luminosity to ensure the SEDs are insensitive

to these. The extremities tested were a source temperature of 30000 K with a corresponding radius of 3.4 $R_\odot$ and a lower source temperature of 15000 K with a radius of 13.7 $R_\odot$. The reported output luminosities are the same within 1 percent and the SED variation is negligible. The luminosity is the driving parameter and the final emission (SED) is the result of re-processed light from the envelope, which remains unchanged. The central mass of the source was not varied. The mass is only used to parametrise the envelope density distribution and any variation can be counteracted by a suitable adjustment of the infall rate.

Effect of Infall Rate

The shape of the SED and silicate feature are primarily determined by the infall rate. A range of infall rates increased over that of the baseline model were run. Too little infall produces a lower density, less opaque envelope which produces an excess of short wavelength infrared photons. A larger infall rate, results in a higher density, more opaque envelope which excessively attenuates the shorter wavelength photons and subsequently re-processes them to produce more flux at longer sub-mm and mm wavelengths. Having such a major effect on the shape of the SED and because the inclination and cavity angle are fixed a minimal χ^2_{SED} ($\sim$ 2.3) was achieved quickly. Variation of the infall by more than $\pm\ 0.3 \times 10^{-4}$ $M_\odot$ yr^{-1} from the optimal value of 1.2×10^{-4} $M_\odot$ yr^{-1} increases χ^2_{SED} significantly and a clear deviation in the quality of the SED fit is observed. The fluxes in the millimetre regime are consistent with the upper limit of Guertler *et al.* (1991).

Investigation of the SEDs for the same model runs but at a different inclination (as these are produced anyway) indicates that other inclinations fit the observed SED reasonably well with different infall rates. Essentially provided the line of

sight optical depths are similar the output fluxes will also be similar. Conceptually, as the mid plane is slightly denser due to the flattened structure, a view in this edge-on direction requires less infall than one that is more pole on direction (but not directly down the cavity). Although such variations are already well documented (e.g. Whitney *et al.*, 2003a) it is important to reiterate that without having a prior estimate of the inclination angle from near IR images a range of infall rates and inclination angles would suitably fit the observed SED of IRS1. Even though edge on and pole on SEDs can be made to fit the observed SED with variations of the infall rate the K-band image is no longer matched.

Interestingly, after varying only the infall rate it is surprising that the model SED fits so well after establishing the other parameters based solely on a near IR image and sensible estimates of the environment from millimetre outflow observations. On the one hand it appears that these models with sensible estimates describe the environment of MYSOs reasonably well. This would be a sensible argument assuming MYSOs form in a similar up-scaled environment as lower mass protostars which the models are based upon. However, it may be coincidental that the SED is such a good fit for IRS1. Clearly other sources need to be modelled in a similar fashion where as many parameters are sensibly constrained from observables rather than allowing 'free reign'. In cases using entirely free parameters SED fits will be possible but the environment parameters will likely be unrealistic and unconstrained.

When comparing the simulated 1300 μm images and visibilities with the interferometric observations it is quickly evident that the flux on the small scales probed by the CARMA B observations are totally underestimated. For the model with an infall rate of 1.2×10^{-4} M$_\odot$ yr^{-1} and $\chi^2_{SED} \sim 2.3$ the corresponding goodness
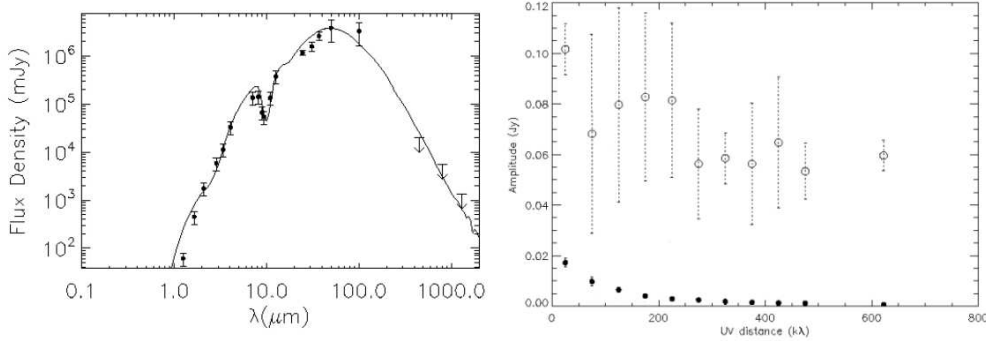
Figure 3.5: Left: SED for the envelope only model (solid line) with all parameters fixed as described in the text but with an infall rate of 1.2×10^{-4} M$_\odot$ yr^{-1}. The model well represents the observed fluxes indicated by the black circles and upper limit arrows. Right: Comparison of the free-free subtracted CARMA B visibilities and the envelope only model that produces the SED in the left image. The open circles indicate the observed data and have associated dashed error bars from baseline and time averaging. The observed data are of a much higher amplitude than the model visibilities shown in solid circles. This envelope only model cannot match the interferometric fluxes at small spatial scales.

of fit to the visibilities is $\chi^2_{vis} \sim 23.3$ and the image flux is only 8.7 mJy. This is a factor of ~ 8 less than observed. To match the visibilities and images much more flux is required in the millimetre regime. At this stage with only the infall rate as a variable parameter an increase of an order of magnitude was made in attempt to reproduce the fluxes in the millimetre regime. The left hand side of Figure 3.6 shows the SEDs of the model where the infall is increased to 1.2×10^{-3} M$_\odot$ yr^{-1}. As previously noted, the larger infall attenuates the short wavelength flux and increases the fluxes at longer mm wavelengths. The SED with an increased infall is a very bad fit to the literature values and $\chi^2_{SED} \sim 10^7$. The increased infall rate did have the positive effect of increasing the millimetre fluxes such that the simulated visibilities are a better match to the CARMA B data. Although, χ^2_{vis} is ~ 15.3 and only the flux on the largest scales probed by the interferometer
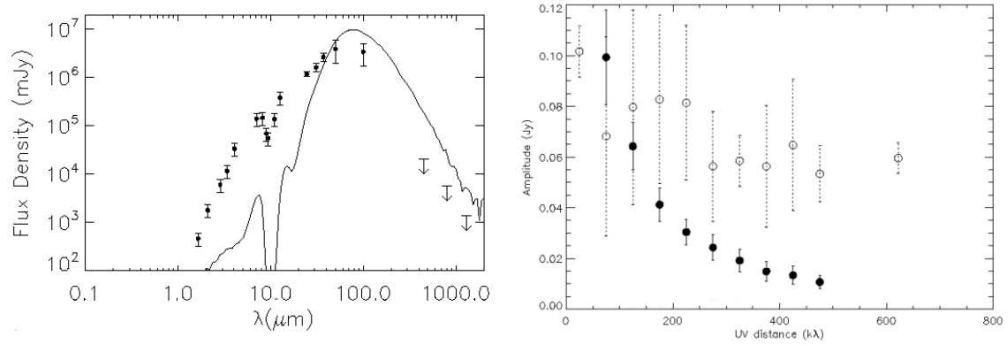
Figure 3.6: Left: SED for the envelope only model (solid line) with all parameters fixed as described in the text but with an infall rate of 1.2×10^{-3} M$_\odot$ yr^{-1}. An order of magnitude larger than the previous optimal model. The model does not represents the observed fluxes indicated by the black circles and upper limit arrows. Right: Comparison of the free-free subtracted CARMA B visibilities and the envelope only model that produces the SED in the left image. The open circles indicate the observed data and have associated dashed error bars from baseline and time averaging. The model visibilities match the observations on the largest spatial scales probed by the interferometer but do not replicate the very smallest spatial scales. The visibilities and SED are not simultaneously fitted.

are matched and there is still a considerable deficit of flux on the smallest scales probed. The right hand side of Figure 3.6 shows how the visibilities cannot be matched with large infall envelope only models.

Confirming the Dust Type

The dust type Whitney *et al.* (2003a) uses for class I and II low mass sources includes a coating of ice in the envelope. This dust has slightly different opacities and albedos which will cause finite changes to the fluxes at given wavelengths as the dust will scatter, absorb and re-emit radiation slightly differently. Figure 3.7 shows the opacities and albedos for the ice coated dust and the mix of warm silicates and amorphous carbon previously used. The ice coated dust type is tested to investigate the whether the emission from the region changes significantly.
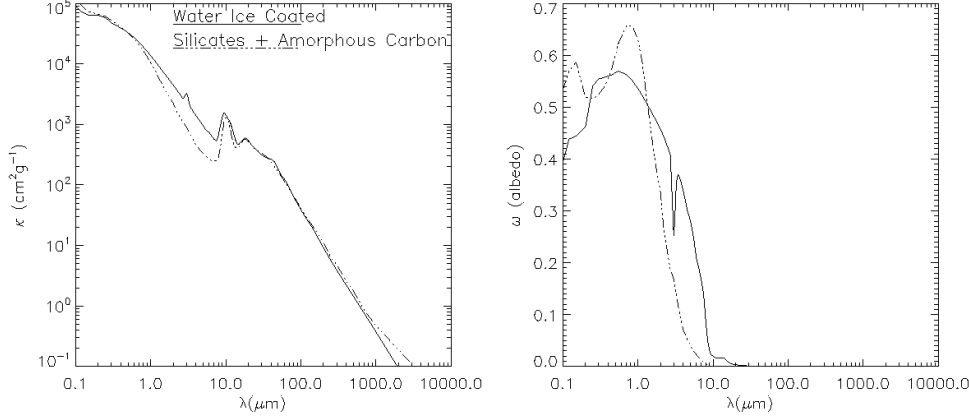
Figure 3.7: Dust opacities (Left) and albedos (Right) of ice covered grains as Whitney *et al.* (2003a), and the mix of warm silicates and amorphous carbon as used here and in de Wit *et al.* (2010). The dust type key is shown in the top right of the opacity plot. The opacities at 1 mm, $\kappa_{1000\mu m}$ are ~ 1.0 cm^2 g^{-1} and are consistent with the values used for mass estimates in Chapter 2. The clear difference in opacity and albedo of the dust in the near/mid IR regime lead to the changes seen in the SEDs at these wavelengths as the dust thermally absorbs/re-emits and scatters light differently.

The χ^2_{SED} for IRS1 is ~ 17 using the optimal infall rate and the ice coated dust. Figure 3.8 shows that the sub-mm/mm fluxes are consistent with observations but the fluxes at wavelengths < 50 μm are underestimated. Note the very jagged shape of the silicate feature at ~ 10 μm which is not evident in the observations (Willner *et al.*, 1982). However, the ice coated dust does replicate the spectral feature at $\sim$ 3 μm usually attributed to water ice particles (Willner *et al.*, 1982). Less infall is required with this dust as it does not scatter as much at shorter wavelengths and is slightly more opaque than the mix of interstellar warm silicates and amorphous carbon dust previously used. The new dust is actually more similar to that used in the scattering models and if the infall rate is lowered towards that originally found in the scattering models a much more agreeable SED fit is attained. $\chi^2_{SED} \sim 4$

for an infall rate of 0.8×10^{-4} $M_\odot$ yr^{-1} (Figure 3.8). The infall rate is still larger than that found from the scatting models alone and confirms that the observed K-band flux is comprised of both scattered and thermal light. Furthermore, the sub-mm/mm flux is beginning to decline and is visually a worse fit than with higher infall rates or when using the warm silicates and amorphous carbon dust type. The dust opacity index β for the ice coated dust is ~ 2 in the sub-mm/mm regime. For the warm silicates and amorphous carbon dust β is ~ 2 between 200 and 900 μm but then becomes shallower ($\beta \sim 1.3$) at longer wavelengths. The decline if flux at longer wavelengths for the ice coated dust is consistent with the lower infall used in order to fit the IR emission and the steeper dust opacity index in the sub-mm/mm regime. Note, the emission after ~ 20 μm is purely thermal for both dust types as the albedo tends to zero. With the ice coated dust the interferometric model visibilities remain similar to the previous models and still do not match the observations.

Altering the dust type noticeably changes the model SEDs, however these changes are primarily at much shorter wavelengths than the millimetre wavelengths of the interferometric observations. The dust type and infall rate are degenerate parameters when altered together. With all other parameters fixed a suitable infall rate can be found for a chosen dust type. Following the rational of de Wit *et al.* (2010) the mix of silicates and amorphous carbon dust is used in further modelling as this better replicates the smooth silicate dip. It is noted that the dust may not be the most optimal for the very short wavelength portion of the SED as it does not reproduce the ~ 3 μm feature, however, the simultaneous fit to the near/mid IR and sub-mm/mm fluxes is much better than for the ice coated dust type. Regardless of the dust type used, these envelope only models presented
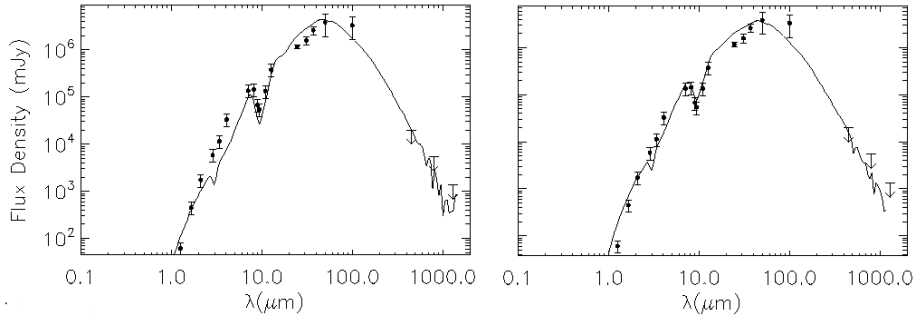
Figure 3.8: Left: SED of IRS1 with the previously found optimal infall rate but a change of envelope dust type from warm silicate and amorphous carbon to dust with a coating of water ice (see Whitney *et al.*, 2003a). The water ice feature at 3.1 μm as observed by Willner *et al.* (1982) is reproduced as is the silicate feature at 9.7 μm. The silicate feature is notably jagged in appearance compared with the previous dust type and SED presented in Figure 3.5. Note how the IR fluxes are a poor match to the observations. Right: SED of IRS1 with the alternative dust type and a modified infall rate. Here the infall rate is 0.8×10^{-4} M$_\odot$ yr^{-1}. This SED is a much better fit than the one where only the dust type was changed.

so far cannot replicate the small scale visibilities at 1.3 mm wavelengths.

Variation of the Envelope Outer Radius

The initial envelope outer radius was established based upon the extent of single dish outflow observations. The outer radius was therefore varied to establish its effect and to investigate whether more small scale millimetre flux could be obtained to provide a better match to the visibilities. A larger outer envelope should provide more colder material which could re-emit photons preferentially at sub-mm and mm wavelengths. However, the emission is likely to be produced on a larger scale and may not provide the added millimetre emission on the smallest scales where it is lacking. An upper limit was placed upon the outer radius of 50000 au corresponding to the edge of the dark cloud IRS1 is embedded within. The distance

is set by the shortest path to the photon-dominated region ~ 70 arcsec to the SE of IRS1. The minimum envelope radius investigated is 8000 au, corresponding to the ~ 11 arcsec beam of the 1300 μm observations by Guertler *et al.* (1991).

While increasing the envelope outer radius an optimum χ^2_{SED} of 2.08 is found using a model with a 45000 au outer radius with the fixed infall rate of 1.2×10^{-4} $M_\odot$ yr^{-1}. The SEDs and visibilities fits however do not differ noticeably from those in previous models while the outer radius is steadily increasing, χ^2_{vis} is still around ~ 23. For smaller radii χ^2_{SED} increases slightly to ~ 3.6. Although the fit does not change significantly the fluxes > 100 μm, which do not contribute to the goodness of fit, are noticeably underestimated. Shorter wavelength emission emitted closer to the source are largely unchanged. The outer radius itself is not a sensitive model parameter given that a factor of 6 change in radius does not significantly alter the SED shortwards of 50 μm. The density distribution is not changed as the outer radius is increased, it is extended. The outer regions are of lower density/opacity and cause little effect of the SED fit and shape (< 50 μm) as most of the photons emitted from the source have already been re-processed and emitted at longer wavelengths which the envelope is less opaque or optically thin to. Although not investigated, it is likely that for a given outer radius, much finer adjustments of the infall rate (the incremental changes were 0.1×10^{-4} $M_\odot$ yr^{-1} when testing the effects of the infall rate) would have the same effect as the large changes in the outer radius. Adjustments of both the infall rate and outer radius alter the density distribution. However, the infall rate is a much more sensitive parameter compared with the outer radius. As noted previously for dust types and infall rates, one parameter must be fixed, or reasonably constrained otherwise the models becomes degenerate between the two free parameters.

Ambient and Cavity Densities

The ambient density essentially parametrises the lower density limit for the envelope structure. It is the infall rate which parametrises the density structure of the envelope according to the TSC (Tereby, Shu, and Cassen) prescription. At a certain radius, if the envelope density based upon the infall rate is less than the ambient density then the ambient density value is used. In order to test the effects of different ambient densities, the best envelope only model was re-run with an increase and decrease of the ambient density by an order of magnitude.

The decreased ambient density had no effect on the results. Because the ambient density is a lower limit, provided the infall rate is large enough for a given envelope outer radius, the infall rate will fully specify the envelope densities out to the outer radius. The ambient density is never considered as the envelope densities never fall to small enough values. On the contrary, an increase in the ambient density does have a significant effect on the SED. Due to the increased ambient density, the envelope density specified by the infall rate, drops below the ambient density value before the outer radius. Here, the turn over occurs at ~ 8000 au and the envelope becomes a constant density after this radius. Consequently χ^2_{SED} is ~ 10 as the density is larger than specified by the infall rate after 8000 au and the envelope absorbs more short wavelength photons and re-emits them at longer wavelengths. The visibilities were not checked here as the SED does not fit well. It is crucial when undertaking such models that the ambient density is set sufficiently low such that the infall rate exclusively parametrises the envelope density as a function of radius, unless a constant density envelope is to be modelled.

The cavity density is not well constrained and is based upon observations and

previous works (Beuther *et al.*, 2002c; Whitney *et al.*, 2003a). Whitney *et al.* (2003a) assume that the cavities become less dense and wider as the central low mass protostars evolve (also see Chapter 1.5.1). Here the cavity densities are increased and decreased by an order of magnitude to investigate the effects for IRS1 and roughly cover the parameter space used by Whitney *et al.* (2003a). The increase of cavity density by a factor of ten to a number density of $\sim 10^5$ cm^{-3} marginally improves χ^2 whereas the decrease provides no change. The visibilities are insignificantly effected. Given the inclination angle of 45° the path of photons being emitted or scattered in the direction of the observer through the cavity will likely be low. Hence the change of density by an order of magnitude is not significant. With a larger cavity density the infrared fluxes change marginally to produce a slightly better fit to the observed SED. As with the other parameters, the same, marginal improvement in the fit could be achieved by finely adjusting the infall rate to change the envelope density distribution. Interestingly, if viewing the SEDs at the smallest angle produced in the thermal code (18°), the change in cavity density by an order of magnitude only has a small effect. There is a marginal flux increase at wavelengths < 5 μm when the cavity density is at a minimum. The small effect is likely due to the same hypothesis as above, the density in the line of sight to the observer through the cavity is small, given that the opening half angle is $< 18°$. If viewing directly pole on down the cavity itself the change in the SED would be significant, although this is not investigated. The cavity density is not a sensitive parameter given the inclination angle of the environment is constrained and well away from pole on orientations.
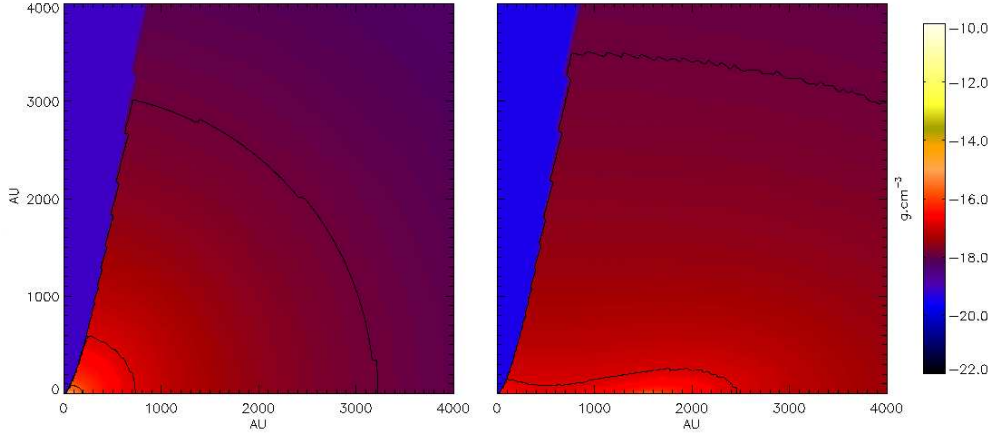
Figure 3.9: Logarithmically scaled slice through the spatial density distribution for the optimal envelope only model with $R_c = 50$ (left) and $R_c = 1500$ (right). The contours levels are at 10^{-16}, 10^{-17} and 10^{-18} g cm^{-3}, although the 10^{-16} is not visible in the $R_c = 1500$ model. Due to the degeneracy between infall rate and R_c, the infall rate was increased to 2.6×10^{-4} M$_\odot$ yr^{-1} in order to obtain a similar or better χ^2_{SED} for the $R_c = 1500$ model. There is a clear flattening of the density distribution away from a more spherical shape displayed by the $R_c = 50$ model. Note, for the $R_c = 1500$ model there is a slight peak of density close to the mid plane of the envelope at a radius of 1500 au, as shown by the lighter colours.

Effect of Centrifugal Radius

The remaining parameter to adjust in an attempt to improve the model visibilities is the centrifugal radius. This value specifies where the density distribution changes from a flatter n $\propto$ r$^{-0.5}$ to n $\propto$ r$^{-1.5}$ distribution. Increasing R_c could mimic a disc-like structure or a rotating toroid as the envelope density distribution is more concentrated to the mid-plane. Figure 3.9 indicates how the density structure of the envelope changes within a 4000 au radius of the source as R_c is increased.

For R_c below ~ 150 au, χ^2_{SED} is relatively unchanged. The effects on the shape of the SED with increasing R_c (> 150 au) while the infall rate remains fixed are as follows: 1) The SED is flatter, i.e. more horizontal, between 2 and 10 μm, 2) The silicate absorption feature becomes shallower and eventually changes into an

emission peak, 3) The mid-IR flux is reduced around 25-35 μm, and 4) The peak of the SED at far-IR wavelengths shifts longwards.

Fitting the near-IR and mid/far-IR fluxes independently indicates that the longer wavelengths are fitted marginally better for larger R_c models than for the $R_c = 50$ au model. However, at near-IR wavelengths the fit is much worse and overall χ^2_{SED} increases. Increasing R_c has a similar effect on the near-IR fluxes and silicate feature as decreasing the infall rate but has minimal effect on the longer wavelength sub-mm and mm tail of the SED. The geometry and density distribution of the hotter inner regions close to the central source are clearly important to the flux distribution at near and mid-IR wavelengths. At larger radii than R_c the cooler more spherical envelope, with an n $\propto$ r$^{-1.5}$ density distribution, produces the longer wavelength emission which is relatively unaffected by the smaller scale changes. There is a noticeable change in flux is observed at infrared wavelengths with increasing R_c and the silicate absorption feature changes to a prominent emission peak when $R_c \sim 1000$ au. The silicate emission feature is due to the exposure of the hot dust emission at certain inclination angles. The amount of cool dust in the envelope decreases in the line of sight at the inclination angle of IRS1 ($\sim$ 45°) when R_c is increased and the infall rate remains fixed. This is a result of the material in the envelope being positioned at larger radii closer to the mid plane (see Figure 3.9).

A set of models were run for each R_c with different infall rates after recognising that an increase in the centrifugal radius has the effect of a decreasing infall rate on the near-IR fluxes. Both the infall and R_c were increased in attempt to produce models with a better visibility fit while still fitting the SED. These models are degenerate and numerous pairings of infall rate and R_c produce good fits with
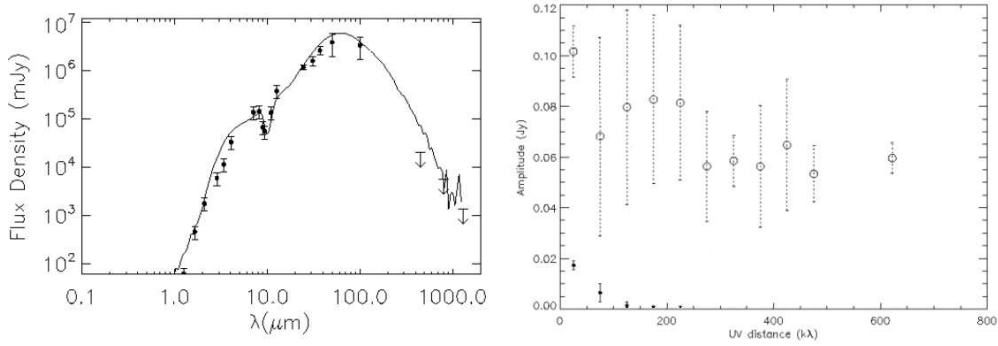
Figure 3.10: As Figure 3.5 except $R_c = 2500$ au and the infall rate $= 3.5 \times 10^{-4}$ $M_\odot$ yr^{-1}. The χ^2_{SED} is 1.57, better than the $R_c = 50$ au model but $\chi^2_{vis} \sim 23.9$ is marginally worse. After a (u, v) distance of ~ 250 kλ, corresponding to ~ 1 arcsecond or ~ 760 au the visibility amplitudes drop to zero. There is no flux on the very smallest scales.

the observed SED. The measured χ^2_{SED} values range from 1.6 to 2.7 before a clear deviation in the SED is seen. Notably, there is no means to independently constrain the centrifugal radius based upon current observations. The visibilities for the best fitting large R_c model according to the SED fit ($R_c = 2500$ au, infall $= 3.5 \times 10^{-4}$ $M_\odot$ yr^{-1}, $\chi^2_{SED} = 1.57$) still do not match those observed and are marginally worse, $\chi^2_{vis} \sim 23.9$, than the low R_c models (Figure 3.10). The increase of the centrifugal radius and correspondingly the infall rate does not produce an increase of the millimetre flux on the smallest scales probed by the interferometer.

Envelope Only Summary

There is a range of envelope-only models that fit the SED equally as well. The majority have the same infall rate but with a range of the other free parameters. The infall rate is the most sensitive parameter. Generally, the variation of the outer envelope and the cavity and ambient densities have little impact upon the SED fits and χ^2_{SED} remains largely unchanged as do the fits to the interferometric

visibilities. Adjusting the centrifugal radius has a noticeable effect on the shape of the SED. Consequently, the infall rate and R_c must be increased together in order to retain a good fit to the observed SED. Increasing these parameters together is degenerate. Provided the free parameters investigated here are reasonably well constrained, and the environment geometry is already known, fine adjustments of the infall rate are all that is required to provide an adequate fit to the observed SED.

It is evident that an envelope only model cannot reproduce the observed SED and interferometric visibilities simultaneously even after variations of free model parameters. Although the millimetre flux summed over the model envelope is consistent with the observed single dish flux upper limits, the emission is more diffuse and not focused to the smaller spatial scales. A compact dusty disc is the natural source of smaller scale millimetre emission.

3.3.5   Including a Dust Disc

A flared accretion disc is included in the best fitting $R_c = 50$ au, envelope only model. All other envelope parameters are unchanged in order to investigate the effect of the disc only. The disc prescription is detailed in Whitney *et al.* (2003b) and follows a standard flared accretion disc density solution. The scale height of the disc increases following a power law function of the radius, $h = h_0 \, r_{disc}(R_*)^\beta$, while the density distribution decreases following a power law as a function of the radius, $n_{disc} \propto r_{disc}^{-\alpha}$. Considering the tentatively resolved CARMA B observations, possibly probing the dust disc, and other literature data available there is no way to constrain either the scale height or density functions. Therefore, $\alpha = 2.25$ and $\beta = 1.25$ while $h_0 = 0.01$ based upon previous observations and models of low mass

protostars (see Whitney *et al.*, 2003a). Note, the power law β here is not to be confused with the dust opacity index and is used only for a consistent reference to the Whitney code. The SEDs and visibilities are compared with the observations as previously undertaken with the envelope only models. Due to the averaging of the visibilities, any model visibilities within the uncertainties (one standard deviation) of the observations are chosen to represent a good fit to the CARMA B observations (i.e. where $\chi^2_{vis} < 1$).

Disc Dust Grains

There are two dust types for the disc. For the denser disc mid plane where $n_{disc,H_2} > 10^8$ cm^{-3} a large dust grain model is used that fits the SED of the HH 30 disc, while the disc surface uses slightly smaller grains that were used to model the HH 30 near-IR scattered light images. The disc surface grains have similar properties to the grains used in the envelope. The mid plane grains have noticeably different opacity coefficients and larger effective grain sizes (see Whitney *et al.*, 2003a). Figure 3.11 shows how the dust opacities are similar at infrared wavelengths but at optical and sub-mm/mm wavelengths the opacities are decreased and increased respectively when changing from envelope to surface disc and mid plane disc dust types. Furthermore, the albedo of the larger mid plane dust grains is increased considerably as scattering efficiency at a given wavelength is related to grain size. The overall consequence is that a given mass of mid plane dust will produce more sub-mm and mm emission compared to the exact same mass of envelope type dust.
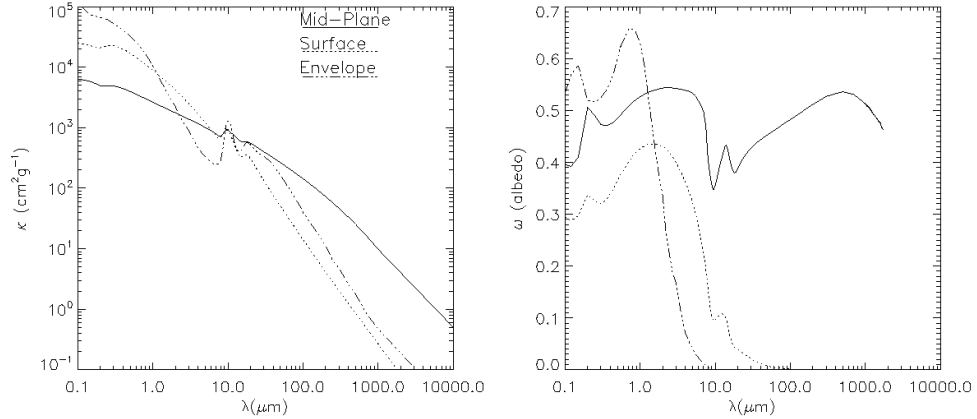
Figure 3.11: Dust opacities (Left) and albedos (Right) of the envelope dust (mix of warm silicates and amorphous carbon), the mid plane and surface disc dust. The dust type key is shown in the top right of the opacity plot. Differences in the opacity and albedo of the dust types are evident over the entire wavelength range. The larger mid plane grains emit and scatter considerably more at longer wavelengths. Note, the albedo after ~ 2 mm for the mid plane dust is constant at the last recorded value, this does not effect the results at 1.3 mm here.

Disc Parameters

The disc mass can be estimated using the free-free corrected CARMA B flux. The mass range calculated uses temperatures from 30 K typical of molecular clouds and cores up to ~ 350 K assuming coupling between dust and gas in disc structures (< 1" from the peak) as found in other MYSOs (Galván-Madrid *et al.*, 2010). Dust opacity coefficients (κ_ν) have values from ~ 0.35 to ~ 7.15 $cm^2 g^{-1}$ at ~ 1.3 mm as taken from the model envelope and disc mid-plane dust types respectively (see Figure 3.11). The resulting disc masses are in the range ~ 0.005 - 1.3 $M_\odot$. The smaller masses are for the highest temperature and using the mid plane dust opacity. This calculation indicates the extent to which the mass can vary when sensible and justified estimates of temperature and dust opacity coefficients are
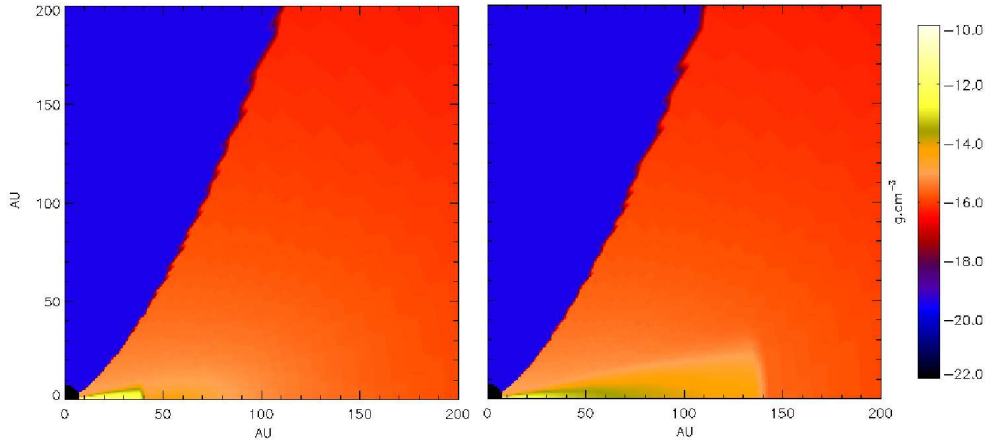
Figure 3.12: Logarithmically scaled slice through the spatial density distribution for two disc models with outer radii of 40 au (Left) and 140 au (Right). Both models have a disc mass of 0.016 $M_\odot$. The colour scale indicates the densities of the regions. The outer disc radii in both models represent a cut off in the extent of the disc as can be seen by the sharp change in density. For the same mass the 140 au disc is noticeably less dense than the 40 au radius disc.

used. Assuming the emission is entirely from a compact disc, there is clearly a variation up to a factor of a hundred when using reasonable input parameters.

The disc radius is not well constrained. A grid of models are therefore run with the disc outer radius ranging from 20 - 500 au for disc masses in the calculated range (0.005 - 1.3 $M_\odot$). The disc inner radius is set at the dust sublimation radius while the upper limit for the outer disc radius is double the resolution of the CARMA B observations. It is not clear whether the disc size estimated in the millimetre regime is the correct input for the models. Figure 3.12 shows the density distribution for two models with dusty discs of mass 0.016 $M_\odot$ and outer radii of 40 and 140 au respectively. It is clear that the disc outer radius is a sharp cut-off to the extent of the disc. The disc radius estimated from the millimetre observations may be effected by the interferometric sensitivities and may not detect the fainter

outer disc.

Variation of Disc Mass and Radius

All model SEDs are relatively unchanged by the inclusion of discs with different masses and radii when compared with envelope-only model SEDs. All χ^2_{SED} values are ~ 2. There is a slight increase of flux at longer wavelengths $> 500~\mu$m. The increase is greater for the large radii, more massive discs. These fluxes are still compatible with the millimetre single dish observations.

A general trend observed is that as the disc mass increases the 1.3 mm flux increases for a given disc radius. However, all discs with an outer radius of 60 au, corresponding to the deconvolved CARMA B disc size of ~ 120 au, and masses $> 0.2~M_\odot$ have similar fluxes. For this radius the discs become optically thick (at millimetre wavelengths) with increasing mass and the emitted flux is seen to decrease slightly and then plateau. Interestingly, at the $0.2~M_\odot$ mass limit the fluxes of these models already surpass that of the observations by a factor of ~ 2. The trend of increasing flux with radius is not found in discs at the lower radius limit, with an outer radii of 20 au. These small discs are already at the optically thick limit with masses as low as $0.008~M_\odot$ and the flux stays constant thereafter. These fluxes are less than required to match the CARMA B visibilities.

For discs well within the optically thick regime, with a mass of $0.5~M_\odot$ for example, an increase in disc radius from 40 au up to 300 au provides an increase in disc flux. This is as expected as the disc is still in the optically thick regime and the larger disc area provides a larger $\tau = 1$ emitting surface. Above this radius upto the maximum radius of 500 au the disc flux decreases. It would appear that the disc starts to become optically thin, and due to a decreased density the flux in

the millimetre regime is decrease. As discussed in Chapter 2, the compact emission is still in the optically thin regime as indicated by the low T_{mb} of the CARMA B observations. A much less massive disc is required to match the observed flux and visibilities while in the optically thin regime. Typically in all disc models the dust temperature is > 300 K at radii of ~ 100 au consistent with the models of W33A by de Wit *et al.* (2010).

There are a range of masses and radii that fit the visibility data equally well and are in the optically thin regime (where increasing mass still provides an increased flux). It appears that a roughly constant density distribution is achieved when both the disc mass and radius are increased in a steady fashion. To fit the observations a minimum disc radius of ~ 40 au is required. A 40 au radius disc with mass of ~ 0.013 M$_\odot$ has a minimum χ^2_{vis} which is < 1. At the upper mass limit of 1.3 M$_\odot$, a disc at the upper 500 au outer radius limit does not provide a good match to the observations, as it is optically thick and has an excess flux. A radius of at least 4600 au is actually required before $\chi^2_{VIS} < 1$. Figure 3.13 shows both the 40 au radius low mass disc and a 4600 au radius high mass disc model images before converting to the simulated observation images. In the top figures with a linear scale both images are very similar. In the bottom figures the logarithmic scaling highlights fainter features. Here a halo of emission can be seen away from the bright central disc region in the bottom right image for the 4600 au radius disc. The halo is absent for the 40 au radius disc. This extended faint disc emission is not detected by the interferometer and subsequently the synthesised images are very similar and hence the output fluxes are coincident.

The mass and radius parameters are degenerate (given the fixed dust type) as both the 40 au, 0.013 M$_\odot$ and the 4600 au, 1.3 M$_\odot$ discs provide equally good fits,

40 au / 0.0013 Mo

4600 au / 1.3 Mo

100 au
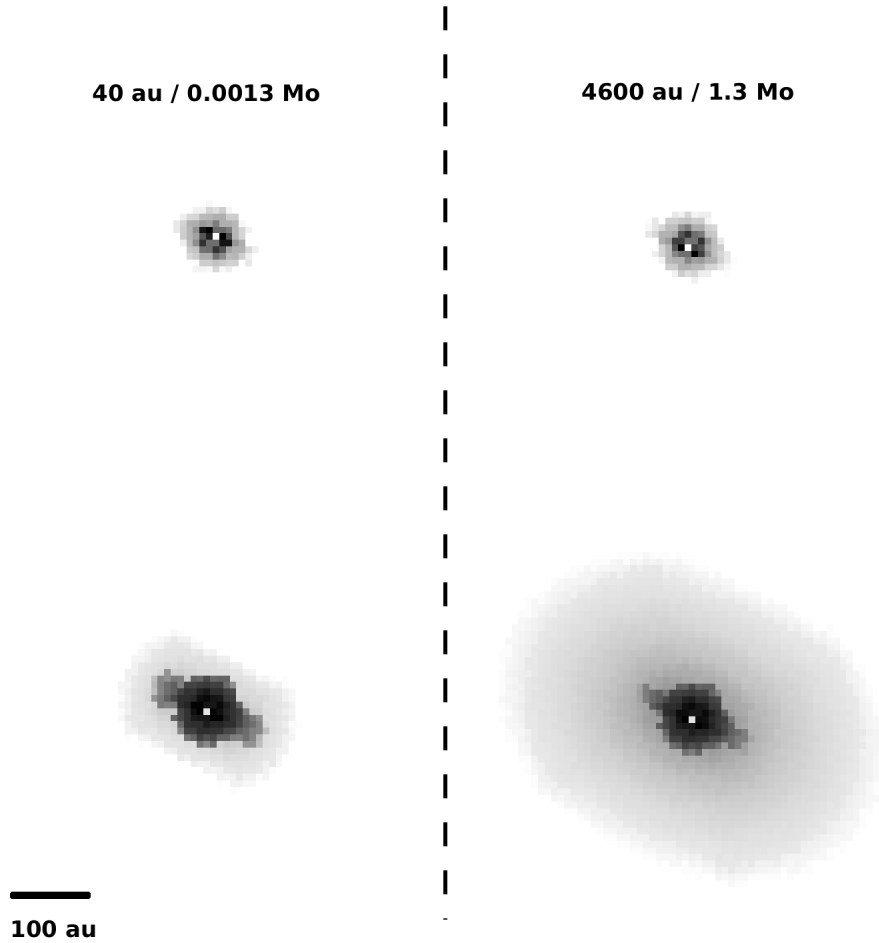
Figure 3.13: Model images of a low mass (0.013 M$_\odot$) 40 au radius disc (Left) and a high mass (1.3 M$_\odot$) 4600 au radius disc (Right) within the best fitting model envelope. The discs are viewed at a 45° inclination angle and have been rotated to a position angle of 45°. The linear scale of the top images ranges from 0.0 to 2.0 mJy/pixel for both disc models. Clearly on linear scales it is hard to differentiate between the models. The logarithmic scale of the bottom images highlights the faint emission from the much larger more massive disc model which is absent in the small disc model. After processing the images with the interferometric coverage the synthesised images behave like the linearly scaled images and the faint extended emission of the larger disc model is not detected. The pixel size is 10 au and a 100 au bar is indicated in the bottom left.

Table 3.2: Summary of envelope-only and disc-envelope models.

Model Description	Infall rate $(M_\odot\ yr^{-1})$	R_c (au)	Disc Mass $(M_\odot)$	Disc Rad. (au)	χ^2_{SED}	Best χ^2_{vis}
Envelope-only:						
$R_c = 50$	1.2×10^{-4}	50	0	0	2.08	23.3
Large R_c	3.4×10^{-4}	2500	0	0	1.57	23.9
Large infall	1.2×10^{-3}	50	0	0	$> 10^7$	15.3
Disc-envelope:						
Disc Radius = 60 au	1.2×10^{-4}	50	0.016	60	2.04	0.43
Minimum mass disc	1.2×10^{-4}	50	0.013	40	2.05	0.67
Most massive disc	1.2×10^{-4}	50	1.3	4600	2.45	0.98

as do discs with mass and radius parameters between these two extremes. Table 3.2 list the parameters for various best fitting envelope only and envelope and disc models discussed. With the CARMA B observations there is currently no way to distinguish which disc mass and radius combination is preferential. Furthermore, these masses are related only to the current dust types used for the disc. If less opaque dust types are used, such as those used for the envelope, then more mass is required for a given radius to provide the same visibilities and fluxes. Essentially, there are three unknown parameters, dust type, mass and radius which can all be varied to suitably fit the observables.

Fixing the Outer Radius

As the disc mass and radius are responsible for setting the density distribution, a model with a disc radius of 60 au, as given by half the deconvolved source size from the CARMA B observations, is adopted. As discussed previously it is not necessarily the correct radius to use, however the aim here is to investigate how
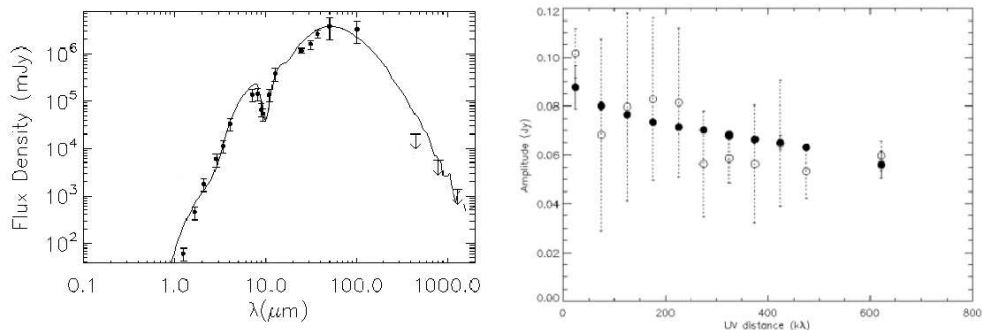
Figure 3.14: Left: SED for the fixed 60 au radius best disc model (solid line). The dots and error bars indicate the observed fluxes. The SED is relatively unchanged from the envelope only model in Figure 3.5. Right: Comparison of the free-free subtracted CARMA B visibilities and the envelope only model that produces the SED in the left image. The open circles indicate the observed data and have associated dashed error bars from baseline and time averaging. The model disc and envelope visibilities (solid dots) provide a good fit to the observe data. χ^2_{vis} is 0.43 for this model.

variable the mass is given a fixed radius, i.e. to examine the disc mass parameter with a finer resolution. For the 60 au radius disc the mass can vary from 0.012 and 0.020 $M_\odot$ while simultaneously fitting the visibilities and the SED. An optimal match of the visibilities is found for a disc mass of ~ 0.016 $M_\odot$. Figure 3.14 indicates the good fit of both the SED and the visibilities. The simulated image yields a peak flux of ~ 71 mJy/beam with an integrated flux of 79 mJy in reasonable agreement with the free-free corrected flux of the CARMA B data (68 $\pm$ 5 mJy). Based upon the visibilities this model is the best fit although the less massive discs have a more agreeable flux. The simulated image does not show any elongation when viewed with the CARMA B (u, v) coverage and is consistent with the disc being unresolved.

Disc Model Summary

Although a few hundred models were investigated to find a match with CARMA B observables, there is not a unique solution other than stating a best fit model via a minimal χ^2_{vis} after constraining certain parameters (e.g. fixing the disc radius). The ranges of model parameters here are not rigid limits and are just an illustration of the models that conform to the visibility fitting limit. The overwhelming result is that regardless of disc parameters the inclusion of a disc is required to fit the SED and interferometric visibilities simultaneously. A compact source in the form of a disc is required in addition to the large scale envelope. Disc structures can reproduce the small scale fluxes in the millimetre regime as observed with high resolution interferometers. Models based solely upon 'pseudo-discs' or toroid structures in the form of a large (> 1000 au) flattened dust envelope cannot properly account for the compact structures observed at 0.3 arcsec resolution ($<$ 500 au) with CARMA B. Within the parameter space investigated, no envelope-only models could be found to match the observed visibilities. A large range of disc models can reproduce the observed visibilities and SED simultaneously. Prior to obtaining the CARMA A array data the requirement of a disc in the models supports the dusty disc interpretation of the CARMA B observations.

3.3.6 Dust Opacity Index

Using the best fitting disc model parameters for a fixed 60 au outer disc radius, simulated images were produced and examined at the lower resolution and longer wavelengths of the SMA and OVRO observations. The flux values for all simulated images are listed in Table 3.3. The integrated fluxes at 1.3 mm are consistent with

observations for the CARMA B and SMA convolved models, whereas the 2.7 and 3.5 mm fluxes are slight underestimates of the observed OVRO values. Note that the limited (u, v) range integrated fluxes for SMA and OVRO 112 are greater than those from the total (u, v) range, this is the same as with the observed data in Section 2.4.2. Although appearing counter intuitive, as more (u, v) coverage should appear to recover more flux, the resolution differences between the total and limited (u, v) ranges has the opposite effect. As the limited (u, v) range images are of lower resolution, more surrounding material from the envelope is attributed to the source during fitting procedures. This in effect means the source is physically larger, has more material and hence more flux is associated with it.

Using the restricted (u, v) range data, such that the resolution is matched, the dust opacity index of the model fluxes is found to be $\beta \sim 1.2$. This is steeper than observed. It is likely that the model dust opacity index may not be perfectly suited to IRS1, as previously noted in Section 3.3.4. The β values for the input dust models are 1.3, 1.6 and 1.3 for the mid plane, disc surface and envelope dust respectively (calculated using wavelengths $> 900~\mu m$). As a crude comparison the model output dust opacity index has become shallower by about 0.2 (on average) due to the integration over the distribution of density and temperature. Applying such a scaling to the observed dust opacity index of 0.7 ± 0.3 implies that a dust with an opacity index, β, of 0.9 ± 0.3 is required to explain the observed data. This suggests the input dust model requires larger grains than currently used to provide more opacity at the longer wavelengths probed and to more accurately match the observations. Here, the current dust models provide a reasonable agreement with the 1.3 mm CARMA B continuum observations and adequately fit both SMA and OVRO observations, of differing wavelengths and resolutions.

Table 3.3: Integrated fluxes of the free-free subtracted observations and best fitting disc model with full and restricted (u, v) coverage.

Array	Freq.	Free-free subtracted	Model Flux	Model Flux$_{5-35k\lambda}$
	(GHz)	Flux (mJy)	(mJy)	(mJy)
CARMA	225	68±5	79	... [a]
SMA	225	117±29	143	174
OVRO 112	112	27±5	21	22
OVRO 86	86	15±4	9	8

[a]There are no baselines within 5-35 kλ for the CARMA data and hence a model image is not produced and no flux measurements are available.

3.3.7 Modelling the CARMA A observations

The highest resolution, high sensitivity CARMA A data presented in Chapter 2 shows that the dusty disc around IRS1 is resolved. With these observations comes the opportunity to investigate the disc models for a more compatible match between visibilities in two dimensions and in the image plane. The previous models fitted the 1D azimuthially averaged visibilities reasonably, however, the images were mostly unresolved. A more focused grid of models has been run with various mass and radii to investigate how the 2D visibilities vary between each model and the observations, and how the images at a higher resolution are changed. Furthermore, the effect of changing the disc density distribution and flaring power laws are tested.

Two Dimensional Visibilities

The MIRIAD reduction software allows the visibilities to be plotted at a projected position angle. Rather than the 1D approach, azimuthally averaging all angles, the visibilities can be examined projected down any position angle. Figure 3.15 shows

an example of how the visibilities are projected and extracted for the major and minor axes of an ideal disc. Sub plot a) is the image of the ideal disc. The major and minor axes are 0.6 and 0.2 arcsec respectively and the position angle is 45°. Sub plot b) shows the Fourier transform of the image in sub plot a). In interferometry large spatial scales in the image, i.e. the major axis, correspond to small visibility distances (spatial frequencies) while small spatial scales in the image, i.e. the minor axis, correspond to large visibility distances (spatial frequencies). In this example sub plot c) shows the CARMA A visibility coverage while sub plot d) shows the visibility coverage orientated in the major and minor axis for detections above the 5σ level. The coverage of the source $> 5\sigma$ has a smaller visibility distance extent than the total coverage and the ideal disc is fully resolved. Sub plot e) is a 3D surface plot of the visibility amplitudes from sub plot b) combined with the sampled positions in sub plot d). The positions of the sampled visibilities and their amplitudes are all known. Here, sub plot e) has been oriented such that the x,y coordinates are the major and minor visibility axes. The black arrows in sub plot e) are the projection for the major and minor axes which produce the visibility images shown in sub plots f) and g). The projection of any position angle (here corresponding to the major and minor position angles) includes all visibilities in that direction, i.e. in the line of sight. The black and blue dots in sub plots f) and g) represent all the projected visibilities.

The sub plots f) and g) show ideal data with 2D Gaussian shaped visibilities. In real observational data the noise produces a more scattered plot (see Figure 3.16). These projected visibilities are therefore not ideal for comparison with models. Baseline averaging can be used to reduce the scatter, however, due to the nature of the projection all visibilities in the line of sight are averaged. This averaging is
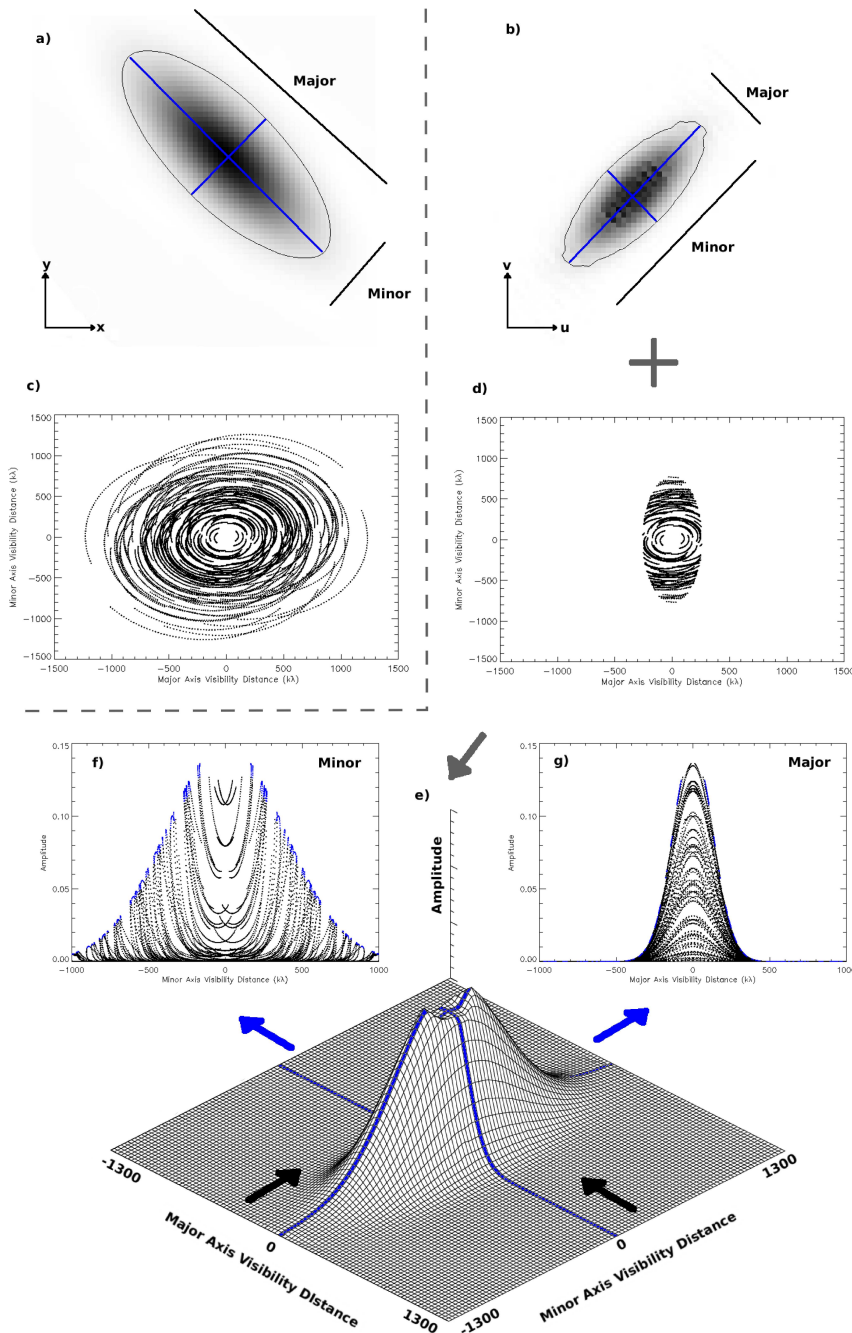
Figure 3.15: Figures to show how ideal data look and how the visibilities are extracted. a) Image of an ideal disc 0.6×0.2" in size at a PA of $45°$. b) Fourier transform of the 'real' image in a). c) Visibility coverage of the CARMA A array. d) Visibility coverage where amplitude is $> 5\sigma$, where the disc is detected. e) 3D surface plot of the ideal disc visibilities. The black arrows represent the projections of the visibilities to create sub plots f) and g). The blue lines indicate the useful visibilities as detailed in the text. f) and g) are the minor and major projected visibilities. The black and blue dots represent the all the visibilities in the line of sight (direction of black arrows in e).The blue dots alone are the extracted

with respect to the projection axis only and irrespective of the physical location of the visibilities in the line of sight. This means the projected baseline averaged values are not the visibilities of the major and minor axes, but those averaged in the direction/line of sight of those axes. For comparison with models it is the visibilities of only the major and minor axes only that are useful. The blue lines in sub plot e) are the lines of the major and minor axes visibilities that are useful and need to be extracted. The blue dots in sub plots f) and g) indicate the extracted visibilities for the minor and major axes respectively. As the locations of all the visibilities are known the extracted visibility slice is $\pm\,250\,\mathrm{k}\lambda$ wide in the projected direction centred about $0\,\mathrm{k}\lambda$, where the major and minor axes intersect. These extracted visibilities can then be averaged with baseline to improve noise (in the observed data) if there are more than two data points in the visibility distance bin. The major and minor axes extracted visibilities from the observations can be recorded and used in conjunction with models to independently constrain the position angle of the observed dusty disc around IRS1 and to establish the best fitting model. A consistency check for this method is to fit the extracted visibilities from the input 2D Gaussian disc (as above). The visibility distance where the amplitudes approach the 3σ level are $\sim\,390$ and $1170\,\mathrm{k}\lambda$ for the major and minor axes respectively according to Gaussian fitting. The corresponding angular sizes are $\sim\,0.22$ and 0.65 arcsec at 1.3 mm wavelengths, coincident with the original input disc size.

Independent Position Angle

Visibilities between the position angles of 20-50° are extracted from the observations to compare with the major axis model visibilities. The corresponding position

angles of 110-140° are extracted for comparison with the minor axis model visibilities. Hence, the major and minor axes visibilities of the models are compared to visibilities at a range of position angles from the observations in order to establish the best fitting position angle. The extracted visibilities from both observations and models are taken from a $\pm$ 250 kλ slice, centred about 0 kλ, in the projection direction (as above) and are binned into 140 kλ wide bins (e.g. Figure 3.16). The observations and models are analysed in exactly the same manner. A grid of 121 models are run and compared with the observations and χ^2_{vis} is calculated for each comparison with the observed visibilities. Given the high SNR of the CARMA A data χ^2_{vis} is suitable for establishing good fitting models, see Section 3.3.4. The models are divided into 11 groups, each with different radii discs. For each radius group there are 11 models which have different masses. Due to the previously noted mass/radius degeneracy, the smaller radius discs begin with a less massive disc while the larger radius discs begin with a slighter larger start mass to minimise the number of unnecessary model runs. The maximum disc radius is set at slightly more than double the measured disc size around IRS1 from image fitting. All discs with a radius 40 and 50 au start with a mass of 0.010 M$_\odot$, 60 and 70 au discs start with 0.011 M$_\odot$, 80 and 90 au discs start with 0.012 M$_\odot$, 100 and 110 au discs start with 0.013 M$_\odot$ and 120, 130 and 140 au discs all start with 0.014 M$_\odot$. For each of the 11 models in each radius group the mass is incrementally increased by 0.001 M$_\odot$. Chi-square fitting is undertaken for the major and minor model axes independently and the results are subsequently combined for the correct major and minor axis pairs, i.e. $\chi^2_{vissum} = \chi^2_{vismaj} + \chi^2_{vismin}$.

Figure 3.17 shows the χ^2 maps for each model minor axis (top), major axis (centre) and combined major and minor axis paired (bottom) visibilities with the
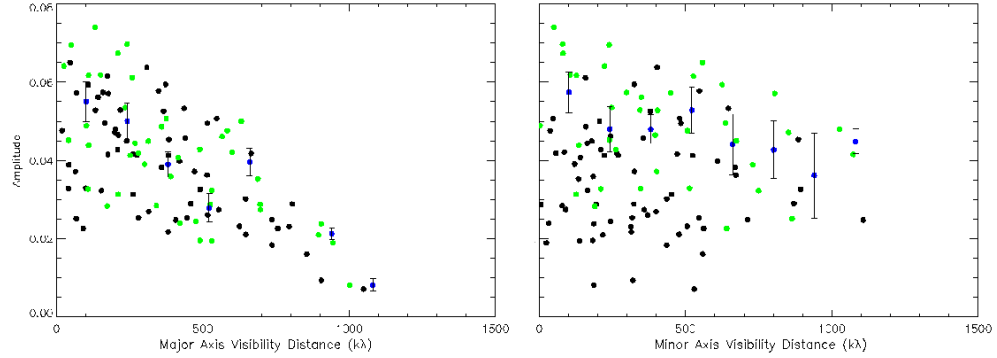
Figure 3.16: The left and right figures plot the visibilities for IRS1 from position angles of 30 and 120° respectively as these are the major and minor position angles according to image fitting. The black dots are the projected visibilities for the axes and the green dots are the slice extracted visibilities in analogy to those from the blue slice in Figure 3.15. Note for the major axis the extracted visibilities (green) have much more scatter and closely match the entire projected visibilities. This is because the line of sight is down the minor axis which is unresolved, as shown in the right hand side plot. Essentially the visibilities in the line of sight cannot be distinguished like in the ideal model in Figure 3.15 as the line of sight is unresolved. In the right hand plot the green dots, although scattered, are tracing the higher amplitude edge of the entire projected visibilities. This is because the projection line of sight is the major axis which is resolved so the minor axis extracted visibilities in the slice trace the higher amplitudes. In both plots the blue dots indicate the binned data with associated errors.

visibilities at a range of position angles extracted from the observations. Model numbers 1-11 are for the 40 au radius disc with increasing mass per model number, likewise models 12-22 are 50 au radius disc models with increasing mass per model number. The changing disc radius and mass create the vertical striping effect (11 stripes for 11 radius groups). The darkest blue regions are those of lowest χ^2 and represent better fits while the red are larger χ^2 values and represent worse fitting models. In order to investigate the position angle dependency for all models the horizontal trends are important. Considering only the fitting of the minor model axis there are two darker horizontal bands centred roughly at position angles of

$\sim$ 117 and $\sim$ 133° where χ^2_{vismin} is clearly lower than the other position angles for the other models in the group. These two position angles are reported to have the minimal χ^2_{vismin} for > 70 percent of the models. These minor position angles correspond to major axis PA of $\sim$ 27 and $\sim$ 43°. Now looking at the vertical stripes the goodness of fit can be discussed in terms of changing radius and mass. In a general sense the larger radius disc appear to provide a better fit to the observables for the range of masses probed. For smaller radius discs the lower masses of the groups provide a better fit whereas the opposite is found for the larger radius discs where higher masses provide a better fit.

The χ^2 map for the model major axis fits shows three wider horizontal bands of low χ^2_{vismax} values for position angles > 40, $\sim$ 27° and < 21° and a narrow band of low χ^2_{vismax} values at $\sim$ 34°. Here < 40 percent of the models have a minimum χ^2_{vismax} at a position angle of > 40°. All the other models have a minimum at exactly 21°. However, this majority is not a real trend and is actually a consequence of the extracted visibilities. For observations at position angles < 25° there are a lack of observed visibilities at larger visibility distances (bins are empty > 1000 kλ) due to the visibility coverage. Therefore at observed position angles > 25° the extra visibility coverage, corresponding to another two bins of data in some cases, means a worse χ^2_{vismax} as the observed fluxes at these farthest visibility distances deviate from the models. Recalculating χ^2_{vismax} for all position angles using only those bins that have flux at < 25° results in horizontal bands of low χ^2_{vismax} at similar position angles as before (Figure 3.18,centre). However, all models now have a minimal χ^2_{vismax} at position angles between 44 and 50°.

χ^2_{vissum} is dominated mainly by variations in χ^2_{vismax} as χ^2_{vismin} follows a similar trend for all models. Prior to the major axis χ^2_{vismax} recalculation $\sim$ 50 percent
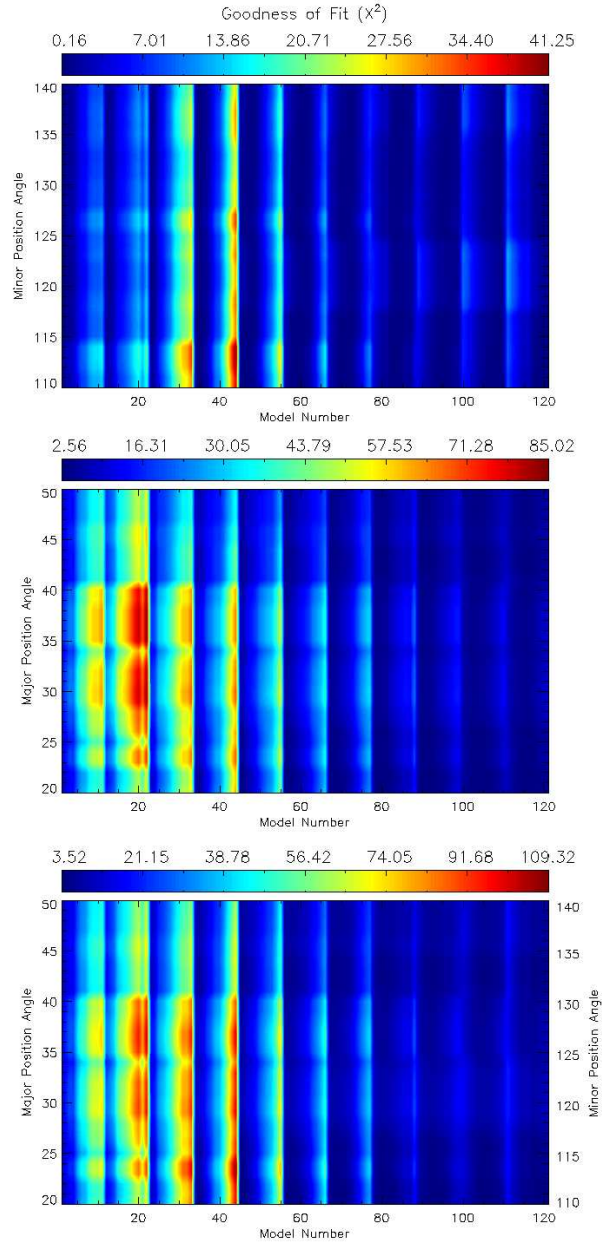
Figure 3.17: χ^2 maps for each model minor axis (top), major axis (centre) and combined major and minor axis paired (bottom) visibilities vs the visibilities of the observations extracted at a variety of position angles. The x and y axis are the model numbers and position angles of the observed visibilities respectively. The colour bars at the top of each plot indicate the χ^2 value. See the text for a more detailed description of the minimal points and the striping effects.
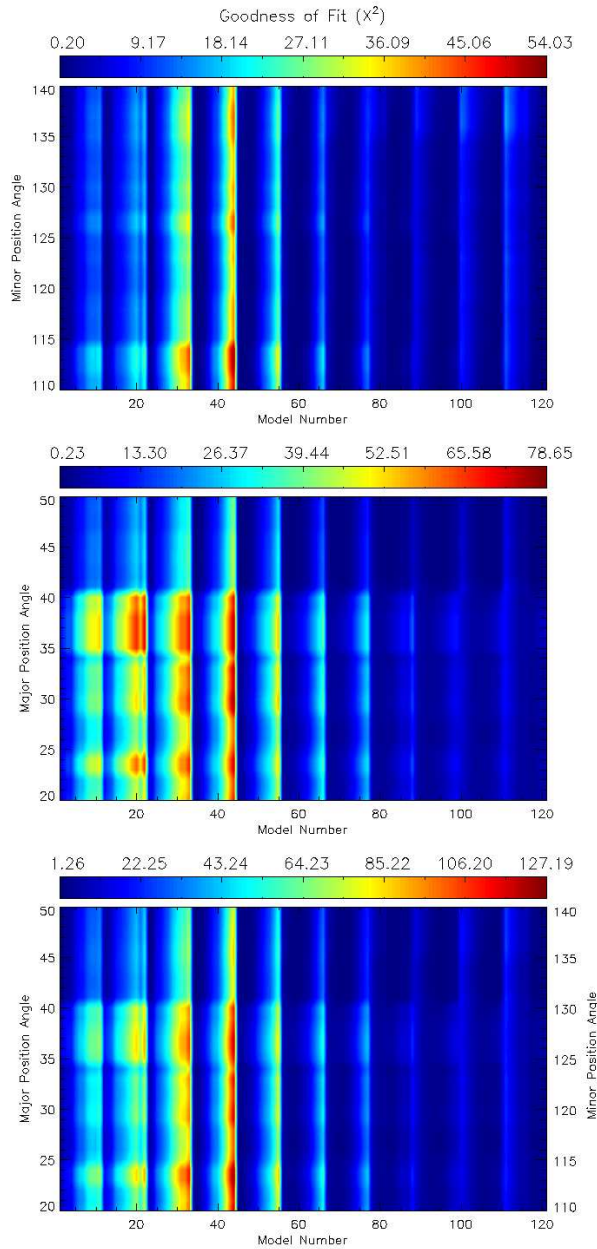
Figure 3.18: As Figure 3.17 but there χ^2 is only calculated for the visibility distance bins that are filled at angles $< 25°$, i.e. to ensure the number of bins in the calculation is constant as the larger number of bins used for χ^2 calculations $> 25°$ resulted in a worse fit due to the extra data point/s. For a detailed explanation see the text.

of the models had a minimum χ^2_{vissum} at major position angles between 42 and 50°, corresponding to minor position angles of 132 and 140°. The other ~ 50 percent of models have a minimum χ^2_{vissum} at the major position angle of 21° due to the limited visibility distances. After the recalculation of χ^2_{vismax} more than 85 percent of the models have a minimal χ^2_{vissum} at major position angles between 42 and 50°. These position angles are more agreeable with the major position angle of the ionised disc wind emission at $\sim 45°$ (Hoare, 2006) than the deconvolved parameters from Gaussian fitting using the UVFIT routine of $\sim 31°$ (see Section 2.4.4). A Gaussian fit to the source emission may not be the correct flux profile to use. The position angles of the remaining models are 21°. Although the beam position angle is $\sim 51°$ from the observations there should be no preference for this angle in the visibility analysis. Both observations and models are binned in the same manner regardless of position angle and the recalculated χ^2_{vismax} considers only bins that are filled at the lower position angles. Position angles at $\sim 50°$ are not preferred over any other angle.

Mass and Radius

It is evident that the variation of mass and radius produce a range of equally well fitting models. Extracting the best χ^2_{vissum} for all the models, a goodness of fit map of mass versus radius can be plotted. Note, each mass and radius model will have different position angles. Figure 3.19 clearly shows a trend of similar χ^2_{vissum} values as both mass and radius are steadily increased. There is a larger trough of low χ^2 values starting at discs with a radius of ~ 70 au and masses > 0.012 $M_\odot$ and extends off the plot to higher masses and radii. As noted previously, very large and massive discs (> 4000 au and >1 $M_\odot$) can still produce adequate fits
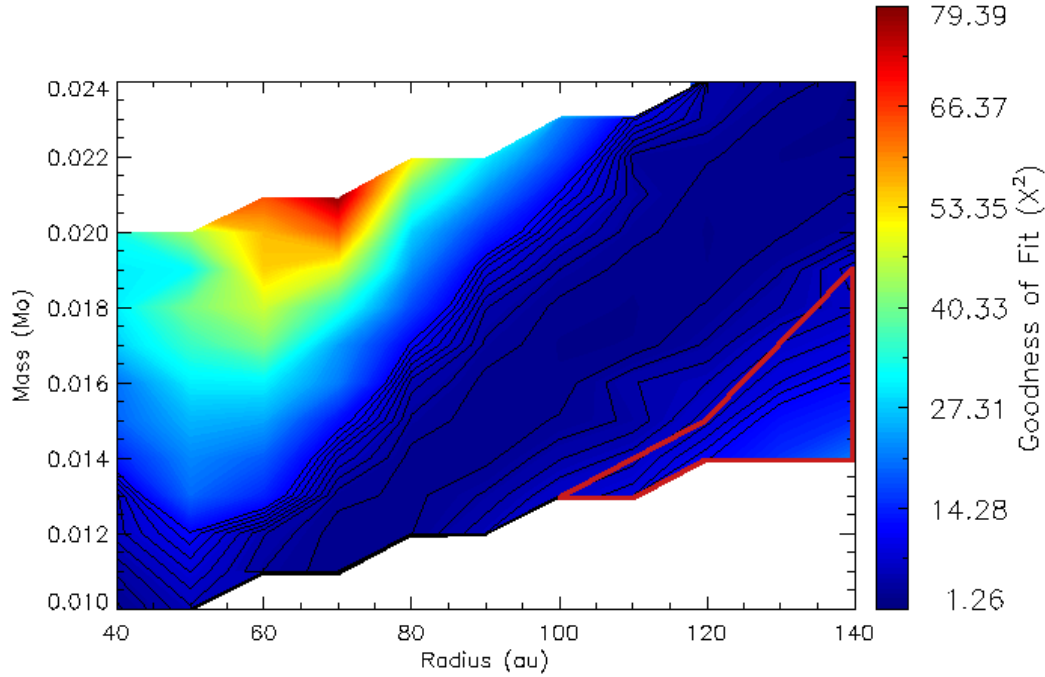
Figure 3.19: χ^2 map of model mass vs. radius in comparison with the observed visibilities. χ^2_{vissum} plotted is the lowest value from fits at different position angles for all model masses and radii. The colour bar of goodness of fit is plotted to the right hand side. More than 85 percent of models have a minimal χ^2_{vissum} value corresponding to major position angles between 42 and 50°. 80 percent of the best fitting models with $\chi^2_{vissum} < 2$ have a PA of 44°. The white areas of the plot are for model mass and radius values that have not been investigated as the mass of the models was selected to increase incrementally with radius due to the known mass-radius degeneracy. It is clear to see the mass-radius degeneracy in this plot as small radius low mass models fit equally as well as larger radius more higher mass models. The black contours indicate χ^2_{vissum} of 2,3,4,5,6,7,8,9,10 from smallest to largest to guide the eye. The red box are models where the lowest χ^2_{vissum} corresponds to a PA of 21°.

Table 3.4: Best fitting disc model parameters

Parameter	Value
Mass of Star	11.1 $M_\odot$
Stellar Radius	4.92 $R_\odot$
Blackbody Temp.	25000 K
Envelope Outer Radius	45000 au
Centrifugal Radius	50 au
Infall Rate	1.2×10^{-4} $M_\odot$ yr^{-1}
Cavity Opening Angle[a]	5.2°
Cavity Shape Exponent	1.5
Cavity Density	10^4 cm^{-3}
Ambient Density	5×10^3 cm^{-3}
Disc Mass	0.02 $M_\odot$
Disc Outer Radius	120 au
Disk Density Exponent	2.25
Disc Flaring Exponent	1.25
Disc Accretion Rate	7.5×10^{-5} $M_\odot$ yr^{-1}

(a) Opening angle corresponds to 7° for an outer radius of 23000 au.

to the observations. The best fitting model matches the observed visibilities at a major position angle of 44° and has a disc radius of 120 au, a mass of 0.02 $M_\odot$, and a χ^2_{vissum} of $\sim$ 1.2. Table 3.4 lists all major parameters inputs to the Whitney code for this model. There are 25 models where $\chi^2_{vissum} < 2$. 20 have a PA of 44°, 4 have a PA of 45° and the remaining model has a PA of 47°. The position angle of the dusty disc is well constrained to $\sim$ 44°, although the mass and radius have a broader parameter range.

The variation of the mass and radius slightly changes the profile of the model flux as a function of visibility distance, as shown in Figure 3.20, although all of the models have an excess flux on the very smallest scales compared to all

major positions angles of the observations. For all minor position angles of the observations it is clear that the disc is unresolved given that the visibility fluxes are approximately equal on all baselines. For models with larger fluxes overall, the minor axis visibility fluxes are slightly greater on large scales compared to the very smallest scales and appear more resolved than the observations. The bottom plots of Figure 3.20 show the visibilities of the observations over-plotted with those of the best fitting model. Here it is much clearer to see the slight difference in the flux profile of the model and the observations on both the major and minor axes. The major axis flux profile differs most significantly on the smaller disc scales after ~ 800 kλ (0.3 arcsec), corresponding to a physical size of ~ 240 au.

It would be natural to progress and check the image plane for variations in an attempt to narrow down the range of 'good' models. However, in reality the image plane is just the Fourier transform of the visibilities and does not yield any further information. The images of all models with $\chi^2_{vissum} < 2$ are very similar. Moreover, the best fitting model image does not appear elongated enough in the major axis but is consistent with being unresolved in the minor axis as the observations.

Disc Density Distribution and Flaring

The disc density distribution and flaring extent are the only other free parameters concerning the disc and can effect the small scale visibilities. It is not clear at this stage with only one wavelength observed at high resolution whether these parameters can be constrained in any detail. In the following modelling steps the mass and radius will remain fixed in order to constrain the effect of the density distribution and flaring on both the visibilities and the images.

Starting with the best fitting model so far the disc flaring exponent is reduced
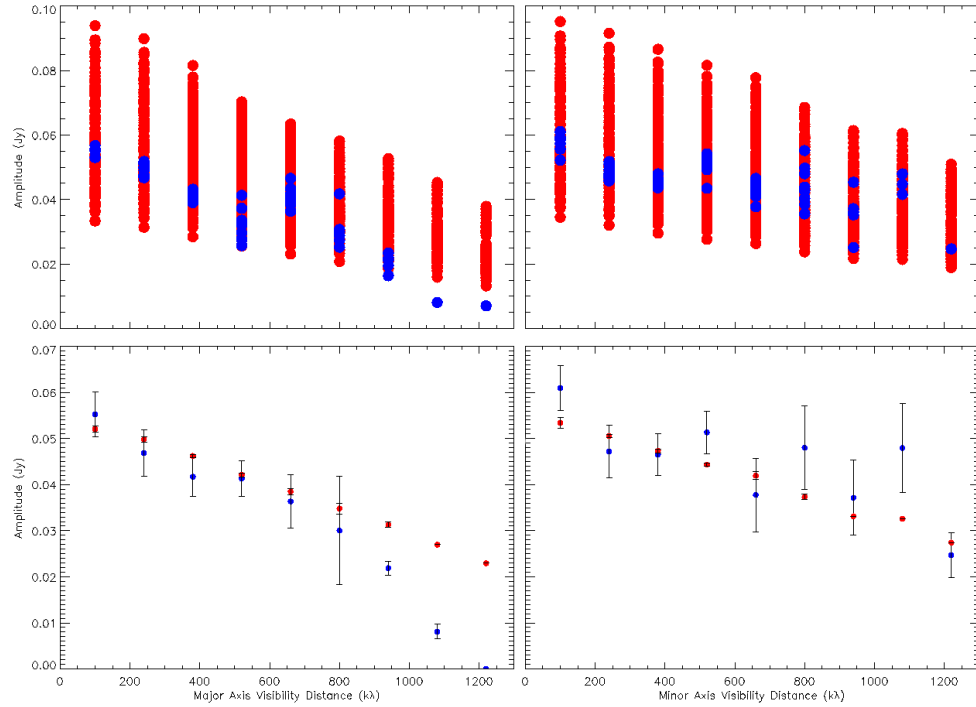
Figure 3.20: Top: The binned visibilities for all models run (red) over-plotted with the visibilities from the observations at various position angles (blue). The left and right plots indicate the visibilities for the major and minor axes respectively. The models run span a reasonably large range of flux but the radial visibility distance profile do not change slope significantly between each one. The models overestimate the small scale flux when compared with the observations on the major axis and the models appear more resolved than the observations on the minor axis. Bottom: The binned visibilities for the best fitting model (red) over-plotted with the visibilities from the observations (blue) where χ^2_{vissum} are a minimum at $44°$ for the major axis and $134°$ for the minor axis. Note the slight discrepancies between the radial visibility distance profiles of the observations and model.
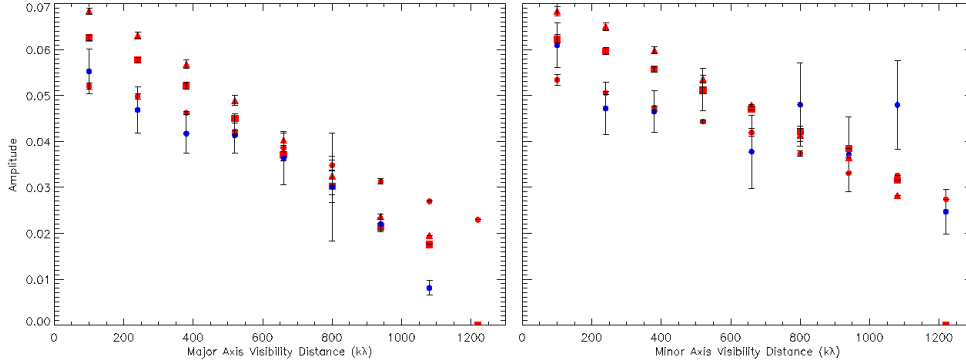
Figure 3.21: As the bottom plots in Figure 3.20 but with the addition of differ-
ent disc models with reduced flaring power law exponents. The circles represent
the previous best fitting model where the flaring exponent was 1.25, the squares
represent the model with a 1.15 flaring exponent and the triangles are for the
model with a 1.10 flaring exponent. Note the increasing flux offset between the
observations and models on larger spatial scales of both the major and minor axes
as the flaring exponent is decreased.

(as current models are over-resolved on the minor axis) until a better match to
the radial visibility profile is attained. Reduction of the disc flaring power has
the effect of increasing the flux of the disc overall. Upon investigation of the
density distribution, the discs with a lower height exponent (flaring) become denser
further out in the disc as the same amount of material is confined to a smaller
volume. Consequently this has the effect of increasing the optical depth at shorter
wavelengths meaning more light is absorbed and then re-emitted at millimetre
wavelengths.

Figure 3.21 compares the different flaring power laws with the observations.
The relative increase of flux at larger radii means that there is more flux at shorter
visibility distances, and less on the small scales. Hence the visibilities appear
more resolved on the major axis. The comparison of the simulated images to the
observations also indicate the disc is better resolved with a smaller disc flaring

exponent (Figure 3.22). The redistribution of flux has altered the radial flux profile of the models. They get steeper for a decreasing flaring exponent and more emission comes from the larger scales. However, for the major axis the fluxes of all models decrease in a linear fashion (larger to smaller scales) and do not match the profile of the observations where the flux reduces noticeably after ~ 800 kλ corresponding to 240 au scales. On the minor axis the model visibilities have an excess flux on larger spatial scales than the unresolved observations, although the images are still consistent with the model disc being unresolved on the minor axis. Furthermore, due to the increase in overall flux a decrease in disc mass is required to improve the χ^2_{vissum} value, which have degraded. If the disc mass was reduced the best fitting model would have a flaring exponent of 1.15. However, on the very smallest scales the flux of the modelled disc is larger than the observations. This discrepancy is also seen in the residual images in Figure 3.22 as the central regions are negative where the model flux has excess small scale flux. The reduced mass disc with decrease flaring exponent would have the correct integrated flux although the flux distribution is not ideal to fit all the observed visibilities. The Whitney code only describes a simple flared disc which may not be entirely realistic for IRS1. More complex discs with different density distributions, where more material is at larger disc radii, could provide a possible explanation.

Geometrically flat discs were also tested to ensure the minor disc axis was unresolved. However, it appears that a limit was reached internally with the ray tracing code where the flaring power law = 1 and model images could not be produced.

Starting back at the best fitting model (before the variation of the flaring exponent) the density distribution exponent is adjusted. This is varied to determine
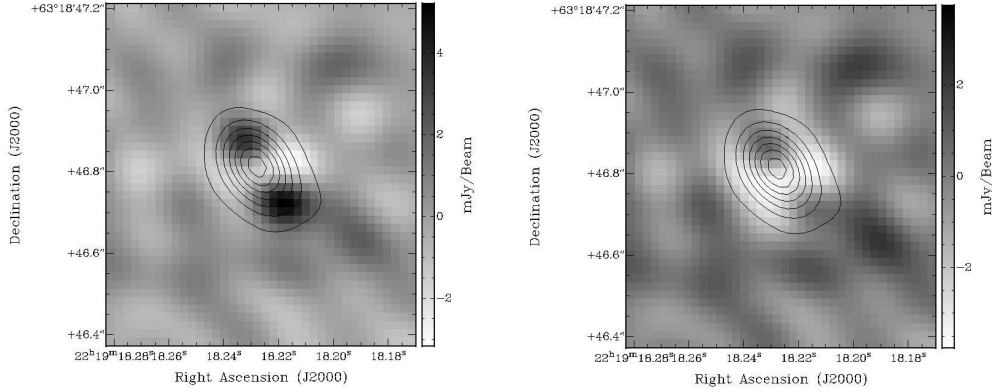
Figure 3.22: Residual images after model images are subtracted from the observed image as presented in the left plot of Figure 2.17. The contours are as those from the observed image of IRS1 as presented in left plot of Figure 2.17. Left: Observations minus the best fitting model with radius of 120 au and mass 0.02 M$_\odot$. The two black patches represent flux left over as the model is not as resolved as the observations. Right: As the left model disc but with the flaring exponent reduced to 1.15. There are no black patches of excess flux. Note the white patches representing negative flux where the models have more flux than the observations. The excess model flux on the minor axis does not effect the overall image and is still consistent with it the model disc being unresolved.

whether the distribution of the material in the disc has a significant effect on the flux profile of the visibilities. Figure 3.23 shows that there is little change in the visibility flux profiles for each of the models where the density exponent has been varied from 1.75 to 2.75 in steps of 0.25. Note the exponent follows a negative power law to the exponent so the flux decreases according to the radius, $n_{disc} \propto r_{disc}^{-\alpha}$ (see Section 3.3.5). Linear fitting of the visibility profiles for the most extreme models results in negative slopes of 2.7×10^{-5} and 2.3×10^{-5} for α values of 2.75 and 1.75. Linear fits are a good representation of the models, which is not the case for the observations at larger visibility distances, as previously discussed. The slopes of the flux profiles are counter intuitive as the steeper density distribution
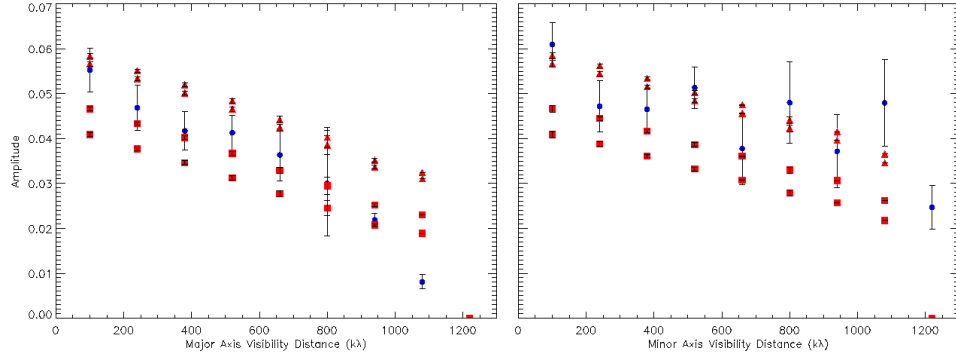
Figure 3.23: As Figure 3.21 but models have different disc density distributions. The blue circles are the observed visibilities, the triangles correspond to an increased density exponent of 2.75 and 2.5 from the upper to lower line and the squares correspond to a reduction in the density exponent to 2.0 and 1.75 from the upper to lower of the two lines. The slope does not change noticeably by eye.

model should have more small scale flux compared with the large scale flux and therefore have a shallower flux profile when plotting against visibility distance, not a steeper one as measured. However, the modelled discs change on scales of ~ 50 au, much smaller than probed by the interferometer. It is probable that the shallower density distributions have a shallower visibility flux profile as the outer disc regions, which the interferometer is sensitive to, have more flux comparable to the larger scale emission than the models with steep density distributions where flux in the inner disc is larger but the outer disc flux is decreased.

An added effect of the altered dust distributions is the change in overall integrated flux. The model with the steepest distribution has 50 percent more flux than the shallowest distribution disc model. The effect is likely cause by opacity changes, as noted above with different disc flaring exponents. The steeper density distribution has a higher density close to the source and hence produces more millimetre emission from reprocessed light. Thus the disc itself provides slightly more

flux. Again, for a fixed radius, the mass would need to be adjusted to achieve better χ^2_{vissum} values. For all models, a reduction in flux starting at physical scales of ~ 200 au (disc radii of ~ 100 au) and continuing to smaller sizes is required to match the observed flux profile of the observations, while the entire disc itself must still provide the same total flux.

CARMA A Modelling Summary

The newly developed 2D visibility analysis allows the position angle of the observations to be independently constrained without assuming a Gaussian flux profile. Regardless of the specific model disc mass and radius the position angle is well fitted at $\sim 44°$ provided that the same number of visibility flux bins are compared. Due to the deviations of the models and observations on smaller spatial scales the best resolved axes initially appeared to be a worse fit.

Using a fine grid of mass and radius models it is clear that a degeneracy exists between these parameters than cannot be solved with only high resolution interferometric observations at a single wavelength. With many mass and radius permutations a constant density distribution is achieved which the interferometer is sensitive to although fainter emission may exist on larger scales, for larger radius discs. There is no way to constrain either the disc radius or mass unless one parameter is fixed. Variation of the disc flaring exponent leads to a slightly more resolved image that provides a better fit to the observations, although the changes are very subtle when comparing the visibilities directly. Adjustment of the disc density profile exponent does not lead to major changes of the visibilities with only a minor change in the slope of the visibility flux profile. In both cases (flaring and density changes) the flux profile of the visibilities does not match the decline of the

observed visibilities after ~ 800 kλ and the integrated fluxes also vary based upon the previous best fitting mass and radius model. All 4 parameters are degenerate. Discs with different density distributions where more material is at larger radii could provided a means to match the visibility profile of the observations, however at this stage such investigation is not possible using the disc model in the Whitney code.

Extracting the visibilities in 2D facilitates the investigation of more model parameters. At this stage it is still very difficult to constrain all of these parameters as the increase in variables under investigation makes the models more degenerate. Overall, a disc and envelope are required to provide the good fit to the observed visibilities, the output simulated image and the SED.

3.4 Conclusions

Radiative transfer modelling is an exceptionally useful tool when multiple observations are available to reduce the degeneracy of tens of parameters, all of which can be finely tuned to offer a good fit to just one set of observations. Multiple wavelength observations are drawn upon to constrain the large scale envelope parameters using less computationally intensive scattering models prior to detailed thermal modelling. Using sensible estimates of the envelope radius and developing models based upon the scattering model parameters a good fit to the spectral energy distribution is achieved relatively quickly. Other envelope parameters are varied but are found to be relatively insensitive. Essentially fine variations of the infall rate (specifying the density distribution) in all situations could replicate the effects of the other parameters even when they are changed by large amounts. The

models are greatly affected by the type of dust used as these determine the strength and wavelength of the scattered and re-emitted radiation. A large degeneracy is found between the infall rate and centrifugal radius, both of which determine the density distribution. Provided one parameter is fixed the other can be varied to find a best fitting model. Currently there are no observations to constrain R_c accurately. Modelling of the envelope only will replicate the SED of the source but cannot simultaneously match the visibilities at millimetre wavelengths and at high angular resolutions even when investigating an extreme range of parameter space.

Inclusion of a compact disc in the models is required to boost the flux on the very smallest scales. Using sensible estimates of the dust opacity and temperature a wide range of masses can provide the detected flux. High mass small discs are seen to become optically thick and the flux does not increase with an increase in mass past a given limit. From the observables the dust disc is thought to be in the optically thin regime although is approaching $\tau \sim 1$. Such a disc can be modelled using a small mass and small radius disc or a large mass and large radius disc.

A new method is developed to extract the projected observed and model visibilities and use those only corresponding to the major and minor axes. This 2D approach has allowed the position angle of the dusty disc to be independently constrained to $\sim 44°$, corresponding to the ionised equatorial disc wind emission at 5 GHz. Model visibility profiles are not limited by choosing only a Gaussian distribution, which does not necessarily match the disc visibility flux profile. The best fitting model is a 120 au radius disc with a mass of 0.020 M$_\odot$, although there are a number of models that fit equally as well that are distributed about this best fitting model. None of the models accurately fit the visibility flux profile of the

observations after ~ 800 kλ where the flux reduces more rapidly than the linear trend. A less flared disc better matches the final image and visibilities although the differences are small. Similarly, changes of the density distribution provide little change to the visibility flux profile other than a general scaling of flux which can be combated with a change of mass given a fixed disc radius. All four parameters, mass, radius flaring and density distribution are degenerate and changes of these do not provide the reduction in flux on the very smallest scales of ~ 100 au while keeping the total disc flux on scales of ~ 240 au (~ 800 kλ) the same as observed. The inclusion of a disc into the previously best fitting model envelope provides an excellent fit to the SED and the visibilities simultaneously. Furthermore, modelling of the SMA and OVRO interferometric data, probing larger scales, finds that the overall underlying dust opacity index is closer to 0.9 rather than the 0.7 as measured directly from the observations. For optically thin sources the low dust opacity index is indicative of grain growth in discs.

With the current large grain dust type used the best fitting model has a very small disc mass. Even with a more ISM-like dust the disc mass is of the order 1-2 percent of the stellar mass of S140 IRS1. The dust disc mass is small regardless of dust type. Although other high angular resolution observations at other wavelengths would be beneficial in constraining the disc outer radius and therefore the mass via modelling, simple estimates of the dust mass using grain opacities and temperatures result in the same conclusion of a low mass disc. As the disc around IRS1 is not very massive it is likely at a stage where it is actually being eroded away, rather than being replenished by the envelope to provide an accretion reservoir for the central MYSO. Such a small size and mass disc fits the picture that IRS1 is a late stage MYSO, pre-UCHII region source that is approaching main se-

quence parameters and is able to power a radiatively driven disc wind. This is the first detailed radiative transfer modelling in 2D visibility space for such an MYSO with an equatorial disc wind. The conclusions of this modelling is complementary to the observations in placing IRS1 as an ionised disc wind source with an eroding dusty disc.

Chapter 4

Core Masses Towards 99 RMS Outflow Sources

Observations of a sample of high mass protostellar sources thought to be at a similar evolutionary stage can provide a means to investigate similarities and difference from lower mass sources. Furthermore, differences between the high mass sources themselves may provide an insight into the evolutionary sequence on smaller timescales. Given observational time constraints, observations in the millimetre regime of large samples are undertaken with single dish telescopes. Although these do not provide the resolution to detect discs, like the observations presented in Chapter 2, they can probe larger scale characteristics such as cores, clumps and outflows. This Chapter presents $C^{18}O$(3-2) molecular line data from 99 MYSOs and HII regions, targeted as outflow candidates, taken with the James Clerk Maxwell Telescope (JCMT).

4.1 Introduction

Dense molecular cores are the formation sites of massive stars (see Chapter 1). To study the densest regions closer to the core the $C^{18}O(3\text{-}2)$ can be used as it is an optically thin tracer (Zhang & Gao, 2009). Tachihara *et al.* (2002) investigate 179 very nearby (< 200 pc) dense $C^{18}O$ cores in low mass star forming regions for differences in properties that would provide insight into star formation in the 9 different regions. They do not find any evidence for the empirical (Larson) relationship between radius and core line widths, even in the case of starless cores that should not have been disturbed by star formation within them. It is possible, however, that the dynamical range of the $C^{18}O$ tracer and/or the range of core sizes sampled are too small to see a firm trend. The authors find that cores with stars have smaller line widths than starless cores. This suggests that turbulent decay leads to star formation within cores. The molecular clouds that harbour the clustered star formation regions all have a head/tail morphology suggesting external shock events triggered the formation. Core line widths do not appear enhanced by this possible formation mechanism, although they are by the injection of energy from the clusters themselves. Interestingly the overall CMF is very similar in profile to the IMF, and assuming a star formation efficiency of 10 percent in all clouds, the estimated mass function matches the IMF very well, except at the higher mass end where the sample is very limited.

More recently large efforts have been made to map specific regions in order to understand the molecular gas properties throughout specific regions of star formation (e.g. Orion A, Buckle *et al.*, 2012). They find evidence to support active massive star formation in the region OMC 1 from higher excitation temper-

atures and stronger molecular emission of the entire region. Furthermore, organic molecules are detected towards OMC 1 and are also indicative of massive star formation. These lines are not observed elsewhere in the Orion cloud. When dividing up the cloud into cores on the 0.1 pc scale the authors find there is more difference between the different regions than there is between starless and protostellar cores. There is no correlation of velocity dispersion with star formation although there is an increase towards the massive star forming region OMC 1. They find a correlation between continuum and $C^{18}O$ emission for both starless and protostellar cores and the same material is traced by both type of observations. There is no significant difference between the type of cores. The authors also find that the cores do not follow the Larson line width and size relationship and suggest that gravity dominates over turbulent motions on the spatial scales of these cores. Based on these properties a possible scenario is that the most abundant and massive star formation has occurred in OMC 1 due to the higher turbulence in this region of the Orion cloud. Consequently, less turbulent regions have less massive cores and lower mass stars, and the lowest number of star forming cores (Buckle *et al.*, 2012).

Here, $C^{18}O$(3-2) molecular line data of 99 MYSO and HII sources are analysed to characterise source environments and the sources themselves for comparison with outflow parameters that are to be calculated from ^{12}CO(3-2) and ^{13}CO(3-2) data (see Chapter 5). In the context of previous studies, these cores are all star forming and probably clustered sites given the distances involved for massive star forming regions. Understanding the core properties is of utmost importance in the case of outflow sources where previously observed trends between outflow and source properties are biased due to heterogeneous source sampling (see Section 1.5.2). In order to investigate a scaled up version of low mass star formation, via

a scaling of outflow properties, the observations of MYSOs from a large, representative sample are required.

This Chapter presents a method to establish core masses and how mass estimates of sources with complex geometries and using other line tracers can also be undertaken. Specifically, the method applies to the calculation of outflow masses. The core masses are compared to a range of other source properties to investigate the completeness of the sample and any observed evolutionary trends for the targets. Furthermore, the velocity ranges of the ambient core material can be adopted in order to differentiate between ambient core and outflow material in subsequent outflow analysis.

4.2   Observations

A selected sample of 99 MYSOs and HII regions taken from the Red-MSX Survey (RMS) were observed with the James Clerk Maxwell Telescope (JCMT) located near the summit of Mauna Kea, Hawaii, as part of projects 07BU16 and 08BU18 throughout 2007 and 2008. The 15 m dish yields a 15.3" beam full width half-maximum (FWHM) at $\sim$ 329 GHz for the $C^{18}O$ (3-2) line. Throughout the observations the typical median system temperatures were $T_{sys} \sim$ 350-550 K. In a few cases system temperatures reached as high as 900 K, although this is reflected in a higher spectral noise level. The observations were taken with Heterodyne Array Receiver Program (HARP) 16 pixel SSB SIS receiver (Buckle *et al.*, 2009). The backend ACSIS correlator (Auto-Correlation Spectral Imaging System) was configured with an operational bandwidth of 250 MHz for the $C^{18}O$ transitions. ^{13}CO was simultaneously observed with $C^{18}O$. The resulting velocity resolution

was 0.0555 km s^{-1}. The C^{18}O data was smoothed to the resolution of the ^{12}CO data (see Chapter 5) to the match velocity bins for later outflow analysis and to improve the signal to noise ratio.

The maps were taken in raster-scan mode with continuous sampling observations (on-the-fly) and position switching to observe a "clean" reference position at the end of each scan row. The majority of the baselines on each of the working receivers were flat, suitable for detecting the weak C^{18}O emission. Some receivers did exhibit sinusoidal modulations and were flagged out from the final maps accordingly. Data reduction and viewing was undertaken with a custom pipeline which utilised the KAPPA, SMURF, GAIA and SPLAT packages which are part of the STARLINK software that are now maintained by the Joint Astronomy Centre (JAC). Linear baselines were fitted to the source spectra over emission free channels and subtracted from the data cubes. The final C^{18}O cubes used in all analysis were made with a 7" spatial pixel scale, and a velocity resolution of 0.423 km s^{-1}. The maps and spectra are presented on the original antenna temperature scale (T_A^*; Kutner & Ulich (1981)). In subsequent calculations conversions are made to the main beam brightness temperature $T_{mb} = T_A^*/\eta_{mb}$ where $\eta_{mb} = 0.66$ as measured by JAC during the commissioning of HARP and via continual planet observations.

The sample sources were initially chosen to be located at a maximal distance of ~ 6 kpc, however subsequent works and updates to the RMS database have found 12 sources to be located at a far kinematic distance beyond this. The original distance cut would have ensured that the sample of sources was complete down to luminosities of $\sim 10^3$ L$_\odot$.

4.3   Mass Determination

Initially IRAS 20126+4104 (G078.1224+03.6320) is analysed as it is an ideal MYSO test source with a disc and outflow, as previously discussed in Chapter 1. In higher resolution interferometric observations by Shepherd *et al.* (2000) there are two cores, possible part of a binary system which are both emitting jets. The more northerly of the two sources is regarded as the primary driver of the outflow. This source is the MYSO, IRAS 20126+4104. Given the JCMT resolution and previous single dish observations of the core emission, via NH$_3$ (1,1) (Estalella *et al.*, 1993), IRAS 20126+4104 is an isolated core with a circular geometry and is ideal for testing different mass calculation methods.

The C^{18}O observations confirm that IRAS 20126+4104 is a roughly circular, isolated region. The right hand plot in Figure 4.1 shows the C^{18}O emission spectra within a three pixel aperture centred on the RMS position of the source. The Gaussian profile centred at the source systemic velocity of -3.5 km s^{-1} (Shepherd *et al.*, 2000) suggests the emission is from a single core with no significant velocity substructure.

Total mass of gas can be calculated assuming that C^{18}O (3-2) is optically thin and in local thermodynamic equilibrium (LTE) with an excitation temperature T_{ex} = 40 K. As shown in Ginsburg *et al.* (2011), a temperature T_{ex} = 40 K provides a minimal estimate of the column density, and hence mass, when following the LTE assumption. Furthermore, the difference in the conversion factor when the T_{CMB} term is removed is negligible for the CO(3-2) transition when higher excitations temperatures (> 35 K) are used. As such, all parameters returned are a minimum when using the LTE approximation for the CO(3-2) transition with the T_{CMB} term
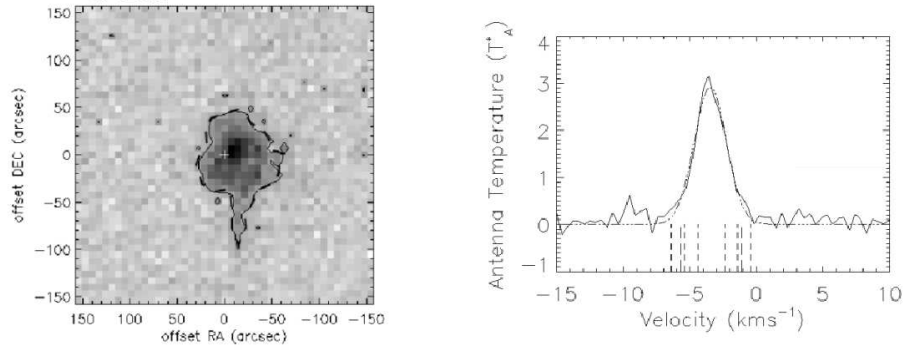
Figure 4.1: Left: Integrated intensity map of the C^{18}O emission from IRAS 20126+4104 within the -5.7 to -1.1 km s^{-1} velocity range. The solid black line indicates the $3\sigma_{MAP}$ contour and the white cross indicates the RMS source location. Emission is summed within the polygon aperture, shown by the dashed line, and traces the $3\sigma_{MAP}$ contour level. Right: C^{18}O line spectra for IRAS 20126+4104 averaged within a 3 pixel diameter aperture centralised on the RMS source location. The spectra is representative of a Gaussian profile, indicated by the dot-dash line. The vertical short dashed lines show the velocity ranges encompassing 68, 95 and 99 percent of the emission (1,2,and 3 standard deviations (σ_{SD})) according to the Gaussian fit, whereas the long dashed line shows the velocity range matching the absolute velocity bins values where emission is integrated within.

removed. The mass is calculated following:

$$M_{gas} = 1.84 \times 10^{-10} \, \theta^2('') \, D^2(\text{kpc}) \, (\text{H}_2/\text{C}^{18}\text{O})$$

$$\times \int T_A^*/\eta_{mb} \, dv \, (\text{M}_\odot) \tag{4.1}$$

where θ is the beam FWHM in arcseconds, D is the distance to the source in kpc and (H$_2$/C^{18}O) is the H$_2$ to C^{18}O abundance ratio taken as 5.1×10^6 (H$_2$/^{12}CO $= 10^4$ and ^{16}O/^{18}O $= 513.4$ (Wilson & Rood, 1994), at the galactocentric distance of 8.1 kpc reported by Shepherd *et al.* (2000) for IRAS 20126+4104). A more detailed explanation and derivation is given in the Appendix A. The mass calculation relies

on the accurate determination of $\int T_A^*/\eta_{mb}\,dv$. The following subsections present numerous methods undertaken to establish the core mass of IRAS 20126+4104.

4.3.1   Individual Spectra analysis

Gaussian fits are made to all spectra in which emission was detected above three times the $1\sigma_{T_A^*}$ spectral noise and where the peak is within 1 km s^{-1} of the system V$_{LSR}$ in order to establish a baseline mass estimate. The noise is an average of the line free spectral noise at each pointing. For IRAS 20126+4104 the $1\sigma_{T_A^*}$ spectral noise is 0.41 K for the 0.423 km s^{-1} resolution data. Summing the flux from all the Gaussian fits results in a calculated core gas mass of 101 $\pm$ 29 M$_\odot$. The uncertainty is the propagation of the uncertainties from the Gaussian fitting process. For the spatial positions where the emission is just above the flux limit the fits are quite uncertain. Gaussian fitting would have less error if using a single summed spectrum taking all emission from the source rather than extracting each individual spectrum. Here the signal to noise would be significantly improved. However, at present the spatial extent of the source is unknown.

When this technique is automated for all sources Gaussian fits will be undertaken for all spectra above the flux cutoff. This causes a major problem as these regions of emission may not correspond to the source itself spatially and could be due to diffuse emission well away from the source. It would be necessary to manually check the positions of all spectra for an association with the source. This is unfeasible for hundreds of spectra per source. Secondly, the source emission must have a Gaussian profile to be fitted well. For the C^{18}O core emission this is a reasonable assumption after viewing the spectra from many sources, however the technique cannot be applied to find the masses of outflows, for example, that do

not have a Gaussian spectral profiles.

4.3.2 Core Velocity Extent

To solve the problem of spectral profiles that deviate from a Gaussian shape a simpler integration over velocity can be done at all positions conforming to the previous flux and velocity limits. This is similar to the method Fontani *et al.* (2012) use. The simple integration analysis is directly relevant to the mass calculation from other line tracers where simple Gaussian fitting cannot be accomplished. First however, a method must be generated to establish the velocity extent of the $C^{18}O$ core.

To set the velocity limits of the core a spectrum is extracted within a 3 pixel ($\sim$ 1.5 FWHM beamwidths) diameter circular aperture centred upon the RMS source location at the system V_{LSR}. The emission is strong and has a Gaussian profile in this case, as shown in Figure 4.1, and can be fitted (as above). Larger apertures are not used as some sources in the sample have no emission outside a 3 pixel diameter aperture and background emission could contaminate the spectra in these cases. Furthermore, some sources are in complex regions with multiple velocity components that are spatially nearby. In these cases incorrect velocity ranges may be inferred by including emission from other nearby cores/sources.

The Gaussian fitting of the central spectrum from IRAS 20126+4104 indicates a V_{LSR} of -3.4 km s^{-1} and an intrinsic velocity width of $\sim$ 1.0 km s^{-1}. The velocity limits for 1, 2, and 3 standard deviations (σ_{SD}) are -4.4 to -2.4, -5.4 to -1.4 and -6.4 to -0.4 km s^{-1} respectively (i.e. encompassing 68, 95 and 99 percent of the emission). Although the spectrum is smoothed to velocity resolution of 0.423 km s^{-1}, the effect upon the intrinsic velocity width is relatively small, of the order

10 per cent. The measured width was ~ 1.1 km s^{-1}. A problem arises during the integration step. Due to the velocity resolution of the data, the $3\sigma_{SD}$ velocity limits do not match the velocity bins that can be chosen for integration. To avoid including noise, or background emission in the case of more complex regions, the velocity range chosen for integration was smaller than the range given by the $3\sigma_{SD}$ values from the Gaussian fitting. For IRAS 20126+4104, the velocity limits corresponding to the spectral bins are -5.7 and -1.1 km s^{-1} and would roughly correspond to $2.5\sigma_{SD}$ according to the Gaussian fitting. The velocity limits from the Gaussian fitting method and the bin velocities selected to integrate within are shown on the right hand plot of Figure 4.1.

The above method to establish the velocity range is again based upon a Gaussian fit. Alternatively, the data cube directly can be analysed directly. The spatial position of the source is located at the system V_{LSR} and the data cube is investigated channel by channel (i.e. velocity bin by velocity bin) outwardly from the V_{LSR}. When emission drops below the noise limit ($1\sigma_{T_A^*}$ or $3\sigma_{T_A^*}$) the velocity of the channel/bin is recorded as the integration limit. Given the low signal to noise of the data cubes, using only the velocity width of the pixel at the source location may not fully represent all emission from the entire core. Therefore, as before with the spectra extraction, the emission within a 3 pixel diameter circular aperture centred upon the RMS source position is used. Flux within the aperture must drop below the flux limits to set the integration velocities. At the $1\sigma_{T_A^*}$ cutoff the velocity limits are $\sim$ -11.2 to 1.1 km s^{-1}, much larger than from the Gaussian fit of the spectrum. In this case a $1\sigma_{T_A^*}$ limit is unsuitable in identifying a sensible velocity extent as noise is clearly selected as representing the core. The velocities are much further from the V_{LSR} than $3\sigma_{SD}$ established from the Gaussian fitting.

On the other hand at a $3\sigma_{T_A^*}$ cutoff the velocity limits are ~ -5.7 to -1.1 km s^{-1} and well matched to the previously established limits. This method removes the requirement of fitting the spectra as the data cubes can be easily investigated.

Summing emission integrated between -5.7 and -1.1 km s^{-1} results in a mass of 102 ± 3 M$_\odot$. The uncertainty is determined via an adjustment of the integration velocity range by $\sim \pm 0.9$ km s^{-1} in total, i.e. one bin width increase or decrease in the velocity extent. Such a range is chosen as it corresponds roughly to the $2\sigma_{SD}$ and $3\sigma_{SD}$ velocity ranges from Gaussian fitting of the 3 pixel spectrum. Although the integration ranges are well selected, spatially the spectra are integrated as long as there is emission above the $3\sigma_{T_A^*}$ spectral noise level and where the peak is within 1 km s^{-1} of the system V_{LSR} (as previously discussed). Hence there is still a problem of including emission from other spatial regions not associated with the source. The next step is to define a summation aperture.

4.3.3 Aperture Definition

For a single source the above procedures can easily be compared and either individually fitting each spectra with a Gaussian profile or integrating each within a velocity range results in comparable masses. However, for a large sample the individual selection and checking of spectra for Gaussian fitting or integration is inefficient. Instead of extracting each individual spectra the entire data cube can be integrated within the selected velocity limit to produce an integrated intensity map. A spatial mask to sum over the extent of the C^{18}O emission associated with the core can then be established. This negates having to manually sieve through all the spectra in order to check that emission is associated with the source prior to the integration or fitting of the spectra. The map shown in the left plot of Figure
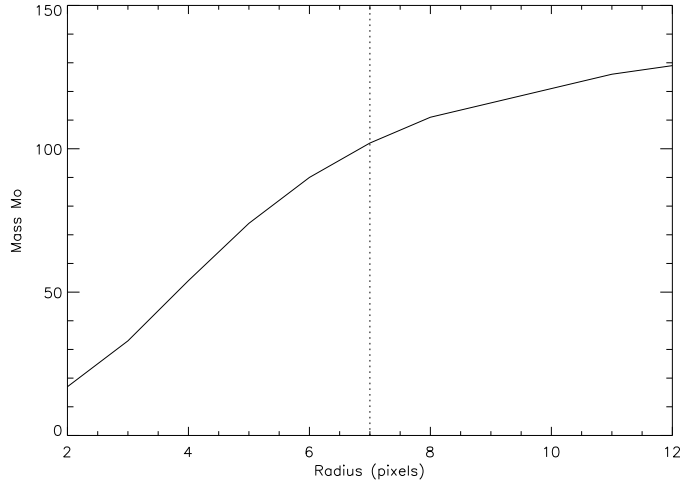
Figure 4.2: Mass plotted against radius for apertures ranging from 2 to 12 pixels in size for IRAS 20126+4104. The solid line indicates the mass at a given aperture radius from the integrated map. A break in the slope is apparent around a 7 pixel radius.

4.1 is integrated between the established velocity limits (-5.7 to -1.1 km s^{-1}).

Emission free regions are investigated to find the map noise. For IRAS 20126+4104 the noise level $1\sigma_{MAP}$ is 0.6 K km s^{-1}. The $3\sigma_{MAP}$ level contour is used to define the edge of emission and create an aperture mask. Note, the aperture mask is not circular in shape, it is a polygon tracing the $3\sigma_{MAP}$ contour level. This means that the mass can be calculated for any geometry. The mass summed within the aperture is 108 ± 3 M$_\odot$, in agreement with both previous estimates from Gaussian fitting and spectral integration methods. The slightly larger mass recovered is due to pixels/spectra that did not previously meet the cutoff limits. Here no cut off limits are imposed before integration. This aperture integration method gives an equally reliable result and significantly reduces analysis and checking time. This method is the easiest to conduct on a large sample.

As a consistency check, because IRAS 20126+4104 is a roughly circular core, the mass in a circular aperture that touches the the $3\sigma_{MAP}$ level contour is estimated. This mass is 106 ± 5 M$_\odot$. The slight reduction in mass is attributed to missing the extended material to the south of the image. As a second check the mass is calculated in increasing radii circular apertures centred about the brightest pixel. The simple circular shape of the IRAS 20126+4104 core facilitates the aperture analysis. A turnover (decrease) in the mass increase rate is found at around a $\sim$ 7 pixel aperture radius. This is interpreted as the edge of the core. There is no immediate edge visually apparent in the integrated map, however, the aperture radius found closely matches the size of the $3\sigma_{MAP}$ contour level. At 1.7 kpc this would make the core radius $\sim$ 0.4 pc in size. The break in the slope of mass versus radius is shown in Figure 4.2. The mass calculated within a 7 pixel radius circular aperture is 103 ± 11 M$_\odot$. The associated uncertainty here is that propagated from the uncertainty in the aperture radius if varied by 1 pixel (i.e. $\pm$ 7" in radius). Aperture radii of 6 and 8 pixels are the two extreme sizes that can be considered to mark the position of the break in the slope in Figure 4.2. The uncertainty due to the noise in the integrated map is $\sim$ 2-3 M$_\odot$. The final consistency check is to ensure the velocity definition does not miss any mass. As the aperture is defined, a summed spectra can be extracted from the data cube (as introduced in Section 4.3.1). The high signal to noise spectra is clearly Gaussian in profile and can easily be fitted (Figure 4.3). The resulting mass is 103 ± 4 which is consistent with all other estimates.

Table 4.1 indicates the masses calculated between the various methods. These are all consistent within the typical few percent uncertainties. The largest uncertainty from the aperture methods is from the variable annulus apertures. The final

Table 4.1: Masses for IRAS 20126+4104 calculated via the different methods as detailed in the text.

Method	Mass
	$(M_\odot)$
Gaussian Fitting	101±29
Integrated Spectra	102±3
Circular Aperture	106±5
Polygon Aperture	108±3
Variable Aperture	103±11
Summed Spectra	103±4
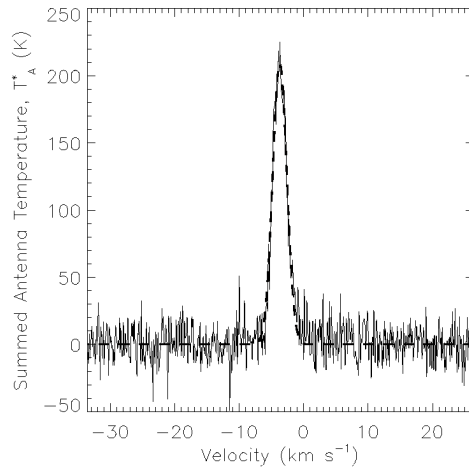
Figure 4.3: The summed $C^{18}O$ spectra of IRAS 20126+4104 created by the summation of all spectra extracted from within the polygon aperture. The resultant spectra has a high signal to noise and is clearly Gaussian in shape.

adopted polygon aperture method is easily repeatable and applicable to multiple sources. Furthermore, such analysis can be applied to various morphologies of any line tracers, e.g. ^{12}CO emission tracing outflows. Although source radii can be assumed these are dependent upon the sensitivity limits of the observations and are relevant to the core size of $C^{18}O$ emission at the flux cutoff level only (see Section 4.4.6).

For IRAS 20126+4104 Shepherd *et al.* (2000) calculate a molecular core mass associated with their interferometric $C^{18}O$ 1-0 observations of 104 $M_{\odot}$. The estimate from the polygon aperture is in excellent agreement with this value, indicating that the optically thin and LTE assumptions used in both works are applicable to both (3-2) and (1-0) line transitions of $C^{18}O$. Interestingly, at a few arcseconds resolution the interferometer does not resolve out a significant amount of the emission (if any). The mass is below that calculated from the NH_3 (1,1) and (2,2) observations of Estalella *et al.* (1993). They find a larger mass of 230 $M_{\odot}$, but the variations could be due to molecular abundances used. Interestingly, the $C^{18}O$ mass found here is in agreement with their virial mass, although they find a smaller line width and use a different flux level to identify the core size.

4.4 $C^{18}O$ Masses

The polygon aperture method is now applied to the other 98 sources, and is also re-applied to IRAS 20126+4104 (G078.1224+03.6320) where the revised distance from the RMS database is used. Table 4.2 lists all the sources, positions and important parameters extracted from the RMS database. For all sources the masses are calculated as per Equation 4.1 but note that $^{16}O/^{18}O$ is varied according to the

relationship $58.8 \times D_{GC}(\mathrm{kpc}) + 37.1$ (Wilson & Rood, 1994). A summed spectra is also taken from each source once the polygon aperture has been defined and a mass is also estimated from Gaussian fitting.

Upon investigation of the data cubes all but 5 sources have strong $\mathrm{C}^{18}\mathrm{O}$ emission above three times the $1\sigma_{T_A^*}$ spectral noise level. 4 of these 5 sources (G023.6566-00.1273, G094.3228-00.1671, G108.4717-02.8176 and G125.7795+01.7285) are YSOs and have emission above the $1\sigma_{T_A^*}$ spectral noise level whereas the other source (G049.5531-00.3302) is a HII region and does not have any obvious $\mathrm{C}^{18}\mathrm{O}$ emission. It is quite possible that an evolved HII region would have no emission as winds and outflows may have blown away any remaining core material. This could be the case for G049.5531-00.3302. For the 4 sources with no emission above the $3\sigma_{T_A^*}$ spectral noise level the velocity width is defined at the $1\sigma_{T_A^*}$ level. In any further analysis mass and velocity parameters will be used with caution as the integration range may be over estimated. 3 of these 4 sources have spectral noise levels around 1.0 K and are the largest noise values found for all observations. This explains why emission is not above $3\sigma_{T_A^*}$. Furthermore, these 4 sources show some evidence for outflow activity which could be dispersing the cores. Re-binning of the $\mathrm{C}^{18}\mathrm{O}$ data could be undertaken to approximately 1 km s^{-1} to improve the signal to noise, however, this resolution does not match that of the outflow observations (see Chapter 5) and could lead to uncertainties in the outflow mass estimates at later stages.

The intrinsic spectral noise of the 0.423 km s^{-1} resolution data, integration velocity limits, map noise, aperture masses and the centroid and FWHM from the Gaussian fitting of the summed spectra are listed in Table 4.3. A column flag indicates whether the source masses are the ones used in further analysis of if they

Table 4.2: Table of source parameters for all sources in the sample. Parameters are taken directly from the RMS survey online archive. Luminosities rounded to nearest 100 $L_\odot$.

RMS Source Name	RA. (J2000)	DEC. (J2000)	Type	V_{LSR} (km s^{-1})	Distance (kpc)	Luminosity ($L_\odot$)	IRAS source (offset)	Other Associations
G010.8411-02.5919	18:19:12.09	-20:47:30.90	YSO	11.4	1.9	23700	18162-2048 (4")	GGD27
G012.0260-00.0317	18:12:01.88	-18:31:55.70	YSO	110.6	11.1	23600	18090-1832 (3")	...
G012.9090-00.2607	18:14:39.56	-17:52:02.30	YSO	35.8	2.4	21700	18117-1753 (11")	W33A
G013.6562-00.5997	18:17:24.38	-17:22:14.80	YSO	48.0	4.1	9000	18144-1723 (2")	...
G017.6380+00.1566	18:22:26.37	-13:30:12.00	YSO	22.5	2.2	53200	18196-1331 (11")	...
G018.3412+01.7681	18:17:58.11	-12:07:24.80	YSO	32.8	2.9	21800	18151-1208 (16")	...
G020.7438-00.0952	18:29:17.00	-10:52:21.40	HII	59.5	11.8	91600	...	GRS G020.79-00.06
G020.7491-00.0898	18:29:16.39	-10:52:01.20	HII	59.5	11.8	90400	...	GRS G020.79-00.06
G020.7617-00.0638	18:29:12.25	-10:50:34.00	YSO	57.8	11.8	17600	...	GRS G020.79-00.06
G023.3891+00.1851	18:33:14.32	-08:23:57.40	YSO	75.4	4.5	42000	18305-0826 (6")	GRS G023.64+00.14
G023.6566-00.1273	18:34:51.56	-08:18:21.60	YSO	81.1	3.2	6200	18321-0820 (6")	GRS G023.34-00.21
G023.7097+00.1701	18:33:53.40	-08:07:20.60	HII	112.6	7.7	128800	1831-0909 (8")	GRS G024.24+00.24 / WC89 G23.71
G025.4118+00.1052	18:37:16.92	-06:38:29.80	YSO	95.6	5.2	7100	18345-0641 (8")	GRS G025.44-00.16
G025.7161+00.0486	18:38:02.80	-06:23:47.30	HII	100.7	9.8	77800	...	GRS G025.74+00.19
G028.2007-00.0494	18:42:58.11	-04:13:57.90	HII	98.1	9.5	414000	18403-0417 (4")	GRS G028.19-00.06
G028.2875-00.3639	18:44:15.09	-04:17:55.20	HII	47.7	11.6	2612400	...	GRS G027.99-00.46
G028.3046-00.3871	18:44:21.96	-04:17:39.50	YSO	84.9	10.0	38500	...	...
G030.1981-00.1691	18:47:03.06	-02:30:36.10	YSO	103.0	7.3	33300	...	GRS G030.29-00.21
G030.5942-00.1273	18:47:37.53	-02:08:19.60	YSO	84.4	4.9	4400	...	GRS G030.14-00.06
G030.6877-00.0729	18:47:36.15	-02:01:50.70	HII	93.4	4.9	49300	...	GRS G030.54-00.06
G030.7206-00.0826	18:47:41.79	-02:00:23.60	HII	93.4	4.9	28100	...	GRS G030.54-00.06
G030.8185+00.2729	18:46:36.58	-01:45:22.40	YSO	97.7	4.9	7800	18440-0148 (4")	GRS G031.04+00.29
G033.3891+00.1989	18:51:33.82	00.29:51.0	YSO	85.8	5.0	10200	18490+0026 (5")	GGD30 IRS3
G037.5536+00.2008	18:59:09.94	04:12:15.60	YSO	84.9	6.7	38100	18566+0408 (2")	GRS G037.54+00.19
G043.9956-00.0111	19:11:51.64	09:49:40.40	YSO	65.0	6.0	16400	19094+0944 (8")	GRS G044.34-00.21

Table 4.2: Table of source parameters for all sources in the sample. Parameters are taken directly from the RMS survey online archive. Luminosities rounded to nearest 100 L$_\odot$ - continued

RMS Source Name	RA. (J2000)	DEC. (J2000)	Type	V$_{LSR}$ (km s^{-1})	Distance (kpc)	Luminosity (L$_\odot$)	IRAS source (offset)	Other Associations
G045.0711+00.1325	19:13:22.10	10:50:53.40	HII	59.0	4.4	159800	19110+1045 (1")	GRS G045.14+00.14
G048.9897-00.2992	19:22:26.66	14:06:46.20	YSO	68.8	5.4	10500	19201+1400 (6")	GRS G048.94-00.26 / W51 complex
G049.5531-00.3302	19:23:38.85	14:35:33.00	HII	62.0	5.4	17900	...	GRS G049.44-00.06 / W51 complex
G050.2213-00.6063	19:25:57.77	15:02:59.60	YSO	41.2	3.3	4500	19236+1456 (3")	GRS G050.24-00.61
G053.5343-00.7943	19:33:16.40	17:52:04.80	YSO	58.3	5.0	7100	19310+1745 (6")	GRS G053.14-00.66
G053.9584+00.0317	19:31:05.22	18:38:16.80	HII	41.6	4.9	17900	19288+1831 (8")	...
G073.0633+01.7958	20:08:10.08	35:59:24.00	YSO	0.7	1.4	1600	20062+3550 (7")	...
G075.7666+00.3424	20:21:40.84	37:25:35.90	YSO	0.0	1.4	4900	20198+3716 (4")	...
G077.9550+00.0058	20:29:31.76	39:01:20.70	HII	-4.2	1.4	1500	...	...
G077.9637-00.0075	20:29:36.72	39:01:21.90	HII	-2.9	1.4	12900	...	...
G078.1224+03.6320	20:14:26.30	41:13:31.40	YSO	-3.6	1.4	4000	20126+4104 (3")	...
G078.8867+00.7087	20:29:24.86	40:11:19.40	YSO	-5.7	3.3	185400	20275+4001 (10")	GL2591
G079.1272+02.2782	20:23:23.83	41:17:39.30	YSO	-2.0	1.4	1800	20216+4107 (1")	...
G079.8749+01.1821	20:30:27.47	41:15:59.00	HII	-3.8	1.4	4600	20286+4106 (13")	..
G080.8624+00.3827	20:37:00.93	41:34:55.80	YSO	-1.6	1.4	1200	20352+4124 (7")	...
G080.8645+00.4197	20:36:52.16	41:36:24.00	HII	-3.1	1.4	16300	20350+4126 (10")	DR20
G080.9383-00.1268	20:39:25.91	41:20:01.60	HII	-1.2	1.4	20000	...	...
G081.7131+00.5792	20:38:57.19	42:22:40.90	YSO	-3.6	1.4	4600	...	...
G081.7133+00.5589	20:39:02.54	42:21:58.30	HII	-3.8	1.4	1800	...	...
G081.7220+00.5699	20:39:01.01	42:22:50.20	HII	-4.7	1.4	400	...	DR21 OH
G081.7522+00.5906	20:39:01.98	42:24:59.10	YSO	-4.1	1.4	1700	...	....
G081.7624+00.5916	20:39:03.72	42:25:29.6	YSO	-4.4	1.4	700	...	...
G081.8652+00.7800	20:38:35.36	42:37:13.70	YSO	10.1	1.4	3400	...	...
G081.8789+00.7822	20:38:37.71	42:37:58.60	HII	9.8	1.4	21000	...	...

Table 4.2: Table of source parameters for all sources in the sample. Parameters are taken directly from the RMS survey online archive. Luminosities rounded to nearest 100 $L_\odot$ - continued

RMS Source Name	RA. (J2000)	DEC. (J2000)	Type	V_{LSR} (km s^{-1})	Distance (kpc)	Luminosity ($L_\odot$)	IRAS source (offset)	Other Associations
G083.0936+03.2724	20:31:35.44	45:05:45.80	HII	-3.0	1.4	12300	...	...
G083.7071+03.2817	20:33:36.51	45:35:44.00	YSO	-3.2	1.4	3900	...	...
G083.7962+03.3058	20:33:48.02	45:40:54.50	HII	-3.7	1.4	4800	...	...
G085.4102+00.0032	20:54:14.36	44:54:04.50	YSO	-36.5	5.5	20500	...	...
G094.3228-00.1671	21:31:45.11	51:15:35.30	YSO	-38.5	4.4	5700	21300+5102 (2")	CPM15
G094.4637-00.8043	21:35:09.11	50:53:09.60	YSO	-44.5	5.0	20800	21334+5039 (3")	...
G094.6028-01.7966	21:39:58.25	50:14:20.90	YSO	-43.9	4.9	43300	21381+5000 (5")	V645Cyg
G100.3779-03.5784	22:16:10.35	52:21:34.70	YSO	-37.5	3.7	17300	22142+5206 (9")	CPM37
G103.8744+01.8558	22:15:09.08	58:49:07.80	YSO	-18.3	1.6	4600	22134+5834 (4")	...
G105.5072+00.2294	22:32:23.99	58:18:58.30	YSO	-52.3	4.6	9600	22305+5803 (4")	S138 complex
G105.6270+00.3388	22:32:45.57	58:28:18.30	HII	-52.1	4.5	48500	22308+5812 (3")	S138 complex
G107.6823-02.2423	22:55:29.82	57:09:24.90	YSO	-55.1	4.7	4100	22534+5653 (3")	...
G108.4714-02.8176	23:02:32.07	56:57:51.30	YSO	-53.9	4.5	5100	...	...
G108.7575-00.9863	22:58:47.25	58:45:01.60	YSO	-50.8	4.3	12900	22566+5828 (14")	...
G109.0775-00.3524	22:58:58.08	59:27:36.40	YSO	-48.3	4.0	2200	...	...
G109.0974-00.3458	22:59:05.52	59:28:23.20	HII	-46.7	3.8	23400	22570+5912 (3")	...
G109.8715+02.1156	22:56:17.97	62:01:54.40	YSO	-11.1	0.7	8400	22543+6145 (9")	Cep A2
G110.0931-00.0641	23:05:24.16	60:08:15.40	YSO	-53.1	4.4	11800	23033+5951 (5")	S156 complex
G110.1082+00.0473	23:05:10.16	60:14:47.70	HII	-50.2	4.3	35600	23030+5958 (6")	S156 complex
G111.2348-01.2385	23:17:21.01	59:28:48.00	YSO	-54.4	4.4	41900	23151+5912 (4")	...
G111.2552-00.7702	23:16:10.39	59:55:28.20	YSO	-44.7	3.6	9900	23139+5939 (8")	...
G111.5234+00.8004	23:13:32.39	61:29:06.20	YSO	-58.0	2.7	11500	...	NGC7538 IRS4
G111.5320+00.7593	23:13:43.91	61:26:57.70	YSO	-57.4	2.7	3900	...	NGC7538S IRS11
G111.5423+00.7776	23:13:45.36	61:28:10.30	HII	-57.2	2.7	152200	23116+6111 (5")	NGC7538 IRS1
G111.5671+00.7517	23:14:01.75	61:27:19.80	YSO	-57.2	2.7	44600	23118+6110 (4")	NGC7538 IRS9

Table 4.2: Table of source parameters for all sources in the sample. Parameters are taken directly from the RMS survey online archive. Luminosities rounded to nearest 100 $L_\odot$ - continued

RMS Source Name	RA. (J2000)	DEC. (J2000)	Type	V_{LSR} (km s^{-1})	Distance (kpc)	Luminosity ($L_\odot$)	IRAS source (offset)	Other Associations
G111.5851+00.7976	23:14:01.71	61:30:17.80	YSO	-56.5	2.7	5300	...	...
G114.0835+02.8568	23:28:27.76	64:17:38.40	YSO	-53.2	4.2	7100	23262+6401 (5")	...
G125.6045+02.1038	01:16:36.21	64:50:38.40	YSO	-53.7	4.1	1700	01133+6434 (5")	...
G125.7795+01.7285	01:17:53.03	64:27:14.30	YSO	-64.5	5.2	5500	01145+6411 (14")	CPM4
G132.1570-00.7241	02:08:05.02	60:46:02.80	HII	-55.6	4.5	20200	02044+6031 (6")	...
G133.6945+01.2166	02:25:30.99	62:06:20.90	YSO	-44.2	2.0	28500	... W3_IRS4	
G133.7150+01.2155	02:25:40.77	62:05:52.40	YSO	-38.7	2.0	206400	02219+6152 (19")	W3 complex
G133.9476+01.0648	02:27:03.85	61:52:24.60	HII	-48.1	2.0	82600	02232+6138 (25")	W3 complex
G134.2792+00.8561	02:29:01.93	61:33:30.50	YSO	-51.5	2.0	3000	02252+6120 (2")	W3 complex
G136.3833+02.2666	02:50:08.57	61:59:52.10	YSO	-42.4	3.3	6600	02461+6147 (5")	...
G138.2957+01.5552	03:01:31.32	60:29:13.20	YSO	-38.0	2.9	14200	02575+6017 (5")	AFGL4029
G139.9091+00.1969	03:07:24.52	58:30:43.30	YSO	-39.5	3.2	10900	03035+5819 (13")	GL437S
G141.9996+01.8202	03:27:38.76	58:47:00.10	YSO	-13.9	0.8	1300	03236+5836 (4")	GL490
G142.2446+01.4299	03:27:31.37	58:19:21.80	HII	-46.7	4.2	15600	03235+5808 (2")	...
G148.1201+00.2928	03:56:15.36	53:52:13.00	YSO	-34.0	3.2	3900	03523+5343 (1")	...
G192.5843-00.0417	06:12:53.57	+18:00:26.3	HII	8.8	2.0	2400	...	S255N
G192.6005-00.0479	06:12:54.01	17:59:23.10	YSO	7.4	2.0	35600	06099+1800 (10")	S255IR
G194.9259-01.1946	06:13:21.11	15:23:57.10	HII	16.3	2.0	2500	06104+1524A (3")	...
G194.9349-01.2224	06:13:16.14	15:22:43.30	YSO	15.9	2.0	2600	06103+1523 (16")	...
G196.4542-01.6777	06:14:37.06	13:49:36.40	YSO	18.0	5.3	94000	06117+1350 (6")	S269 IRS2
G203.3166+02.0564	06:41:10.12	09:29:33.70	YSO	7.4	0.6	1100	06384+0932 (13")	GL989
G207.2654-01.8080	06:34:37.74	04:12:44.20	HII/YSO	12.6	1.0	2300	06319+0415 (2")	GL961
G212.0641-00.7395	06:47:13.36	00:26:06.50	YSO	45.0	4.7	13800	06446+0029 (7")	...
G233.8306-00.1803	07:30:16.72	-18:35:49.10	YSO	44.6	3.3	10400	07280-1829 (2")	...
G234.6358+00.8281	07:35:38.97	-18:48:51.40	HII	46.8	3.5	10500	07334-1842 (29")	...

are estimates due to confused or merged sources. The flags are described below. The integrated images, polygon apertures and summed Gaussian spectra of all the 99 sources are presented in Appendix B.

Following the integration, 3 sources (G049.5531-00.3302, G108.4714-02.8176, G125.7795+01.7285) have no emission above three times the $1\sigma_{MAP}$ noise level and no apertures for mass calculation are defined. The sources are a sub set of the 5 sources with weak spectral emission and are flagged as (n). The HII regions G077.9637-00.0075 and G080.9383-00.1268 are also flagged as (n). Although masses are calculated for these two sources the emission is surrounding the RMS source and is not considered to be associated with it. The morphology suggests the material located at the source position has been blown away or eroded.

There are strange morphologies of the integrated $C^{18}O$ emission for a number of sources. Some maps indicate extended faint/weak filamentary emission far from the RMS source location. In the extreme cases the size of the polygon aperture is restricted to exclude the contribution from these regions to the mass estimate and impose a roughly circular aperture. Upon investigation the mass contribution from these extended regions are typically within the uncertainties of the mass estimates themselves. This is exemplified by the slight mass difference calculated for IRAS 20126+4104 within the circular aperture compared with the polygon aperture. The sources with masses calculated directly from within an aperture are flagged as (0) and those where filamentary extensions have been removed from the aperture are flagged as (1). All these source masses are used in the analysis stages.

Four MYSO sources have a least two peaks of emission very close together within a single core. The masses for each cannot be isolated and the entire core mass is measured in these cases. These sources are flagged as (2) and
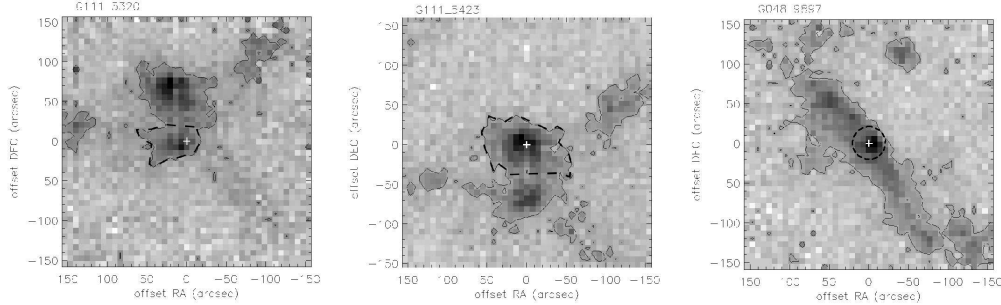
Figure 4.4: Left and Centre: Integrated intensity maps of the sources G111.5320+00.7593 and G111.5423+00.7776. The solid black line indicates the $3\sigma_{MAP}$ contour and the white cross indicates the RMS source location. Emission is summed within the polygon aperture tracing the $3\sigma_{MAP}$ contour level, as Figure 4.1, however the aperture is divided to split the sources in each case. The apertures summed within are indicated by the dashed black line. Right: Integrated intensity map of G048.9897-00.2992. The lines and symbols are the same as the left and centre figures, however here the aperture is a circle with a radius set where the aperture intersects the $3\sigma_{MAP}$ noise level.

the masses are not used in comparisons as they are overestimates. The sources G081.7131+00.5792, G081.7133+00.5589, G081.7220+00.5699, G081.7522+00.5906 and G081.7624+00.5916 are all part of the same large filamentary cloud complex where the emission is always above the $3\sigma_{MAP}$ noise limit. Their masses are arbitrarily summed within a 3 pixel diameter (slightly over 1 beam FWHM) and are lower limits. The masses calculated within these apertures are not used in future analysis.

There are also a number of sources that are not isolated and are joined to other regions of significant emission, not faint filamentary regions as the above sources flagged as (1). In these cases the emission is arbitrarily split midway between the sources in clear cut cases. Figure 4.4 depicts such a case. In more complex cases the aperture mask is defined as a circle centred upon the source. The radius is set as the shortest distance between the RMS source location and the $3\sigma_{MAP}$ noise

level. An example is also shown in Figure 4.4. In total there are 12 sources with masses defined in this manner and flagged as (4). Although most of the mass is likely associated with the most massive star in the core a cautious approach is taken and the masses are not used primarily in the analysis stages. In Table 4.3 there are also 7 sources flagged as (5). These sources fall into a range of the other flag categories dependant upon their mass estimates, however, they all have luminosity estimates that are not from multi-wavelength SED fitting. These sources are not used in mass and luminosity comparisons (see Section 4.4.4).

Overall there are 66 sources that are regarded as having good mass and luminosity estimates and are flagged as (0) or (1) sources.

Figure 4.5 plots the aperture method mass against the masses from a Gaussian fit of the spectra summed within the aperture masks. Note that for the particularly weak emission from G094.3228-00.1671 a suitable Gaussian fit cannot be attained and the mass is not estimated via this method for this source. The majority of masses from the two methods agree within uncertainties and supports the definition of the integrated velocity range. For a few sources the Gaussian fitting recovers significantly more mass than the summation within an aperture, the most prominent case being source G020.7438-00.0952. The aperture mask for this source overlaps with that of G020.7491-00.0898. Although the integration and summation method finds a narrow velocity width for G020.7438-00.0952, which acts to minimise the influence of the second source, the masses of each source are probably overestimates as there is still a spatial overlap at these velocities. Including G020.7438-00.0952 there are 8 sources in which the Gaussian mass is 50 per cent larger than that from the integration and summation method. The masses for G081.8652+00.7800 and G081.8789+00.7822 are regarded as upper limits in

Table 4.3: Table of spectral noise intrinsic to the 0.423 km s^{-1} resolution data, the integration limits and the map noise for all sources. The masses are listed from the polygon aperture method and the Gaussian summation fitting where applicable. These include uncertainties by variation of the integrated range for the map by one velocity bin at each the lower and upper velocity limits for the aperture method and those returned from the Gaussian fitting procedure respectively.

RMS Source Name	Type	Spectral (K)	Vel. Range (km s^{-1})	Map Noise (K km s^{-1})	FWHM (km s^{-1})	Centroid (km s^{-1})	Aperture Mass (M$_\odot$)	Gaussian Mass (M$_\odot$)	Flag
G010.8411-02.5919	YSO	0.56	(9.95,14.61)	0.9	1.89	12.16	226.8 ±3.2	219.7 ± 5.6	1
G012.0260-00.0317	YSO	0.9	(110.39,112.09)	0.98	3.16	110.94	80.6 ±21.5	141.4 ± 27.7	0
G012.9090-00.2607	YSO	0.42	(32.60,40.22)	1.11	4.41	36.35	360.9 ±9.0	374.1 ± 8.8	4
G013.6562-00.5997	YSO	0.96	(46.40,48.94)	1.07	3.06	47.81	36.1 ±6.6	48.6 ± 7.4	0
G017.6380+00.1566	YSO	0.42	(19.94,25.86)	0.77	2.58	22.31	259.4 ±5.4	251.6 ± 8.1	1
G018.3412+01.7681	YSO	0.47	(31.15,35.80)	0.85	2.32	32.76	352.6 ±10.9	357.4 ± 11.4	1
G020.7438-00.0952	HII	0.67	(59.99,60.80)	0.54	3.29	59.1	324.8 ±143.5	1338.9 ± 81.5	5
G020.7491-00.0898	HII	0.52	(56.14,62.07)	1.21	3.79	58.82	3316.1 ±138.0	3483.7 ± 207.7	5
G020.7617-00.0638	YSO	0.67	(55.30,58.26)	0.86	3.57	56.38	291.5 ±50.9	421.6 ± 47.6	0
G023.3891+00.1851	YSO	0.52	(73.75,76.71)	0.67	2.02	75.31	89.0 ±6.9	93.5 ±7.6	0
G023.6566-00.1273	YSO	0.73	(79.59,82.13)*	0.87	2.02	80.49	2.8 ±0.5	4.1 ± 1.5	0
G023.7097+00.1701	HII	0.91	(110.64,114.87)	1.34	3.9	112.8	705.0 ±55.3	831.4 ± 59.9	1
G025.4118+00.1052	YSO	0.65	(94.28,96.82)	0.84	2.22	95.53	41.5 ±3.9	47.3 ± 6.3	0
G025.7161+00.0486	HII	0.36	(98.51,102.75)	0.66	4.42	100.21	685.6 ±63.8	876.4 ± 45.5	0
G028.2007-00.0494	HII	0.36	(90.05,101.05)	1.03	4.78	95.84	2332.3 ±38.0	2253.7 ± 65.1	1
G028.2875-00.3639	HII	0.6	(45.13,50.63)	0.98	2.69	47.84	4784.4 ±162.6	4749.2 ± 174.3	0
G028.3046-00.3871	YSO	0.34	(81.65,88.00)	0.66	3.45	85.0	3201.9 ±58.8	3257.1 ± 86.6	0
G030.1981-00.1691	YSO	0.38	(100.89,105.55)	0.82	2.23	103.03	250.1 ±7.4	247.2 ± 11.0	4
G030.5942-00.1273	YSO	0.6	(84.00,85.27)	0.57	1.67	84.69	16.9 ±5.6	22.8 ± 4.0	0
G030.6877-00.0729	HII	0.86	(90.92,93.88)	1.07	3.45	92.19	264.5 ±40.8	351.1 ± 27.0	4
G030.7206-00.0826	HII	0.86	(90.50,96.00)	1.48	5.15	93.27	588.7 ±44.8	715.6 ± 32.4	4
G030.8185+00.2729	YSO	0.56	(97.25,99.36)	0.59	3.09	97.96	23.0 ±5.2	35.7 ± 5.3	0

Table 4.3: Table of spectral noise intrinsic to the 0.423 km s^{-1} resolution data, the integration limits and the map noise for all sources. The masses are listed from the polygon aperture method and the Gaussian summation fitting where applicable. These include uncertainties by variation of the integrated range for the map by one velocity bin at each the lower and upper velocity limits for the aperture method and those returned from the Gaussian fitting procedure respectively - continued.

RMS Source Name	Type	Spectral (K)	Vel. Range (km s^{-1})	Map Noise (K km s^{-1})	FWHM (km s^{-1})	Centroid (km s^{-1})	Aperture Mass (M$_\odot$)	Gaussian Mass (M$_\odot$)	Flag
G033.3891+00.1989	YSO	0.71	(83.96,86.08)	0.91	2.06	85.37	55.1 ±9.4	67.2 ± 8.8	0
G037.5536+00.2008	YSO	0.79	(84.14,85.41)	0.76	3.45	84.91	60.4 ±21.7	135.2 ± 22.0	0
G043.9956-00.0111	YSO	0.57	(64.17,66.71)	0.67	2.05	65.23	164.4 ±20.1	183.7 ± 16.8	0
G045.0711+00.1325	HII	0.64	(53.46,63.19)	1.57	5.39	58.95	447.1 ±8.8	464.3 ± 21.0	0
G048.9897-00.2992	YSO	0.50	(64.72,70.65)	0.85	4.36	67.65	418.7 ±23.9	463.6 ± 20.2	4
G049.5531-00.3302	HII	0.59	...	...	...	...	...		n
G050.2213-00.6063	YSO	0.64	(38.44,42.68)	0.88	3.68	40.72	142.1 ±11.0	160.5 ± 11.8	0
G053.5343-00.7943	YSO	0.49	(57.47,59.59)	0.55	2.05	58.38	25.6 ±4.2	30.3 ± 6.2	0
G053.9584+00.0317	HII	0.72	(40.06,43.44)	0.94	3.18	41.61	132.7 ±15.0	154.1 ± 15.3	0
G073.0633+01.7958	YSO	0.48	(-0.21,1.91)	0.56	1.63	0.75	5.9 ±0.6	6.5 ± 0.7	0
G075.7666+00.3424	YSO	0.49	(-4.87,1.48)	1.02	3.56	-1.21	61.1 ±1.8	63.5 ± 2.2	4
G077.9550+00.0058	HII	0.62	(-4.87,-2.76)	0.75	1.71	-3.76	16.4 ±2.1	17.7 ± 1.6	0
G077.9637-00.0075	HII	0.62	(-4.03,-2.76)	0.57	1.9	-3.15	11.2 ±4.0	17.0 ± 2.1	n
G078.1224+03.6320	YSO	0.40	(-5.72,-1.07)	0.67	2.57	-3.73	75.3 ±1.8	75.2 ± 2.7	0
G078.8867+00.7087	YSO	0.39	(-10.38,-1.91)	0.84	3.4	-5.94	718.7 ±8.6	688.2 ± 18.2	0
G079.1272+02.2782	YSO	0.36	(-3.60,0.21)	0.55	1.69	-1.57	31.7 ±1.0	31.1 ± 1.4	0
G079.8749+01.1821	HII	0.46	(-6.41,-0.91)	0.79	2.74	-4.08	117.5 ±1.8	120.3 ± 4.1	0
G080.8624+00.3827	YSO	0.44	(-4.86,1.06)	0.8	2.18	-1.56	78.7 ±0.8	76.0 ± 2.9	1
G080.8645+00.4197	HII	0.44	(-5.29,0.22)	0.76	2.29	-2.86	89.2 ±1.3	89.5 ± 3.0	1
G080.9383-00.1268	HII	0.42	(-2.11,-1.27)	0.3	1.53	-2.35	24.7 ±10.0	52.9 ± 2.0	n
G081.7131+00.5792	YSO	0.42	(-6.13,0.22)	0.81	3.06	-3.55	13.1 ±0.4	13.0 ± 0.6	3
G081.7133+00.5589	HII	0.42	(-6.13,-1.48)	0.75	2.62	-3.32	11.6 ±0.5	11.8 ± 0.5	3
G081.7220+00.5699	HII	0.42	(-7.83,1.91)	1.05	4.69	-3.4	33.0 ±0.3	33.4 ± 0.7	3

Table 4.3: Table of spectral noise intrinsic to the 0.423 km s^{-1} resolution data, the integration limits and the map noise for all sources. The masses are listed from the polygon aperture method and the Gaussian summation fitting where applicable. These include uncertainties by variation of the integrated range for the map by one velocity bin at each the lower and upper velocity limits for the aperture method and those returned from the Gaussian fitting procedure respectively - continued.

RMS Source Name	Type	Spectral (K)	Vel. Range (km s^{-1})	Map Noise (K km s^{-1})	FWHM (km s^{-1})	Centroid (km s^{-1})	Aperture Mass (M$_\odot$)	Gaussian Mass (M$_\odot$)	Flag
G081.7522+00.5906	YSO	0.38	(-6.55,-1.05)	0.66	2.43	-4.06	15.3 ±0.3	15.3 ± 0.4	3
G081.7624+00.5916	YSO	0.38	(-6.98,-2.32)	0.63	2.23	-4.42	11.6 ±0.2	11.6 ± 0.4	3
G081.8652+00.7800	YSO	0.73	(7.26,13.61)	1.45	3.29	9.84	336.1 ±10.4	347.5 ± 10.3	5
G081.8789+00.7822	HII	0.73	(6.84,11.92)	1.31	3.3	9.88	331.9 ±15.9	355.7 ± 10.9	5
G083.0936+03.2724	HII	0.48	(-4.65,-1.27)	0.66	1.76	-3.25	37.4 ±1.5	37.5 ± 1.7	0
G083.7071+03.2817	YSO	0.46	(-5.22,-1.83)	0.71	2.68	-2.98	107.4 ±11.0	123.5 ± 4.3	2
G083.7962+03.3058	HII	0.37	(-6.69,-0.76)	0.68	4.09	-3.4	59.9 ±2.6	64.8 ± 2.7	1
G085.4102+00.0032	YSO	0.49	(-39.33,-33.41)	0.91	3.66	-36.54	446.1 ±14.0	466.6 ± 45.1	0
G094.3228-00.1671	YSO	0.85	(-40.72,-33.94)*	1.68	3.66	-39.42	17.1 ±1.1	2.2 ± 1.8	0
G094.4637-00.8043	YSO	0.56	(-46.33,-43.36)	0.74	2.57	-44.92	173.7 ±19.6	197.4 ± 19.0	0
G094.6028-01.7966	YSO	0.45	(-45.51,-41.70)	0.7	2.34	-43.96	212.7 ±10.3	226.7 ± 17.5	0
G100.3779-03.5784	YSO	0.41	(-38.60,-36.06)	0.48	1.61	-37.37	76.3 ±5.4	78.7 ± 6.3	0
G103.8744+01.8558	YSO	0.82	(-19.86,-16.89)	1.06	1.71	-18.37	41.3 ±2.4	42.3 ± 3.7	0
G105.5072+00.2294	YSO	0.51	(-54.80,-50.57)	0.79	2.42	-52.23	115.3 ±0.4	120.9 ± 20.1	0
G105.6270+00.3388	HII	0.46	(-54.65,-49.57)	0.84	3.44	-51.9	358.6 ±16.1	393.9 ± 25.3	0
G107.6823-02.2423	YSO	0.41	(-56.48,-54.37)	0.4	1.4	-55.33	84.6 ±8.0	89.8 ± 8.9	0
G108.4714-02.8176	YSO	0.94	(-56.55,-52.31)*	1.19	...	...	...	...	n
G108.7575-00.9863	YSO	0.41	(-52.96,-48.31)	0.71	2.43	-50.98	2133.8 ±55.0	2139.1 ± 56.5	2
G109.0775-00.3524	YSO	0.42	(-49.02,-46.48)	0.56	2.59	-47.6	117.7 ±20.8	153.4 ± 16.8	1
G109.0974-00.3458	HII	0.42	(-47.75,-43.94)	0.73	1.94	-45.74	258.9 ±6.9	261.3 ± 14.0	0
G109.8715+02.1156	YSO	0.42	(-16.57,-4.29)	1.43	3.61	-10.64	157.6 ±0.9	152.8 ± 2.7	2
G110.0931-00.0641	YSO	0.41	(-55.29,-51.09)	0.62	2.68	-53.08	409.5 ±23.3	429.1 ± 22.4	1
G110.1082+00.0473	HII	0.69	(-50.63,-49.36)	0.65	2.1	-50.2	227.7 ±73.2	344.7 ± 27.7	0

Table 4.3: Table of spectral noise intrinsic to the 0.423 km s^{-1} resolution data, the integration limits and the map noise for all sources. The masses are listed from the polygon aperture method and the Gaussian summation fitting where applicable. These include uncertainties by variation of the integrated range for the map by one velocity bin at each the lower and upper velocity limits for the aperture method and those returned from the Gaussian fitting procedure respectively - continued.

RMS Source Name	Type	Spectral (K)	Vel. Range (km s^{-1})	Map Noise (K km s^{-1})	FWHM (km s^{-1})	Centroid (km s^{-1})	Aperture Mass (M$_\odot$)	Gaussian Mass (M$_\odot$)	Flag
G111.2348-01.2385	YSO	0.49	(-56.48,-52.67)	0.87	2.48	-54.7	189.7 ±13.8	200.8 ± 16.5	0
G111.2552-00.7702	YSO	0.41	(-47.11,-42.03)	0.68	2.29	-44.37	206.8 ±5.8	200.1 ± 12.4	0
G111.5234+00.8004	YSO	0.62	(-59.93,-56.12)	0.81	3.02	-57.99	354.5 ±26.5	400.1 ± 19.8	4
G111.5320+00.7593	YSO	0.81	(-59.64,-53.72)	2.0	4.35	-56.35	353.9 ±16.6	389.6 ± 21.4	4
G111.5423+00.7776	HII	0.96	(-61.05,-53.43)	1.93	4.4	-56.92	1079.9 ±30.1	1133.7 ± 43.9	4
G111.5671+00.7517	YSO	1.03	(-57.45,-56.18)	1.25	4.4	-57.34	10.6 ±4.4	23.6 ± 5.3	0
G111.5851+00.7976	YSO	0.40	(-57.74,-55.63)	0.46	1.54	-56.49	17.8 ±1.9	18.7 ± 2.0	4
G114.0835+02.8568	YSO	0.46	(-54.46,-52.35)	0.48	1.51	-53.49	52.0 ±4.0	52.8 ± 7.8	0
G125.6045+02.1038	YSO	0.52	(-54.44,-53.17)	0.48	1.74	-53.64	27.1 ±7.7	37.2 ± 5.7	0
G125.7795+01.7285	YSO	0.55	(-64.64,-62.95)*	0.57	...	...	...	...	n
G132.1570-00.7241	HII	0.52	(-57.10,-53.71)	0.61	3.0	-55.24	133.5 ±13.3	152.0 ± 19.3	0
G133.6945+01.2166	YSO	0.54	(-48.89,-40.00)	1.42	6.95	-42.02	1253.4 ±73.5	1698.8 ± 37.1	5
G133.7150+01.2155	YSO	0.54	(-42.97,-33.23)	1.5	5.57	-38.79	758.8 ±16.6	801.6 ± 21.5	5
G133.9476+01.0648	HII	.93	(-50.21,-44.29)	1.89	4.31	-47.32	497.7 ±21.4	549.6 ± 23.7	0
G134.2792+00.8561	YSO	0.57	(-52.75,-49.78)	0.84	1.51	-51.34	35.4 ±1.8	35.2 ± 2.9	0
G136.3833+02.2666	YSO	0.41	(-44.24,-40.43)	0.58	2.8	-42.1	51.7 ±3.0	58.8 ± 5.3	0
G138.2957+01.5552	YSO	0.41	(-41.28,-36.20)	0.73	1.98	-38.17	495.9 ±10.3	490.8 ± 14.8	0
G139.9091+00.1969	YSO	0.41	(-40.86,-37.89)	0.52	2.26	-39.84	653.1 ±72.0	744.0 ± 26.7	0
G141.9996+01.8202	YSO	0.38	(-16.15,-11.07)	0.7	2.32	-13.0	32.3 ±1.0	33.1 ± 1.0	0
G142.2446+01.4299	HII	0.38	(-48.09,-45.13)	0.51	1.9	-46.68	113.5 ±7.3	117.3 ± 10.9	0
G148.1201+00.2928	YSO	0.37	(-35.85,-33.31)	0.45	1.68	-34.39	160.4 ±13.5	170.8 ± 9.9	0
G192.5843-00.0417	HII	0.37	(5.85,11.35)	0.68	3.0	8.56	219.7 ±4.2	226.9 ± 6.7	4
G192.6005-00.0479	YSO	0.37	(4.58,11.35)	0.74	2.46	7.3	336.9 ±2.8	325.9 ± 6.2	4

Table 4.3: Table of spectral noise intrinsic to the 0.423 km s^{-1} resolution data, the integration limits and the map noise for all sources. The masses are listed from the polygon aperture method and the Gaussian summation fitting where applicable. These include uncertainties by variation of the integrated range for the map by one velocity bin at each the lower and upper velocity limits for the aperture method and those returned from the Gaussian fitting procedure respectively - continued.

RMS Source Name	Type	Spectral (K)	Vel. Range (km s^{-1})	Map Noise (K km s^{-1})	FWHM (km s^{-1})	Centroid (km s^{-1})	Aperture Mass (M$_\odot$)	Gaussian Mass (M$_\odot$)	Flag
G194.9259-01.1946	HII	0.47	(15.43,17.12)	0.47	1.34	16.38	35.6 ±5.2	37.5 ± 3.5	0
G194.9349-01.2224	YSO	0.47	(14.16,17.97)	0.65	2.9	15.97	41.8 ±2.9	44.8 ± 3.6	0
G196.4542-01.6777	YSO	0.41	(16.82,20.63)	0.6	3.38	18.18	478.8 ±46.1	589.0 ± 37.7	0
G203.3166+02.0564	YSO	0.57	(5.84,10.50)	0.8	2.97	7.86	82.2 ±3.2	86.6 ± 2.7	2
G207.2654-01.8080	HII/YSO	0.51	(11.07,14.88)	0.68	2.52	12.71	20.0 ±1.3	21.9 ± 1.6	0
G212.0641-00.7395	YSO	0.48	(43.32,45.86)	0.58	2.96	44.87	69.6 ±11.8	96.5 ± 12.6	0
G233.8306-00.1803	YSO	0.47	(43.44,46.40)	0.65	2.2	44.85	138.2 ±10.7	151.2 ± 11.5	0
G234.6358+00.8281	HII	0.51	(45.98,48.10)	0.56	1.71	46.68	37.6 ±6.3	43.5 ± 6.7	5

* - Integration velocity limits are from the $1\sigma_{T_A^*}$ level.

Mass flags follow the scheme:

0 - Masses calculated directly from within aperture tracing the $3\sigma_{MAP}$ level.

1 - Faint filamentary structures are not included in mass calculation and are outside the aperture.

2 - More than 2 cores very close within the aperture.

3 - Source mass estimated within a 3 pixel diameter aperture.

4 - Complex/multiple source regions and individual masses are not isolated.

5 - Luminosities are not from SED fitting.

n - No mass estimated or mass not associated directly with RMS source.
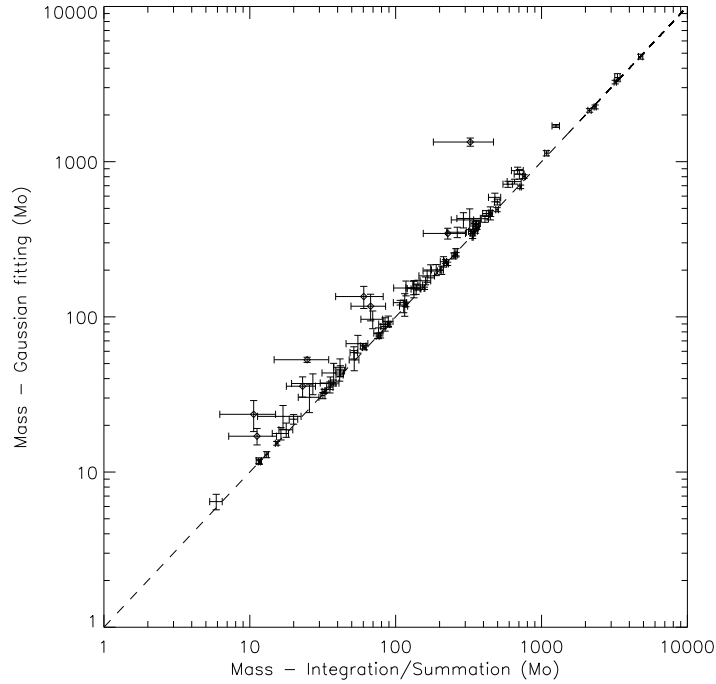
Figure 4.5: Comparison of the masses estimated from the integration and summation within a polygon aperture vs the mass calculated via fitting a Gaussian to the spectra summed within the same polygon aperture. In the majority of cases the masses are directly comparable. The dashed line is the line of equal mass.

both cases as the aperture masks overlap spatially and both the integration and summation masses and the Gaussian fitting masses will be overestimated.

4.4.1 Sample Completeness

The sample, as previously noted, was chosen to be a representative, distance limited sample of all MYSOs and HII regions from the RMS survey to date as of 2007. Figure 4.6 shows the distance versus luminosity for all 99 sources. Note, these values are taken from the RMS database and are listed in Table 4.2. There is a clear bias towards higher luminosities for the more distant sources ($>$ 6 kpc)

that were subsequently found to be further away than the initial criterion of the sample. These distant sources conform to the RMS survey luminosity completeness of 10^4 $L_\odot$ out to a distance of $\sim$ 14 kpc (Urquhart *et al.*, 2011a). However, to have the same luminosity completeness limit for the sources here would reduce the sample by more than a half. Instead, the distance is again limited to 6 kpc where the RMS survey is complete to $\sim 10^3$ $L_\odot$ CITEUrquhart2011. This leaves 87 sources in the sample for further analysis (depending on mass flags) for trends involving luminosity and to calculate outflow parameters at a later stage. There are no Malmquist biases for the sample as a broad range of luminosities and distances are probed and there is no emerging trend at this stage to indicate the more distant sources are the most luminous. The 87 source at distances $<$ 6 kpc are a representative sample of MYSOs and HII regions for luminosities $> 10^3$ $L_\odot$.

4.4.2 Continuum Masses

For comparison with the $C^{18}O$ core masses literature sub-millimetre continuum fluxes have been used and converted to dust masses. These are listed in Table 4.4. For dust emission that is optically thin the mass is calculated via:

$$M = \frac{g\, S_\nu\, d^2}{\kappa_\nu\, B_\nu(T_d)} \tag{4.2}$$

where S_ν is the source flux, g is the gas-to-dust ratio = 100, $B_\nu(T_d)$ is the Planck function for a black-body at dust temperature T_d, d is the distance to the source and κ_ν is the dust opacity coefficient. The dust opacity coefficients are calculated via $\kappa_\nu = \kappa_0\, (\nu/\nu_0)^\beta$, adopting $\kappa_0 = 1.0$ cm^2 g^{-1} at 250 GHz (Ossenkopf & Henning, 1994) and $\beta = 2$, as Beuther *et al.* (2002b). Although the dust temperatures
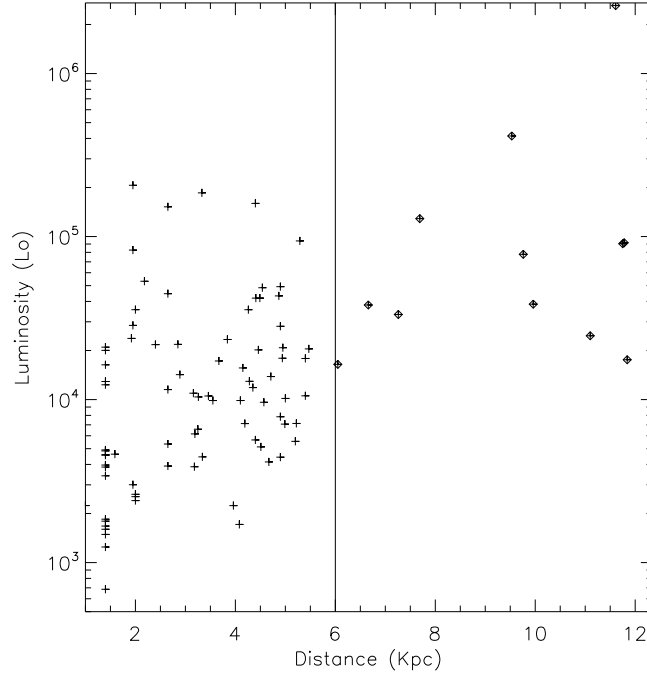
Figure 4.6: Comparison of the RMS distance and luminosities of the 99 sources. A clear divide is evident at 6 kpc where all sources under 10^4 $L_\odot$ are below the completeness limit of the RMS survey. 87 sources have distances < 6 kpc.

likely varies from source to source, for the purposes of a simple comparison the temperature is fixed at 40 K here for consistency with the temperature used to calculate the $C^{18}O$ masses.

The $C^{18}O$ masses are compared with those calculated from the 850 μm integrated fluxes from the SCUBA legacy survey (Di Francesco *et al.*, 2008), Bolocam 1.1 mm (http://irsa.ipac.caltech.edu/data/Bolocam_GPS/) integrated fluxes and other 1.2 mm observations from Beuther *et al.* (2002b); Faúndez *et al.* (2004); Hill *et al.* (2005). Figure 4.7 shows that the 850 μm SCUBA, 1.1 mm Bolocam and various 1.2 mm observations correlate with the $C^{18}O$ masses. There are slight offsets in some of the mass values themselves, as can be seen in Table 4.4. The Bolocam

masses are typically smaller than the $C^{18}O$ and SCUBA masses from the shorter wavelength observations. This is likely caused by the assumed temperature of the continuum emission. The continuum masses are dependent upon the temperature and dust opacity chosen and can easily vary by a factor of ~ 6 for a temperature change to 10 from 40 K (Hill *et al.*, 2005) for example. A temperature of 20 K may be more appropriate for the 1.1 mm dust that Bolocam detects. There are also a number of outlier sources where all the dust continuum masses are noticeably larger than the $C^{18}O$ masses. This could be due to different integration areas for the continuum and $C^{18}O$ emission as well as variations in temperature or dust opacity. As discussed in Section 3.3.5, the dust opacity used to model disc observations can vary by a factor of 20 depending upon the adopted grain types and sizes. On the larger scales probed here the overall grain properties should not have such an extreme range as they do for S140 IRS1 on scales probing a disc. However, when considering temperature variations, grain opacity changes and possibly different gas-to-dust ratios a mass discrepancy of a factor of 10 could easily be explained between the continuum masses and $C^{18}O$ masses before concluding that these cores are depleted of $C^{18}O$.

A Spearman correlation coefficient is undertaken for the $C^{18}O$ masses and both the SCUBA 850 μm and Bolocam masses where they have been calculated (regardless of $C^{18}O$ mass flag). As the sample size changes the reported correlation coefficients ρ will change while still representing a correlation at a given significance level. For example, a ρ value of 0.79 is required to reject the null hypothesis (no correlation) at the 0.01 significance level (also refereed to as P-value) for a sample of 10, whereas a ρ value of 0.36 rejects the null hypothesis at the same significance level for a sample of 50 (see Table A2.5, Wall & Jenkins, 2003). ρ, the P-value

Table 4.4: Table of continuum masses for a number of sources in the sample. Not all sources have a measured continuum mass and are not included.

RMS Source Name	Type	Bolocam Mass ($M_\odot$)	Scuba Mass ($M_\odot$)	Other 1.2 Mass ($M_\odot$)
G010.8411-02.5919	YSO	...	86.46	134.65
G012.0260-00.0317	YSO	183.77	801.78	540.06
G012.9090-00.2607	YSO	95.68	470.18	660.65
G013.6562-00.5997	YSO	...	331.47	343.85
G017.6380+00.1566	YSO	53.2	161.64	...
G018.3412+01.7681	YSO	...	152.18	213.62
G020.7491-00.0898	HII	655.33	...	...
G020.7617-00.0638	YSO	280.25	...	...
G023.3891+00.1851	YSO	67.21	...	...
G023.7097+00.1701	HII	339.19	...	1296.05
G025.4118+00.1052	YSO	57.04	211.6	278.69
G025.7161+00.0486	HII	342.97	...	...
G028.2007-00.0494	HII	1193.46	5533.37	4644.43
G028.2875-00.3639	HII	921.26	3551.0	5022.07
G028.3046-00.3871	YSO	383.13	...	797.19
G030.1981-00.1691	YSO	...	308.8	...
G030.6877-00.0729	HII	...	...	438.51
G030.7206-00.0826	HII	394.92	...	719.16
G030.8185+00.2729	YSO	33.42	91.1	99.98
G033.3891+00.1989	YSO	31.66	...	...
G037.5536+00.2008	YSO	240.95	475.26	518.46
G043.9956-00.0111	YSO	53.06	245.38	...
G045.0711+00.1325	HII	199.59	175.46	...
G048.9897-00.2992	YSO	304.59	1230.84	...
G049.5531-00.3302	HII	39.22	...	...
G050.2213-00.6063	YSO	...	110.76	...
G053.9584+00.0317	HII	51.72	...	...
G073.0633+01.7958	YSO	...	17.53	...
G075.7666+00.3424	YSO	30.79	73.02	...
G077.9550+00.0058	HII	2.9	...	...
G078.1224+03.6320	YSO	...	51.94	83.05
G078.8867+00.7087	YSO	137.01	584.91	...
G079.1272+02.2782	YSO	...	10.83	22.91
G079.8749+01.1821	HII	12.53	...	...
G080.8624+00.3827	YSO	11.22	60.04	...
G080.8645+00.4197	HII	15.58	78.42	...
G080.9383-00.1268	HII	12.47	29.71	...
G081.7133+00.5589	HII	...	197.98	...
G081.7220+00.5699	HII	104.35	247.96	...

Table 4.4: Table of continuum masses for a number of sources in the sample. Not all sources have a measured continuum mass and are not included - continued.

RMS Source Name	Type	Bolocam Mass ($M_\odot$)	Scuba Mass ($M_\odot$)	Other 1.2 Mass ($M_\odot$)
G081.7522+00.5906	YSO	37.15	140.84	...
G081.8789+00.7822	HII	75.1	...	...
G085.4102+00.0032	YSO	122.29	584.13	...
G094.6028-01.7966	YSO	...	280.7	...
G103.8744+01.8558	YSO	...	33.15	46.17
G105.6270+00.3388	HII	...	382.12	...
G109.0775-00.3524	YSO	...	56.73	...
G109.0974-00.3458	HII	...	131.03	226.22
G109.8715+02.1156	YSO	...	80.2	...
G110.0931-00.0641	YSO	...	344.11	483.83
G110.1082+00.0473	HII	...	336.09	...
G111.2348-01.2385	YSO	...	167.09	284.16
G111.2552-00.7702	YSO	31.86	153.86	211.75
G111.5234+00.8004	YSO	40.39	136.82	...
G111.5320+00.7593	YSO	...	658.83	...
G111.5423+00.7776	HII	283.27	830.58	...
G111.5671+00.7517	YSO	...	248.93	...
G111.5851+00.7976	YSO	...	5.8	...
G133.6945+01.2166	YSO	126.36	725.44	...
G133.7150+01.2155	YSO	172.69	821.95	...
G133.9476+01.0648	HII	157.45	751.76	...
G134.2792+00.8561	YSO	8.74	32.0	...
G136.3833+02.2666	YSO	13.32	94.48	...
G138.2957+01.5552	YSO	50.66	202.79	...
G139.9091+00.1969	YSO	...	199.85	...
G141.9996+01.8202	YSO	...	24.47	...
G192.5843-00.0417	HII	52.33	163.41	128.58
G192.6005-00.0479	YSO	46.93	173.09	116.89
G196.4542-01.6777	YSO	...	388.97	...
G203.3166+02.0564	YSO	...	20.33	...
G207.2654-01.8080	HII/YSO	...	38.99	...

and the sample number will be given for every correlation investigated.

There are strong correlations between the SCUBA 850 μm masses and the C^{18}O masses where $\rho = 0.68$ and P $\ll 0.01$ and for the Bolocam masses with the C^{18}O masses where $\rho = 0.76$ and P $\ll 0.01$. The samples comprise of 56 and 42 source for the SCUBA and Bolocam comparisons respectively. The correlations of the independently calculated masses suggest that the same material is being traced by both the continuum and the C^{18}O (3-2) emission. This is also confirmed by the correlation between the SCUBA and Bolocam masses where $\rho = 0.95$ and the P-value is $\ll 0.01$ for the 30 sources with both mass estimates. When changing the samples to include only good mass flags of (0) and (1) the correlations are still present. $\rho = 0.66$, P $\ll 0.01$ for the SCUBA correlations and $\rho = 0.74$, P $\ll$ 0.01 for the Bolocam correlations while the sample sizes are reduced to 39 and 28 respectively.

When considering the MYSOs with good C^{18}O mass estimates the coefficients ρ change to 0.55 and 0.56, the sample sizes are now 30 and 18, and the P-values are 0.001 and 0.01 for the SCUBA and Bolocam correlations. According to Table A2.5 of Wall & Jenkins (2003) the MYSO C^{18}O and Bolocam masses are not correlated at the 0.01 significance level as the critical ρ value is 0.6. Furthermore, the correlation between MYSO C^{18}O and SCUBA masses is weaker than the correlation for all sources as ρ is only just above the critical value for the sample of 30 sources at the 0.002 significance level. At the P-value of 0.001, the MYSO C^{18}O and SCUBA masses are uncorrelated according to the ρ value. For HII regions only, $\rho = 0.86$ and 0.95, the sample sizes are 8 and 10, and the P-values are 0.006 and $\ll 0.01$ for the SCUBA and Bolocam correlations. The C^{18}O and SCUBA masses are only weakly correlated at a 0.01 significance level, and not correlated at the reported

significance level. However, the correlation is stronger than that for the MYSOs. The $C^{18}O$ and Bolocam masses are quite strongly correlated given the high ρ value at the very low significance level.

There appears to be a discrepancy in the correlations for MYSO and HII region sources. The discrepancy occurs because there are low $C^{18}O$ mass MYSOs (< 100 $M_\odot$) with larger continuum masses compared to no HII regions with $C^{18}O$ masses < 100 $M_\odot$. These low $C^{18}O$ mass MYSOs are typically lower luminosity sources L $< 10^4$ $L_\odot$ and could have larger differences from the assumed temperatures, dust opacities or gas-to-dust ratios. The regions forming the lower mass range of stars could be intrinsically different and may have more diffuse, wide spread continuum emission, leading to a much larger continuum integration area and much larger continuum masses. It does not appear to be down to evolution as the sources have a broad spread in $21/8$ μm fluxes which is a rough tracer of evolution (see Lumsden *et al.*, 2002). Buckle *et al.* (2012) find that the continuum and $C^{18}O$ do not always have exactly the same distributions. This could also be the case here. Depletion of $C^{18}O$ could explain why these sources have $M_{cont}/M_{C^{18}O} \gg 1$. Overall there is still a correlation between the masses traced by the continuum emission and the $C^{18}O$ emission. At the resolution of the JCMT the $C^{18}O$ and SCUBA 850 μm emission should trace the same regions and the longer wavelength continuum data should probe roughly the same structures on a slightly larger scale.

4.4.3 $C^{18}O$ Mass and Distance

Figure 4.8 shows that a wide range of masses are sampled irrespective of distance out to around 6 kpc. There are no biases towards more massive cores being the most distant ones. After 6 kpc however, there is a deficit of lower mass objects
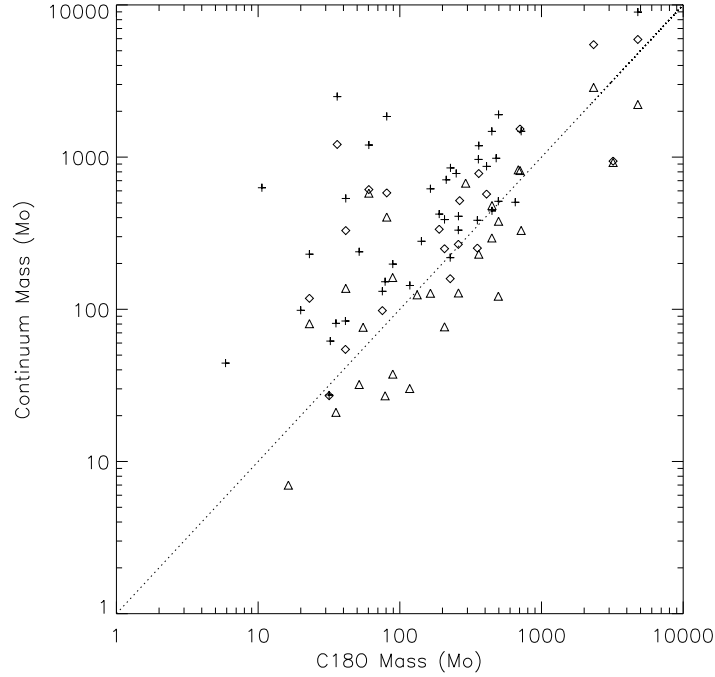
Figure 4.7: Comparison of the $C^{18}O$ masses estimated from the integration and summation within a polygon aperture vs the 850 μm SCUBA masses (plus symbols), the 1.1 mm Bolocam masses (triangle symbols) and 1.2 mm observations of various other surveys (diamond symbols). Upper limit and 3 pixel aperture masses are not plotted even if there is a continuum counterpart. Note the offset in the Bolocam masses as they are consistently smaller than all other mass estimates. The dashed line is the line of equal mass.

and, as previously discussed, the sample is not representative of lower luminosity sources which could also be the least massive. Although sources > 6 kpc do have a range of masses from a few hundred $M_\odot$ to thousands, the very lowest mass sources are absent. It is possible in some cases that the most massive of these sources have been assigned a far distance rather than the respective near distance in resolving the kinematic distance ambiguities and these source masses would be reduced accordingly. At the resolution of the observations the cores are not fully resolved at distances < 6 kpc and sources > 6 kpc likely contain more than one massive

source (see Bontemps *et al.*, 2010, for an example of a close region). Some distant sources are part of much more complex regions where there are clearly multiple peaks of emission present (flagged 2 and 4). When excluding sources more distant than 6 kpc there are no core masses above ~ 2000 $M_\odot$ where there is a single peak in the $C^{18}O$ emission. The three cores with masses > 1000 $M_\odot$ (G108.7575-00.9863, G111.5423+00.7776 and G133.6945+01.2166) are part of complex structures and the masses are potentially a combination of multiple massive star forming cores. The likely upper mass limit for the core mass associated with a single massive source is < 1000 $M_\odot$ (see Section 4.4.5).

4.4.4 $C^{18}O$ Mass and Luminosity

Any relationship between mass and luminosity can provide insights into star formation efficiency, evolution or clustering in the cores. A linear relationship is observed for both MYSOs and HII regions when plotting $C^{18}O$ mass versus luminosity for sources with distances < 6 kpc and where the masses are not upper limits or calculated within the 3 pixel diameter apertures (58 sources in total). The luminosities are estimated from multi-wavelength SED fits and are not crude IRAS upper limits (flag (5) sources), for details see Mottram *et al.* (2011b). These luminosities are likely dominated by the massive source targeted. Figure 4.9 shows the linear log-log trend in mass and luminosity for MYSOs and HII regions (plus and triangle symbols respectively). For all sources the luminosity-mass relationship is $L_\odot \propto M_\odot^{0.63}$. This is much shallower than the expected relationship for main sequence stars ($L_\odot \propto M_\odot^{3.3}$). The Spearman's correlation coefficient (ρ) for this fit is 0.67 and the P-value is $\ll 0.01$ which is interpreted as a strong correlation between the core mass and luminosity down to a very small significance level.
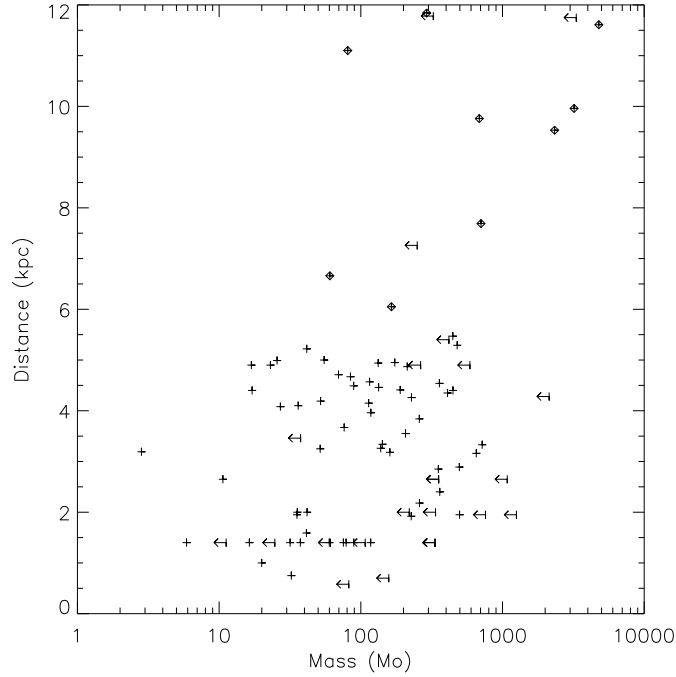
Figure 4.8: Plot of mass vs. distance for all sources flagged as (0) and (1) are plotted as plus symbols. The sources from complex regions where there maybe a mass overestimate are represented by the upper mass limit arrows (flags (2) and (4)). The distant sources, > 6 kpc are boxed by a diamond symbol. It is clear that a wide range of masses below 6 kpc but are biased to more massive sources above 6 kpc.

The solid line in Figure 4.9 represents the luminosity expected if $M_{core} = M_{star}$ and $L_\odot = M_\odot^{3.3}$. This is the max luminosity attainable if the core mass is directly converted into a star up to a maximum mass of ~ 150 $M_\odot$. Cesaroni (2005) divide their sample of hot cores into light and heavy sources depending on whether they are to the left or right side of the line. Light sources are in a region where their stellar masses exceed their core mass as their stellar luminoisites exceeded the luminosity limit set if their core and stellar masses are equal. The core emission measured in this case is likely to be associated only with the most massive star in

the cluster. Heavy sources are interpreted as cores that contain multiple massive stars that have formed in a clustered region. Here the core mass of the entire cluster is measured. All but 3 sources here are classified as heavy sources. Evolution could provide an alternative explanation for lighter sources. The light sources would simply be in more evolved clusters where material from the natal core has been dispersed/expelled due to winds or outflows. This would effectively move sources leftwards in Figure 4.9 assuming that the protostars have reached their zero age main sequence (ZAMS) luminosity. Positioning the sources on the pre-main sequence tracks from Molinari *et al.* (2008) indicates that they have all reached their ZAMS luminosities. Most sources should be in the contraction phase of their stellar evolution (see Section 1.2.4). It is unclear then why the light sources are not HII regions as at least one is very luminous. Cesaroni (2005) list IRAS20126+4104 as a light source when they calculate a low mass of ~ 7 M$_\odot$ assuming the Keplerian rotation of a molecular disc. Here IRAS 21026+4104 it is a heavy source. This supports the first explanation as a source is classified as a light source when the mass of the core is associated with the single massive protostar rather than the mass of the cluster of stars. The majority of sources in the sample are in clusters at the resolution of the observations.

In Figure 4.9 the long dashed line represents the luminosities expected from the most massive star in the core following the relationship L$_\odot$ = M$_\odot^{3.3}$. Here the total mass of stars $M_{stars} = M_{core}$ and the masses are distributed according to the Salpeter power law IMF. The core luminosity should be dominated by the most massive star and the line should be a good representation of that expected from the cores. In all but 3 cases the sources all conform to the luminosity limit. One possible explanation (assuming the luminosity is accurate) for the over-massive
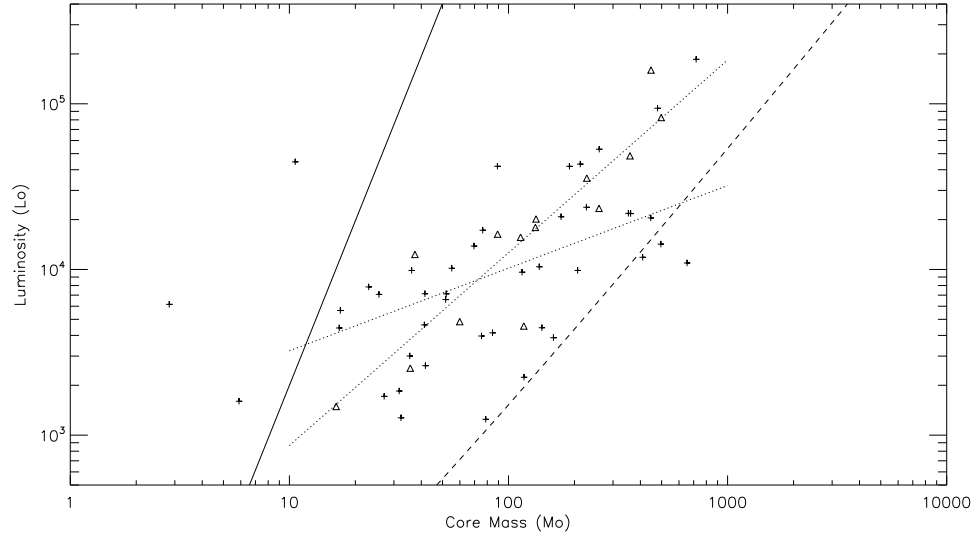
Figure 4.9: Mass-luminosity plots for all sources where the mass is calculated well. The plot excludes all upper mass limits and estimates of masses within 3 pixel diameter apertures. Sources further than 6 kpc away are not plotted or considered in the analysis although they do follow the general trend shown. The solid line is the expected luminosity if a single star has a mass $M = M_{core}$ and $L_\odot = M_\odot^{3.3}$, the long dashed line is the luminosity expected from the most massive star in the core when the stellar masses are distributed according to the Salpeter IMF. The best fit line for MYSOs and HII regions are plotted as the short dashed lines with slopes of 0.49 and 1.16 respectively.

and under-luminous cores is that they are much less evolved than the rest of the sample. However, the $21/8\,\mu$m flux ratios are only large (redder) in two sources. A second, more simple explanation is that the sources do conform to the limit given the uncertainties. All other sources appear over luminous. This extra luminosity can in part be accounted for by the other stars in the cluster as only the most massive star's luminosity has been used, but it is insufficient to match the observed values. The discrepancy between the luminosity line and the source luminosities can provide insight into the mass locked up in stars. The luminosity line of the most massive stars is calculated based upon the current core mass which has been

reduced as star formation has already occurred. Therefore the mass of the most massive star in the core would be larger if the pre-star formation core mass was larger. Increasing the core mass has the effect of lifting the long dashed line to higher luminosities more centrally positioned between the source luminosities. Such scaling crudely suggests a high star formation efficiency. If the initial core mass is that now locked up in stars added to the core mass measured, and none has been lost from the region, the low core masses measured now suggests a large fraction has been used to form the stars.

For MYSOs and HII regions the relationships between mass and luminosity follow $L_\odot \propto M_\odot^{0.50}$ and $L_\odot \propto M_\odot^{1.16}$ respectively. The Spearman's correlation coefficients (ρ) for MYSOs (43 sources) and HII (14 sources) are 0.60 and 0.94 respectively. Both have P-values $\ll 0.01$. Although a major difference in ρ is caused by the sample size there is divide of correlation strengths for MYSOs and HII regions. The P-value for HII regions is a factor of 100 smaller than that for MYSOs. MYSOs core masses could be said to have a medium correlation with source luminosity, whereas HII regions have a strong correlation between core mass and luminosity when considering the same significance level. The slope for HII regions is coincident with the IR-primary sources from Molinari *et al.* (2008) which are suggested as high mass analogues to low mass class I sources. Here the HII regions appear to be generally more evolved due to the difference in slopes between the two source types. Notably, this may not always be the case as larger sources are much more luminous and would generate HII regions much earlier in their lifetimes (i.e. HII regions are not more evolved in terms of age but are in terms of observable characteristics). However, the shallower slope for MYSOs could be influenced by a larger spread in the evolution of these sources. There is a noticeable overlap

between many MYSOs and HII regions but there are also MYSOs that would be less evolved given the location on PMS tracks. MYSOs have a wide range of parameters given their evolutionary classification as MYSOs. The differences could represent sub classes of the same overall source type.

4.4.5 C^{18}O Mass and Stellar Mass

An estimate of the stellar mass of the most massive star can be made using the source luminosity. Here the stellar masses are estimated according to the ZAMS source properties listed in Davies *et al.* (2011). Figure 4.10 plots the stellar mass calculated from the source luminosities against the mass of the cores. The dashed line represents the stellar mass of the most massive star taking $M_{stars} = M_{core}$ and distributing the stellar masses according to the Salpeter IMF, as Section 4.4.4. Essentially this is an alternative way of showing that the most massive star in the core is compatible with the distribution of mass following the IMF provided the core mass now is that locked within stars (as was done in Section 4.4.4 using source luminosities directly). There is no difference between the source types suggesting that all sources have reached or are very close to their ZAMS luminosities.

The calculation of the most massive star according to the IMF distribution is done under the assumption that the core gas mass can be calculated from the remaining C^{18}O in the core and that an equal amount of gas has been locked up within stars (i.e. 50 percent of the initial core mass before star formation began). It is questionable whether this is a reasonable assumption to make. As the calculated stellar masses are generally larger than those of the most massive star in the core following the Salpeter IMF the original core mass must have been greater than currently calculated from the C^{18}O emission. The offset between the
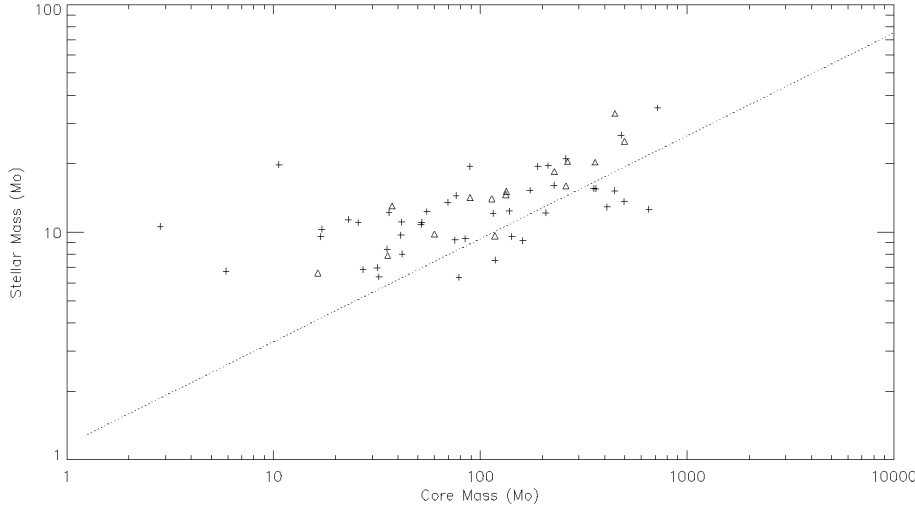
Figure 4.10: $C^{18}O$ core mass plotted against the stellar mass calculated from the source luminosity. The dashed line corresponds to the fit of the most massive star in the core assuming $M_{stars} = M_{core}$ with stellar masses distributed according to the Salpeter power law IMF.

most massive star from the IMF distribution of the core mass and the calculated stellar mass from luminosity is roughly constant for the full range of core masses. The constant offset could be interpreted as a constant star formation efficiency for the range of stellar masses investigated, i.e. a constant scaling between initial core mass and core mass now.

4.4.6   Larson relationships

Larson (1981) found a relationship between the radius of molecular clouds and their velocity dispersion. The turbulent velocity dispersion for a cloud structure is related to the size of the structure via a power law ($\sigma \propto R^{\alpha}$). Their data probe cloud sizes from ~ 0.1 to ~ 100 pc, whereas the cores presented here are of a much tighter size range. However, the trend is still seen in Larson (1981)

on similar size scales as presented here. The one dimension velocity dispersion calculated from the FWHM of the summed spectra Gaussian fits is used as an analog to the full three dimensional velocity dispersion. The effective radius for all cores is calculated using $R_{eff} = \sqrt{area/\pi}$, where the area is that within the aperture used to calculate the core masses. Figure 4.11 shows that there is no relationship between line width and core radius for the sources with good masses and at distances < 6 kpc. ρ is only 0.23 for these sources and the P-value is 0.08. Thus the null hypothesis of a random distribution is not rejected at a significance level of 0.01 or lower. As other authors found (e.g. Buckle *et al.*, 2012; Tachihara *et al.*, 2002), the small range of physical scales probed and the scatter of the data points, compared to the range investigated by Larson (1981) could prevent any relationship from being detected. The cores all have similar properties and there is no difference between MYSOs or HII regions.

Including sources more distant than 6 kpc (Square symbols), ρ improves to 0.37 and the P-value $= 0.002$. For the 66 sources the ρ value indicates there is a significant correlation. Furthermore, some sources have large velocity dispersion although they are very small (~ 0.15 pc). These sources are removed to check their influence on the correlation as the more distant ones are unresolved. For the remaining 62 sources ρ is 0.44 and the P-value is 0.0002. The correlation can be considered stronger than it previously was. On these larger scales the cores likely contain many more sources with differing properties which could act to increase turbulence (winds, infall, outflows, rotation etc.). However, as discussed, the sample could be biased with only larger sources being detected at larger distances and an artificial correlation would result. The sources with radii > 1 pc are the most massive, distant cores in the sample and fit the trend, however, some distant

sources are coincident with the closer sources in terms of mass and radius values. If sources were in virial equilibrium the velocity dispersion would be expected to increase with mass (Larson, 1981) (Bottom, Figure 4.11). This is confirmed by the ρ and P-values for a mass/velocity dispersion correlation of 0.44 and 0.0002 for the 66 sources and the tentative correlation for the 58 close sources as $\rho = 0.36$ and the P-value $= 0.006$. Virialised cores could be the underlying reason for the correlation between radius and velocity dispersion as the source size is very strongly correlated with mass ($\rho = 0.93$, P-value $\ll 0.0001$) which in turn is correlated with the velocity dispersion for sources more distant than > 6 kpc. On the scales probed the velocity dispersions measured do not vary greatly and turbulence may not be the dominant source.

The line width size relationship can also be investigated with an alternative dense gas tracer. In the RMS survey there are 86 sources out of the original 99 sources here that have ammonia emission from dense gas ($\sim 10^4$ cm^{-3}) (Urquhart et $al.$, 2011b). There is a strong correlation of the C^{18}O line widths and those of the thermally excited NH$_3$(1,1) and (2,2) lines as $\rho = 0.75$ and 0.76 and both P values are $\ll 0.0001$ for NH$_3$(1,1) and (2,2) respectively. The correlations suggest the same motions are being detected by both the C^{18}O and the NH$_3$. Again a correlation is found between the NH$_3$(1,1) and (2,2) line widths and the sizes associated with the C^{18}O cores for the sources when including those at distances > 6 kpc. The same conclusion is reached that the underlying relationship could be influenced by the mass and velocity dispersion correlation.

Larson (1981) also found that all their clouds appear to be gravitationally bound and in virial equilibrium. Provided that the mass of the cloud is greater than the virial mass, the cloud will be gravitationally bound. Otherwise, clouds
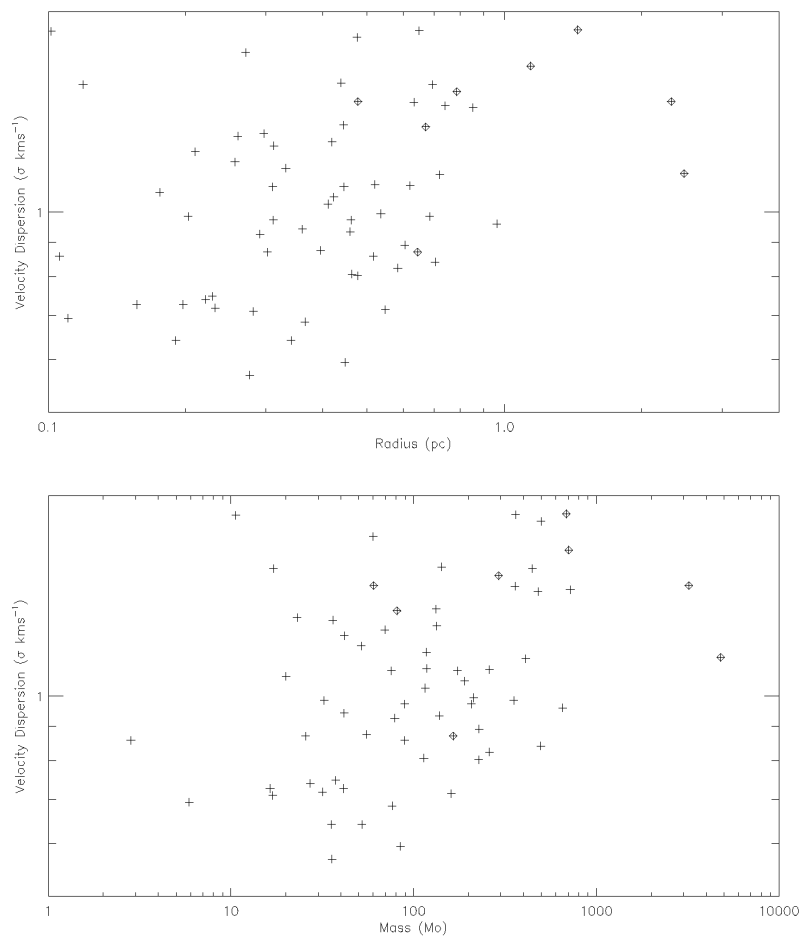
Figure 4.11: Top: The 1D velocity dispersion calculated from the FWHM of the $C^{18}O$ emission from Gaussian fitting plotted against the effective radius of the core assuming that it is spherical. There is no correlation for sources with good mass estimates and at distances < 6 kpc. But a strong correlation when distance sources are included (> 6 kpc). Bottom: Plot of the 1D velocity dispersion against the mass of the core. Correlations are present for sources at distances < 6 kpc and when including those at distance > 6 kpc.

with masses less than the virial mass must be pressure confined by the surrounding medium or they would be free to dissipate. Following MacLaren *et al.* (1988) the virial masses of the cores are calculated via:

$$M_{vir}(\mathrm{M}_\odot) = 126R(\mathrm{pc})\,\Delta V^2(\mathrm{km\,s}^{-1}), \qquad (4.3)$$

where R is the effective radius, as calculated from the area, ΔV is the FWHM of the $\mathrm{C}^{18}\mathrm{O}$ emission and the core is spherical, not magnetised and has a $\rho \propto \mathrm{r}^{-2}$ density distribution. Figure 4.12 shows the relation between the virial and core masses. The correlation is strong as ρ is 0.81 and $\mathrm{P} \ll 0.001$ for all sources where the core mass is calculated well (flags (0) and (1)). The majority of sources have virial masses greater than their core masses. This would suggest that all the cores are not gravitationally bound/dominated, which is counter intuitive given that the cores have collapsed and harbour at least one massive star. The virial masses are on average a factor of ~ 4 larger than the core masses.

There are a number of possible explanations. Molecular outflows or HII region energetics could artificially increase the velocity dispersion or the effective core radius calculated for a spherical cloud could simply be an overestimate. As shown above, the velocity dispersions do not vary greatly between cores and follow a relationship with mass. A systematic reduction in radius would lead to a direct agreement between the virial and core masses given the scatter in each parameter. The virial mass of IRAS 20126+4104 at 1.7 kpc was ~ 100 $\mathrm{M}_\odot$ from Estalella *et al.* (1993) using the contour at half the peak brightness to calculate the radius. This agrees with the core mass when calculated at the same distance (see Section 4.3.3). Alternatively, the core masses at the observed size scales are expected to

be lower than the virial masses for cores that have ongoing star formation. As mentioned in Section 4.4.5, the core masses measured are likely reduced from the initial mass due to star formation. This is consistent with the fact that the core masses must have been larger than the virial masses for the core to collapse and stars to form initially. This conclusion however would imply that the size and velocity dispersion have remained largely unchanged from the initial conditions. At the resolution of the observations the source is a single core, however this will be a combination of smaller cores and diffuse material at higher resolutions. The core mass measured may not be dominated by the most massive source. Under the assumption that the mass is dominated by the most massive source the radius here is going to be an over estimate for the core associated with that source. Therefore the definition of the radius is the most probable source of the discrepancy between the calculated virial masses and the core masses. Higher resolution observations are required to probe these regions in more detail and revise both the mass and radius estimates.
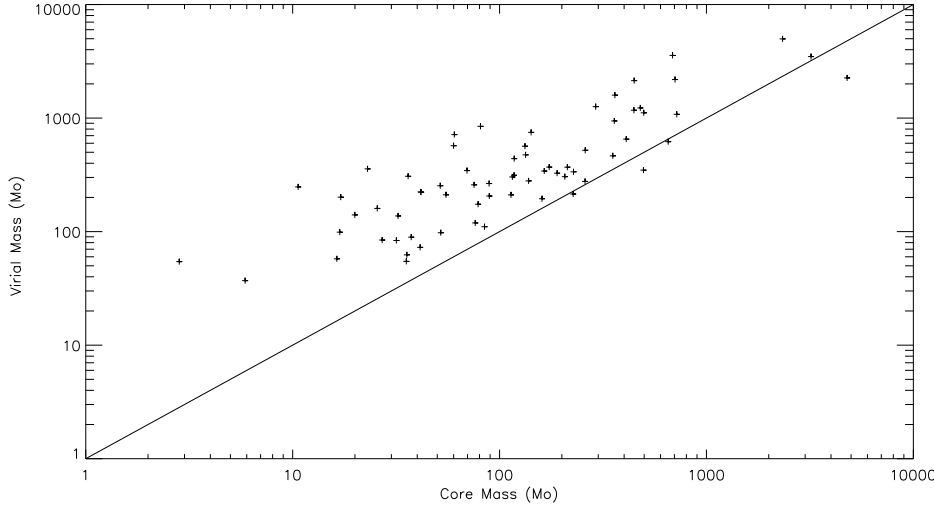
Figure 4.12: The core mass calculated from the C^{18}O emission plotted against the calculated virial mass from the core size and line width. The solid line represents $M_{core} = M_{vir}$. Most cores have larger virial masses than core masses and appear gravitationally unbound. A systematic reduction in radius would position all sources about the solid line.

4.5 Conclusions

The core masses of a sample of MYSOs and HII regions have been established via the summation of the integrated source emission in a polygon shaped aperture closely following the $3\sigma_{MAP}$ noise level. The integration of the source emission was done over the velocity range in which the emission from within ~ 1 beam pointing centred upon the source was above 3σ of the spectral noise limit. The methodology was tested by establishing the mass of a test source with a circular core morphology via circular aperture integration. The aperture analysis method is valid for integrating all the emission from any molecular line tracer and will be the methodology adopted to calculate the masses of outflows from this sample of sources. Furthermore, the velocity ranges of the ambient cores will be used to

remove low velocity core material from the ^{12}CO and ^{13}CO emission that traces the outflows and reduce confusion with core material.

The sample of outflow sources presented is reduced from 99 to 87 when considering a luminosity limit of 10^3 L$_\odot$. The velocity limits have been established for all but 5 sources from the total sample above the 3σ spectral noise level, and at the 1σ spectral noise level for 4 of the remaining sources. One source has no detected C^{18}O emission although the spectral noise level was typical of the observations. The masses are established for all but 3 sources overall but only 66 of these are used in the analysis as upper limits or masses of cores within complex filamentary regions are not included due to their uncertainty. There is a distribution of different mass cores at a variety of distances and there are no biases in the sample towards more massive cores being the most distant.

A correlation is found between the dust continuum masses and the core masses established for the C^{18}O emission. There is a noticeable offset in the absolute mass value between Bolocam masses and the C^{18}O core masses presented here. Such a systematic offset can be accounted for with variations in assumed dust temperatures or opacities, or could be due to the different area the emission is integrated within. In a number of sources the core mass derived from the C^{18}O emission emission is many factors less than the continuum mass. In these cases depletion of CO could explain the discrepancy of the mass values although a detailed investigation of these sources for other possible factors has not been undertaken. Overall, at the resolution of the observations both the dust continuum emission and C^{18}O emission trace the same material and structures in both MYSO and HII regions.

A clear relationship is present between mass and luminosity for the sample of sources with good mass estimates and conforming to the distance limit. All but 3

sources lie to the heavy side of a line where $M_{core} = M_{star}$ and $L_\odot = M_\odot^{3.3}$. The majority of sources in the sample are clustered at the spatial scales investigated. Most sources conform to the luminosity limit set by assuming $M_{core} = M_{stars}$ where the masses are distributed according to the Salpeter IMF and the luminosity is calculated from the mass of the most massive star via $L_\odot = M_\odot^{3.3}$. The luminosity from the majority of cores are dominated by the most massive star in the cluster. The sources below the limit could be at a different evolutionary stage but do agree with the limit given the uncertainties in their mass and luminosity values. If the luminosity is dominated by the most massive star then all the cores are over luminous. However, the initial core mass would have been larger than the core mass measured now, after star formation has taken place. The correlation between mass and luminosity is stronger for HII regions which span a narrower range in parameter space than MYSOs. The position of the sources on PMS tracks is consistent with HII regions being more evolved than MYSOs, although there is considerable overlap. All sources appear to have reached an evolutionary stage where the luminosity is close to that at birth on the main sequence. This positions them in the contraction phase of their PMS lives.

The estimated mass of the most massive stars derived from the core masses distributed according to the Salpeter IMF is less than those calculated directly from the source luminosities. This reiterates that the initial core mass (before star formation began) must have been much greater in order for a percentage of it to be distributed according to the IMF and form the most massive star currently seen in the core. The constant offset between the stellar masses over the range probed suggests that star formation efficiency is constant for a wide range of masses.

The Larson line width and size relationship is not seen for the sample of sources

< 6 kpc. The linear size scale probed is very narrow and only ranges from ~ 0.1 to 0.8 pc and may not be sufficiently different to see the observed relationship given the scatter between sources. A strong correlation is found when sources > 6 kpc are included. It is unclear whether this is due to the line width and mass relationship for virialised cores via the underlying relationship between mass and size. On the scales probed it is likely that the turbulent motions are dominated by similar processes for all sources and may not vary significantly. A strong correlation is found between the $C^{18}O$ line width and ammonia line widths that trace similar densities and there is still no correlation with core size for sources < 6 kpc. The virial mass is strongly correlated with the core masses although these are a factor of 4 smaller. The discrepancy is most likely due to the definition of the source radius. Higher resolution observations are required to probe the material directly associated with the most massive cores.

The overall properties of the sampled sources are globally similar and there are no discrepancies between MYSOs and HII regions and no biases towards more distant, luminous or massive sources (when distance < 6 kpc). MYSOs span a broader range in mass-luminosity diagrams compared to HII regions which are positioned as the most evolved sources. The sample is genuinely representative of MYSOs and HII regions and will provide an excellent footing to investigate outflow parameters and how they may change between the two source types and differing evolutionary stages.

Chapter 5

Testing Outflow Analysis Methodology

This Chapter presents a methodology to analyse the ^{12}CO(3-2) and ^{13}CO(3-2) molecular line data from 99 MYSOs and HII regions targeted as outflow candidates and observed with the James Clerk Maxwell Telescope (JCMT). These observations are similar to those undertaken towards much lower mass sources, where outflows are a ubiquitous phenomena. A link between outflow parameters of both low and high mass stars would be key evidence for a similar formation scenario. Chapter 4 concluded that the sample of outflow sources here is a representative sample to investigate such links. Once a comprehensive outflow analysis methodology is established comparisons can be made between source and outflow parameters, and with the studies of low mass outflow sources.

5.1 Introduction

There are many inherent problems when analysing molecular outflow data, even if the source sample is homogeneous and does not suffer from biases (see Section 1.5.2). It is difficult to identify outflows in the complex background of the star formation region. In the blind outflow survey by Ginsburg *et al.* (2011) it is very hard to distinguish the velocity components of the outflow from those of the molecular cloud itself. In some sources there may be velocity components reminiscent of Doppler shifted lines wings but not created by a molecular outflow. Observations by Beuther *et al.* (2002c) for example, show large velocity ranges for at least three regions that have confusing morphologies and consequently are not classified as outflows. Typically, observations are spatially limited (low resolution maps) or single pointing measurements (e.g. Shepherd & Churchwell, 1996; Wilking *et al.*, 1990; Wu *et al.*, 2005) when using single dish telescopes compared to interferometers, indicating just how confusing some outflow regions can be (e.g. Beltrán *et al.*, 2011b; Beuther *et al.*, 2002a; Wang *et al.*, 2011). Some single dish maps by Ridge & Moore (2001) appear to be entirely filled by emission and it is unclear what constitutes the outflow in such cases. In addition, the main outflow tracer, ^{12}CO, requires a correction as it is usually optically thick and suffers from self-absorption in some cases (e.g. Choi *et al.*, 1993).

A source of error in the calculated outflow parameters is introduced through the chosen outflow velocity range. As outflows from MYSOs have a much larger mass fraction at low velocities (Ridge & Moore, 2001) the divide between the ambient core and outflow material can significantly affect the calculated outflow mass, and subsequent parameters. Secondly, the maximal velocity extent that is used in

calculating momentum, energy and other dynamic parameters is dependant upon the sensitivity of the observations. The choice of the outflow line wing velocity ranges are usually rather subjective. Specifically, there is no justified measurement of the lower velocity limits. Often, using channel maps, the spatial separation of the blue and red shifted outflow wings at certain velocities allows such an estimate. However with line of sight outflows only a velocity shift exist and makes such methods redundant.

This Chapter details the various methods commonly used to calculate the outflow parameters, such as mass and momentum as well as dynamical parameters such as timescales and flow rates. Furthermore, three different calculations of the optical depth from ^{12}CO and ^{13}CO line ratios are made. The higher line transition CO(3-2) is favourable as an outflow tracer than lower transitions (e.g. Takahashi *et al.*, 2008) as warmer temperatures are required and should better trace outflow regions. A useful consequence of a higher temperature tracer is that there is less confusion with line of sight material which could aid in defining a lower velocity limit. However, Ginsburg *et al.* (2011) caution that CO(3-2) may be sub-thermally excited and following assumptions of local thermodynamic equilibrium (LTE) could lead to incorrectly calculated masses. They do not correct for optical depth however, which could also cause the mass deficiency reported. A unique method for identifying the lower velocity limits of the outflow lobes is also undertaken using the previously analysed C^{18}O emission (see Chapter 4).

5.2 Observations

The observations and reduction are as detailed in Section 4.2. Here however the operational bandwidth was 1000 MHz and resulted in a velocity resolution of 0.423 km s^{-1} for the ^{12}CO data. The spatial resolution at the slightly shorter wavelength of the ^{12}CO emission is $\sim$ 14". The final data cubes are identical to those of the C^{18}O data and have a spatial pixel scale of 7".

5.3 Calculating the Outflow Mass

Chapter 4 describes how the mass of any emission line tracer can be found by integrating over a suitable velocity range and then summing the emission within an aperture defined by the $3\sigma_{MAP}$ noise level from the map. This method is adopted here to find the mass of the bipolar outflow from the test source, IRAS 20126+4104 (G078.1224+03.6320). The line free regions of the spectra from all positions of the ^{12}CO data cube have an average spectral noise of $1\sigma_{T_A^*} = 0.51$ K. After investigation of emission above the $3\sigma_{T_A^*}$ level the maximal velocity extent of the blue and red shifted outflow lobes is found to be $\sim$ -40 to 40 km s^{-1}. The limiting low velocity boundary of the outflow is defined from the maximal velocity range of the C^{18}O core emission, i.e. -5.7 to -1.1 km s^{-1} for the blue and red shifted lobes respectively.

Using the $3\sigma_{T_A^*}$ threshold to define the integrated velocity range may miss some very high velocity emission below the cutoff. Lebrón et $al.$ (2006) show very high velocity emission extending out to $\sim$ 50 and -50 km s^{-1}, for the blue and red wings respectively, in their very sensitive observations. Here the observed data clearly detects the very high velocity material out to this extent although it is

below $3\sigma_{T_A^*}$. It is likely that the mass associated with the outflow wings, in total, is underestimated due to the reduced integration range. The difference in mass however, is probably not significant as the mass is dominated by the high intensity, low velocity material and not the faint, high velocity emission. The mass would be underestimated by only 0.005 M$_\odot$ per 7" pixel within the outflow over the $\sim$ 10 km s^{-1} velocity extent assuming the emission is optically thin and at the $3\sigma_{T_A^*}$ spectra noise level (as expected at high velocities). However, as both momentum and energy are a product of velocity a more significant deficit could be evident in those parameters for IRAS 20126+4104 when limiting the velocity range, see Section 5.4.

The integrated map noise $1\sigma_{MAP}$ evaluated in emission free regions of the blue and red shifted outflow maps is 2.5 K km s^{-1} for both. An aperture mask region is defined based upon emission at the $3\sigma_{MAP}$ contour level from the integrated maps. Figure 5.1 shows the blue and red outflow lobe integrated intensity maps, the $3\sigma_{MAP}$ contour and the aperture masks used to sum emission within.

There is a faint emission shell around the bright, spatially offset outflow lobes in both the blue and red shifted maps. The more chaotic structure is due to the lower velocity material. At higher velocities a clear bipolar structure is evident with the blue shifted outflow lobe extending to the north-west and the red shifted emission to the south-east (see Figure 5.2). Even at lower velocities it is the spatially offset material that provides the majority of the mass, not the chaotic regions. Shepherd *et al.* (2000) integrate emission from $\pm$ 2.7 km s^{-1} of the V_{LSR} to the maximal extent of the outflow seen in their ^{12}CO data. The mass calculated within this range is attributed entirely to the outflow and the following kinematic and dynamic parameters. They also note the chaotic morphology of the very lowest
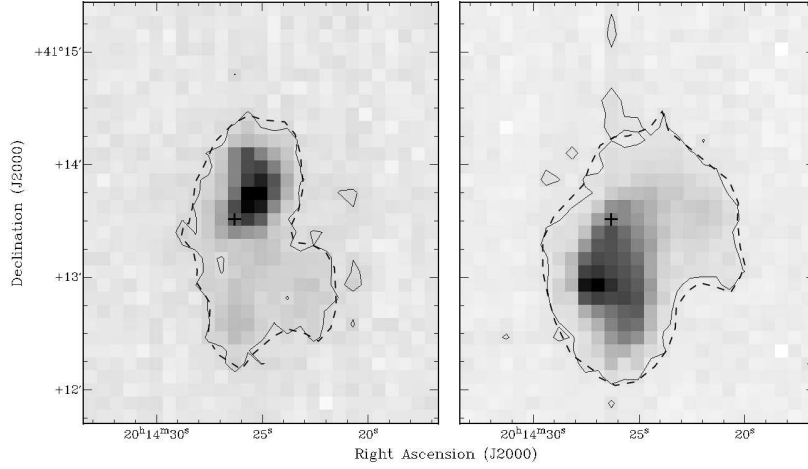
Figure 5.1: Left: Blue shifted outflow lobe integrated intensity map from source IRAS 20126+4104 overlaid with the dashed black polygon representing the aperture mask. The integrated velocity range is -40.0 to -5.7 km s^{-1}. The thin black line indicates the $3\sigma_{MAP}$ contour level. Right: As left, but for red shifted outflow lobe where the integrated velocity range is -1.1 to 40.0 km s^{-1}.
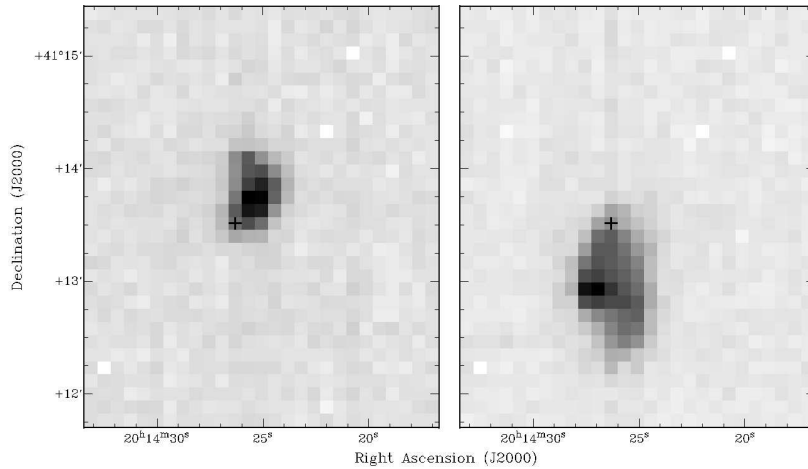

Figure 5.2: Left and right images as Figure 5.1 except the integrated velocity ranges are -40.0 to -8.0 km s^{-1} and 2.5 to 40.0 km s^{-1} for the blue and red shifted outflows respectively.

velocity outflow material which is clearly seen in their Figure 3. However, in their Figure 1 they indicate only the highest velocity material to illustrate the bi-polarity of the outflow lobes, as in Figure 5.2 here. This however leads to some ambiguity regarding the actual spatial ranges the emission is summed within in Shepherd *et al.* (2000). For example, does a noise level of the integrated map created from the limited high velocity range set the spatial aperture to sum within? Or is a spatial aperture defined from the noise level of maps created by integrating between the full velocity ranges stated? Notably, the spatial apertures are not specifically defined in most outflow papers (e.g. Beuther *et al.*, 2002c; Zhang *et al.*, 2001) and it is not made clear which material constitutes to the outflow mass and if the core ambient emission is spatially excluded. Critically, the spatial areas of outflow lobes in the integrated maps are shown here and unambiguously indicate the regions regarded as outflow emission.

The gas mass of the outflow lobes can be calculated from the ^{12}CO data, after the emission has been summed within the defined apertures following the equation:

$$M_{gas} = 1.79 \times 10^{-10} \, \theta^2('') \, D^2(\text{kpc}) \, (\text{H}_2/^{12}\text{CO})$$
$$\times \, \tau_{12}/(1 - e^{-\tau_{12}}) \int T_A^*/\eta_{mb} \, dv \, (\text{M}_\odot) \quad \quad (5.1)$$

where all parameters are as equation 4.1 and τ_{12} is the ^{12}CO optical depth. As with Chapter 4, the detailed derivation is given in Appendix A.

5.3.1 Optically Thin Assumption

First the mass is calculated assuming the emission is optically thin for comparison with the various opacity corrected methods. The optical depth term $\tau_{12}/(1-e^{-\tau_{12}})$ is unity here. The sum of the integrated emission in the aperture masks are 1.2 $\pm$ 0.2 and 2.6 $\pm$ 0.2 M$_\odot$ for the blue and red shifted outflow lobes respectively. The uncertainty is calculated by creating maps integrated over larger and smaller velocity ranges. The range of integration is altered by $\sim$ 0.9 km s^{-1} as discussed in Chapter 4. The main variation in mass is due to the change of outflow range by one velocity bin at low outflow velocities where the emission is greatest. This associates more core material, up to $\sim$ 17 percent, to the optically thin outflow masses. Assuming that the mass is underestimated at the very highest velocities by $\sim$ 0.005 M$_\odot$ per pixel and using the approximate area of the high velocity emission as $\sim$ 45 pixels in each outflow lobe, then the calculated underestimate is of the order $\sim$ 0.2 M$_\odot$ for each outflow lobe in the optically thin regime. Although within the quoted uncertainties the optically thin mass calculate underestimated by $\sim$ 10 percent overall.

5.3.2 Optical Depth Correction

The intensity ratio of two lines of the same transition, but different isotopologues, is the same as the ratio of their respective optical depths. Hence the ^{12}CO outflow masses can be correct for optical depth effects by comparing with the ^{13}CO emission. Under the assumption that the ^{13}CO transition is optically thin, the optical depth τ_{12} can be calculated directly from the observed ^{12}CO and ^{13}CO antenna temperatures via:

$$\frac{T_A^*(^{12}CO)}{T_A^*(^{13}CO)} \simeq \frac{1 - e^{-\tau_{12}}}{1 - e^{-\tau_{13}}} = \frac{1 - e^{-\tau_{12}}}{1 - e^{(-\tau_{12}/68.4)}} \tag{5.2}$$

Where τ_{12} and τ_{13} denote the optical depths of the ^{12}CO and ^{13}CO lines respectively. The abundance ratio of $[^{13}$CO$]/[^{12}$CO$] = \tau_{13}/\tau_{12} = 1/68.4$ (at the galactocentric distance of 8.1 kpc (Wilson & Rood, 1994)). For IRAS 20126+4104 the distance of 1.7 Kpc (Shepherd *et al.*, 2000) is used during these tests for ease of comparisons with literature work. τ_{12} is calculated numerically and thus the correction in equation 5.1, $(\tau_{12}/(1 - e^{-\tau_{12}}))$, can be applied to the ^{12}CO intensities in order to corrected the outflow masses. Choi *et al.* (1993) find an average line ratio $T_A^*(^{12}$CO$)/T_A^*(^{13}$CO$)$ of $\sim$ 10, which yields an optical depth $\tau_{12} \sim 7.2$, for their seven high mass sources. For IRAS 20126+4104 an average of $\bar{\tau}_{12}(blue) = 10.5$ and $\bar{\tau}_{12}(red) = 6.5$ is found by Wilking *et al.* (1990) averaged over the entire line wings and all spatial position. These estimates are comparable within the factor of 2 accuracy associated with mass determination including global optical depth corrections (Cabrit & Bertout, 1990).

Multiple techniques for calculation of the line ratios are investigated:

Method 1 - Velocity Averaged

Integrated maps are created within the velocity range where both ^{12}CO and ^{13}CO exist. These are simply divided to find the velocity averaged optical depth values for the blue and red shifted outflow lobes respectively. The ^{13}CO emission is the driver in determining the velocity range as the ^{12}CO emission is more abundant and is detected out to higher velocities. Due to the low signal to noise of the ^{13}CO observations a $1\sigma_{T_A^*}$ threshold (0.33 K) is employed to define the velocity

extent of the ^{13}CO wings. The maximal velocity extents are -16 to 8 km s^{-1} for the blue and red outflow lobes respectively. The lower limits are set by the C^{18}O core emission as previously detailed. Optical depth corrections are not calculated or applied beyond these limits.

After applying the optical depth correction and adding the mass contribution from the optically thin higher velocity regions the masses are 10.1 $\pm$ 3.7 and 14.6 $\pm$ 3.8 M$_\odot$ for the blue and red shifted outflow lobes respectively. The high velocity optically thin regions of both the blue and red shifted outflows contribute to only 0.2 and 0.8 M$_\odot$ of these final masses. 98 percent of the blue outflow mass and 95 percent of the red outflow mass is provided by the low velocity optical depth corrected emission. The mass deficit due to the limited velocity ranges of $\pm$ 40 km s^{-1} is now negligible given the corrected low velocity masses. The uncertainties are established as previously described.

The velocity averaged optical depths $\tau_{12}(blue)$ and $\tau_{12}(red)$ range from 1 to 36 for the blue shifted outflow lobe and 1 to 53 for the red shifted lobe for different spatial regions within the aperture mask. Figure 5.3 shows the optical depth maps of the blue and red shifted lobes within the apertures. Notice in Figure 5.3 that for both outflow lobes there are larger optical depth values towards the edge of the lobes as defined by the apertures. High optical depths are a result of smaller line ratios, where the integrated ^{13}CO value is similar to, or in some cases larger than, the ^{12}CO value. This primarily occurs in regions where the detection of either ^{12}CO or ^{13}CO is weak or close to the map noise. For example, where $\tau_{12}(blue) = 36$, the line ratio is $2.4^{+2}_{-1.2}$ according to the noise of each map as the ^{13}CO value is only slightly above the $2\sigma_{13CO\,MAP}$ level. $\tau_{12}(blue)$ can therefore range from $\sim$ 17 to $\sim$ 100. There is clearly a large uncertainty associated with these correction
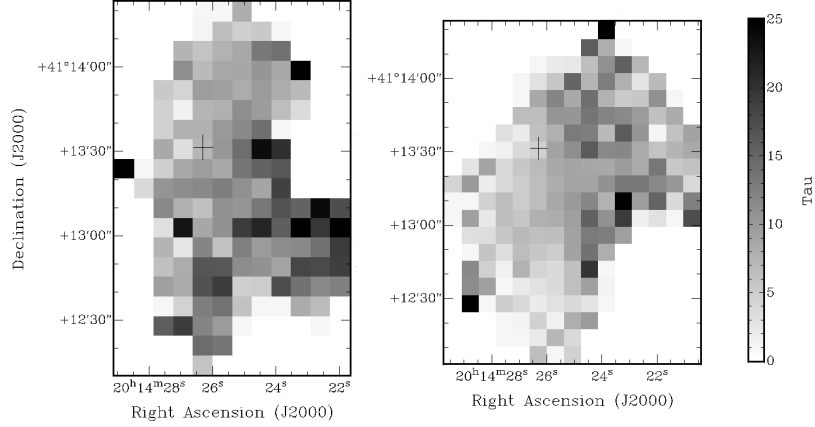
Figure 5.3: Left: Map showing the velocity averaged optical depth for the blue outflow lobe of IRAS 20126+4104 within the aperture mask. The velocity range integrated over is -16 to -5.7 km s^{-1}. The image scales are set to be linear from 0 to 25 and all pixels above $\tau = 25$ are saturated. Pixels with no correction and outside the aperture have an optical depth of zero and are blanked out. Right: As left, but map showing red outflow lobe optical depths integrated within the velocity range -1.1 to 8 km s^{-1}.

values. Overall the effect of large correction factors on the final masses should be minimal as the original ^{12}CO emission they correspond to at the edges of the map are typically small.

A simple clipping method was used to investigate the influence of the higher correction factors due to the noisy edge regions. Any values above a $1\sigma_{\tau 12}$ deviation from the mean were set to unity. The mean and σ were calculated including the higher correction factors. The resulting values are $\tau_{12}(\text{blue}) = 10.7$, $\sigma(\text{blue}) = 6.4$, $\tau_{12}(\text{red}) = 7.5$ and $\sigma(\text{red}) = 6.0$. The revised masses after clipping are 8.5 ± 2.8 and 12.9 ± 2.5 M$_\odot$ respectively. The clipping, although reducing the masses overall, is unnecessary as both mass estimates are comparable given the uncertainties after optical depth correction. Table 5.1 lists masses from this method and methods 2 and 3.

Method 2 - Velocity and Spatially Averaged

Method 2 spatially averages the previously calculated velocity averaged optical depths from method 1. The mean and median τ values within the spatial aperture masks are then used to correct the ^{12}CO only within the optically thick velocity ranges. Method 2 assumes that a single value of τ represents the correction for all emission within the outflow lobe apertures. The mean and median τ values are also recalculated after the clipping performed in method 1. The uncertainties are carried from the variation of the mean and median optical depths when calculated using different velocity ranges as was done previously rather than from the statistical uncertainties used to calculate σ. For IRAS 20126+4104, method 2 provides similar masses to method 1. The masses range from 8.8 to 10.9 $M_\odot$ and 12.1 to 14.3 $M_\odot$ for the blue and red shifted outflow lobes respectively (see Table 5.1). Given the uncertainties, both methods 1 and 2 result in comparable estimates.

It is important that the correction for optical depth is robust if using the averaging methods. There is a deviation up to ~ 2.5 $M_\odot$ when using the same data for methods 1 and 2. Although the variation is within the uncertainties a unified method is required in order to minimise calculation differences between studies and source samples. The velocity averaged optical depth method will underestimate the corrections applied at the very lowest velocities which dominate the emission and overestimates the higher velocity components' contribution. The mass distribution will be the same as the observed flux distribution using a spatially averaged optical depth, and therefore does not correct for regions that are either more or less optically thick. Such over and under corrections will propagate into other outflow parameters. For example, when calculating momentum or energy
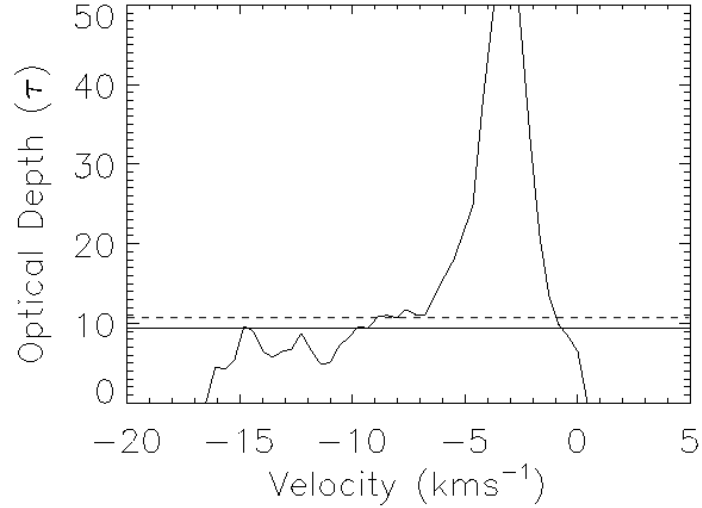
Figure 5.4: Plot of optical depth throughout the blue outflow lobe. The optical depths are larger at lower velocities and decrease towards higher velocities. The velocity averaged optical depth from method 1 is 9.4 and is indicated by the solid horizontal line while the spatial mean from method 2 (10.7) is indicated by the dashed line.

using the mass and velocity of each data cube pixel the use of average optical depth corrections will overestimate the totals of these parameters. Figure 5.4 shows the variation of the optical depth at each velocity increment throughout the blue shifted outflow lobe at the position with the largest ^{13}CO velocity extent. For this particular position the optical depth calculated at every velocity bin is within a factor of 2 of the velocity averaged value from method 1, but at larger velocities the average τ_{12} value a clear overestimate. The step of averaging spatially in method 2 and assuming a single value of τ for the entire region does not represent the optical depth of the emission which varies at all positions. The averaging methods are not representative of the optical depth corrections required at every position and in each velocity bin.

Method 3 - Full Cube Analysis

In order to fully describe the optical depth at every spatial pointing and every velocity, a division of the data cubes is made (method 3). As in method 1, a $1\sigma_{T_A^*}$ threshold is used for the ^{13}CO velocity range. The optical depth is not calculated for any pixel element outside of the maximal velocity extent of the ^{13}CO emission. The correction factor for pixels outside the limiting velocities are set to unity. For every velocity slice τ_{12} is not calculated outside the polygon aperture mask defined by the $3\sigma_{T_A^*}$ level of the ^{12}CO emission. In effect the optical depth is calculated within a variable aperture region for each velocity slice of the data cube. By applying these velocity and spatial limits to the data cubes the computational time required to analytically solve for the optical depths is significantly reduced (compared to dividing and analysing all pixels).

Correcting the ^{12}CO data for optical depths calculated in this manner results in masses of 9.6 ± 3.9 and 14.9 ± 4.0 M$_\odot$ for the blue and red shifted outflow lobes respectively. The uncertainties are estimated as previously noted. Histograms of the calculated optical depth values for the velocities corresponding to the blue and red shifted lobes are shown in Figure 5.5. Tests were done without the aperture limits for each cube slice and resulted in outlier correction values up to ~ 100. There are no such outliers evident in Figure 5.5. The mean values are 10.0 and 7.7 for the blue and red shifted lobes and are similar to those from the earlier methods and in the literature. The masses calculated from these mean values are within the uncertainties of those from the full cube analysis method, but are not exactly the same. The mean values actually over corrects the blue shifted emission and under corrects the red shifted emission overall. Furthermore, there is still the problem
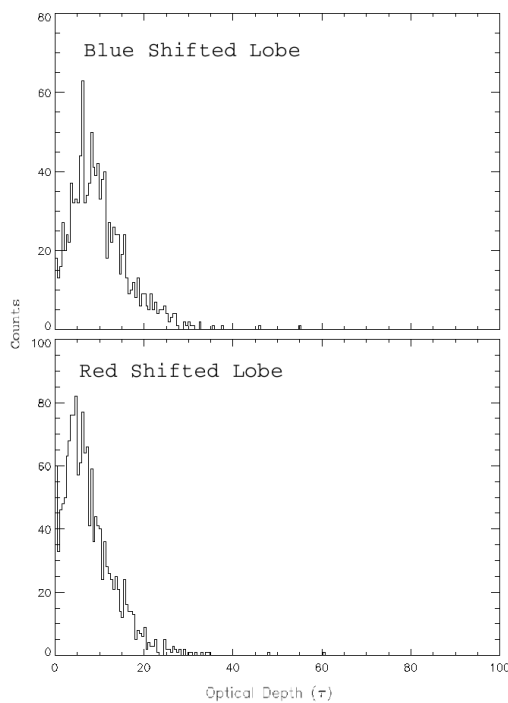
Figure 5.5: Histograms of the optical depth for blue and red shifted outflow lobes within the velocities -16 to -5.7 and 1.1 to 8.0 km s^{-1} respectively.

that averages would over or under correct each pixel and could cause significant variations in other mass based parameters. The full correction method is found to be as easily implemented as the crude averaging methods. Method 3 will therefore be implemented in subsequent analysis as it fully represents the variation in optical depth throughout all velocities and at all spatial positions.

Table 5.1: Masses calculated via all methods. The uncertainties are carried from the mass difference when altering the integration velocities by one velocity bin at the upper and lower velocity limits of each outflow lobe.

Method	Blue Shifted Mass ($M_\odot$)	Red Shifted Mass ($M_\odot$)
Method 1:		
Velocity Average	10.1±3.7	14.6±3.8
1σ Clip from Mean	8.5±2.8	12.9±2.5
Method 2:		
Spatial Mean	10.9±3.8	14.3±3.7
Spatial Median	10.0±3.8	12.9±3.3
1σ Clipped Spatial Mean	8.8±3.3	12.1±3.1
1σ Clipped Spatial Median	8.8±4.2	12.5±3.1
Method 3:		
Full Cube Analysis	9.6±3.9	14.9±4.0

5.4   Outflow Kinematics

Estimates of the momentum (P) and energy (E) can now be made based upon the corrected masses. Both parameters are dependant upon the velocity of the outflowing material with respect to the V_{LSR}. A number of methods presented by different authors are investigated;

Garden *et al.* (1991):

$$P = M|\bar{v}| \tag{5.3}$$

$$E = \frac{1}{2}M|\bar{v}|^2 \tag{5.4}$$

Beuther *et al.* (2002c):

$$P = M|v_{max}| \tag{5.5}$$

$$E = \frac{1}{2}M|v_{max}|^2 \tag{5.6}$$

and Cabrit & Bertout (1990):

$$P = \sum M_i v_i \tag{5.7}$$

$$E = \frac{1}{2} \sum M_i v_i^2 \tag{5.8}$$

In the former two methods the masses calculated in Section 5.3.2 are directly multiplied with a mean or maximum velocity value with respect to the V_{LSR}. The latter method calculates the momentum and energy for each mass M_i in the velocity bin i at the velocity v_i relative to the V_{LSR}. This method fully calculates momentum and energies for each velocity bin and at each spatial pointing, akin to how the optical depth was evaluated at every position and velocity. The V_{LSR} of ~ -3.5 km s^{-1} for Shepherd *et al.* (2000) is used. The extent of the blue and red outflow lobes are therefore -36.5 to -2.2 and 2.4 to 43.5 km s^{-1} with respect to the V_{LSR}.

Table 5.2 indicates the momentum and energy parameters established from the maximum velocity, mean velocity and summation velocity (Garden, Beuther and Cabrit) methods. The uncertainties for the max/mean velocity methods are carried from the original mass uncertainties as this is the major source of error compared with a variation of the max/mean velocity of the outflow by one velocity bin element. The summation method follows the same principles as used when establishing mass uncertainties, i.e. the velocity ranges are varied by $\pm$ one velocity bin when integrating.

The largest parameter values are obtained from the maximum velocity method, as expected. The maximum velocity values potentially overestimate the momentum and energy as the calculation assumes the momentum and energy are a result

Table 5.2: Momentum and Energy values as calculated from the mean, max and summation methods. The use of blue and red is with regards to the blue and red velocity shifted outflow lobes.

Method	Blue mom. $(M_\odot \text{ km s}^{-1})$	Red mom. $(M_\odot \text{ km s}^{-1})$	Total mom. $(M_\odot \text{ km s}^{-1})$	Blue energy (ergs)	Red energy (ergs)	Total energy (ergs)
Vel. Mean	187.2 ± 76.1	342.7 ± 92.4	529.9 ± 119.7	$3.6 \pm 1.5 \times 10^{46}$	$7.8 \pm 2.1 \times 10^{46}$	$11.4 \pm 2.6 \times 10^{46}$
Vel. Max	350.4 ± 142.3	648.0 ± 174.1	998.4 ± 224.9	$1.3 \pm 0.5 \times 10^{47}$	$2.8 \pm 0.8 \times 10^{47}$	$4.1 \pm 0.9 \times 10^{47}$
Summation Vel.	40.3 ± 8.2	77.5 ± 8.3	117.8 ± 11.7	$2.7 \pm 0.2 \times 10^{45}$	$7.4 \pm 0.2 \times 10^{45}$	$10.1 \pm 0.3 \times 10^{45}$

of all the mass in the outflow placed at the maximal velocity from the V_{LSR}. The overestimate would be even larger if the maximal velocity limits of Lebrón *et al.* (2006) are used. In the case of an outflow created by a jet bow shock, the maximum momentum and energy is assumed to be deposited at the same place as the maximum velocity emission (see Figure 2, Arce *et al.*, 2007). However, calculating the momentum and energy in this way assumes the underlying outflow formation method is known and hence an investigation of the various models cannot be undertaken. Even for IRAS 20126+4104, where jets are thought to power the outflow, the mass is distributed at a wide range of velocities, mostly much lower than the maximal value. The crude estimate of momentum and energy assuming all the mass is at the maximal velocities is clearly incorrect and strictly an upper limit. When using a mean velocity between the minimal and maximum velocities of the outflow lobes, the momentum and energy parameters are reduced in comparison to the maximal velocity values. This method still does not account for the mass distribution at different velocities, as now all material is simply placed at an average value. Both mean and maximum velocity calculated momentum and energy values do not parametrise the outflow in a useful fashion and are based upon the sensitivity of the observations and the highest velocities where outflow emission is detected. Using these velocities does not account for the physical matter distribution at all outflow velocities and does not allow the test of various outflow driving methods.

To re-iterate, a source with a large maximal velocity extent would have very high momentum/energy values when calculated using the max/mean velocity methods even if the majority of the mass was at much lower velocities. The mass is theoretically positioned at velocities larger than it physically observed at in these

methods. The velocity extent of the outflow dominates the calculations. Take another source of similar total mass but with majority of the material positioned at larger velocities from the V_{LSR} compared with the first source. This source however, has a smaller velocity extent than the first source. The calculated momentum/energy parameters from the max/mean method would be less than those of the first source, whereas the actual momentum/energy should be larger than the first source as there is physically more material observed at larger velocities. Consequently, any comparisons made between sources in a sample using the max/mean method values and parameters based on these, such as mechanical force and mechanical luminosity, will be disproportionate and not represent the sources correctly. Low momentum sources are actually calculated as high momentum ones and vice versa. Using a summation method, the momentum and velocity estimates are more representative as mass distribution at different velocities is accounted for.

For IRAS 20126+4104 the summation momentum/energy is much lower than that simply calculated from the max or mean velocity methods even though the outflow is thought to be jet driven. The momentum and energy estimates are an order of magnitude less than the maximum velocity method. This is because the majority of the mass is at lower velocities compared to the max and mean velocities. The summation methods will allow the comparison of true high momentum/energy sources (where more material is detected at high velocities) and their parameters with low momentum/energy sources (with the majority of material observed at relatively low velocities) for the full sample of sources. Furthermore, the momentum can be analysed in a spatial sense in order to investigate the different outflow generation models. This also exemplifies why the optical depth correction must be undertaken at all positions and velocities as the simple averages would

not have the correct mass distributions to base the momentum and energy calculations on. With the summation method the momentum and energy values are no longer dependant upon the sensitivity of the observations where weak emission is detected out to larger velocities. Considering the high velocity emission missed due to the velocity extent cutoff the summation method may underestimate the total momentum by ~ 10 percent and energy by ~ 40 percent. The momentum is within the uncertainties of the summation method itself, however, the energy missed is larger than the summation method uncertainties but is well below the max and mean velocity estimates.

For all calculations however, the velocity is assumed to be entirely in the line of sight. Therefore the true outflow velocity is underestimated, unless the outflow is actually directly in the line of sight. For IRAS 20126+4104 this is not the case as a clear spatial offset is observed between the blue and red shifted outflow lobes. A correction could be made via $(1/\cos(\theta))$ under the assumption that the path of the outflow is linear. For more complex geometries, if the outflow follows a parabolic path, the inclination will vary at different spatial positions. Without correction Cabrit & Bertout (1990) report that objects at an inclination of $\sim 70°$ (where $0°$ is an outflow entirely in the line of sight) could have parameters an order of magnitude too small. Assuming the summation method values are correct, being the closest possible method to an ideal integral, then the maximal velocity method results in parameters nearly two orders of magnitude larger. Although the maximum (and mean) velocity methods are extremely fast, they are not robust and they do not result in representative source parameters. The summation method will be used in all future analysis.

5.5 Outflow Dynamics

The remaining parameters to establish are based upon the mass, momentum and energy. These are the dynamical timescale (T_{dyn}), the mass outflow rate $(\dot{M})$, the mechanical force (F_m) (also referred to as the momentum supply rate/flux) and the mechanical luminosity (L_m). The latter three parameters depend directly upon the calculation of the dynamical timescale itself. This is the time required for the outflow to cross a specific flow dimension, (R).

5.5.1 Calculating the Dynamical timescale

The dynamical timescale can be calculated in a number of ways. Beuther et $al.$ (2002c) employ a simplistic method to estimate T_{dyn}, using the maximal radius of the outflow R_{max} divided by the maximum flow velocity V_{max}. Snell et $al.$ (1984) use a different characteristic velocity, the intensity weighted velocity $\langle V \rangle = P_{total}/M_{total}$, where the momentum for each spatial position has been calculated via $P_i = \sum M_i v_i$. The authors also use a different outflow extent, $R_{max}/2$. Dynamical time estimation using V_{max} will always result in a shorter time than any other methodology for the same R value. Thus, the corresponding outflow rate, force and luminosity would be maximal values. An R_{peak} distance parameter is also introduced below for an alternative comparison. This is the average of the distances from the central source to the location of peak mass in the blue and red integrated maps. Furthermore, a method similar to the one introduced by Lada & Fich (1996) is applied to high mass outflows for the first time. Here both R and $\langle V \rangle$ are calculated at all spatial positions in the outflow lobes. From the integrated maps $R_{x,y}$ is the outflow extent at a given pixel (x, y) offset from the source and

$\langle V_{x,y} \rangle$ is the intensity weighted velocity calculated from $P_{x,y}/M_{x,y}$ at each spatial location. Therefore the dynamical timescale, mass outflow rate, mechanical force and mechanical luminosity maps can be produced.

For IRAS 20126+4104, $R_{max} = 81$" (0.66 pc), $R_{peak} = 38$" (0.31 pc), $V_{max} = 40$ km s^{-1} and $\langle V \rangle = P_{total}/M_{total} = 5.4$ km s^{-1}. The resulting dynamical timescales (T_{dyn}) span over one order of magnitude from 7.5×10^3 yrs to 1.2×10^5. Table 5.3 lists all average values of T_{dyn} and indicated the method used to calculate each estimate. The weighted mean flow velocities calculated at each spatial position vary between 2.4 and 9.6 km s^{-1} for the blue shifted outflow lobe and 2.6 and 22.5 km s^{-1} for the red shifted outflow lobe. The larger velocities are generally located at greater distances from the central source. The spatial average for the entire outflow lobes are $\langle \bar{V} \rangle_{blue} \sim 3.7$ and $\langle \bar{V} \rangle_{red} \sim 6.2$ km s^{-1}. The overall average is ~ 5 km s^{-1}, close to that calculated simply from P_{total}/M_{total}. Using the overall average velocity as a lower velocity limit, $T_{dyn} = 1.3 \times 10^5$ yrs is an upper limit when $R = R_{max}$.

The dynamical timescales calculated for each pixel element (x, y) range from 8.1×10^3 to 2.3×10^5 yrs and roughly coincide with the absolute values calculated from the spatial averages. The larger timescales are located at the aforementioned morphologically chaotic positions at lower velocities (see Section 5.3). Lower dynamical timescales, of the order 10^4 yrs are located in regions where the outflow lobes are spatially separated and at higher velocities. Figure 5.6 clearly shows the variation of the dynamical timescales for the blue and red shifted outflow lobes. A gradient in T_{dyn} is seen when moving outwards from the centre to the north-west and south-east for the blue and red shifted outflow lobes respectively. The largest timescales estimated in the lobe regions are the furthest away as the velocities de-
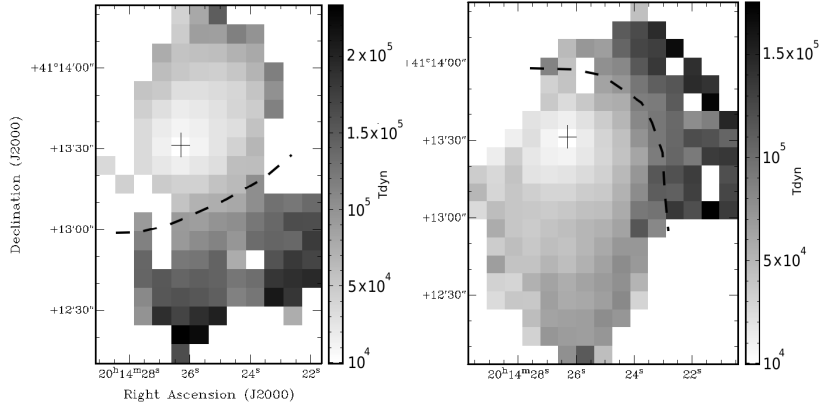
Figure 5.6: Left: Map showing the variation of the dynamical timescale calculated at all spatial positions within the blue shifted outflow lobe aperture mask. The plus symbol indicates the central location of the source, IRAS 20126+4104. The dashed black line indicated the rough divide between the slower moving 'chaotic' structured material and the higher velocity, northerly offset blue shifted outflow lobe. Note the shorter dynamical timescales of the order 10^4 for the spatially offset higher velocity material. Right: As left but map for the red shifted outflow lobe. Plus symbol and dashed line have same meaning.

crease at the very furthest extents of the outflow lobes. For comparison with the previous T_{dyn} values, the spatial average here is $T_{dyn} = \langle R_{x,y}/\langle V_{x,y} \rangle \rangle = 8.0 \times 10^4$ yrs (see Table 5.3). Shepherd *et al.* (2000) list a dynamical timescale of 6.4×10^4 yrs whereas earlier work by Wilking *et al.* (1990) provide a much lower estimate of 2.1×10^4 yrs. Both are comparable with the estimates here.

Dynamical timescales are often used to represent the age of the outflow and the jet or wind driving source, however, this may not be the case. Curtis *et al.* (2010) find no correlation between T_{dyn} and the age of the central source (based upon source bolometric temperature). Furthermore, methods using a single distance parameter do not represent the range of timescales that could be present within the outflow due to different velocity components at different spatial locations (assuming that all material has flowed out from the central source position

and the velocity is along the outflow axis). Generally the outflow material is swept up from the surrounding envelope due to a wind or jet (see Chapter 1, or Cabrit *et al.* (1997)). Provided the molecular material is travelling at the velocity of the jet/wind at the observed spatial location, then T_{dyn} will relate to the timescale of the jet/wind propagating from the central source and the following flow, force and luminosity estimates will be related to the driving jet or wind. Realistically, the jet/wind and molecular material may not be at the same velocity dependent on the interaction between them. In their models of low mass jet driven outflows Downes & Cabrit (2007) find the spatial calculation is more representative of the jet lifetime than that calculated from the overall weighted velocity and R_{max}. However, the authors also find that V_{max} gives the best representation of the true jet advance speed and consequently the best estimate of T_{dyn}. This may mean that using the intensity weighted velocities, which represent the bulk mass of the outflow, actually overestimate T_{dyn} at all spatial locations. Due to the ease of each T_{dyn} calculation all the methods will be undertaken for the full sample in order to compare each method for the different sources. If the sources in the sample span a range of evolutionary stages there may be intrinsic difference or trends in the alternative T_{dyn} estimates.

5.5.2 Outflow rate, force and luminosity

The mass outflow rate $(\dot{M})$ $M_{x,y}/T_{dyn,(x,y)}$, the mechanical force (F_m) $P_{x,y}/T_{dyn,(x,y)}$ and the mechanical luminosity (L_m) $E_{x,y}/T_{dyn,(x,y)}$ can be calculated at each spatial position following the spatial calculation of the dynamical timescale. Figure 5.7 shows the maps for the outflow rate, force and luminosity. Regions which had larger timescales contribute less to the mass outflow, mechanical force and mechanical

Table 5.3: Dynamical timescales estimates from various methods.

Method	T_{dyn} (yrs)
$\frac{R_{max}}{V_{max}}$	1.6×10^4
$\frac{R_{max}}{\langle V \rangle}$	1.2×10^5
$\frac{R_{max}}{\langle V \rangle}$	1.3×10^5
$\frac{R_{peak}}{V_{max}}$	7.5×10^3
$\frac{R_{peak}}{\langle V \rangle}$	5.6×10^4
$\frac{R_{peak}}{\langle V \rangle}$	6.1×10^4
$\langle \frac{R_{x,y}}{\langle V_{x,y} \rangle} \rangle$	8.0×10^4

Note. The large angular brackets around the (x, y) data represent the spatial average of all values the dynamical timescale at all x, y locations within the aperture masks.

luminosity whereas regions with lower timescales contribute the most. It is obvious that spatial positions with larger mass, momentum and energy provide a larger fraction of the dynamical parameters. For IRAS 20126+4104, the spatial regions that contribute most to the dynamic parameters are those which are coincident with the higher velocity outflow lobes (see Figure 5.2), located away from the central regions, to the north-west and south-east for the blue and red shifted lobes respectively. The low velocity, chaotically structured material does not contribute a significant fraction to the dynamical parameters, as expected.

The total mass outflow rate is $\dot{M} = 6.2 \times 10^{-4}$ M$_\odot$ yr^{-1}, the mechanical force is $F_m = 3.2 \times 10^{-3}$ M$_\odot$ km s^{-1} yr^{-1} and the mechanical luminosity is 2.5 L$_\odot$ when each map is summed within the defined aperture masks. Upper and lower limits for the outflow rate, force and luminosity are calculated directly using the lower and upper limits of T_{dyn} above and are 3.2×10^{-3} M$_\odot$ yr^{-1}, 15.7×10^{-3} M$_\odot$
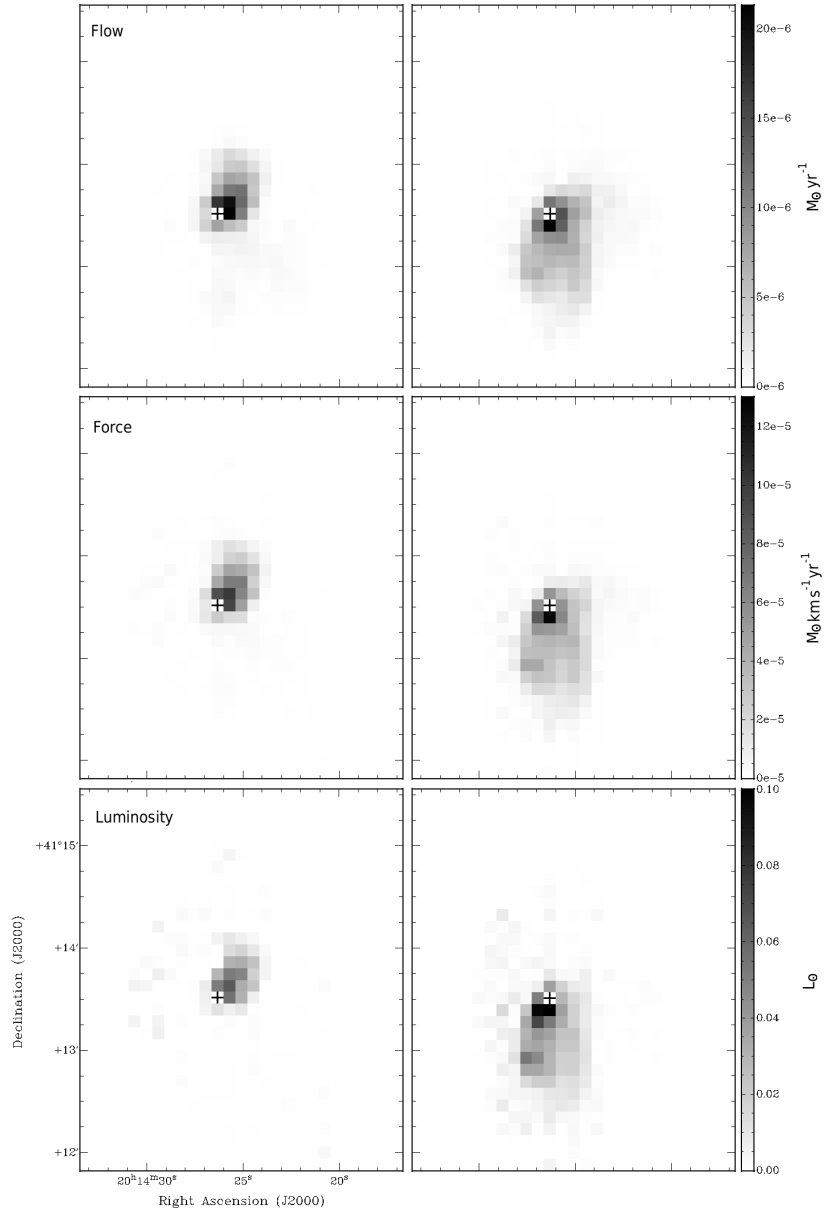
Figure 5.7: Plots of the mass outflow rate, mechanical force and mechanical luminosity from top to bottom and as indicated in the top left of each plot on the left hand side of the figure. The blue shifted outflow lobes are plotted on the left hand side while the red shifted outflow lobes are plotted on the right. The majority of the flow, force and luminosity are from regions with lower dynamical timescales (Figure 5.6) and large velocities (Figure 5.2). There is emission right up to the edge of the aperture masks however it is a factor of ~ 100 less than the peak value and difficult to see on the linear colour scale. The faint emission only corresponds to ~ 5 percent more emission compared to what can be clearly defined and corresponds directly to high velocity regions as Figure 5.2. The plus symbol marks the RMS source location.

km s^{-1} yr^{-1}, 19.3 L$_\odot$ and 1.9$\times$10^{-4} M$_\odot$ yr^{-1}, 9.1$\times$10^{-4} M$_\odot$ km s^{-1} yr^{-1}, 1.1 L$_\odot$ respectively. Note, the upper limits from the lowest T_{dyn} calculated via R_{peak}/V_{max} could be more representative of these parameters for a jet driven outflow. The method of calculating the dynamical timescales at each spatial position allows the mass outflow rate, mechanical force and mechanical luminosity to be investigated spatially and provides an extra means to compare outflows from different sources. As above, all methods are easy to implement for dynamical parameters and will be compared for the full source sample. Furthermore, comparisons to models of outflows from MYSOs and HII, possibly scaled up from low mass source, would be very useful in establishing whether there is a unified outflow driving mechanism and hence unified star formation scenario.

5.6   IRAS 21026+4104 Summary

The selected analysis pathway has lead to values comparable with other outflow sources (Beuther *et al.*, 2002c; Ridge & Moore, 2001; Shepherd & Churchwell, 1996, e.g.). For IRAS 21026+4104 a slight decrease of the dynamic parameters are found compared with Shepherd *et al.* (2000). The lower mass is the driver of the smaller momentum and energy values. It is likely that mass previously associated with the outflow in other works is not part of the outflow in following the $3\sigma_{T_A^*}$ spectral velocity limit and the $3\sigma_{MAP}$ level contour aperture masks. This cannot be confirmed without knowing the exact spatial mask used in the literature. Furthermore, the contribution of core material to the mass of the outflow has been removed here using the C^{18}O line as a proxy for the core velocity range. This has not been undertaken by Shepherd *et al.* (2000) and their calculated outflow masses

Table 5.4: IRAS 20126+4104 outflow parameters

Parameter	Value
Distance (kpc)	1.7
Outflow mass:	
Redshifted ($M_\odot$)	14.9
Blueshifted ($M_\odot$)	9.6
Total ($M_\odot$)	24.5
Momentum ($M_\odot$ km s^{-1})	118
Kinetic energy (ergs)	1.1×10^{46}
Average dynamical timescale (yr)	8.0×10^4
$\dot{M}$ ($M_\odot$ yr^{-1})	6.2×10^{-4}
Mechanical force ($M_\odot$ km s^{-1} yr^{-1})	3.2×10^{-3}
Mechanical Luminosity ($L_\odot$)	2.5

may be contaminated by core material. Furthermore, the CO(3-2) transition is less likely contaminated by core emission compared to the CO(1-0) transition where lower excitation temperatures means there is significantly more ambient emission. The parameters reported here also conform to the upper limits as listed in Lebrón *et al.* (2006) where V_{max} velocities are used in their calculations. Table 5.4 indicates the final adopted source parameters.

5.7 Consistency Checks

Before applying the established methodology to the full sample of 99 sources another two well known outflow sources are investigated as a consistency check. Because outflow regions are complex the methodology established for the isolated test source IRAS 21026+4104 may not be ideal in representing other sources. The two consistency check sources are G010.8411-02.5919 and G012.9090-00.2607. These

are also known as GGD27 and W33A and were both introduced in Chapter 1. The methodology is undertaken in a step by step manner. First the velocity limits are established, then the outflow lobe integrated maps are produced and apertures defined. The mass, momentum, energy, kinematic and dynamic parameters are then calculated.

The main outflow from G010.8411-02.5919 is close to the plane of the sky in a north-south direction. Although the ^{12}CO data indicates an overlap in the blue and red shifted lobes suggesting the outflow is not perfectly in the plane of the sky assuming the velocity component is in the direction of the outflow away from the source. G012.9090-00.2607 has an outflow in the south-east to north-west direction and is inclined to the line of sight. The blue shifted outflow lobe is coincident with the near-infrared reflection nebula to the south-east of the RMS source location. Similar to the source S140-IRS1 (Chapter 2 and 3), the nebula is created by light reflected from the inner walls of the cavity carved out by the blue shifted outflow material.

Using the $3\sigma_{T_A^*}$ spectral noise threshold the velocities of the blue and red shifted material are easily defined and integrated outflow lobe maps are generated. However, for GGD27 the $3\sigma_{MAP}$ integrated map noise contour level does not clearly define the outflow region due to the strength of the emission elsewhere in the map. Instead a vast area of the map is selected as the outflow spatial extent. There is clearly emission not associated with the outflow within the aperture. For W33A there is strong emission over the majority of the blue and red shifted outflow integrated maps and σ_{MAP} cannot be defined as there are no emission free regions. Using the empirical calculation, $\sigma_{MAP}=\sigma_{T_A^*} \sqrt{n} \, \delta v$, σ_{MAP} is ~ 1.2 K km s^{-1} for both the blue and red shifted outflow maps. All map emission is well above $3\sigma_{MAP}$,
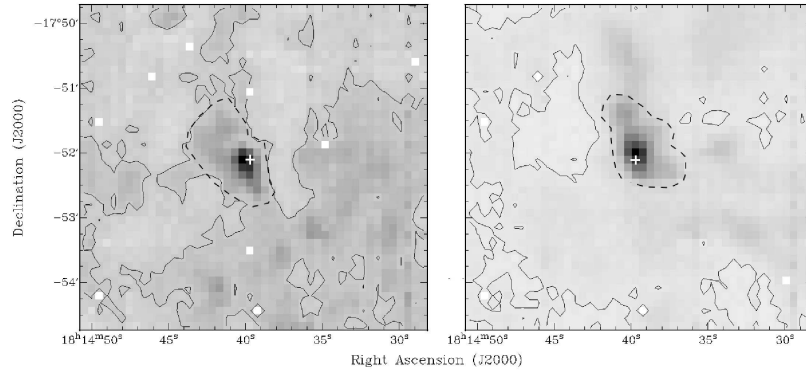
Figure 5.8: Left: Map of the blue shifted outflow lobe produced when integrating between 7.0 and 32.6 km s^{-1} for the source W33A. The contour level corresponds to $20\sigma_{MAP}$ which does not define the outflow emission well. The dashed line indicates where the outflow emission would be selected if done by eye. The plus symbol corresponds to the RMS source location. Right: As left but for the red shifted outflow lobe where velocities were integrated between 40.2 and 73.0 km s^{-1}.

and only at $\sim 30\sigma_{MAP}$ does the contour level define the outflow edge as would be defined by eye (see Figure 5.8).

Variable limits from $3\sigma_{MAP}$ and in excess of $10\sigma_{MAP}$ have recently been used to analyse similar JCMT CO outflow data (Mark Thompson, private communication). However, such analysis diverts from a consistent method for all sources. There is no justification in selecting a particular noise level for a given source. The $3\sigma_{MAP}$ limit would grossly overestimate the total mass of the outflow from W33A and the directly dependant parameters of momentum and energy. If the ambient material is at a low velocity with respect to the V_{LSR} and distant from the RMS source location the dynamical timescale will be significantly larger than the material in the outflow itself. As can be seen in Figure 5.7 the mass outflow rate, force and luminosity are dominated by the lower dynamical timescale, high velocity regions which trace the outflow lobes in the case of IRAS 20126+4104.

Therefore these parameters should not be overestimated even in the case where the mass apertures are ill defined.

The established $3\sigma_{MAP}$ noise aperture mask method is not ideally suited to other well known complex outflow regions. Furthermore, the choice of an aperture mask at different noise levels will result in considerably different outflow masses. The mass variability exemplifies why a consistent methodology is required. A new summation aperture definition is needed. A $3\sigma_{MAP}$ noise aperture mask could be defined from the ^{13}CO emission which is used to correct for optical thick regions. However, it is very likely that higher velocity emission is more spatially extended and would be missed with such an aperture definition. An aperture mask defined from the optically thin ^{12}CO emission would have to be used in conjunction with the ^{13}CO aperture mask. Alternatively, a different noise level definition be employed. The aperture mask could be defined as all emission above $3\sigma_{MAP}$ of the median map emission. Such a description allows a single consistent methodology to be followed that justifies why the absolute noise level varies. For a source such as IRAS 20126+4104, where the majority of the integrated map is noise, the median will be close to zero. Hence the aperture mask defined by emission above $3\sigma_{MAP}$ of the median will be close to the actual $3\sigma_{MAP}$ noise level itself. For a source such as W33A it is expected that the median will be a representative value of the ambient emission much larger than the $3\sigma_{MAP}$ noise level. The emission above $3\sigma_{MAP}$ of the median would then define the outflow spatial extent. These new methods are yet to be tested, however, they must result in values consistent with those from the $3\sigma_{MAP}$ noise aperture mask for the initial test source IRAS 20126+4104.

5.8 Conclusions

Multiple methods have been investigated for estimating source outflow parameters. A particular methodology has been identified to calculate outflow masses, kinematic and dynamic parameters from massive YSOs. From the ^{12}CO outflow data emission above a $3\sigma_{T_A^*}$ spectral noise threshold is used to define the maximal velocity extent of the outflow. Previously analysed C^{18}O data is used to define the lower velocity limits for the outflow. Spatial aperture masks are defined based upon the $3\sigma_{MAP}$ integrated map noise contour level for the ideal, isolated test source IRAS 21026+4104. This noise level is a good representation of the integrated outflow emission as would likely be selected by eye in this case. In order to establish outflow masses, the optical depth is accounted for by means of comparison with ^{13}CO emission. Optical depths are only calculated for velocities where the ^{13}CO emission is present above the $1\sigma_{T_A^*}$ spectral noise level and ^{12}CO emission is present above the $3\sigma_{T_A^*}$ spectral noise level. The correction factors are calculated at every position and velocity rather than from simple velocity or spatially averaged intensity ratios.

Momentum and energy parameters are also calculated at every spatial position and in every velocity bin where emission is detected. The aforementioned velocity ranges and apertures are used as the integration and summation limits. Average or maximal velocities are not used in momentum or energy calculation as the resulting parameters mis-represent the outflow sources and are typically upper limits. For IRAS 21026+4104 such crude estimates suggest the source outflow energy is nearly two orders of magnitude larger than it ought to be. The full spatial and velocity analysis method is much more robust in describing outflow sources as this process

is closest to an ideal integral.

The average dynamic timescales reported are not used directly except as upper and lower limits, although the lower limits could be more representative of a jet driven outflows. Calculation of the dynamical timescale at different positions allows any variations to be mapped. The mass outflow rate, the mechanical force and the mechanical luminosity at every spatial position is easily calculated following the spatial analysis of the dynamical timescale. Mass outflow rate, mechanical force and mechanical luminosity maps highlight which regions contribute most to each parameter. In the case of IRAS 20126+4104 regions closer to the source with lower velocities, or more distant but with larger velocities are responsible for larger percentages of the total flow, force and luminosity. A spatial summation within the previously defined $3\sigma_{MAP}$ integrated map apertures is used to attain the final source parameters. The various methods explored to calculate the dynamical parameters will all be investigated for the full sample as they are easy to implement. Differences may arise in the parameters for different source types or evolutionary stages.

IRAS 20126+4104 is an ideal and isolated test source where the ^{12}CO emission is solely associated with the source itself. Further consistency checks have discovered that for two more complex outflow sources, GGD27 and W33A, the $3\sigma_{MAP}$ contour level is not representative of the emission associated with the outflow. Alternative methods have been suggested. Apertures could be defined by a combination of the ^{13}CO and optically thin ^{12}CO emission or by using a contour level corresponding to emission above $3\sigma_{MAP}$ of the median emission. The median value should represent the general ambient emission in the region. Testing of these new methods must conform to the parameters established for IRAS 20126+4104

using the $3\sigma_{MAP}$ contour level aperture mask.

Once the aperture mask is defined the core and outflow parameters can be compared in order to investigate variation with evolution, source type, source stellar type, and core and stellar masses. Furthermore, velocity and momentum maps can be compared and contrasted with those from models to establish whether a single outflow driving method is predominant or whether multiple methods are required to explain the full range of outflows observed. Similarly, more detailed modelling of MYSO outflows is required to fully understand the dynamical parameters and the interaction between the driving jet or wind and the molecular emission observed. Finally, comparisons can be made between these massive star forming regions and low mass outflow sources to investigate whether outflow parameters scale with stellar properties.

Chapter 6

Conclusions

This thesis contains both high resolution millimetre continuum observations and detailed RT modelling of a unique archetypal ionised disc wind source as well as lower resolution single dish sub-millimetre line observations of 99 MYSOs and HII regions. The high resolution observations have allowed S140 IRS1 to be investigation in unprecedented detail at the smallest scales accessible, while the cores and outflow work has confirmed that the sample is representative, unlike some previous samples, and can be used in a more statistical sense. The following Sections summarise each science Chapter in this thesis, provide an overview on how the work is related and also discusses possible avenues for future work.

6.1   Summary

The new, high resolution (~ 0.1"), high sensitivity, CARMA A millimetre wavelength continuum observations presented in Chapter 2 are the first to confirm that S140 IRS1 is indeed an ionised disc wind source. A dust disc is found to align with the radio emission and is also perpendicular to both the bipolar CO emission and

near-IR speckle images tracing the outflow. Models by Drew *et al.* (1998) suggest that ionised disc winds can arise in sources with near main sequence parameters when radiation pressure on the surface of the disc becomes important. Confirming the disc wind nature of S140 IRS1 suggests that radiation pressure is an important feedback process for the later stages of MYSOs. The observed low mass of the disc around S140 IRS1 supports such an evolutionary stage and actually positions the protostar as a pre-UCHII region source that has nearly attained main sequence parameters.

Comparing S140 IRS1 and Cep A HW2, two sources of very similar luminosity, provides more evidence for the late evolutionary stage of S140 IRS1. Cep A HW2 is deeply embedded and not visible at 24.5 μm while S140 IRS1 is visible. The CO molecular outflow from Cep A HW2 is much more collimated than that from S140 IRS1 which is very diffuse, even when observed with interferometers (see Chapter 2). The outflow from S140 IRS1 could have originally been jet driven and well collimated (similar to Cep A HW2) but as envelope material has been ejected and dispersed over time the outflow opening angle could have become wider. Cep A HW2 is still deeply embedded, probably swollen and accreting large amounts of material and has a CO outflow powered by a collimated jet. It is probably a much younger source and is less evolved. Swollen protostellar phases are required in population synthesis models in order to match observed luminosity distributions of MYSOs (Davies *et al.*, 2011). Similarly, GGD27 is an embedded MYSO with a very collimated radio jet, a bipolar CO molecular outflow and a ~ 500 au rotating molecular structure surrounding compact millimetre continuum emission (Aspin, 1994; Fernández-López *et al.*, 2011b; Yamashita *et al.*, 1989).

Both GGD27 and Cep A HW2 appear to be much higher mass analogs of low

mass protostars. S140 IRS1 however is different and is likely more evolved. One possible scenario is that it has began to contract towards ZAMS parameters and heat up (Hosokawa & Omukai, 2009). It is probably no longer actively powering the outflow via a jet as there is no evidence for radio jets or Herbig-Haro objects in the outflow direction. Radiation pressure will have increased over time and S140 IRS1 become sufficiently hot to ionise the surface of the surrounding dust disc to produce the radio wavelength disc wind emission observed, but crucially, has not ionised the surrounding material. Following this scenario the final transition stage for S140 IRS1, before producing a large scale HII region, would be the development of a bipolar HII region similar to the other known disc wind source S106 IR (Hoare *et al.*, 1994). There is no evidence of a smooth, large scale disc or torus around S106 IR (Richer *et al.*, 1993) but there is a compact, hot disc disc as inferred from strong CO band-head emission (Chandler *et al.*, 1995). It is likely S106 IR is contracted onto the main sequence and hence able to ionise the less dense bipolar regions that could have been excavated by strong jets and outflows earlier in its evolution. There is no evidence for a larger scale or bipolar HII region around S140 IRS1 at low resolutions (Evans *et al.*, 1989) like that observed for S106 IR (Bally *et al.*, 1983).

Chapter 3 detailed the modelling of the prototype source S140 IRS1 with the Whitney code adapted to massive star forming regions. This is the first time the millimetre visibilities and images, IR image and SED of an MYSO have been modelled with a 2D axi-symmetric environment. Comparisons of the models were made with literature observations, alongside the presented CARMA A and B interferometric data, in order to constrain the cavity geometry, spectral energy distribution and millimetre visibilities simultaneously. Initial 1D azimuthally averaged visibili-

ties of the CARMA B observations indicate that a low mass disc is required in the models as the envelope itself cannot provide flux on the smallest scales probed. The small size and mass of the modelled disc strongly agrees with the conclusion that S140 IRS1 is a pre-UCHII region source with an eroding disc.

Using the highest resolution CARMA A data a new method was developed to extract the two dimensional major and minor axis visibilities in order to constrain the position angle of the disc around S140 IRS1 using a representative model rather than common Gaussian fitting. The 2D method found the PA to be $\sim 44°$ which corresponds directly to the PA of the ionised equatorial disc wind emission detected at 5 GHz. The result provides further support that S140 IRS1 is a prototype equatorial ionised disc wind source. The best fitting disc radius and mass were 120 au and 0.020 $M_\odot$ although there is a distribution of parameters that produce other well fitting models.

The optically thin $C^{18}O$ (3-2) emission associated with the cores of 99 MYSOs and HII regions is analysed in Chapter 4. The final sample of 87 sources are complete to a luminosity limit of 10^3 $L_\odot$ and distance limit of 6 kpc. This is currently the largest homogeneous and representative sample of such sources to be investigated. A consistent methodology for establishing the masses of the cores is defined via velocity integration and summation with an aperture. The reduced sample of sources have a range of masses and luminosities independent of distance and are representative of MYSOs and HII regions. All the cores are consistent with containing at least one massive protostar which has attained its ZAMS luminosity. Although HII regions occupy a specific region in mass-luminosity diagrams there is still a considerable overlap with MYSOs. Within the MYSO category there are massive protostars at slightly different evolutionary stages according to their

position on model PMS tracks (Molinari *et al.*, 2008) and from their infrared colours. Dependent on the sources evolutionary stage, variations may arise in their outflow parameters. The majority of core masses measured are associated with the cluster of sources in the region and not just that associated with the massive protostar.

The line width and size relationship (Larson, 1981) is not observed for the representative sample of sources at distances < 6 kpc, but a correlation is found when including source at distances > 6 kpc. Other authors report similar findings and arrive at the same conclusion that the spatial range traced by $C^{18}O$ is limited and turbulence does not vary significantly and is not the main driver of the line widths measured (Buckle *et al.*, 2012). The velocity dispersions are correlated with the core masses as expected for virialised cores. The strong correlation between mass and radius could be the underlying reason for the line width and size relationship when sources > 6 kpc are included. The core and virial masses are strongly correlated although the virial masses are a factor of 4 lower. The discrepancy initially suggests the cores are not in virial equilibrium, however, the absolute difference in mass estimates can be reconciled by adjusting the core radius to better suit that associated with the most massive source rather than that of the cluster.

Chapter 5 investigates numerous outflow analysis methods in order to document a consistent process and apply that to the representative sample of outflow candidates. Uniquely, the inner velocity limits separating the outflow and core material are set by the velocity extent of the core from the $C^{18}O$ (3-2) emission. For an ideal, isolated test source the method used to estimate the core masses can be used to estimate the outflow masses from ^{12}CO (3-2) emission. Further outflow parameters are found to be most representative when calculated at all velocities

and spatial positions where emission is mapped rather than using crude averages or maximal velocity assumptions. The current mass aperture method is difficult to undertake for more complex regions where significant ^{12}CO emission is present and the outflow spatial extent is unclear. An alternative definition is required to fulfil the original criterion of a consistent, repeatable outflow analysis method.

6.2   Overview

The large samples of source taken with the JCMT provides a statistical overview of the sources. However, it is imperative that these sources are investigated in detail with high resolution observations as was done for S140 IRS1. To provide a much more comprehensive picture the spatial scales between the single dish and very highest resolution observations must also be probed.

The core emission for S140 IRS1 measured at lower resolutions is a combination of that from the IRS and SMM sources as well as the diffuse inter core material. The single dish C^{18}O observations by Minchin *et al.* (1995b) show how the core associated with S140 IRS1 is of a similar size to those from the sample presented in Chapter 4. The material observed even at the lower interferometer resolutions with OVRO and SMA (Chapter 2) however, is definitely dominated by that associated with the MYSO, S140 IRS1, alone. In mass luminosity diagrams S140 IRS1 would be classified as a light source given the small core mass from the interferometric observations. Scaling the ZAMS stellar mass to a core mass and plotting again in the mass luminosity diagram would position S140 IRS1 as a heavy source along the same best fit line as the HII regions from Chapter 4. When using the information from both spatial scales the general consensus is that S140 IRS1 is still positioned

as a more evolved MYSO. The mass luminosity diagram presented in Chapter 4 using single dish observations is a useful tool in establishing the rough evolutionary stage of a wide sample of sources.

Using the core mass and source luminosity as a first estimate of source evolutionary status the final outflow parameters can also be investigated for evolutionary trends. The single dish outflow parameters for S140 IRS1 (Hayashi *et al.*, 1987) are at least an order of magnitude less than those calculated for the source IRAS 20126+4104 (Chapter 5). The result that S140 IRS1 is a late stage MYSO, in conjunction with its weakly collimated outflow suggests that outflows do evolve with time and become less collimated, less massive and less energetic when radiative feedback becomes important. S140 IRS1 may be at a very rare stage in evolution where the outflow is very weak and the ionised disc wind is observable before a full HII region develops. Similar sources may be found in the representative sample of MYSOs and HII regions from the RMS survey. These sources can be targeted as disc wind candidates and be investigated at higher resolutions to add further pieces to the sparsely filled jigsaw that is massive star formation.

6.3   Future Work

It has been noted multiple times that large scale surveys are required at high resolutions. The Leeds led e-MERLIN legacy program has guaranteed time to observe ~ 75 MYSOs at sub-arcsecond resolutions at centimetre wavelengths. The distance limited sample selected from the RMS survey will probe the ionised emission from these sources and be used in conjunction with the JCMT outflow data to establish the likely source of the ionised emission, be it from jets or disc winds. In order to

confirm radio emission from jets or disc winds comparable resolution millimetre observations, like those presented in Chapter 2, are required. For southern sources such observations are possible with ALMA. The e-MERLIN sources however, are too northern to be targeted and larger time allocations on current interferometric arrays (CARMA, SMA, PdBI) are required. Furthermore, Zeeman splitting of maser emission will be used during the e-MERLIN survey to investigate the magnetic fields of MYSOs (e.g. Vlemmings, 2008). The magnetic field direction for the previously discussed source Cep A HW2 is aligned with the jet and outflow emission. The agreement could suggest that magnetic fields are important in the formation and collimation of jets in younger MYSOs and the regulation of the infall and outflow close to the source (Vlemmings *et al.*, 2010). Maser emission is present around S140 IRS1 and a similar investigation could provide insights into the evolution or lack of magnetic fields for more evolved sources.

In the context of the millimetre/sub-millimetre wavelength observations presented in this thesis, sensitive observations at resolutions higher than ~ 0.3" probing scales < 1000 au for sources out to ~ 3 kpc are becoming easily accessible and are required to probe the disc scales around MYSOs. CARMA can already achieve resolutions of ~ 0.1 arcsec which is currently the highest resolution available in the northern hemisphere. The planned upgrade to PdBI, NOEMA (Northern Extended Millimetre Array), will yield similar resolutions to CARMA A but cover a wider frequency range, have a much larger bandwidth and greater sensitivity in comparison to both the current PdBI and CARMA arrays. ALMA is already achieving resolutions of ~ 0.4 arcsec at 350 GHz in cycle 0 observations and has detected a candidate circumbinary disc around the source G35.20-0.74N (Sánchez-Monge *et al.*, 2013). These observations detect the CH_3CN molecular line typically

used to trace disc rotation (see Chapter 1). When fully commissioned ALMA will provide a resolution < 0.05 arcsec at millimetre wavelengths and produce images of unprecedented detail and fidelity. Observations of the dust continuum emission and molecular line known to trace rotation in discs, such as CH_3CN, HC_3N, SO_2 and CH_3OH can also be used to investigate the temperature structures of sources, while any differences in chemistry between sources could be due evolution. The increased bandwidth capabilities would permit the investigation of a variety of different species beyond the typical hot core and disc rotation tracers. Such data used in conjunction with that available in the literature (as Chapters 2 and 3) will provide a firm footing for understanding massive star formation.

Although single wavelength observations themselves can provide detailed information about discs or jets, for example, it is the combination of multiple observations at different wavelengths and resolutions in conjunction with models that will help answer the remaining questions in massive star formation. Near-infrared spectroscopy has found that commonly detected emission lines, Brγ, H_2 and the CO band-head vary between different MYSOs and HII regions (Cooper *et al.*, 2013). It would be interesting to investigate how these lines correlate with CO molecular outflows observed in the millimetre regime as the current consensus is that the strength of these lines and the outflow force are correlated with source luminosity. Both Brγ and H_2 are produced in outflow sources and may provide a more direct link to the powering jet or wind in comparison to parameters calculated from molecular outflow data. Do more luminous, more massive sources produce more powerful jets/winds/outflows or are the line strengths related more to accretion rates? If the sources are at their ZAMS luminosities a sub-sample of similar luminosity sources would allow source age to be investigate as differences in some

parameters could be directly caused by different luminosities and not necessarily by age (Beuther & Shepherd, 2005). Furthermore, the difference in chemistry in the millimetre regime could be correlated with the differences at IR wavelengths and provide further information on the chemical evolution of the sources with age or luminosity. Imaging and detections or non-detections of sources at near and mid-infrared wavelengths similar to those by Alvarez *et al.* (2004a); de Wit *et al.* (2009) could further constrain the collimation of outflows, via models (e.g. Chapter 3), and indicate how embedded and hence how old the sources are. More embedded sources may generate more H_2 and Herbig-Haro objects physically close to the MYSO due to the amount of material available to interact with in the immediate vicinity while more evolved sources may have little evidence of such emission. This is exemplified by the differences between Cep A HW2 and GGD27 with S140 IRS1 as discussed above. Furthermore, the millimetre dust emission may also be related to the CO band-head emission, for example, and could separate genuine accretion disc sources from toroids where the much larger scale envelope is rotating. This emission in turn could also evolve with source age and luminosity.

The discrepancy between radio emission from an ionised jet or disc wind has been discussed above for Cep A HW2 and S140 IRS1. The younger MYSO, Cep A HW2, is though to be bloated, and therefore cool, and cannot ionise its surroundings even though it is luminous enough. Promising evidence for bloated protostars comes from the X-shooter spectra of the source B275 (Ochsendorf *et al.*, 2011) where the de-reddened spectrum is fitted with a large radius massive star consistent with a B7 spectral type although it would be a B1 type star when on the main sequence. Interestingly this source also has CO band-head emission with a strong blue shoulder indicative of a near edge on disc. However, it is rare that such

sources are observable in the visible spectrum and similar observations may not be possible for the deeply embedded MYSOs that are likely the most swollen. Overall, multi-wavelength, variable resolution imaging and spectroscopic observations are required to build a fully coherent picture.

6.4   Final Remarks

High resolution observations and large scale collaborations between international groups will provide a plethora of observational data of MYSOs. Furthermore, the extraordinary capabilities of ALMA will provide unprecedented quality observations in the millimetre/sub-millimetre regime which, in combination with observations at other facilities that are due to be upgraded, will greatly help in establishing a detailed picture of massive star formation in the coming decade.

Appendix A

CO column density and mass calculation

In this appendix the average column density and mass equations are derived following from the result of Garden *et al.* (1991) but for the CO(3-2) transition. The masses listed in both Chapters 4 and 5 are calculated following the method detailed.

The total column density of a linear, rigid rotor molecule under conditions of local thermodynamic equilibrium (LTE), with the populations of all levels characterised by a single excitation temperature, T_{ex}, is obtained from the integral of the optical depth over the line profile:

$$N_{tot} = \frac{3k}{8\pi^3 B\mu^2} \frac{exp[hBJ(J+1)/kT_{ex}]}{(J+1)} \frac{T_{ex} + hB/3k}{[1 - exp(-h\nu/kT_{ex})]} \int \tau_\upsilon \, d\upsilon \qquad \text{(A.1)}$$

where B is the rotational constant, μ is the permanent dipole moment of the molecule and J is the rotational quantum number of the lower state, in this case

J=2 for the CO(3-2) transition. k and h are the Boltzmann and Planck constants respectively. The temperature T_{ex} is 40 K for all sources.

The brightness temperature, T_{mb}, which is the antenna temperature of the telescope divided by the beam efficiency, T_A^*/η_{mb}, corresponds to the Rayleigh-Jeans brightness of a source minus the brightness of the cosmic microwave background (CMB) averaged over the beam:

$$\frac{T_A^*}{\eta_{mb}} = \frac{h\nu}{k}\left[\frac{1}{exp(h\nu/kT_{ex})-1} - \frac{1}{exp(h\nu/kT_{bg})-1}\right] \times [1-exp(-\tau)]f \quad (A.2)$$

Using the above equation and rearranging to make the beam filling factor the subject cases where the molecular emission does not uniformly fill the beam can be accounted for. In the limit where $T_{ex} \gg T_{bg}$ (=2.75 K):

$$f = \frac{T_A^*/\eta_{mb}}{(h\nu/k)[exp(h\nu/kT_{ex})-1]} \times \frac{1}{[1-exp(-\tau)]} \quad (A.3)$$

Combining equations A.1 and A.3 the beam averaged column density for an optical thin tracer ($\tau \ll 1$) such as C^{18}O is:

$$\bar{N} = \frac{3k}{8\pi^3 B\mu^2}\frac{exp[hBJ(J+1)/kT_{ex}]}{(J+1)}\frac{1}{(h\nu/k)}\frac{T_{ex}+hB/3k}{[exp(-h\nu/kT_{ex})]}$$
$$\times \int T_A^*/\eta_{mb}\,d\upsilon \quad (A.4)$$

The permanent dipole moment for ^{12}CO and C^{18}O are $\mu = 0.1098$ and 0.1101 respectively (Chackerian & Tipping, 1983). Conforming to cgs units typically used in such analysis B=58.14 GHz, k=1.381 × 10^{-16} erg K^{-1}, h=6.626 × 10^{-27}erg s,

$\nu(\mathrm{C^{18}O}) = 329.33055$ GHz, velocity υ is input in cms^{-1}, $\mu(\mathrm{C^{18}O}) = 0.1101 \times 10^{-18}$ StatC cm or $\mu(\mathrm{^{12}CO}) = 0.1098 \times 10^{-18}$ StatC cm (where 1 statC $= 1$ g$^{1/2}$ cm$^{3/2}$ s$^1 = 1$ erg$^{1/2}$ cm$^{1/2}$) and the adopted excitation temperature, T_{ex}, is 40 K. Hence for the $J{=}3{-}2$ transition the beam averaged column densities for $\mathrm{^{12}CO}$ and $\mathrm{C^{18}O}$ are calculated using:

$$\bar{N}(\mathrm{^{12}CO}) = 4.51 \times 10^{14} \int T_A^*/\eta_{mb} \times \frac{\tau}{[1 - exp(-\tau)]} \, d\upsilon \; (\mathrm{cm}^{-2}) \qquad \text{(A.5)}$$

and

$$\bar{N}(\mathrm{C^{18}O}) = 4.62 \times 10^{14} \int T_A^*/\eta_{mb} \, d\upsilon \; (\mathrm{cm}^{-2}) \qquad \text{(A.6)}$$

The mass of the core or outflow can be calculated from the beam averaged column density by the following:

$$M_{gas} = \bar{N}(\mathrm{CO})[\frac{\mathrm{H_2}}{\mathrm{CO}}]\mu_g \, m_{(\mathrm{H_2})}(\pi\theta^2/4)D^2 \qquad \text{(A.7)}$$

where $\mu_g = 1.36$ is the atomic weight of the gas, the abundance ratio [H$_2$/CO] is a combination of H$_2$/^{12}CO $= 10^4$ and ^{16}O/^{18}O $= 58.8 \times D_{GC}(\mathrm{kpc}) + 37.1$ (Wilson & Rood, 1994), where D_{GC} is the galactocentric distance and D is the distance of the source to the sun, both in kpc. θ can be defined in two ways dependent on the methodology used to calculate the mass. As in Cabrit & Bertout (1990) there are two methods of calculation. One calculation simply assumes the column density

in a single, central pointing of an outflow region as $\bar{N}$ and multiplies this with the projected area of the source, hence θ in equation A.7 is the angular scale of the outflow on the sky. Alternately, if the region has been well sampled, as is the case for the core and outflow maps in Chapters 4 and 5, then the mass is calculated via the summation of the average column densities of each pointing multiplied by the telescope beam size. θ in this latter case is the FWHM beam size. The masses are calculated following from equations A.8 and A.9 using:

$$M(^{12}\text{CO}) = 1.79 \times 10^{-10}\,\theta^2('')\,D^2(\text{kpc})\,[\frac{\text{H}_2}{^{12}\text{CO}}]\int T_A^*/\eta_{mb}$$
$$\times \frac{\tau}{[1 - exp(-\tau)]}\,d\upsilon\ (\text{M}_\odot) \qquad (\text{A.8})$$

and

$$M(\text{C}^{18}\text{O}) = 1.84 \times 10^{-10}\,\theta^2('')\,D^2(\text{kpc})\,[\frac{\text{H}_2}{\text{C}^{18}\text{O}}]\int T_A^*/\eta_{mb}\,d\upsilon\ (\text{M}_\odot) \qquad (\text{A.9})$$

where θ is measured in arcsec and the distance is given in kpc. As θ is the beam FWHM, the above equation is evaluated at each spatial position and the total mass of the source is the summation of these values. The masses are summed only over the aperture regions defined.

Appendix B

$C^{18}O$ integrated maps and summed spectra

The following pages present the integrated $C^{18}O$ core emission maps and summed spectra for each of the 99 outflow sources from Chapter 4. Each sub plot is the integrated map between the selected velocity ranges of the $C^{18}O$ core emission as detailed in Chapter 4 and listed in Table 4.3. The black contour level is three times the $1\sigma_{MAP}$ noise level also listed in Table 4.3. Each spectra is that summed within the integration aperture or from a limited aperture in the case of complex source regions. The apertures closely follow the $3\sigma_{MAP}$ noise level and are over plotted on the integrated map as the black dashed line (as in Figures 4.1 and 4.4). A Gaussian fit is over plotted as the dashed line for each summed spectra.
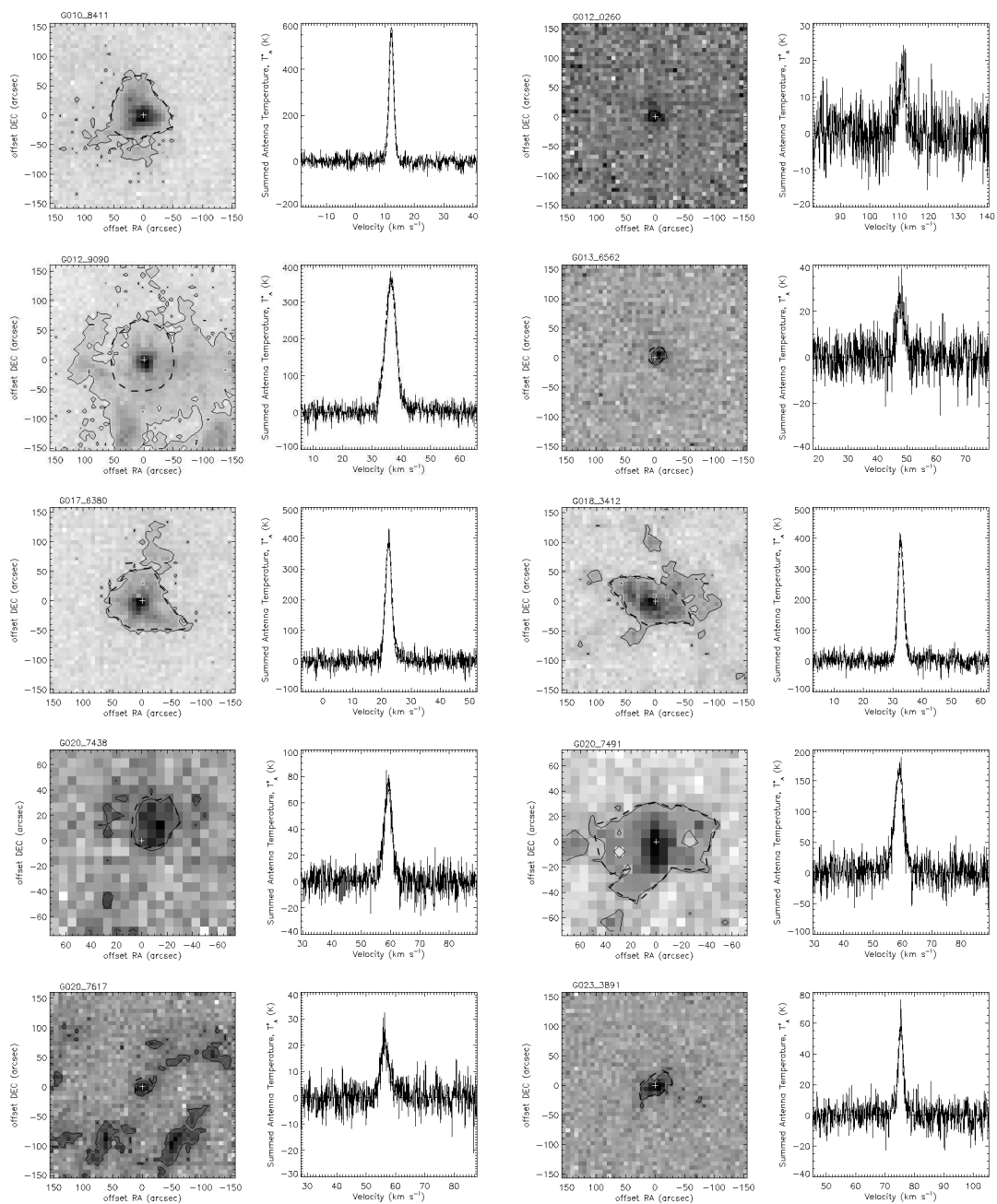
Figure B.1: Integrated $C^{18}O$ core emission and summed spectra from outflow sources

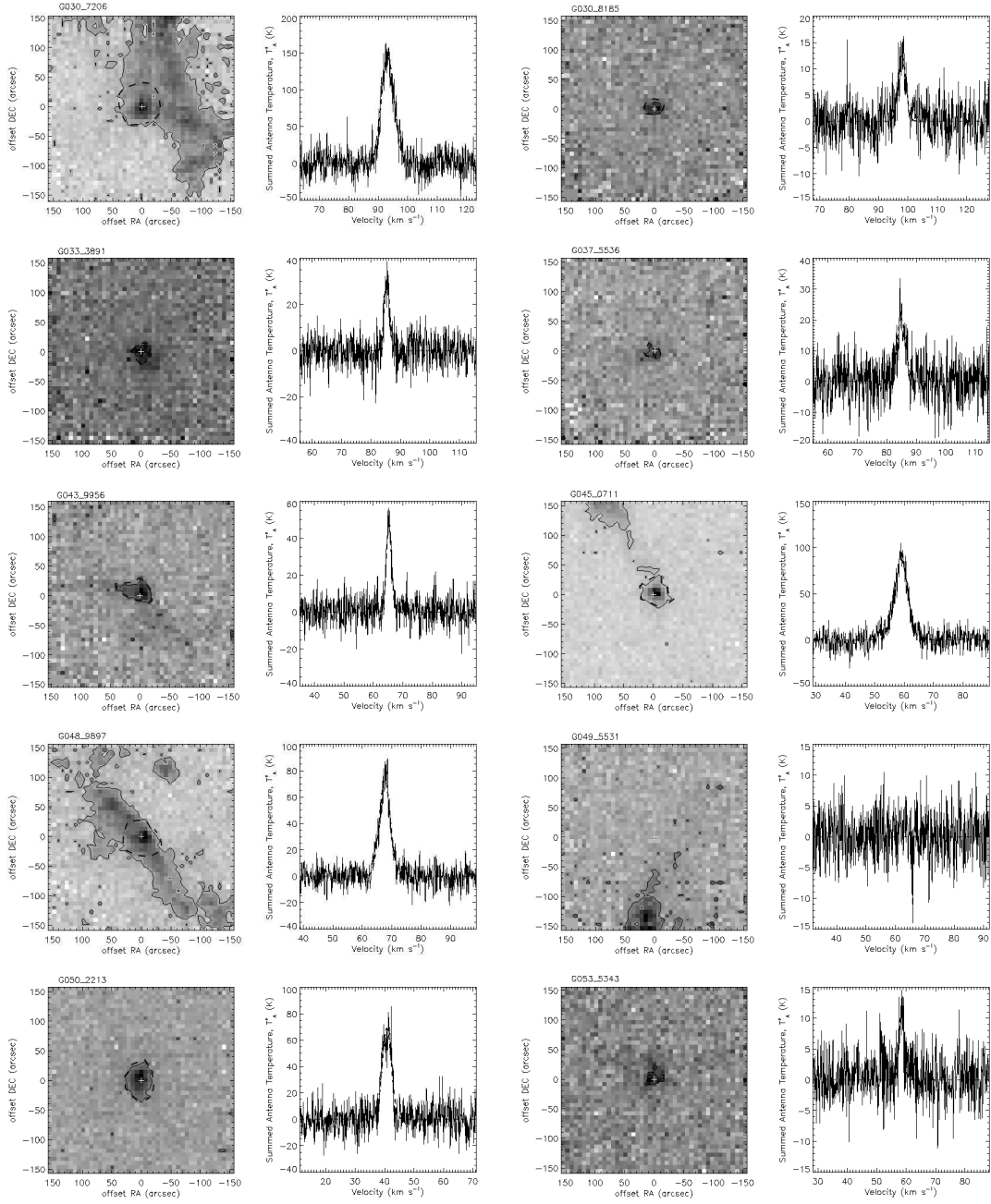**Figure B.1:** Integrated C^{18}O core emission and summed spectra from outflow sources - continued

278

Figure B.1: Integrated C^{18}O core emission and summed spectra from outflow sources - continued

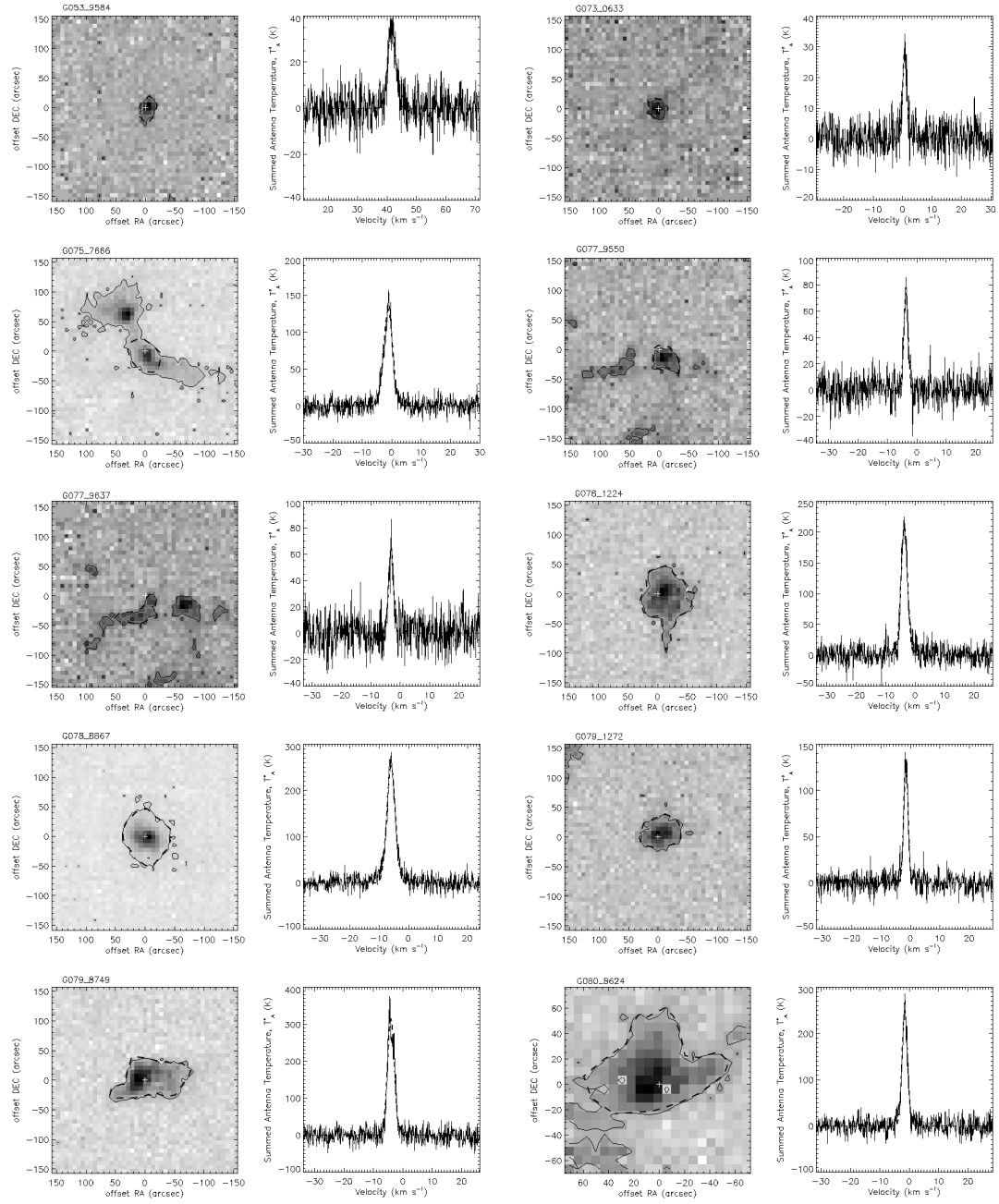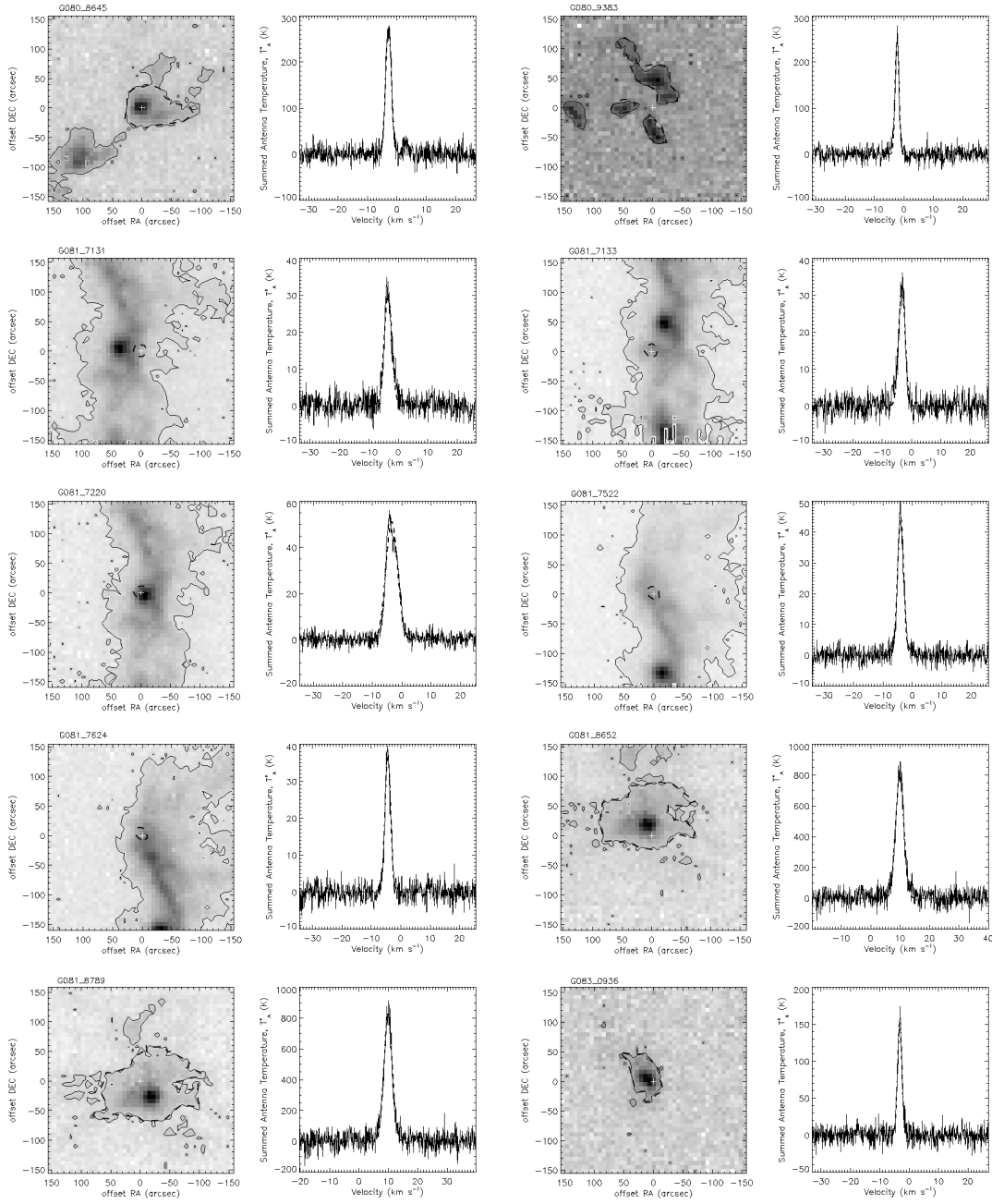**Figure B.1:** Integrated C^{18}O core emission and summed spectra from outflow sources - continued

Figure B.1: Integrated $C^{18}O$ core emission and summed spectra from outflow sources - continued
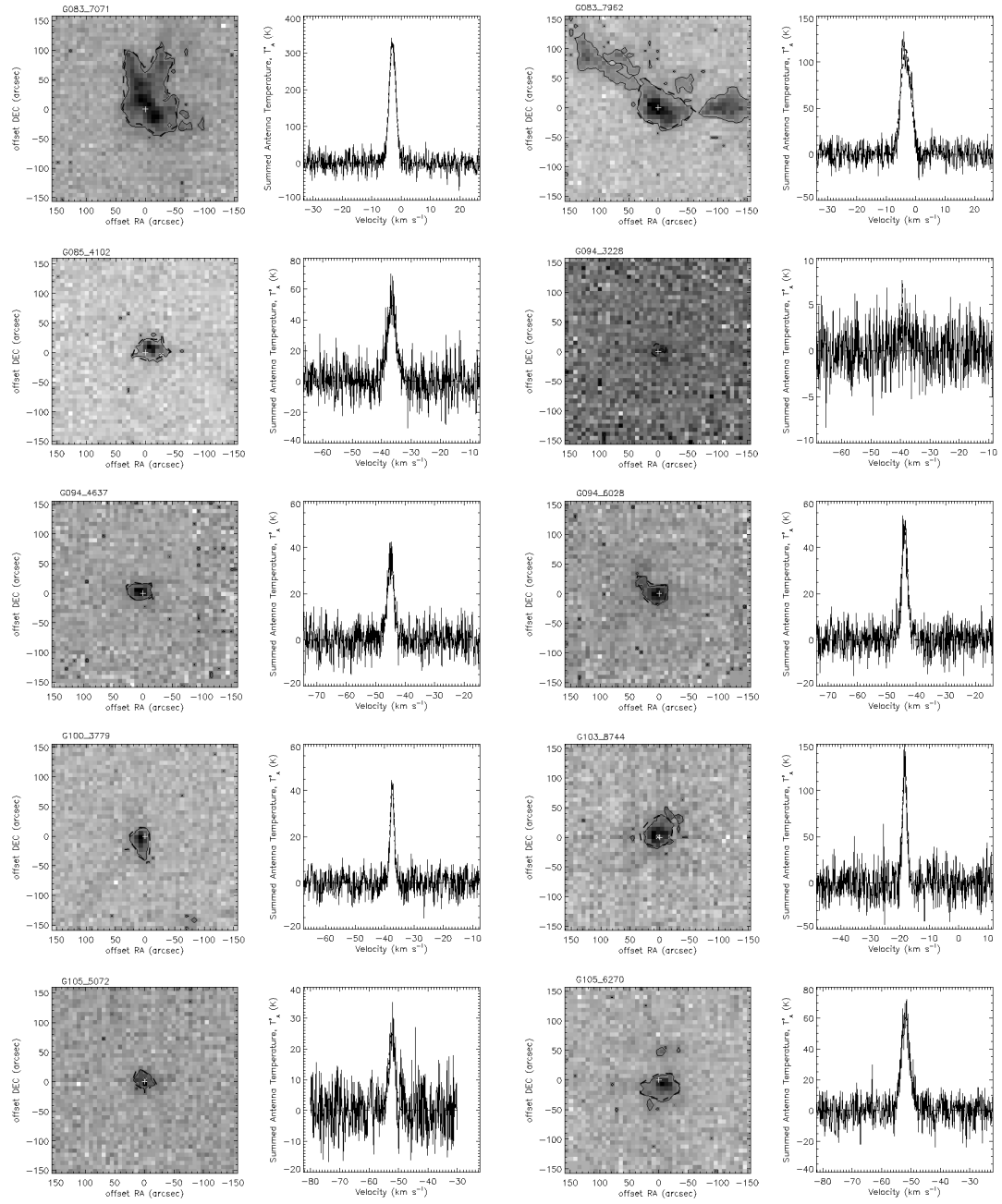
Figure B.1: Integrated $C^{18}O$ core emission and summed spectra from outflow sources - continued
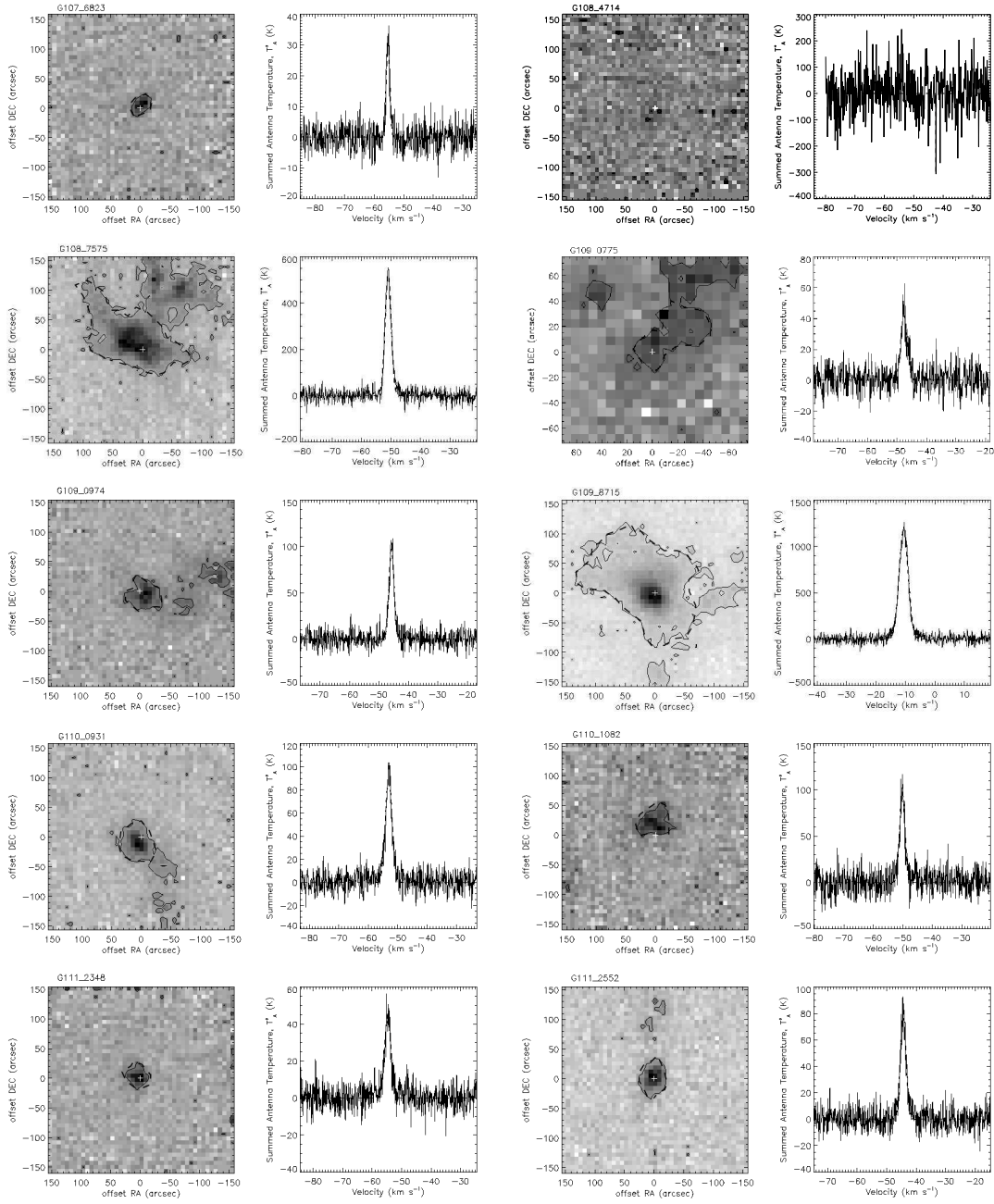
Figure B.1: Integrated C^{18}O core emission and summed spectra from outflow sources - continued

Figure B.1: Integrated C^{18}O core emission and summed spectra from outflow sources - continued

Figure B.1: Integrated $C^{18}O$ core emission and summed spectra from outflow sources - continued
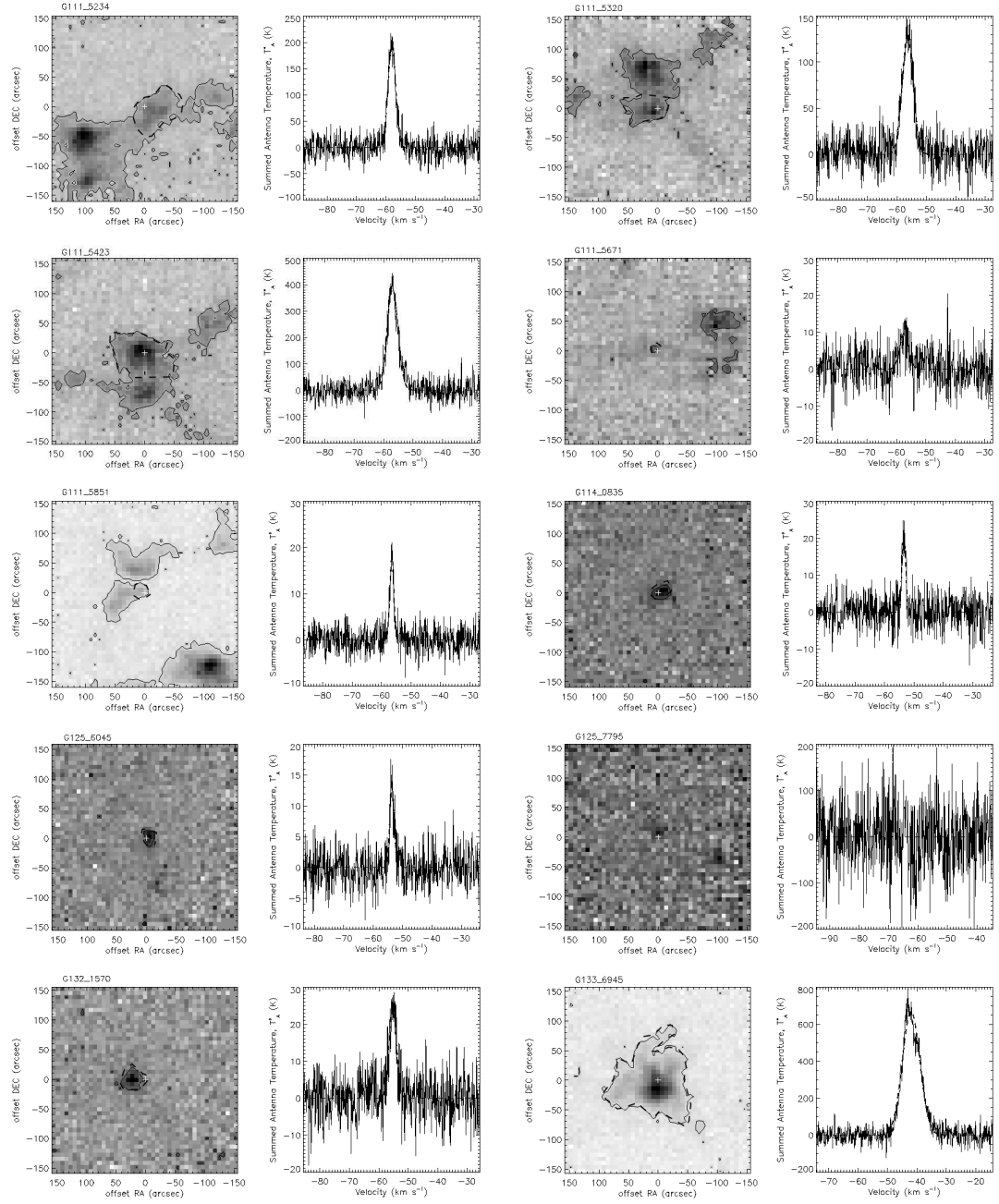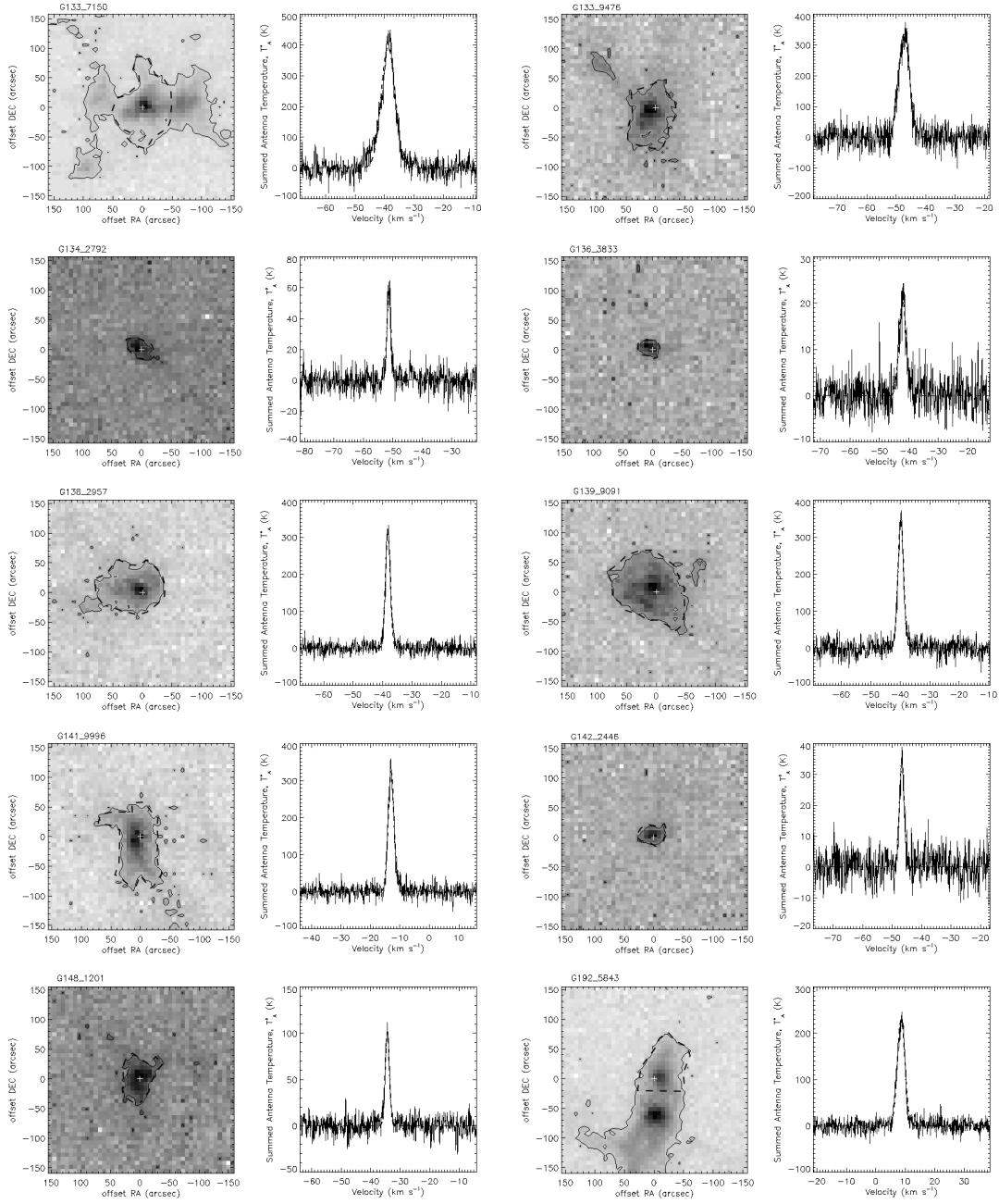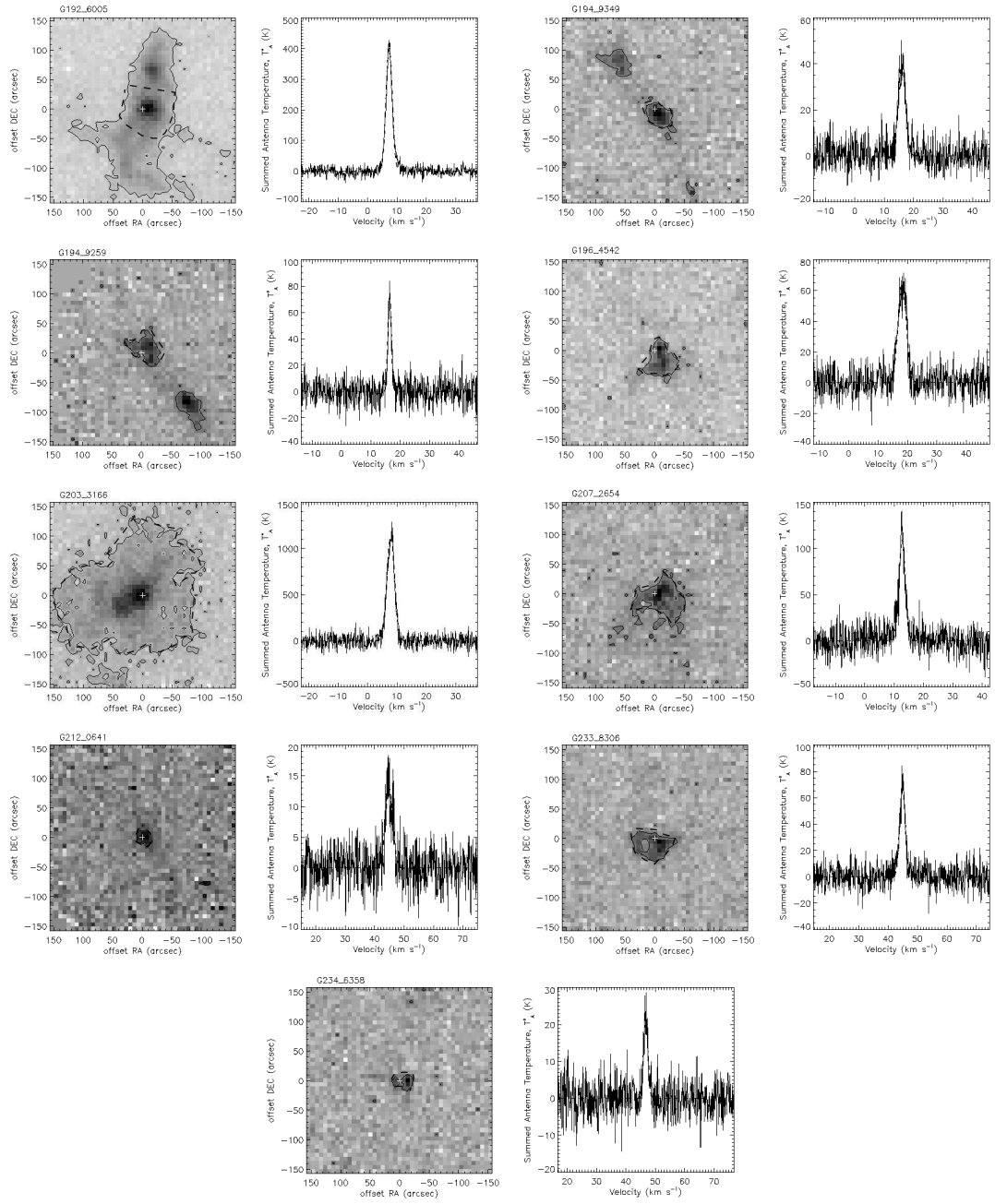
Figure B.1: Integrated C^{18}O core emission and summed spectra from outflow sources - continued

References

ADAMS, F.C., LADA, C.J. & SHU, F.H. (1987). Spectral evolution of young stellar objects. ApJ, **312**, 788–806. 5

AGRA-AMBOAGE, V., DOUGADOS, C., CABRIT, S. & REUNANEN, J. (2011). Sub-arcsecond [Fe ii] spectro-imaging of the DG Tauri jet. Periodic bubbles and a dusty disk wind? A&A, **532**, A59. 30

ALVAREZ, C., HOARE, M., GLINDEMANN, A. & RICHICHI, A. (2004a). Near-IR speckle imaging of massive young stellar objects. A&A, **427**, 505–518. 43, 268

ALVAREZ, C., HOARE, M. & LUCAS, P. (2004b). Constraints in the circumstellar density distribution of massive Young Stellar Objects. A&A, **419**, 203–213. 112

ARAYA, E., HOFNER, P., KURTZ, S., OLMI, L. & LINZ, H. (2008). Thermal Methanol Observations of the Outflow from the G31.41+0.31 Hot Molecular Core. ApJ, **675**, 420–426. 13

ARCE, H.G., SHEPHERD, D., GUETH, F., LEE, C.F., BACHILLER, R., ROSEN, A. & BEUTHER, H. (2007). Molecular Outflows in Low- and High-Mass Star-forming Regions. *Protostars and Planets V*, 245–260. 29, 30, 31, 241

ASANOK, K., ETOKA, S., GRAY, M.D., THOMASSON, P., RICHARDS, A.M.S. & KRAMER, B.H. (2010). OH and Water masers towards the star-forming region S140-IRS1. MNRAS, **404**, 120–133. 73, 92, 93, 94

ASPIN, C. (1994). Scattered near-IR CO emission bands in GGD27-IRS: Observing the circumstellar environment of heavily obscured young PMS stars. A&A, **281**, L29–L32. 25, 260

BALLY, J., SNELL, R.L. & PREDMORE, R. (1983). Radio images of the bipolar H II region S106. ApJ, **272**, 154–162. 261

BALLY, J., REIPURTH, B. & DAVIS, C.J. (2007). Observations of Jets and Outflows from Young Stars. *Protostars and Planets V*, 215–230. 29

BEICHMAN, C.A., BECKLIN, E.E. & WYNN-WILLIAMS, C.G. (1979). New multiple systems in molecular clouds. ApJ, **232**, L47–L51. 40, 42, 109

BELTRÁN, M.T., CESARONI, R., NERI, R., CODELLA, C., FURUYA, R.S., TESTI, L. & OLMI, L. (2004). Rotating Disks in High-Mass Young Stellar Objects. ApJ, **601**, L187–L190. 13

BELTRÁN, M.T., CESARONI, R., NERI, R., CODELLA, C., FURUYA, R.S., TESTI, L. & OLMI, L. (2005). A detailed study of the rotating toroids in G31.41+0.31 and G24.78+0.08. A&A, **435**, 901–925. 13

BELTRÁN, M.T., GIRART, J.M. & ESTALELLA, R. (2006). Who is eating the outflow? High-angular resolution study of an intermediate-mass protostar in L1206. A&A, **457**, 865–876. 75

Beltrán, M.T., Cesaroni, R., Neri, R. & Codella, C. (2011a). Rotating toroids in G10.62-0.38, G19.61-0.23, and G29.96-0.02. A&A, **525**, A151. 23, 24

Beltrán, M.T., Cesaroni, R., Zhang, Q., Galván-Madrid, R., Beuther, H., Fallscheer, C., Neri, R. & Codella, C. (2011b). Molecular outflows and hot molecular cores in G24.78+0.08 at sub-arcsecond angular resolution. A&A, **532**, A91. 224

Beuther, H. & Shepherd, D. (2005). Precursors of UCHII Regions and the Evolution of Massive Outflows. In M. S. N. Kumar, M. Tafalla, & P. Caselli, ed., *Cores to Clusters: Star Formation with Next Generation Telescopes*, 105–119. 8, 34, 35, 36, 268

Beuther, H., Schilke, P., Gueth, F., McCaughrean, M., Andersen, M., Sridharan, T.K. & Menten, K.M. (2002a). IRAS 05358+3543: Multiple outflows at the earliest stages of massive star formation. A&A, **387**, 931–943. 224

Beuther, H., Schilke, P., Menten, K.M., Motte, F., Sridharan, T.K. & Wyrowski, F. (2002b). High-Mass Protostellar Candidates. II. Density Structure from Dust Continuum and CS Emission. ApJ, **566**, 945–965. 198, 199

Beuther, H., Schilke, P., Sridharan, T.K., Menten, K.M., Walmsley, C.M. & Wyrowski, F. (2002c). Massive molecular outflows. A&A, **383**, 892–904. 14, 33, 34, 81, 110, 131, 224, 229, 238, 244, 250

Beuther, H., Hunter, T.R., Zhang, Q., Sridharan, T.K., Zhao, J.H., Sollins, P., Ho, P.T.P., Ohashi, N., Su, Y.N., Lim, J. & Liu, S.Y.

(2004). Submillimeter Array Outflow/Disk Studies in the Massive Star-forming Region IRAS 18089-1732. ApJ, **616**, L23–L26. 80

BEUTHER, H., CHURCHWELL, E.B., MCKEE, C.F. & TAN, J.C. (2007). The Formation of Massive Stars. *Protostars and Planets V*, 165–180. 8, 9, 14

BJORKMAN, J.E. & WOOD, K. (2001). Radiative Equilibrium and Temperature Correction in Monte Carlo Radiation Transfer. ApJ, **554**, 615–623. 108

BLAIR, G.N. & VANDEN BOUT, P.A. (1974). Infrared Sources Assocated with 2. 6 mm Carbon Monoxide "Hot Spots" In Small Hα Emission Regions. In *Bulletin of the American Astronomical Society*, vol. 6 of *Bulletin of the American Astronomical Society*, 452. 40

BLAIR, G.N., EVANS, N.J., II, VANDEN BOUT, P.A. & PETERS, W.L., III (1978). The energetics of molecular clouds. II - The S140 molecular cloud. ApJ, **219**, 896. 40, 41

BOCK, D., BOLATTO, A.D., HAWKINS, D.W., KEMBALL, A.J., LAMB, J.W., PLAMBECK, R.L., POUND, M.W., SCOTT, S.L., WOODY, D.P. & WRIGHT, M.C.H. (2006). First results from CARMA: the combined array for research in millimeter-wave astronomy. In *Society of Photo-Optical Instrumentation Engineers (SPIE) Conference Series*, vol. 6267 of *Society of Photo-Optical Instrumentation Engineers (SPIE) Conference Series*. 48

BOK, B.J. & REILLY, E.F. (1947). Small Dark Nebulae. ApJ, **105**, 255. 10

BONNELL, I.A. & BATE, M.R. (2002). Accretion in stellar clusters and the collisional formation of massive stars. MNRAS, **336**, 659–669. 6

BONNELL, I.A., BATE, M.R., CLARKE, C.J. & PRINGLE, J.E. (1997). Accretion and the stellar mass spectrum in small clusters. MNRAS, **285**, 201–208. 7

BONTEMPS, S., MOTTE, F., CSENGERI, T. & SCHNEIDER, N. (2010). Fragmentation and mass segregation in the massive dense cores of Cygnus X. A&A, **524**, A18. 206

BUCKLE, J.V., HILLS, R.E., SMITH, H., DENT, W.R.F., BELL, G., CURTIS, E.I., DACE, R., GIBSON, H., GRAVES, S.F., LEECH, J., RICHER, J.S., WILLIAMSON, R., WITHINGTON, S., YASSIN, G., BENNETT, R., HASTINGS, P., LAIDLAW, I., LIGHTFOOT, J.F., BURGESS, T., DEWDNEY, P.E., HOVEY, G., WILLIS, A.G., REDMAN, R., WOOFF, B., BERRY, D.S., CAVANAGH, B., DAVIS, G.R., DEMPSEY, J., FRIBERG, P., JENNESS, T., KACKLEY, R., REES, N.P., TILANUS, R., WALTHER, C., ZWART, W., KLAPWIJK, T.M., KROUG, M. & ZIJLSTRA, T. (2009). HARP/ACSIS: a submillimetre spectral imaging system on the James Clerk Maxwell Telescope. MNRAS, **399**, 1026–1043. 172

BUCKLE, J.V., DAVIS, C.J., FRANCESCO, J.D., GRAVES, S.F., NUTTER, D., RICHER, J.S., ROBERTS, J.F., WARD-THOMPSON, D., WHITE, G.J., BRUNT, C., BUTNER, H.M., CAVANAGH, B., CHRYSOSTOMOU, A., CURTIS, E.I., DUARTE-CABRAL, A., ETXALUZE, M., FICH, M., FRIBERG, P., FRIESEN, R., FULLER, G.A., GREAVES, J.S., HATCHELL, J., HOGERHEIJDE, M.R., JOHNSTONE, D., MATTHEWS, B., MATTHEWS, H., RAWLINGS, J.M.C., SADAVOY, S., SIMPSON, R.J., TOTHILL, N.F.H., TSAMIS, Y.G., VITI, S., WOUTERLOOT, J.G.A. & YATES, J. (2012). The JCMT Legacy

Survey of the Gould Belt: mapping ^{13}CO and C^{18}O in Orion A. MNRAS, **422**, 521–541. 170, 171, 204, 213, 263

BUNN, J.C., HOARE, M.G. & DREW, J.E. (1995). Observations of the IR recombination line emission from massive young stellar objects. MNRAS, **272**, 346–354. 26

BURROWS, C.J., STAPELFELDT, K.R., WATSON, A.M., KRIST, J.E., BALLESTER, G.E., CLARKE, J.T., CRISP, D., GALLAGHER, J.S., III, GRIFFITHS, R.E., HESTER, J.J., HOESSEL, J.G., HOLTZMAN, J.A., MOULD, J.R., SCOWEN, P.A., TRAUGER, J.T. & WESTPHAL, J.A. (1996). Hubble Space Telescope Observations of the Disk and Jet of HH 30. ApJ, **473**, 437. 21

CABRIT, S. & BERTOUT, C. (1990). CO line formation in bipolar flows. II - Decelerated outflow case and summary of results. ApJ, **348**, 530–541. 231, 239, 243, 273

CABRIT, S. & BERTOUT, C. (1992). CO line formation in bipolar flows. III - The energetics of molecular flows and ionized winds. A&A, **261**, 274–284. 33

CABRIT, S., RAGA, A. & GUETH, F. (1997). Models of Bipolar Molecular Outflows. In B. Reipurth & C. Bertout, eds., *Herbig-Haro Flows and the Birth of Stars*, vol. 182 of *IAU Symposium*, 163–180. 30, 31, 247

CALVET, N., D'ALESSIO, P., HARTMANN, L., WILNER, D., WALSH, A. & SITKO, M. (2002). Evidence for a Developing Gap in a 10 Myr Old Protoplanetary Disk. ApJ, **568**, 1008–1016. 80

CARILLI, C.L., CARLSTROM, J.E. & HOLDAWAY, M.A. (1999). Millimeter Interferometry. In G.B. Taylor, C.L. Carilli & R.A. Perley, eds., *Synthesis Imaging in Radio Astronomy II*, vol. 180 of *Astronomical Society of the Pacific Conference Series*, 565. 57

CARR, J.S. (1989). Near-infrared CO emission in young stellar objects. ApJ, **345**, 522–535. 25

CARRASCO-GONZÁLEZ, C., RODRÍGUEZ, L.F., ANGLADA, G., MARTÍ, J., TORRELLES, J.M. & OSORIO, M. (2010). A Magnetized Jet from a Massive Protostar. *Science*, **330**, 1209–. 37

CESARONI, R. (2005). Hot molecular cores. In R. Cesaroni, M. Felli, E. Churchwell & M. Walmsley, eds., *Massive Star Birth: A Crossroads of Astrophysics*, vol. 227 of *IAU Symposium*, 59–69. 207, 208

CESARONI, R., WALMSLEY, C.M. & CHURCHWELL, E. (1992). Hot ammonia toward ultracompact H II regions. A&A, **256**, 618–630. 11

CESARONI, R., CHURCHWELL, E., HOFNER, P., WALMSLEY, C.M. & KURTZ, S. (1994). Hot ammonia towards compact HII regions. A&A, **288**, 903–920. 11, 12

CESARONI, R., FELLI, M., TESTI, L., WALMSLEY, C.M. & OLMI, L. (1997). The disk-outflow system around the high-mass (proto)star IRAS 20126+4104. A&A, **325**, 725–744. 15

CESARONI, R., HOFNER, P., WALMSLEY, C.M. & CHURCHWELL, E. (1998). Sub-arcsecond structure of hot cores in the NH_3 (4,4) line. A&A, **331**, 709–725. 13

CESARONI, R., FELLI, M., JENNESS, T., NERI, R., OLMI, L., ROBBERTO, M., TESTI, L. & WALMSLEY, C.M. (1999). Unveiling the disk-jet system in the massive (proto)star IRAS 20126+4104. A&A, **345**, 949–964. 14, 15, 79, 88

CESARONI, R., GALLI, D., LODATO, G., WALMSLEY, C.M. & ZHANG, Q. (2007). Disks Around Young O-B (Proto)Stars: Observations and Theory. *Protostars and Planets V*, 197–212. 22, 24

CESARONI, R., HOFNER, P., ARAYA, E. & KURTZ, S. (2010). The structure of hot molecular cores over 1000 AU. A&A, **509**, A50. 13, 14

CESARONI, R., BELTRÁN, M.T., ZHANG, Q., BEUTHER, H. & FALLSCHEER, C. (2011). Dissecting a hot molecular core: the case of G31.41+0.31. A&A, **533**, A73. 13

CESARONI, R., MASSI, F., ARCIDIACONO, C., BELTRÁN, M.T., MCCARTHY, D., KULESA, C., BOUTSIA, K., PARIS, D., QUIRÓS-PACHECO, F. & XOMPERO, M. (2013). A close-up view of a bipolar jet: Sub-arcsecond near-infrared imaging of the high-mass protostar IRAS 20126+4104. A&A, **549**, A146. 15

CHABRIER, G. & HENNEBELLE, P. (2010). Star Formation: Statistical Measure of the Correlation between the Prestellar Core Mass Function and the Stellar Initial Mass Function. ApJ, **725**, L79–L83. 11

CHACKERIAN, C., JR. & TIPPING, R.H. (1983). Vibration-rotational and rotational intensities for CO isotopes. *Journal of Molecular Spectroscopy*, **99**, 431–449. 272

CHANDLER, C.J., CARLSTROM, J.E. & SCOVILLE, N.Z. (1995). Infrared CO Emission from Young Stars: Accretion Disks and Neutral Winds. ApJ, **446**, 793. 261

CHOI, M., EVANS, N.J., II & JAFFE, D.T. (1993). Extremely High Velocity Outflows. ApJ, **417**, 624. 224, 231

COOPER, H.D.B., LUMSDEN, S.L., OUDMAIJER, R.D., HOARE, M.G., CLARKE, A.J., URQUHART, J.S., MOTTRAM, J.C., MOORE, T.J.T. & DAVIES, B. (2013). The RMS survey: near-IR spectroscopy of massive young stellar objects. MNRAS, **430**, 1125–1157. 17, 267

CURIEL, S., HO, P.T.P., PATEL, N.A., TORRELLES, J.M., RODRÍGUEZ, L.F., TRINIDAD, M.A., CANTÓ, J., HERNÁNDEZ, L., GÓMEZ, J.F., GARAY, G. & ANGLADA, G. (2006). Large Proper Motions in the Jet of the High-Mass YSO Cepheus A HW2. ApJ, **638**, 878–886. 22, 27

CURTIS, E.I., RICHER, J.S., SWIFT, J.J. & WILLIAMS, J.P. (2010). A submillimetre survey of the kinematics of the Perseus molecular cloud - II. Molecular outflows. MNRAS, **408**, 1516–1539. 35, 246

CYGANOWSKI, C.J., BROGAN, C.L., HUNTER, T.R., ZHANG, Q., FRIESEN, R.K., INDEBETOUW, R. & CHANDLER, C.J. (2012). The Protocluster G18.67+0.03: A Test Case for Class I CH$_3$OH Masers as Evolutionary Indicators for Massive Star Formation. ApJ, **760**, L20. 18

DAVIES, B., LUMSDEN, S.L., HOARE, M.G., OUDMAIJER, R.D. & DE WIT, W.J. (2010). The circumstellar disc, envelope and bipolar outflow of the massive young stellar object W33A. MNRAS, **402**, 1504–1515. 25, 26, 33

DAVIES, B., HOARE, M.G., LUMSDEN, S.L., HOSOKAWA, T., OUDMAIJER, R.D., URQUHART, J.S., MOTTRAM, J.C. & STEAD, J. (2011). The Red MSX Source survey: critical tests of accretion models for the formation of massive stars. MNRAS, **416**, 972–990. 14, 211, 260

DE WIT, W.J., HOARE, M.G., OUDMAIJER, R.D. & MOTTRAM, J.C. (2007). VLTI/MIDI 10 μm Interferometry of the Forming Massive Star W33A. ApJ, **671**, L169–L172. 103

DE WIT, W.J., HOARE, M.G., FUJIYOSHI, T., OUDMAIJER, R.D., HONDA, M., KATAZA, H., MIYATA, T., OKAMOTO, Y.K., ONAKA, T., SAKO, S. & YAMASHITA, T. (2009). Resolved 24.5 micron emission from massive young stellar objects. A&A, **494**, 157–178. 27, 43, 44, 46, 111, 118, 268

DE WIT, W.J., HOARE, M.G., OUDMAIJER, R.D. & LUMSDEN, S.L. (2010). The origin of mid-infrared emission in massive young stellar objects: multi-baseline VLTI observations of W33A. A&A, **515**, A45+. 90, 101, 102, 103, 108, 117, 126, 127, 140

DI FRANCESCO, J., JOHNSTONE, D., KIRK, H., MACKENZIE, T. & LEDWOSINSKA, E. (2008). The SCUBA Legacy Catalogues: Submillimeter-Continuum Objects Detected by SCUBA. ApJS, **175**, 277–295. 199

DINERSTEIN, H.L., LESTER, D.F. & RANK, D.M. (1979). Detection of a near-infrared complex associated with S140 IRS. ApJ, **227**, L39–L41. 42

DOWNES, T.P. & CABRIT, S. (2007). Jet-driven molecular outflows from class 0 sources: younger and stronger than they seem? A&A, **471**, 873–884. 247

DRAINE, B.T. (2006). On the Submillimeter Opacity of Protoplanetary Disks. ApJ, **636**, 1114–1120. 79

DRAINE, B.T. & LEE, H.M. (1984). Optical properties of interstellar graphite and silicate grains. ApJ, **285**, 89–108. 115

DREW, J.E., PROGA, D. & STONE, J.M. (1998). A radiation-driven disc wind model for massive young stellar objects. MNRAS, **296**, L6+. 27, 91, 260

DULLEMOND, C.P., DOMINIK, C. & NATTA, A. (2001). Passive Irradiated Circumstellar Disks with an Inner Hole. ApJ, **560**, 957–969. 98

EGAN, M.P., SHIPMAN, R.F., PRICE, S.D., CAREY, S.J., CLARK, F.O. & COHEN, M. (1998). A Population of Cold Cores in the Galactic Plane. ApJ, **494**, L199. 10

EGAN, M.P., PRICE, S.D. & KRAEMER, K.E. (2003). The Midcourse Space Experiment Point Source Catalog Version 2.3. In *American Astronomical Society Meeting Abstracts*, vol. 35 of *Bulletin of the American Astronomical Society*, 1301. 17

EISNER, J.A., PLAMBECK, R.L., CARPENTER, J.M., CORDER, S.A., QI, C. & WILNER, D. (2008). Proplyds and Massive Disks in the Orion Nebula Cluster Imaged with CARMA and SMA. ApJ, **683**, 304–320. 21

ELMEGREEN, B.G. & LADA, C.J. (1977). Sequential formation of subgroups in OB associations. ApJ, **214**, 725–741. 4

Estalella, R., Mauersberger, R., Torrelles, J.M., Anglada, G., Gomez, J.F., Lopez, R. & Muders, D. (1993). The Molecular Cores in the L1287, AFGL 5142, and IRAS 20126+4104 Regions. ApJ, **419**, 698. 15, 174, 183, 216

Evans, N.J., Shirley, Y.L., Mueller, K.E. & Knez, C. (2002). The Formation and Early Evolution of Massive Stars. In P. Crowther, ed., *Hot Star Workshop III: The Earliest Phases of Massive Star Birth*, vol. 267 of *Astronomical Society of the Pacific Conference Series*, 17. 8

Evans, N.J., II (1999). Physical Conditions in Regions of Star Formation. ARA&A, **37**, 311–362. 10

Evans, N.J., II, Mundy, L.G., Kutner, M.L. & Depoy, D.L. (1989). The nature of the radio and infrared sources in S140. ApJ, **346**, 212–219. 42, 46, 71, 73, 93, 261

Faúndez, S., Bronfman, L., Garay, G., Chini, R., Nyman, L.Å. & May, J. (2004). SIMBA survey of southern high-mass star forming regions. I. Physical parameters of the 1.2 mm/IRAS sources. A&A, **426**, 97–103. 199

Fernández-López, M., Curiel, S., Girart, J.M., Ho, P.T.P., Patel, N. & Gómez, Y. (2011a). Millimeter and Submillimeter High Angular Resolution Interferometric Observations: Dust in the Heart of IRAS 18162-2048. AJ, **141**, 72. 85

Fernández-López, M., Girart, J.M., Curiel, S., Gómez, Y., Ho, P.T.P. & Patel, N. (2011b). A Rotating Molecular Disk Toward IRAS 18162-2048, the Exciting Source of HH 80-81. AJ, **142**, 97. 260

Fontani, F., Giannetti, A., Beltrán, M.T., Dodson, R., Rioja, M., Brand, J., Caselli, P. & Cesaroni, R. (2012). High CO depletion in southern infrared dark clouds. MNRAS, **423**, 2342–2358. 177

Forrest, W.J. & Shure, M.A. (1986). Unipolar bubbles in star-forming regions. ApJ, **311**, L81–L84. 42

Galván-Madrid, R., Zhang, Q., Keto, E., Ho, P.T.P., Zapata, L.A., Rodríguez, L.F., Pineda, J.E. & Vázquez-Semadeni, E. (2010). From the Convergence of Filaments to Disk-outflow Accretion: Massive Star Formation in W33A. ApJ, **725**, 17–28. 76, 79, 88, 90, 106, 137

Garden, R.P., Hayashi, M., Hasegawa, T., Gatley, I. & Kaifu, N. (1991). A spectroscopic study of the DR 21 outflow source. III - The CO line emission. ApJ, **374**, 540–554. 238, 271

Gibb, A.G. & Hoare, M.G. (2007). A high-frequency radio continuum study of massive young stellar objects. MNRAS, **380**, 246–262. 45, 75, 76, 77, 78, 93

Gibb, A.G., Hoare, M.G., Mundy, L.G. & Wyrowski, F. (2004). A Search for Disks around Massive Young Stellar Objects. In M.G. Burton, R. Jayawardhana & T.L. Bourke, eds., *Star Formation at High Angular Resolution*, vol. 221 of *IAU Symposium*, 425. 78

Ginsburg, A., Bally, J. & Williams, J.P. (2011). JCMT HARP CO 3-2 observations of molecular outflows in W5. MNRAS, **418**, 2121–2144. 174, 224, 225

GUERTLER, J., HENNING, T., KRUEGEL, E. & CHINI, R. (1991). Dust continuum radiation from luminous young stellar objects. A&A, **252**, 801–811. 111, 115, 118, 122, 129

GUETH, F. & GUILLOTEAU, S. (1999). The jet-driven molecular outflow of HH 211. A&A, **343**, 571–584. 30

GUETH, F., SCHILKE, P. & MCCAUGHREAN, M.J. (2001). An interferometric study of the HH 288 molecular outflow. A&A, **375**, 1018–1031. 34

HARKER, D., BREGMAN, J., TIELENS, A.G.G.M., TEMI, P. & RANK, D. (1997). The infrared reflection nebula around the embedded sources in S 140. A&A, **324**, 629–640. 46

HARVEY, P.M., ADAMS, J.D., HERTER, T.L., GULL, G., SCHOENWALD, J., KELLER, L.D., DE BUIZER, J.M., VACCA, W., REACH, W. & BECKLIN, E.E. (2012). First Science Results From SOFIA/FORCAST: Super-Resolution Imaging of the S140 Cluster at 37\micron. *ArXiv e-prints*. 111, 118

HAYASHI, M., HASEGAWA, T., OMODAKA, T., HAYASHI, S.S. & MIYAWAKI, R. (1987). The bright-rimmed molecular cloud around S140 IRS. II - Bipolar outflow from S140 IRS 1. ApJ, **312**, 327–336. 40, 41, 81, 84, 265

HERBIG, G.H. (1962). The properties and problems of T Tauri stars and related objects. *Advances in Astronomy and Astrophysics*, **1**, 47–103. 2

HILL, T., BURTON, M.G., MINIER, V., THOMPSON, M.A., WALSH, A.J., HUNT-CUNNINGHAM, M. & GARAY, G. (2005). Millimetre continuum obser-

vations of southern massive star formation regions - I. SIMBA observations of cold cores. MNRAS, **363**, 405–451. 199, 200

HIROTA, T., ANDO, K., BUSHIMATA, T. & ET AL., C. (2008). Astrometry of H_2O Masers in Nearby Star-Forming Regions with VERA III. IRAS 22198+6336 in Lynds1204G. PASJ, **60**, 961–. 40, 86

HO, P.T.P., MORAN, J.M. & LO, K.Y. (2004). The Submillimeter Array. ApJ, **616**, L1–L6. 47

HOARE, M.G. (2002). High-Resolution Radio Observations of Massive Young Stellar Objects. In P. Crowther, ed., *Hot Star Workshop III: The Earliest Phases of Massive Star Birth*, vol. 267 of *Astronomical Society of the Pacific Conference Series*, 137. 27, 28

HOARE, M.G. (2006). An Equatorial Wind from the Massive Young Stellar Object S140 IRS 1. ApJ, **649**, 856–861. 26, 43, 44, 88, 93, 155

HOARE, M.G. & FRANCO, J. (2007). *Massive Star Formation*, 61. Springer Dordrecht. 8, 14, 18, 23

HOARE, M.G. & MUXLOW, T.B. (1996). MERLIN Observations of Luminous Young Stellar Objects. In A.R. Taylor & J.M. Paredes, eds., *Radio Emission from the Stars and the Sun*, vol. 93 of *Astronomical Society of the Pacific Conference Series*, 47. 26, 43

HOARE, M.G., ROCHE, P.F. & GLENCROSS, W.M. (1991). Submillimetre emission and the dust content of compact H II regions. MNRAS, **251**, 584–599. 79

HOARE, M.G., DREW, J.E., MUXLOW, T.B. & DAVIS, R.J. (1994). Mapping the radio emission from massive young stellar objects. ApJ, **421**, L51–L54. 26, 45, 261

HOARE, M.G., GLINDEMANN, A. & RICHICHI, A. (1996). Near-IR Speckle Imaging of Luminous Young Stellar Objects. In H. U. Käufl & R. Siebenmorgen, ed., *The Role of Dust in the Formation of Stars*, 35. 43

HOSOKAWA, T. & OMUKAI, K. (2009). Evolution of Massive Protostars with High Accretion Rates. ApJ, **691**, 823–846. 19, 37, 91, 261

HOSOKAWA, T., YORKE, H.W. & OMUKAI, K. (2010). Evolution of Massive Protostars Via Disk Accretion. ApJ, **721**, 478–492. 91

HUGHES, A.M., ANDREWS, S.M., ESPAILLAT, C., WILNER, D.J., CALVET, N., D'ALESSIO, P., QI, C., WILLIAMS, J.P. & HOGERHEIJDE, M.R. (2009). A Spatially Resolved Inner Hole in the Disk Around GM Aurigae. ApJ, **698**, 131–142. 103

IKEDA, N. & KITAMURA, Y. (2009). A $C^{18}O$ Study of the Origin of the Power-Law Nature in the Initial Mass Function. ApJ, **705**, L95–L98. 12

IKEDA, N. & KITAMURA, Y. (2011). Similarity Between the $C^{18}O$ (J = 1-0) Core Mass Function and the Initial Mass Function (IMF) in the S140 Region. ApJ, **732**, 101. 11, 12

ILEE, J.D., WHEELWRIGHT, H.E., OUDMAIJER, R.D., DE WIT, W.J., MAUD, L.T., HOARE, M.G., LUMSDEN, S.L., MOORE, T.J.T., URQUHART, J.S.

& Mottram, J.C. (2013). CO bandhead emission of massive young stellar objects: determining disc properties. MNRAS, **429**, 2960–2973. 24

Jiang, Z., Tamura, M., Hoare, M.G., Yao, Y., Ishii, M., Fang, M. & Yang, J. (2008). Disks around Massive Young Stellar Objects: Are They Common? ApJ, **673**, L175–L179. 44, 45, 46

Jiménez-Serra, I., Zhang, Q., Viti, S., Martín-Pintado, J. & de Wit, W.J. (2012). Chemical Segregation toward Massive Hot Cores: The AFGL2591 Star-forming Region. ApJ, **753**, 34. 13

Jørgensen, J.K. (2011). Interferometric Studies of Low-Mass Protostars. In J. Cernicharo & R. Bachiller, eds., *IAU Symposium*, vol. 280 of *IAU Symposium*, 53–64. 21

Kahn, F.D. (1974). Cocoons around early-type stars. A&A, **37**, 149–162. 6

Klaassen, P.D., Juhasz, A., Mathews, G.S., De Gregorio-Monsalvo, J.C.M.I., van Dishoeck, E.F., Takahashi, S., Akiyama, E., Chapillon, E., Espada, D., Hales, A., Hogerheijde, M.R., Rawlings, M., Schmalzl, M. & Testi, L. (2013). ALMA detection of the rotating molecular disk wind from the young star HD 163296. *ArXiv e-prints*. 32

Klessen, R.S. (2011). Star Formation in Molecular Clouds. In C. Charbonnel & T. Montmerle, eds., *EAS Publications Series*, vol. 51 of *EAS Publications Series*, 133–167. 9, 10

Kraus, S., Hofmann, K.H., Menten, K.M., Schertl, D., Weigelt, G., Wyrowski, F., Meilland, A., Perraut, K., Petrov, R., Robbe-

Dubois, S., Schilke, P. & Testi, L. (2010). A hot compact dust disk around a massive young stellar object. Nature, **466**, 339–342. 25

Kroupa, P. (2002). The Initial Mass Function of Stars: Evidence for Uniformity in Variable Systems. *Science*, **295**, 82–91. 11, 12

Krumholz, M.R., Klein, R.I., McKee, C.F., Offner, S.S.R. & Cunningham, A.J. (2009). The Formation of Massive Star Systems by Accretion. *Science*, **323**, 754–. 8, 21

Kuiper, R., Klahr, H., Beuther, H. & Henning, T. (2010). Circumventing the Radiation Pressure Barrier in the Formation of Massive Stars via Disk Accretion. ApJ, **722**, 1556–1576. 8, 21

Kuiper, R., Klahr, H., Beuther, H. & Henning, T. (2011). Three-dimensional Simulation of Massive Star Formation in the Disk Accretion Scenario. ApJ, **732**, 20. 8, 21

Kurtz, S., Cesaroni, R., Churchwell, E., Hofner, P. & Walmsley, C.M. (2000). Hot Molecular Cores and the Earliest Phases of High-Mass Star Formation. *Protostars and Planets IV*, 299–326. 9, 12

Kutner, M.L. & Ulich, B.L. (1981). Recommendations for calibration of millimeter-wavelength spectral line data. ApJ, **250**, 341–348. 173

Lada, C.J. & Fich, M. (1996). The Structure and Energetics of a Highly Collimated Bipolar Outflow: NGC 2264G. ApJ, **459**, 638. 244

Lada, C.J. & Shu, F.H. (1990). The formation of sunlike stars. *Science*, **248**, 564–572. 1, 5

LADA, C.J., MUENCH, A.A., RATHBORNE, J., ALVES, J.F. & LOMBARDI, M. (2008). The Nature of the Dense Core Population in the Pipe Nebula: Thermal Cores Under Pressure. ApJ, **672**, 410–422. 11

LARSON, R.B. (1981). Turbulence and star formation in molecular clouds. MN-RAS, **194**, 809–826. 7, 212, 213, 214, 263

LARSON, R.B. (1994). The Evolution of Molecular Clouds. In T.L. Wilson & K.J. Johnston, eds., *The Structure and Content of Molecular Clouds*, vol. 439 of *Lecture Notes in Physics, Berlin Springer Verlag*, 13. 10

LAUNHARDT, R., NUTTER, D., WARD-THOMPSON, D., BOURKE, T.L., HENNING, T., KHANZADYAN, T., SCHMALZL, M., WOLF, S. & ZYLKA, R. (2010). Looking Into the Hearts of Bok Globules: Millimeter and Submillimeter Continuum Images of Isolated Star-forming Cores. ApJS, **188**, 139–177. 10

LAY, O.P., CARLSTROM, J.E., HILLS, R.E. & PHILLIPS, T.G. (1994). Protostellar accretion disks resolved with the JCMT-CSO interferometer. ApJ, **434**, L75–L78. 120

LEBRÓN, M., BEUTHER, H., SCHILKE, P. & STANKE, T. (2006). The extremely high-velocity molecular outflow in IRAS 20126+4104. A&A, **448**, 1037–1042. 45, 226, 241, 251

LESTER, D.F., HARVEY, P.M., JOY, M. & ELLIS, H.B., JR. (1986). Far-infrared image restoration analysis of the protostellar cluster in S140. ApJ, **309**, 80–89. 75, 89, 111, 118

Lister, M.L., Cohen, M.H., Homan, D.C., Kadler, M., Kellermann, K.I., Kovalev, Y.Y., Ros, E., Savolainen, T. & Zensus, J.A. (2009). MOJAVE: Monitoring of Jets in Active Galactic Nuclei with VLBA Experiments. VI. Kinematics Analysis of a Complete Sample of Blazar Jets. AJ, **138**, 1874–1892. 29

Lumsden, S.L., Hoare, M.G., Oudmaijer, R.D. & Richards, D. (2002). The population of the Galactic plane as seen by MSX. MNRAS, **336**, 621–636. 16, 204

Lumsden, S.L., Hoare, M.G., Urquhart, J.S., Oudmaijer, R.D., Davies, B., Mottram, J.C., Cooper, H.D.B. & Moore, T.J.T. (2013). The Red MSX Source Survey: the Massive Young Stellar Population of our Galaxy. *ArXiv e-prints*. 16

Lynds, B.T. (1962). Catalogue of Dark Nebulae. ApJS, **7**, 1. 40

MacLaren, I., Richardson, K.M. & Wolfendale, A.W. (1988). Corrections to virial estimates of molecular cloud masses. ApJ, **333**, 821–825. 216

Marti, J., Rodriguez, L.F. & Reipurth, B. (1993). HH 80-81: A Highly Collimated Herbig-Haro Complex Powered by a Massive Young Star. ApJ, **416**, 208. 14

Mauersberger, R., Wilson, T.L., Mezger, P.G., Gaume, R. & Johnston, K.J. (1992). The internal structure of molecular clouds. III - Evidence for molecular depletion in the NGC 2024 condensations. A&A, **256**, 640–651. 10

McKee, C.F. & Tan, J.C. (2003). The Formation of Massive Stars from Turbulent Cores. ApJ, **585**, 850–871. 7

Minchin, N.R., White, G.J. & Padman, R. (1993). A Multitransitional Molecular and Atomic Line Study of S:140. A&A, **277**, 595. 40, 81, 82, 84

Minchin, N.R., Ward-Thompson, D. & White, G.J. (1995a). A submillimetre continuum study of S 140/L 1204: the detection of three new submillimetre sources and a self-consistent model for the region. A&A, **298**, 894. 40, 41, 71, 72, 73, 92, 93, 111, 112, 118

Minchin, N.R., White, G.J. & Ward-Thompson, D. (1995b). ˆ13ˆCO and Cˆ18ˆO observations of S140: delineation. of the outflow structure, a study of fractionation effects and comparison with CI observations. A&A, **301**, 894. 264

Molinari, S., Brand, J., Cesaroni, R. & Palla, F. (1996). Ammonia on YSOs IRAS sources (Molinari+ 1996). *VizieR Online Data Catalog*, **330**, 80573. 16

Molinari, S., Pezzuto, S., Cesaroni, R., Brand, J., Faustini, F. & Testi, L. (2008). The evolution of the spectral energy distribution in massive young stellar objects. A&A, **481**, 345–365. 208, 210, 263

Mookerjea, B., Casper, E., Mundy, L.G. & Looney, L.W. (2007). Kinematics and Chemistry of the Hot Molecular Core in G34.26+0.15 at High Resolution. ApJ, **659**, 447–458. 12

Mottram, J.C., Hoare, M.G., Lumsden, S.L., Oudmaijer, R.D., Urquhart, J.S., Meade, M.R., Moore, T.J.T. & Stead, J.J. (2010).

The RMS survey: far-infrared photometry of young massive stars. A&A, **510**, A89. 17

MOTTRAM, J.C., HOARE, M.G., DAVIES, B., LUMSDEN, S.L., OUDMAIJER, R.D., URQUHART, J.S., MOORE, T.J.T., COOPER, H.D.B. & STEAD, J.J. (2011a). The RMS Survey: The Luminosity Functions and Timescales of Massive Young Stellar Objects and Compact H II Regions. ApJ, **730**, L33. 17, 110

MOTTRAM, J.C., HOARE, M.G., URQUHART, J.S., LUMSDEN, S.L., OUDMAIJER, R.D., ROBITAILLE, T.P., MOORE, T.J.T., DAVIES, B. & STEAD, J. (2011b). The Red MSX Source survey: the bolometric fluxes and luminosity distributions of young massive stars. A&A, **525**, A149. 109, 206

MOZURKEWICH, D., SCHWARTZ, P.R. & SMITH, H.A. (1986). Luminosities of sources associated with molecular outflows. ApJ, **311**, 371–379. 109

MYERS, P.C., LINKE, R.A. & BENSON, P.J. (1983). Dense cores in dark clouds. I - CO observations and column densities of high-extinction regions. ApJ, **264**, 517–537. 1

NATTA, A., TESTI, L., NERI, R., SHEPHERD, D.S. & WILNER, D.J. (2004). A search for evolved dust in Herbig Ae stars. A&A, **416**, 179–186. 80

OCHSENDORF, B.B., ELLERBROEK, L.E., CHINI, R., HARTOOG, O.E., HOFFMEISTER, V., WATERS, L.B.F.M. & KAPER, L. (2011). First firm spectral classification of an early-B pre-main-sequence star: B275 in ¡ASTROBJ¿M 17¡/ASTROBJ¿. A&A, **536**, L1. 268

OSSENKOPF, V. & HENNING, T. (1994). Dust opacities for protostellar cores. A&A, **291**, 943–959. 75, 198

OUDMAIJER, R.D., WHEELWRIGHT, H.E., CARCIOFI, A.C., BJORKMAN, J.E. & BJORKMAN, K.S. (2011). Spectrally and spatially resolved Hα emission from Be stars: their disks rotate Keplerian. In C. Neiner, G. Wade, G. Meynet & G. Peters, eds., *IAU Symposium*, vol. 272 of *IAU Symposium*, 418–419. 26

PALLA, F. & STAHLER, S.W. (1992). The evolution of intermediate-mass protostars. II - Influence of the accretion flow. ApJ, **392**, 667–677. 19

PARKIN, E.R., PITTARD, J.M., HOARE, M.G., WRIGHT, N.J. & DRAKE, J.J. (2009). The interactions of winds from massive young stellar objects: X-ray emission, dynamics and cavity evolution. MNRAS, **400**, 629–645. 110

PATEL, N.A., CURIEL, S., SRIDHARAN, T.K., ZHANG, Q., HUNTER, T.R., HO, P.T.P., TORRELLES, J.M., MORAN, J.M., GÓMEZ, J.F. & ANGLADA, G. (2005). A disk of dust and molecular gas around a high-mass protostar. Nature, **437**, 109–111. 14, 22

PÉREZ, L.M., LAMB, J.W., WOODY, D.P., CARPENTER, J.M., ZAUDERER, B.A., ISELLA, A., BOCK, D.C., BOLATTO, A.D., CARLSTROM, J., CULVERHOUSE, T.L., JOY, M., KWON, W., LEITCH, E.M., MARRONE, D.P., MUCHOVEJ, S.J., PLAMBECK, R.L., SCOTT, S.L., TEUBEN, P.J. & WRIGHT, M.C.H. (2010). Atmospheric Phase Correction Using CARMA-PACS: High Angular Resolution Observations of the FU Orionis Star PP 13S*. ApJ, **724**, 493–501. 57, 63

PLUME, R., JAFFE, D.T. & EVANS, N.J., II (1992). A survey of CS J = 7 - 6 in regions of massive star formation. ApJS, **78**, 505–515. 12

PREIBISCH, T. & SMITH, M.D. (2002). The outflow activity of the protostars in S140 IRS. A&A, **383**, 540–547. 45, 88, 93

PREIBISCH, T., BALEGA, Y.Y., SCHERTL, D., SMITH, M.D. & WEIGELT, G. (2001). High-resolution near-infrared study of the deeply embedded young stellar object S140 IRS 3. A&A, **378**, 539–545. 75, 86

PROGA, D. (2003). On Resonance-Line Profiles Predicted by Radiation-driven Disk-Wind Models. ApJ, **592**, L9–L12. 28

PROGA, D. (2004). Mass Outflows from Accretion Disks: Old and New Challenges. In G.T. Richards & P.B. Hall, eds., *AGN Physics with the Sloan Digital Sky Survey*, vol. 311 of *Astronomical Society of the Pacific Conference Series*, 141. 27, 28

PROGA, D. (2007). Theory of Winds in AGNs. In L.C. Ho & J.W. Wang, eds., *The Central Engine of Active Galactic Nuclei*, vol. 373 of *Astronomical Society of the Pacific Conference Series*, 267. 28

PROGA, D., STONE, J.M. & DREW, J.E. (1998). Radiation-driven winds from luminous accretion discs. MNRAS, **295**, 595. 28

PROGA, D., STONE, J.M. & KALLMAN, T.R. (2000). Dynamics of Line-driven Disk Winds in Active Galactic Nuclei. ApJ, **543**, 686–696. 27

PUDRITZ, R.E., BANERJEE, R. & OUYED, R. (2009). *The role of jets in the formation of planets, stars and galaxies*, 84. Cambridge University Press. 29, 31, 32

QIU, K., ZHANG, Q., BEUTHER, H. & FALLSCHEER, C. (2012). Forming an O Star via Disk Accretion? ApJ, **756**, 170. 88

RATHBORNE, J.M., GARAY, G., JACKSON, J.M., LONGMORE, S., ZHANG, Q. & SIMON, R. (2011). Hot Molecular Cores in Infrared Dark Clouds. ApJ, **741**, 120. 10

REIPURTH, B., HARTIGAN, P., HEATHCOTE, S., MORSE, J.A. & BALLY, J. (1997). Hubble Space Telescope Images of the HH 111 Jet. AJ, **114**, 757–780. 30

RICHER, J.S., PADMAN, R., WARD-THOMPSON, D., HILLS, R.E. & HARRIS, A.I. (1993). The molecular environment of S106 IR. MNRAS, **262**, 839–854. 261

RICHER, J.S., SHEPHERD, D.S., CABRIT, S., BACHILLER, R. & CHURCH-WELL, E. (2000). Molecular Outflows from Young Stellar Objects. *Protostars and Planets IV*, 867. 29, 30, 31

RIDGE, N.A. & MOORE, T.J.T. (2001). A single distance sample of molecular outflows from high-mass young stellar objects. A&A, **378**, 495–508. 14, 33, 34, 35, 224, 250

RIEKE, G.H. & LEBOFSKY, M.J. (1985). The interstellar extinction law from 1 to 13 microns. ApJ, **288**, 618–621. 115

ROBITAILLE, T.P., WHITNEY, B.A., INDEBETOUW, R. & WOOD, K. (2007). Interpreting Spectral Energy Distributions from Young Stellar Objects. II. Fitting Observed SEDs Using a Large Grid of Precomputed Models. ApJS, **169**, 328–352. 109

SALPETER, E.E. (1955). The Luminosity Function and Stellar Evolution. ApJ, **121**, 161. 11

SÁNCHEZ-MONGE, Á., CESARONI, R., BELTRÁN, M.T., KUMAR, M.S.N., STANKE, T., ZINNECKER, H., ETOKA, S., GALLI, D., HUMMEL, C.A., MOSCADELLI, L., PREIBISCH, T., RATZKA, T., VAN DER TAK, F.F.S., VIG, S., WALMSLEY, C.M. & WANG, K.S. (2013). A candidate circumbinary Keplerian disk in G35.20-0.74 N: A study with ALMA. A&A, **552**, L10. 266

SAULT, R.J., TEUBEN, P.J. & WRIGHT, M.C.H. (1995). A Retrospective View of MIRIAD. In R. A. Shaw, H. E. Payne, & J. J. E. Hayes, ed., *Astronomical Data Analysis Software and Systems IV*, vol. 77 of *Astronomical Society of the Pacific Conference Series*, 433. 47

SCHERTL, D., BALEGA, Y., HANNEMANN, T., HOFMANN, K., PREIBISCH, T. & WEIGELT, G. (2000). Diffraction-limited bispectrum speckle interferometry and speckle polarimetry of the young bipolar outflow source S140 IRS1. A&A, **361**, L29–L32. 43, 44, 88

SCHNEIDER, N., BONTEMPS, S., SIMON, R., OSSENKOPF, V., FEDERRATH, C., KLESSEN, R.S., MOTTE, F., ANDRÉ, P., STUTZKI, J. & BRUNT, C. (2011). The link between molecular cloud structure and turbulence. A&A, **529**, A1. 3, 10

Schwartz, P.R. (1989). Jets and bullets in S140. ApJ, **338**, L25–L28. 41, 42

Scoville, N.Z., Sargent, A.I., Sanders, D.B., Claussen, M.J., Masson, C.R., Lo, K.Y. & Phillips, T.G. (1986). High-resolution mapping of molecular outflows in NGC 2071, W49, and NGC 7538. ApJ, **303**, 416–432. 81

Sharpless, S. (1959). A Catalogue of H II Regions. ApJS, **4**, 257. 40

Shepherd, D.S. & Churchwell, E. (1996). Bipolar Molecular Outflows in Massive Star Formation Regions. ApJ, **472**, 225. 33, 224, 250

Shepherd, D.S. & Kurtz, S.E. (1999). A 1000 AU Rotating Disk around the Massive Young Stellar Object G192.16-3.82. ApJ, **523**, 690–700. 14

Shepherd, D.S., Yu, K.C., Bally, J. & Testi, L. (2000). The Molecular Outflow and Possible Precessing Jet from the Massive Young Stellar Object IRAS 20126+4104. ApJ, **535**, 833–846. 15, 45, 174, 175, 183, 227, 229, 231, 239, 246, 250

Shu, F.H., Adams, F.C. & Lizano, S. (1987). Star formation in molecular clouds - Observation and theory. ARA&A, **25**, 23–81. 1, 2

Shu, F.H., Lizano, S., Ruden, S.P. & Najita, J. (1988). Mass loss from rapidly rotating magnetic protostars. ApJ, **328**, L19–L23. 31, 32

Shu, F.H., Najita, J.R., Shang, H. & Li, Z.Y. (2000). X-Winds Theory and Observations. *Protostars and Planets IV*, 789. 31, 32

Simon, M., Felli, M., Massi, M., Cassar, L. & Fischer, J. (1983). Infrared line and radio continuum emission of circumstellar ionized regions. ApJ, **266**, 623–645. 42

SIMPSON, R.J., NUTTER, D. & WARD-THOMPSON, D. (2008). The initial conditions of star formation - VIII. An observational study of the Ophiuchus cloud L1688 and implications for the pre-stellar core mass function. MNRAS, **391**, 205–214. 11

SIMPSON, R.J., JOHNSTONE, D., NUTTER, D., WARD-THOMPSON, D. & WHITWORTH, A.P. (2011). The initial conditions of isolated star formation - X. A suggested evolutionary diagram for pre-stellar cores. MNRAS, **417**, 216–227. 10

SMITH, R.J., CLARK, P.C. & BONNELL, I.A. (2009). Fragmentation in molecular clouds and its connection to the IMF. MNRAS, **396**, 830–841. 11

SNELL, R.L., SCOVILLE, N.Z., SANDERS, D.B. & ERICKSON, N.R. (1984). High-velocity molecular jets. ApJ, **284**, 176–193. 244

SOLLINS, P.K., HUNTER, T.R., BATTAT, J., BEUTHER, H., HO, P.T.P., LIM, J., LIU, S.Y., OHASHI, N., SRIDHARAN, T.K., SU, Y.N., ZHAO, J.H. & ZHANG, Q. (2004). Mapping the Outflow from G5.89-0.39 in SiO J = 5-4. ApJ, **616**, L35–L38. 35

SRIDHARAN, T.K., BEUTHER, H., SCHILKE, P., MENTEN, K.M. & WYROWSKI, F. (2002). High-Mass Protostellar Candidates. I. The Sample and Initial Results. ApJ, **566**, 931–944. 16

STRÖMGREN, B. (1939). The Physical State of Interstellar Hydrogen. ApJ, **89**, 526. 17

Swift, J.J. & Williams, J.P. (2008). On the Evolution of the Dense Core Mass Function. ApJ, **679**, 552–556. 11

Tachihara, K., Onishi, T., Mizuno, A. & Fukui, Y. (2002). Statistical study of $C^{18}O$ dense cloud cores and star formation. A&A, **385**, 909–920. 170, 213

Takahashi, S., Saito, M., Ohashi, N., Kusakabe, N., Takakuwa, S., Shimajiri, Y., Tamura, M. & Kawabe, R. (2008). Millimeter- and Submillimeter-Wave Observations of the OMC-2/3 Region. III. An Extensive Survey for Molecular Outflows. ApJ, **688**, 344–361. 225

Taylor, G.B., Carilli, C.L. & Perley, R.A., eds. (1999). *Synthesis Imaging in Radio Astronomy II*, vol. 180 of *Astronomical Society of the Pacific Conference Series*. 50, 51, 53, 57

Terebey, S., Shu, F.H. & Cassen, P. (1984). The collapse of the cores of slowly rotating isothermal clouds. ApJ, **286**, 529–551. 100, 106

Testi, L., Natta, A., Shepherd, D.S. & Wilner, D.J. (2003). Large grains in the disk of CQ Tau. A&A, **403**, 323–328. 80

Thompson, A.R., Moran, J.M. & Swenson, G.W., Jr. (2001). *Interferometry and Synthesis in Radio Astronomy, 2nd Edition*. Wiley-Interscience. 50, 53, 120

Tofani, G., Felli, M., Taylor, G.B. & Hunter, T.R. (1995). Exploring the engines of molecular outflows. Radio continuum and H_2O maser observations. A&AS, **112**, 299. 14, 43

Torrelles, J.M., Patel, N.A., Curiel, S., Ho, P.T.P., Garay, G. & Rodríguez, L.F. (2007). The Circumstellar Structure and Excitation Effects around the Massive Protostar Cepheus A HW 2. ApJ, **666**, L37–L40. 22, 85

Trinidad, M.A., Torrelles, J.M., Rodríguez, L.F. & Curiel, S. (2007). Multiple Sources toward the High-Mass Young Star S140 IRS 1. AJ, **134**, 1870–1876. 93

Ulrich, R.K. (1976). An infall model for the T Tauri phenomenon. ApJ, **210**, 377–391. 100, 106

Urquhart, J.S., Busfield, A.L., Hoare, M.G., Lumsden, S.L., Clarke, A.J., Moore, T.J.T., Mottram, J.C. & Oudmaijer, R.D. (2007). The RMS survey. Radio observations of candidate massive YSOs in the southern hemisphere. A&A, **461**, 11–23. 17

Urquhart, J.S., Busfield, A.L., Hoare, M.G., Lumsden, S.L., Oudmaijer, R.D., Moore, T.J.T., Gibb, A.G., Purcell, C.R., Burton, M.G., Maréchal, L.J.L., Jiang, Z. & Wang, M. (2008). The RMS survey. ^{13}CO observations of candidate massive YSOs in the northern Galactic plane. A&A, **487**, 253–264. 17

Urquhart, J.S., Hoare, M.G., Purcell, C.R., Lumsden, S.L., Oudmaijer, R.D., Moore, T.J.T., Busfield, A.L., Mottram, J.C. & Davies, B. (2009). The RMS survey. 6 cm continuum VLA observations towards candidate massive YSOs in the northern hemisphere. A&A, **501**, 539–551. 17

Urquhart, J.S., Moore, T.J.T., Hoare, M.G., Lumsden, S.L., Oudmaijer, R.D., Rathborne, J.M., Mottram, J.C., Davies, B. & Stead, J.J.

(2011a). The Red MSX Source survey: distribution and properties of a sample of massive young stars. MNRAS, **410**, 1237–1250. 198

Urquhart, J.S., Morgan, L.K., Figura, C.C., Moore, T.J.T., Lumsden, S.L., Hoare, M.G., Oudmaijer, R.D., Mottram, J.C., Davies, B. & Dunham, M.K. (2011b). The Red MSX Source survey: ammonia and water maser analysis of massive star-forming regions. MNRAS, **418**, 1689–1706. 214

Urquhart, J.S., Hoare, M.G., Lumsden, S.L., Oudmaijer, R.D., Moore, T.J.T., Mottram, J.C., Cooper, H.D.B., Mottram, M. & Rogers, H.C. (2012). The RMS survey: resolving kinematic distance ambiguities towards a sample of compact H II regions using H I absorption. MNRAS, **420**, 1656–1672. 17

Vaidya, B., Fendt, C., Beuther, H. & Porth, O. (2011). Jet Formation from Massive Young Stars: Magnetohydrodynamics versus Radiation Pressure. ApJ, **742**, 56. 36, 37, 91

van der Tak, F.F.S., van Dishoeck, E.F., Evans, N.J., II, Bakker, E.J. & Blake, G.A. (1999). The Impact of the Massive Young Star GL 2591 on Its Circumstellar Material: Temperature, Density, and Velocity Structure. ApJ, **522**, 991–1010. 99

van der Tak, F.F.S., van Dishoeck, E.F., Evans, N.J., II & Blake, G.A. (2000). Structure and Evolution of the Envelopes of Deeply Embedded Massive Young Stars. ApJ, **537**, 283–303. 99, 100, 118

Velusamy, T. & Langer, W.D. (1998). Outflow-infall interactions as a mechanism for terminating accretion in protostars. Nature, **392**, 685–687. 30

VLEMMINGS, W.H.T. (2008). A new probe of magnetic fields during high-mass star formation. Zeeman splitting of 6.7 GHz methanol masers. A&A, **484**, 773–781. 266

VLEMMINGS, W.H.T., SURCIS, G., TORSTENSSON, K.J.E. & VAN LANGEVELDE, H.J. (2010). Magnetic field regulated infall on the disc around the massive protostar CepheusAHW2. MNRAS, **404**, 134–143. 266

WALL, J.V. & JENKINS, C.R. (2003). *Practical Statistics for Astronomers*. Cambridge University Press. 200, 203

WALMSLEY, M. (1995). Dense Cores in Molecular Clouds. In S. Lizano & J.M. Torrelles, eds., *Revista Mexicana de Astronomia y Astrofisica Conference Series*, vol. 1 of *Revista Mexicana de Astronomia y Astrofisica, vol. 27*, 137. 18

WANG, K., ZHANG, Q., WU, Y. & ZHANG, H. (2011). Hierarchical Fragmentation and Jet-like Outflows in IRDC G28.34+0.06: A Growing Massive Protostar Cluster. ApJ, **735**, 64. 224

WANG, K.S., VAN DER TAK, F.F.S. & HOGERHEIJDE, M.R. (2012). Kinematics of the inner thousand AU region around the young massive star ¡AS-TROBJ¿AFGL 2591-VLA3¡/ASTROBJ¿: a massive disk candidate? A&A, **543**, A22. 24

WEIGELT, G., BALEGA, Y.Y., PREIBISCH, T., SCHERTL, D. & SMITH, M.D. (2002). Bispectrum speckle interferometry of the massive protostellar object S140 IRS 1: Evidence for multiple outflows. A&A, **381**, 905–913. 44, 45, 46, 73, 87, 88, 93, 94, 113, 117

WHEELWRIGHT, H.E., BJORKMAN, J.E., OUDMAIJER, R.D. & CARCIOFI, A.C. (2012). Spectroastrometry and NLTE Modeling of the Disk Around the Be Star β CMi. In A.C. Carciofi & T. Rivinius, eds., *Circumstellar Dynamics at High Resolution*, vol. 464 of *Astronomical Society of the Pacific Conference Series*, 205. 26

WHELAN, E.T., RAY, T.P., BACCIOTTI, F., NATTA, A., TESTI, L. & RANDICH, S. (2005). A resolved outflow of matter from a brown dwarf. Nature, **435**, 652–654. 29

WHITNEY, B.A. (2011). Monte Carlo radiative transfer. *Bulletin of the Astronomical Society of India*, **39**, 101–127. 107

WHITNEY, B.A. & HARTMANN, L. (1992). Model scattering envelopes of young stellar objects. I - Method and application to circumstellar disks. ApJ, **395**, 529–539. 98, 108, 112

WHITNEY, B.A. & HARTMANN, L. (1993). Model scattering envelopes of young stellar objects. II - Infalling envelopes. ApJ, **402**, 605–622. 108, 112

WHITNEY, B.A., WOOD, K., BJORKMAN, J.E. & COHEN, M. (2003a). Two-dimensional Radiative Transfer in Protostellar Envelopes. II. An Evolutionary Sequence. ApJ, **598**, 1079–1099. 38, 98, 99, 101, 106, 112, 123, 125, 126, 128, 131, 136

WHITNEY, B.A., WOOD, K., BJORKMAN, J.E. & WOLFF, M.J. (2003b). Two-dimensional Radiative Transfer in Protostellar Envelopes. I. Effects of Geometry on Class I Sources. ApJ, **591**, 1049–1063. 38, 98, 99, 100, 102, 106, 108, 110, 135

WHITNEY, B.A., INDEBETOUW, R., BJORKMAN, J.E. & WOOD, K. (2004). Two-Dimensional Radiative Transfer in Protostellar Envelopes. III. Effects of Stellar Temperature. ApJ, **617**, 1177–1190. 99, 101, 106, 110, 119

WHITNEY, B.A., ROBITAILLE, T.P., INDEBETOUW, R., WOOD, K., BJORK-MAN, J.E. & DENZMORE, P. (2005). 2-D and 3-D radiation transfer models of high-mass star formation. In R. Cesaroni, M. Felli, E. Churchwell & M. Walmsley, eds., *Massive Star Birth: A Crossroads of Astrophysics*, vol. 227 of *IAU Symposium*, 206–215. 98

WILKING, B.A., BLACKWELL, J.H. & MUNDY, L.G. (1990). High-velocity molecular gas associated with cold IRAS sources. AJ, **100**, 758–770. 224, 231, 246

WILLNER, S.P., GILLETT, F.C., HERTER, T.L., JONES, B., KRASSNER, J., MERRILL, K.M., PIPHER, J.L., PUETTER, R.C., RUDY, R.J., RUSSELL, R.W. & SOIFER, B.T. (1982). Infrared spectra of protostars - Composition of the dust shells. ApJ, **253**, 174–187. 111, 115, 118, 126, 128

WILSON, T.L. & ROOD, R. (1994). Abundances in the Interstellar Medium. ARA&A, **32**, 191–226. 175, 184, 231, 273

WOLFIRE, M.G. & CASSINELLI, J.P. (1987). Conditions for the formation of massive stars. ApJ, **319**, 850–867. 6

WOOD, D.O.S. & CHURCHWELL, E. (1989a). Massive stars embedded in molecular clouds - Their population and distribution in the galaxy. ApJ, **340**, 265–272. 17

WOOD, D.O.S. & CHURCHWELL, E. (1989b). The morphologies and physical properties of ultracompact H II regions. ApJS, **69**, 831–895. 18

WRIGHT, A.E. & BARLOW, M.J. (1975). The radio and infrared spectrum of early-type stars undergoing mass loss. MNRAS, **170**, 41–51. 77

WU, Y., WEI, Y., ZHAO, M., SHI, Y., YU, W., QIN, S. & HUANG, M. (2004). A study of high velocity molecular outflows with an up-to-date sample. A&A, **426**, 503–515. 34, 35

WU, Y., ZHANG, Q., CHEN, H., YANG, C., WEI, Y. & HO, P.T.P. (2005). CO J = 2-1 Maps of Bipolar Outflows in Massive Star-forming Regions. AJ, **129**, 330–347. 224

YAMASHITA, T., SUZUKI, H., KAIFU, N., TAMURA, M., MOUNTAIN, C.M. & MOORE, T.J.T. (1989). A new CO bipolar flow and dense disk system associated with the infrared reflection nebula GGD 27 IRS. ApJ, **347**, 894–900. 260

YORKE, H.W. & SONNHALTER, C. (2002). On the Formation of Massive Stars. ApJ, **569**, 846–862. 6, 8

ZHANG, L.Y. & GAO, Y. (2009). Characteristics of Massive Star-forming Molecular Cores: The Spectral Observations of ^{12}CO, ^{13}CO and C^{18}O and the Statistical Comparison. CA&A, **33**, 32–47. 170

ZHANG, Q., HUNTER, T.R., BRAND, J., SRIDHARAN, T.K., MOLINARI, S., KRAMER, M.A. & CESARONI, R. (2001). Search for CO Outflows toward

a Sample of 69 High-Mass Protostellar Candidates: Frequency of Occurrence. ApJ, **552**, L167–L170. 14, 33, 229

Zhang, Q., Hunter, T.R., Brand, J., Sridharan, T.K., Cesaroni, R., Molinari, S., Wang, J. & Kramer, M. (2005). Search for CO Outflows toward a Sample of 69 High-Mass Protostellar Candidates. II. Outflow Properties. ApJ, **625**, 864–882. 14

Zhang, Q., Hunter, T.R., Beuther, H., Sridharan, T.K., Liu, S.Y., Su, Y.N., Chen, H.R. & Chen, Y. (2007). Multiple Jets from the High-Mass (Proto)stellar Cluster AFGL 5142. ApJ, **658**, 1152–1163. 79

Zhou, S., Evans, N.J., II, Mundy, L.G. & Kutner, M.L. (1993). New VLA Observations of NH 3 in S140. ApJ, **417**, 613. 42, 93

Zinnecker, H. & Yorke, H.W. (2007). Toward Understanding Massive Star Formation. ARA&A, **45**, 481–563. 4